Modeling of neuron-astrocyte interaction : application to signal and image processing

Jhunlyn Lorenzo

UBFC
UNIVERSITÉ
BOURGOGNE FRANCHE-COMTÉ

UNIVERSITÉ DE BOURGOGNE

THÈSE DE DOCTORAT

DE L'ÉTABLISSEMENT UNIVERSITÉ BOURGOGNE FRANCHE-COMTÉ

PRÉPARÉE À L'UNIVERSITÉ DE BOURGOGNE

École doctorale n°37

Sciences Pour l'Ingénieur et Microtechniques

Doctorat d'Instrumentation et Informatique de l'Image

par

JHUNLYN LORENZO

Modeling of neuron-astrocyte interaction: application to signal and image processing

Thèse présentée et soutenue à Dijon, le 27 septembre 2022

Composition du Jury :

GOUTON PIERRE	Professeur à l'Université de Bourgogne	Président
BUHRY LAURE	Maître de confeérences à l'Universiteé de Lorraine	Rapporteure
VIDAL ALEXANDRE	Maître de conférences à Universiteé d'Evry Val d'Essonne	Rapporteur
THOMAS ELIZABETH	Maître de conférences à l'Université de Bourgogne	Examinatrice
CESSAC BRUNO	Directeur de recherche à l'Universiteé Côte d'Azur	Examinateur
XU BINBIN	Maître de conférences à l'Ecole des Mines Alès	Examinateur
BINCZAK STÉPHANE	Professeur à l'Université de Bourgogne	Co-Directeur de thèse
JACQUIR SABIR	Professeur à l'Université Paris-Saclay	Directeur de thése

N° 9 8 3 7 0

ACKNOWLEDGMENTS

I would like to recognize my supervisors' invaluable support and guidance, Prof. Sabir Jacquir, and Prof. Stéphane Binczak. I came here to France not knowing a single soul, and I am deeply grateful that I met such kind, understanding, and supportive advisors. Thank you for the opportunity to pursue my Ph.D., the experiences during my studies, and the sincere career advice. It is my pleasure to work with you, and I will be forever grateful to know you.

I would like to express my deepest appreciation to the thesis committee. I sincerely thank Dr. Laure Buhry and Dr. Alexandre Vidal for their time and effort in reviewing our work and sharing their knowledge significant for the success of our work. I would like to recognize the effort of Prof. Pierre Gouton, Dr. Elizabeth Thomas, Dr. Bruno Cessac, and Dr. Binbin Xu for participating in my thesis defense as Examiners.

This research would not have been possible without the support from the Commission of Higher Education, Philippines, and the Embassy of France in the Philippines (CHED-PhilFrance). Thank you for your vital assistance that allowed me to study abroad. I thank the ED SPIM, and Laboratoire ImViA for the opportunities opened to me during my Ph.D. student years. I would also like to thank HPC-Europa3 and the Barcelona Computing Center for sharing their resources and helping us with our research. To Prof. Juan Antonio Rico-Gallego of the University of Extremadura, Spain, thank you for sharing your knowledge and being a great host during my stay in Spain.

I want to pay my special regard to Cavite State University, Philippines, for motivating me to pursue my doctoral degree, especially to our College Dean, Dr. David Cero. Thank you for your support and patience, and most of all, for believing that I will be a doctor one day. My heartfelt appreciation to Sheryl, Geboy, and Aivar, my friends who are always just one call away.

Special thanks to my colleagues and friends in ImViA, to Abdennacer and Solomon who are like brothers to me, to Ichraf and Thao, my sisters through good and tough times, and to Kibrom who inspires me to dream again.

And most importantly, to my family, who always make me feel loved and special, I can't thank you enough. To Mama and Papa, Jayzen and Jeanelle, thank you for always supporting my dreams; this one is for you. Remember, my love for you is never-ending. I am coming home soon.

Jhunlyn Juance LORENZO Dijon, September 2022

ACRONYMS

2LM	–	Two-layer model
AdEX	–	Adaptive exponential integrate-and-fire
AI	–	Artificial Intelligence
AIS	–	Axon initial segment
AMPAR	–	α-amino-3-hydroxy-5-methyl-4-isoxazolepropionic acid receptor
ANN	–	Artificial neural network
AP	–	Action potential
ATP	–	Adenosine triphosphate
bAP	–	Backpropagating action potential
CA	–	*Cornu Ammonis* (hippocampal subfield)
Ca^{2+}	–	Calcium
Ca_v	–	Voltage-gated calcium channel
CICR	–	Calcium-induced calcium-release
CNS	–	Central nervous system
DG	–	Dentate Gyrus
EAAT	–	Excitatory amino acid transporter
EIF	–	Exponential integrate-and-fire
EPSC	–	Excitatory postsynaptic current
EPSP	–	Excitatory postsynaptic potential
ER	–	Endoplasmic reticulum
FFT	–	Fast Fourier Transform
FHN	–	FitzHugh-Nagumo
GABA	–	γ-aminobutyric acid
GEM	–	Gemeralized exponential model
GEVI	–	Genetically encoded voltage indicator
GIF	–	Generalized integrate-and-fire
GJC	–	Gap junction connection
GLAST	–	Glutamate/aspartate transporter
GLM	–	Generalized linear model
Glu^-	–	Glutamate
GluT	–	Glutamate transporter
GLT-1	–	Glutamate transporter-1
GPCR	–	G-protein coupled receptors
HCN	–	Hyperpolarization-activated cyclic nucleotide-gated
HH	–	Hodgkin-Huxley
hLN	–	Hierarchical Linear-Nonlinear
HVA	–	High-voltage-activated channel
ICW	–	Intercellular calcium wave
IF	–	Integrate-and-Fire
iGluR	–	Ionotropic glutamate receptor

IO	–	Input-Output
IP-5P	–	Inositol Polyphosphate 5-phosphatase
IP_3	–	Inositol triphosphate
IP_3-3K	–	Inositol triphosphate 3-Kinase
IPSP	–	Inhibitory postsynaptic potential
IPR	–	IP_3 receptor
K^+	–	Potassium
K_v	–	Voltage-gated potassium channel
LIF	–	Leaky integrate-and-fire
LNP	–	Linear-Nonlinear Poisson
LTP	–	Long-term potentiation
mGluR	–	Metabotropic glutamate receptor
ML	–	Machine Learning
MNIST	–	modified National Institute of Standards and Technology
Na^+	–	Sodium
Na_v	–	Voltage-gated sodium channel
NCX	–	Na^+/Ca^{2+} exchanger
NKA	–	Na^+/K^+ ATPase
NMDAR	–	N–Methyl-D–aspartate receptor
NR2B	–	NMDA receptor subunit 2B
PAP	–	Perisynaptic Astrocytic Process
PKC	–	Protein kinase C
PLC	–	Phopholipase C
PMCA	–	Plasma membrane calcium ATPase
PSD	–	Postsynaptic density
QIF	–	Quadratic integrate-and-fire
RC	–	Resistance-capacitance
RRP	–	Readily releasable pool of vesicles
SERCA	–	Sarco-endoplasmic reticulum calcium ATPase
SIC	–	Slow inward current
SLMV	–	Synaptic-like microvesicle
SNAP-25	–	Synaptosome-associated protein 25
SNARE	–	Soluble N-ethylmaleimide-sensitive factor attachment protein receptor
SNAN	–	Spiking Neuron-Astrocyte Network
SNN	–	Spiking Neural/Neuron Network
STD	–	Short-term depression
STDP	–	Spike-timing-dependent plasticity
STED	–	Stimulated-emission-depletion
STF	–	Short-term facilitation
SYT1	–	Synaptotagmin 1 protein
TMM	–	Tsodyks-Markram model
VDCC	–	Volatge-dependent calcium channels
VGC	–	Voltage-gated channel

Contents

1

INTRODUCTION

What makes the brain so powerful? Is it the millions of tightly packed but well-organized neurons efficiently intercommunicating via synapses? Is it its capacity to learn information, store it in memory, and retrieve it for future use? Or is it the multilayer networks executing parallel computations while systematically allocating the brain energy resources? For decades, these questions have been the subject of neuroscience investigation, and the brain continuously inspires neural engineers. As technology advances, our understanding of the brain (its components, organization, and processes) becomes ever more complex. Indeed, it is a well-grounded knowledge that neurons are the fundamental computing elements of the brain, whose cellular activities are driven by the interplay between their chemical and electrical dynamics. With the advent of neurophysiological measurement tools, neuroscientists recently introduced astrocytes, a type of glial cells, as an active component capable of executing neuron-like functions, such as information transmission and computation, but within a longer time scale and with an entirely chemical activation. This concept, hence, reshapes our perspective regarding the brain – which is now a more powerful system than ever.

As the name implies, astrocytes are star-shaped glial cells constituting 20% to 40% of the total number of cells in the brain [1]. Previously, astrocytes are thought of as passive elements, directing the axons, enwrapping synapses, providing metabolic and structural support to neurons and blood vessels, and maintaining brain homeostasis by regulating extracellular molecules. Glial cells outnumber neurons, and the astrocyte-to-neuron ratio can be one depending on the brain region [2, 3]. An astrocyte fills the interstitial space between neurons, allowing the astrocytic processes to cover thousands of synapses formed by hundreds of neurons passing through its territory. Therefore, the proximity of astrocytes to neurons, especially in the synapses, hints that astrocytes can be more than structural support but may also influence neuronal communication. More than 20 years ago, shortly after Araque et al. [4] proposed the concept of tripartite synapse, where the astrocyte forms the third component in pre- to postsynaptic neuronal communication, the research on astrocyte-mediated neuronal signaling expanded considerably.

Astrocytes are electrically passive, and the signaling mechanisms are slow; howbeit, astrocytes display numerous similarities with neurons.

- Presynaptic neurotransmitters-mediated activation of metabotropic glutamate (Glu^{-}) receptors (mGluRs) on the astrocytic process membrane activates the production of a secondary messenger called Inositol trisphosphate (IP_3) that triggers the IP_3-dependent calcium (Ca^{2+}) oscillation in the cytosol [5, 6]. Therefore, astrocytes indirectly integrate presynaptic signals (like postsynaptic neurons) via intracellular Ca^{2+} diffusion.

- Astrocytes are active in terms of their cytosolic Ca^{2+} concentration ($[Ca^{2+}]$) levels, where $[Ca^{2+}]$ above a threshold generates Glu^{-} spikes in the extrasynaptic space [7, 8]. In neurons, membrane potential above a certain threshold generates an action potential (AP).
- The released extrasynaptic Glu^{-} diffuses to the pre- or postsynaptic neuron membranes, creating signaling pathways – the same in neurons with its released neurotransmitters (synaptic Glu^{-}) diffusing through the synaptic or extracellular space [7].
- If neurons communicate via the synapses (neuronal junctions), astrocytes communicate via gap junctions [9].
- Lastly, Ca^{2+} imaging techniques suggest that astrocytes form a network where cells communicate via intercellular Ca^{2+} wave (ICW) propagation [10].

Neurons and astrocytes together form a spiking neuron-astrocyte network. In artificial intelligence (AI), spiking networks are the next-generation networks that closely mimic brain computation and whose signal transmission operates on spike events [11] . Neural engineers are now recognizing the computational capabilities of astrocytes and incorporating their slow dynamics into applications such as network synchrony [12], fault tolerance [13], and autoencoders [14]. Though there are numerous studies on their biological characteristics and signaling mechanisms, the definite influence of astrocytes in network information transmission is not fully defined yet. In addition, research on the potential of astrocytes as computational units in neural networks, be it biological or artificial, is just beginning.

In this study, we explore the capacity of astrocytes to influence neural activities, from cellular level computation to network-level neural coding. The primary defined influence of astrocytes is their modulation of synaptic plasticity [15]; accordingly, we study the cellular elements and network formation comprising the hippocampus, the brain region responsible for memory formation and learning. Inspired by the biological neuron-astrocyte interactions, we then develop an astrocyte-mediated spiking neural network for deep learning applications. Here, we implement a bottom-up strategy, modeling the neuronal and astrocytic signaling mechanisms, the information transfer within the tripartite synapse, the signal integration leading to neuronal and astrocytic activation, and the neuron-astrocyte network communication. Specifically, we aim to

1. Model a biologically plausible tripartite synapse to identify the extent to which synaptic plasticity benefits from gliotransmission,
2. Simulate the ICW propagation in the astrocytic network and determine the impact of astrocytic heterogeneity in neural communication,
3. Develop a neuron-astrocyte network using simplified models capable of recognizing images using unsupervised learning, and
4. Propose an integration scheme for faster learning.

The tripartite synapse is a multivariable and complex system, and developing a biologically plausible network means that we must delve deeper into the extracellular connection between neurons and astrocytes and their intracellular processes. Chapter 2 presents the network formation in the hippocampus consisting of the so-called trisynaptic circuit and the roles of this region in memory storage and learning. Furthermore, it defines the biophysical characteristics of pyramidal neurons and their AP generating mechanisms. In parallel, it presents the computational models describing the electrical dynamics of the

membrane leading to the AP activation in the axon initial segment (AIS) and its transmission along the myelinated axon through saltatory conduction. Chapter 3 is about the neural transmission from the pre- to the postsynaptic neuron. The transmission starts from the slow and fast Ca^{2+} dynamics triggering the neurotransmitter release into the synaptic cleft to the synaptic integration by the postsynaptic neuron. It simultaneously presents the mathematical models describing the neuronal synaptic integration and neural coding scheme. Chapter 4 describes the biophysical characteristics and chemical signaling pathways in astrocytes and the related computational models, specifically the slow IP_3-dependent Ca^{2+} dynamics driven by the presynaptic signals and the astrocytic Glu- modulating the pre- and postsynaptic activities. As the astrocytes create a network separate from the neurons, a syncytium connected via gap junctions and communicate through ICW propagation, Chapter 4 also presents the general framework of the astrocytic network detailing the intra- and extracellular Ca^{2+} diffusions within.

We illustrate and model the interconnection between the neurons and astrocytes forming the tripartite synapse based on the biological characteristics of the cellular elements in the CA3-CA1 hippocampal region in Chapter 5. This chapter consists of two parts. First, it focuses on the tripartite synapse dynamics with the stochastic neurotransmitter release process and where the astrocytic Glu- signaling pathway forms a feedback system by modulating the presynaptic release probabilities. Here, we determined the astrocytic influence on synaptic efficacy. Then, we extend the tripartite synapse communication into a neuron-astrocyte network. In this part, the astrocyte creates feedforward and feedback pathways that modulate the presynaptic release probability and the postsynaptic membrane potential. In addition, the astrocytes perform Ca^{2+} integration, and ICW propagates in the astrocytic network with varying connectivity. Then, we discussed the influence of heterogeneity of the astrocytic network on the communication strength between neurons. The models were developed using MATLAB and simulated using the high-performance computing (HPC) resources of the Université de Bourgogne.

The simulation results in Chapter 5 indicate that astrocytes enhance neural activities depending on the astrocytic connectivity and network topology. Inspired by their biological impact, we developed an artificial spiking neuron-astrocyte network capable of recognizing features and classifying images and presented the results in Chapter 6. The handwritten digits from the standard MNIST (Modified National Institute of Standards and Technology) dataset [16] are converted into spiking frequencies that trigger the spiking activities of the Poisson neurons in the Input layer. The synapses are densely connected with the adaptive Integrate-and Fire (AIF) neurons with later inhibitions of the First layer. Between these two neuron layers is the astrocytic layer that integrates the presynaptic signals and creates additional inputs that modulate the postsynaptic neurons. The neurons learn following the spike-timing-dependent plasticity algorithm. The classifier unit determines the input class based on the spiking patterns produced by the First layer neurons. The networks were simulated using the Brian2 simulator with the python programming language. This study is a collaboration with the Department of Computer Systems, Engineering and Telematics of the University of Extremadura, Spain, and is funded by the HPC-Europa3 Transnational Programme (INFRAIA-2016-1-730897) with the Barcelona Computing Center, which provided the computing resources. To our knowledge, this is one of the first studies on the development of spiking networks utilizing astrocytes as computational components for deep learning purposes.

Researchers suggest that learning is branch-specific rather than cell-specific. Chapter 7 shows that neurons perform more complex computations than formerly presumed. Here,

we present a multilayer and multiplexer dendritic integration scheme based on the CA3 pyramidal neuron from the rat hippocampus. The dendritic abstraction integrates fast and slow inputs (i.e., from neurons and astrocytes) while considering the voltage decay and signal delay resulting from the signals travel from the synapses to the soma along the dendritic length for neural coding. Therefore, we introduce an Input-Output (IO) transformation method and present an activation function dependent on the synaptic locations and number of activated synapses. The CA3 pyramidal neuron model was developed using the NEURON simulation platform [17]. We analyzed the spatiotemporal signals and determined the activation function parameters using the R programming language.

Lastly, we conclude our study and offer our perspectives for future research in Chapter 8. Then, Chapter 9 shows the list of our publications and communications.

2

Biophysical Properties and Dynamics of Neurons

2.1/ Introduction

The brain is perhaps the most complex and sophisticated system that nature has devised. It comprises billions of tightly packed cellular elements communicating and cooperating via molecular and electrical events to perform multiple functions simultaneously and efficiently. It is widely known that the cellular elements called neurons are the primary underlying component of the brain. Myriads of these neurons create subsystems that interact with each other in a complicated manner. Recently, neuroscientists introduced astrocytes, a type of glial cells, as information processing units rather than merely as structural supports, making the system even more complicated. To understand how the human brain works, we have to delve closer to the organization of its biological substrate. Then, to artificially recreate the neuron-astrocyte system, we have first to understand the fundamental biological components of the brain and their dynamics regarding information processing.

This chapter focuses on the subregion of the temporal lobe called the hippocampus. A comprehensive collection of studies on the hippocampus demonstrates its critical function in memory formation, storage, and retrieval. However, it is challenging to determine the exact capacity of the hippocampus since information and memory processes are carried out in various timescales, from milliseconds to days even. So, why are we focusing on the hippocampus? It is because of the very same reason that it can store memory, learn from past experiences, retrieve information, use them to simulate the future, and cooperate with the prefrontal cortex for decision making, which is the main principle behind artificial neural networks, for instance, in deep learning.

This chapter defines the hippocampus, its subfields and cellular components, and its importance in brain information processing and memory. It focuses on the morphology, internal structures, and molecular components of the hippocampal neurons. Then, we describe the ion transfer through voltage-gated ion channels and illustrate its electrical influence on the membrane potential. We describe the interplay between the chemical dynamics and the electrical dynamics and how they result in action potentials (APs), the primary information-carrying signal in the brain. In parallel, this chapter also includes the state-of-the-art describing the neuron processes, AP generation, and spiking mechanisms. We then tackle the AP propagation from the AIS, as it travels through the series of myelinated segments and nodes of Ranvier until reaching the synaptic axon terminals. These models are significant in further understanding of the biological properties and computational capacity of the neuron.

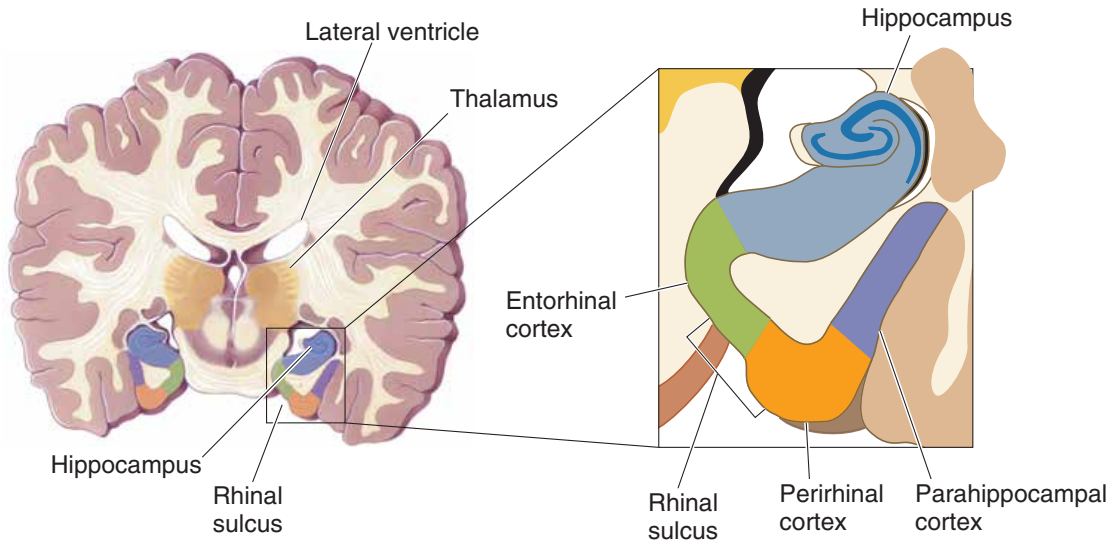

Figure 2.1: The location of the hippocampus in the brain. The brain section, sliced coronally, shows the hippocampus and the parahippocampal region of the medial temporal lobe. The image was extracted from Bear et al. [21].

2.2/ The Hippocampus

The hippocampus is a critical brain structure, especially in learning, memory, and cognition [18–20]. The morphological structure of the hippocampus resembles a Greek mythical creature called the 'hippocampus' or a seahorse [21], thus the name. It is a complex and folded structure located in the medial temporal lobe. The coronal brain slice in Figure 2.1 shows the hippocampal system divided into the hippocampal formation and the parahippocampal region, which includes the cortical regions ventral to the hippocampus (the entorhinal cortex, the perirhinal cortex, and the parahippocampal cortex) [22]. Therefore, the hippocampus location in the temporal lobe is vital to its time-dependent memory functions [23, 24] and its association with the decision-making function of the prefrontal cortex via the entorhinal cortex [22, 25]. In the 1960s, researchers discovered that the hippocampus can be removed from the brain of experimental animals, sliced, and still be alive *in vitro* [21]. The brain slice preparation paved the way for thousands of studies on the hippocampus (and because the hippocampal structures in the human brain also exist in monkey and rat brains [22]), making it one of the most studied subregions of the brain [18, 21].

2.2.1/ Hippocampal Trisynaptic Circuit

The hippocampus comprises distinct and interconnected subfields: the dentate gyrus (DG) and the *Cornu Ammonis* (from CA1 to CA4) subfields, which form two sheets of neurons folded onto each other, and the subiculum [18, 20, 21]. Figure 2.2a displays the coronal (perpendicular to the long axis) section of the main body of the hippocampus. Note that the distribution of the subfields is nonuniform and that the connections extend along the hippocampal length [18, 27]. We focus on the arrangement in the hippocampus widely recognized as the trisynaptic circuit, which is the three sets of connections from the entorhinal cortex through the DG subfield and to the CA3 and CA1 areas [21, 28].

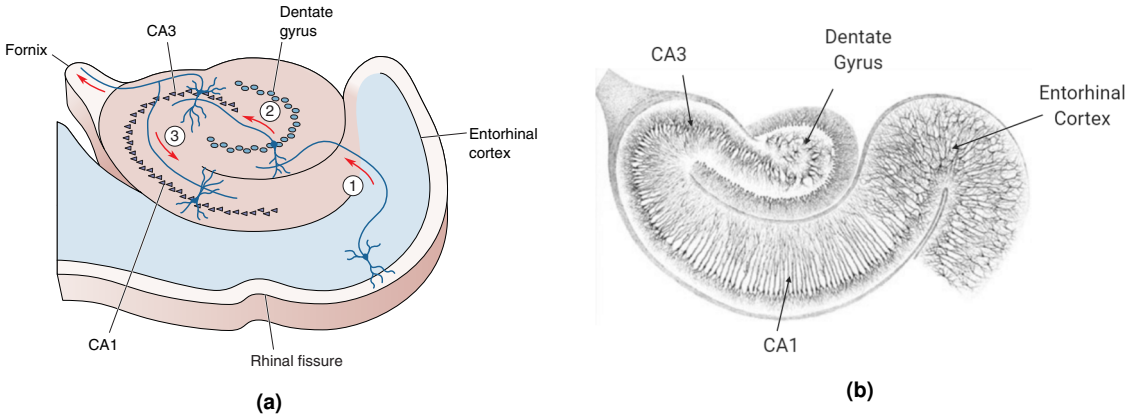

Figure 2.2: Coronal section of the main body of the hippocampus showing the signal flow through the trisynaptic circuit. (a) (1) From the entorhinal cortex, inputs enter the hippocampus via the perforant pathways to the DG. (2) Then, DG granule cells send signals to the pyramidal neurons in the CA3 area through its mossy fibers. (3) Signals sent by the CA3 neurons along the Schaffer collaterals drives the pyramidal neurons in the CA1 area. The image was extracted from [21]. (b) To further visualize the trisynaptic circuit, here is the hippocampus histology of a neonatal kitten originally drawn by Camillo Golgi, published in 1903 [26].

Researchers deduced that this unique and unidirectional trisynaptic circuit is the principal signal route in the hippocampus (Figure 2.2a) [22, 28]. Here, neurons of the entorhinal cortex send information to the hippocampus through the perforant path that connects to the DG. The DG mossy fibers then transmit the information to the CA3 cells. When activated, signals from the CA3 Schaffer collaterals can either exit the hippocampus to the fornix or enter the CA1 region. The subiculum and the CA1 neurons then feed the signal back to the entorhinal cortex, forming a loop [18, 21, 22, 28, 29].

Camillo Golgi drew the histology of the hippocampus based on the silver chromate staining of a neonatal kitten hippocampal section, showing the neuronal distributions and morphology in the subfields (Figure 2.2b) [26]. This histology helps visualize the neuronal connectivity in the trisynaptic circuit. The three subfields in the trisynaptic circuit perform distinctive functions: granule cells of DG for pattern separation, pyramidal CA3 neurons for pattern completion, and pyramidal CA1 neurons for input integration [18, 27, 28]. Therefore, the simple neural architecture in the hippocampus of the mammalian brain is suitable for studies on information processing [21].

2.2.2/ The Role of the Hippocampus in Memory and Learning

As many research suggests, memory functions and learning processes, such as episodic and autobiographical memory, contextual and associative memory, recollection, encoding, and retention, are associated with the hippocampus [19, 20, 30]. The hippocampus first learns and temporarily stores the incoming sensory signals and then guides the activated cortical regions during ”slow learning” [31]. However, the interplay of memory and learning includes an extensive range of challenging tasks to categorize in that the hippocampal subfields perform heterogeneously distributed tasks. Consequently, it is quite challenging to determine the exact function of the hippocampus. For an overall view of its capacity, we take note of the following fundamental functions.

Memory Consolidation. Memory consolidation is the process in which the hippocampus strengthens the newly-established, temporary, and unstable memory into a stable, long-lasting memory that is insusceptible to interference (but can still be modified and updated) [31, 32]. The hippocampus stores temporary information until it can be combined with preexisting memory traces in the cortical region for long-term storage until the cortical regions become independent of the hippocampus [31, 33].

Spatial Learning. The hippocampus supports spatial memory and spatial awareness by encoding a cognitive map of space and location of objects for spatial navigation, spatial discrimination, and scene imagination [21, 30, 34]. The notion of spatial learning and memory started with discovering 'place cells' in rats that spike when the rats are in a specific position in space [32, 34, 35]. Familiarization with the location stabilizes the memory for long-term storage [35].

Memory Retrieval. The length of time a memory remains in the hippocampus is still unclear because memory stored in the hippocampus can last from seconds to days [21]. Neuroimaging works showed that the hippocampus aids with the retrieval of memory representation and with future simulation [25, 36]. During retrieval, the hippocampus reactivates the specific memory representation by reconstructing cortical activity patterns observed while learning [37, 38], where the retrieved patterns help imagine the future and decision-making [25, 39].

2.2.3/ Cellular Elements in the Hippocampus

How many neurons and astrocytes are there in the human brain exactly? Here is one of the most enduring questions in neuroscience [40]. Neurons and astrocytes, occupying more than 90% of the functional tissue of the brain, are distributed heterogeneously and interacts with each other via a chemical release [41, 42]. In the human brain, the neurons outnumber the astrocytes slightly with a regional difference, in that there are ~80 billion neurons and ~60 billion glial cells (20-40% are astrocytes) [40]. These cells are dominant in the cortex and hippocampus [43]. Therefore, the astrocyte-neuron ratio is comparable with the ratio in the mouse hippocampus, where the overall reported astrocyte to neuron ratio is 0.68 [44]. Cell bodies in the hippocampal CA strata are morphologically nonuniform though their composition per stratum is similar [44]. It is essential to identify these cells in the brain region and their cell density and connectivity to understand the computational processes and capabilities of the hippocampus and reconstruct and simulate the neuron-astrocyte network [41, 44].

2.3/ Fundamental Biological Structure of a Neuron

Neurons are the fundamental computational and processing units of the central nervous system (CNS). Their cell densities are higher in the hippocampus and the neocortex compared to other brain regions [45]. In the hippocampus, most of the neurons are of the pyramidal neuronal type [29, 46]. Though they share principal functional properties, these pyramidal neurons vary in the cellular architecture and biophysical structure [29, 45]. The distinct properties enable the pyramidal neurons to perform specialized functions within the neural network [29].

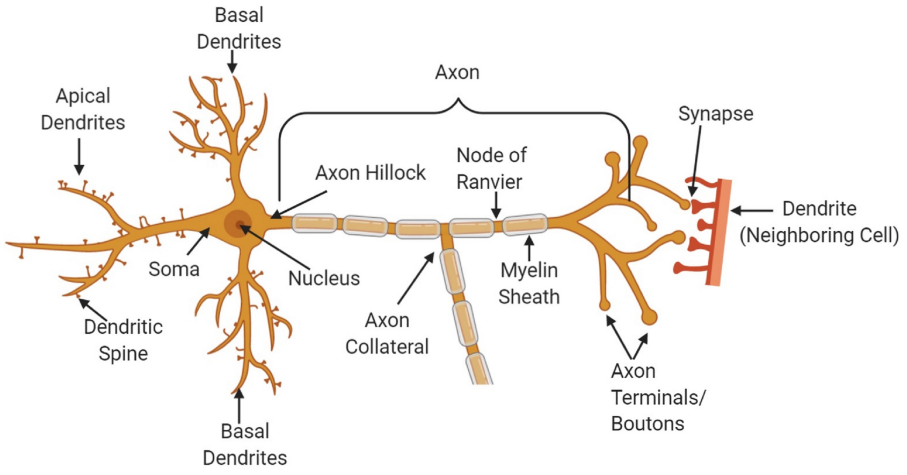

Figure 2.3: Fundamental parts of a pyramidal neuron.

Figure 2.3 depicts the basic biological structure of a pyramidal neuron. A neuron has two main parts: the soma and the neurites. The central region (cell body) called the **soma** (plural: somata) contains the **nucleus** of the neuron [21]. The soma of the pyramidal neuron type is pyramidal in shape, as the name implies [45, 46]. Pyramidal neurons have soma ranging from 20 to 120 μm in diameter [47]. Then, the **neurites** are the thin tubes emerging from and radiating away from the soma. The pyramidal neuron is a bipolar cell, as shown by the opposite directions of its neurites [46]. The **axon** radiates from the base of the soma while the **dendrites** develop towards the other direction [46]. The axon comprises three parts: the axon hillock, the axon proper, and the axon terminals [21]. The **axon hillock**, also called the **axon initial segment** (AIS), emerging from the base of the cell body, forms the first axon segment and connects the axon proper to the soma [21, 48]. The **axon proper** is a long tube covered with periodic **myelin segments**. Then, the **nodes of Ranvier** are the axonal section in between the myelinated segments. Along the axon proper, branches called **axon collaterals** may appear [30, 48]. They can spread and reach other neurons [30], or in the case of **recurrent collaterals**, return and communicate with the cell itself [21]. At the unmyelinated branches at the end of the axon (**terminal arbors**) are protrusions that resemble swollen disks called the **axon terminals** or **boutons**, which serve as the input side of the synapse [21]. The **synapse** is the site of transmission between the axon of one neuron and the dendrites of the neighboring neuron [21]. The dendritic arborizations are collectively called a **dendritic tree**, and each branch a **dendritic branch** [21]. There are two dendrites divisions that characterize a pyramidal neuron, the **basal dendrites**, which are the short and fine dendritic structures directed downward from the base of the soma, and the **apical dendrites** projecting upward from the cell body [45]. There are also protrusions on the dendritic branch called **dendritic spines**, where synaptic input enters the dendritic length [46].

No two neurons are the same, even though they have the same cell type and belong to the same hippocampal subfield. Neurons are heterogeneous due to the variations in cell development and maturation, variations in input signals, and changes in the cell environment [49]. Pyramidal neurons in CA1 and CA3 subfields are diverse and substantially varied in their morphology. However, their dendrites bifurcate extensively in the distal apical region to form the apical tuft [46]. Figure 2.4 are the Golgi stains of the neurons from the hippocampus of rats. Figure 2.4a and Figure 2.4b show the morphology of the pyrami-

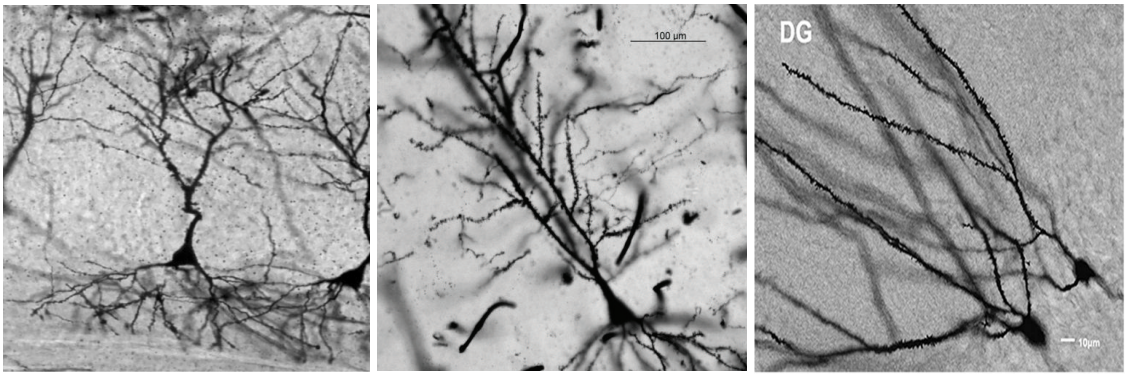

Figure 2.4: Morphology of the (a) CA3 [51] and (b) CA1 [52] pyramidal neurons and (c) DG granule [53] cell in rat hippocampus. Even though neurons belong in the same subfields, their morphology is diverse and distinct. Granule cells are smaller than the pyramidal neurons.

dal neurons in the CA3 and CA1 subfields, respectively. Furthermore, in the DG subfield, the prominent cell type is the granule cell [50]. Granule cells shown in Figure 2.4c are multipolar neurons with short axons and are smaller than pyramidal cells with a cell body of less than 20 μm in diameter [47]. There is a small number of dendrites, also covered with spines, protruding from their oval-shaped soma [22].

The soma contains most of the organelles found in other cell types necessary for the maintenance and neuronal functions [47, 54], most proteins and membrane synthesis as well as gene transcription [47, 55]. The **neuronal membrane** is a 5nm thick barrier, made up of phospholipid bilayer and associated proteins, that encloses the internal cellular structures and separates them from the substances floating in the extracellular fluid bathing the neuron [21, 55]. The neuronal membrane also plays a crucial role in information processing and signaling between neurons, which we later discuss in detail. Inside the neuronal membrane of the cell body are the nucleus and the cytoplasm. The **cytoplasm** is a collective term for everything, including the organelles, the cytosol (fluid), and excluding the nucleus, enclosed by the neuronal membrane. Synthesized proteins and membranes are packaged inside the vesicles and transported along the axon via the **microtubules** [55]. Microtubules are tubular polymeric proteins 24 nm in diameter and up to 1mm in length and extend along the axonal length (except the terminals) [21, 47].

Another organelle crucial to signaling and information processing is the **endoplasmic reticulum** (ER). The ER is a membrane-bound organelle that originates as part of the nuclear envelope [56]. The ER forms a network through the neuron by expanding and morphing into an intricate reticulum (another term for the web- or net-like structure) [56]. The ER forms vesicles that traverse and access the long axons, apical and distal dendrites, as well as the synapses [56, 57]. There are two types of ER in the neuron: the rough ER, which is constituted with membrane-associated ribosomes and engaged with protein synthesis, and the smooth ER, which lacks ribosomes and plays a role in lipid and steroid biosynthesis [56]. Of these two types of ER, the smooth ER can reach the axon and dendrites. It plays a principal function in Ca^{2+} signaling, especially in regulating neuronal excitability and synaptic plasticity [56, 57].

2.4/ THE NEURONAL MEMBRANE

The phospholipid bilayer neuronal membrane separates the extracellular liquid from the intracellular environment and plays a significant role in neuron signaling [21, 58, 59]. In nonsynaptic areas, the neuronal membrane contains pore-forming macromolecular proteins called **ion channels** that control the passage of ions from the extra- to the intracellular area of the neuron, or vice versa [58, 60]. Ionic concentration fluctuation between the inside and outside of the neuron results in fast voltage changes across the neuron membrane. Ion channels can be potential-dependent, in the case of voltage-gated channels controlled by transmembrabe voltage, or ligand-dependent, in the case of receptors in the synaptic areas which are activated by signal molecules.

2.4.1/ ION CHANNELS

Ion channels are protein assemblies that allow selective passage of ionic current in and out of the cell and control the membrane permeability for corresponding ion transfer [58, 60, 61]. At any given moment, an ion channel can occupy one of the multiple possible discrete states: closed-activable, open (conducting, activated) that permits ion to flow, or a closed (non-conducting, inactivable) state that prevents ion passage [60–62]. The stochastic transition between states occurs <1 μs and is driven by thermal agitation [60]. For voltage-gated channels (VGCs) or potential-dependent channels, the transition probability between states is dependent on the membrane potential [58, 60]. These channels consist of primary voltage sensing subunits and auxiliary subunits responsible for controlling membrane targeting and kinetics of activation and inactivation of the channel [63].

Protein-protein interactions along the somatodendritic and axonal domains create specific ion channel distribution and density in the cell membrane, defining the electrophysiological properties and unique functioning of different subtypes of neurons [63, 64]. Pyramidal neuron domains express a wide variety of voltage-gated channels, such as sodium (Na_v), potassium (K_v), and calcium (Ca_v) channels that contain a selectivity filter for each corresponding Na^+, K^+, and Ca^{2+} ions, as well as hyperpolarization-activated cyclic nucleotide-gated (HCN) channels [58, 63, 64]. Ion selectivity means that a specific channel attracts its corresponding ions, while other ions cannot pass through the channel [58].

Sodium channels. The most abundant sodium channels in the hippocampal pyramidal neurons are the $Na_v1.1$, $Na_v1.2$, and $Na_v1.6$ generating different types of depolarizing currents critical for AP generation: fast activation or transient (I_{NaT}), persistent (I_{NaP}), and resurgent (I_{NaR}) [63, 65]. Voltage-gated sodium channels in the AIS primarily generate I_{NaT}, which is responsible for developing the upstroke of the AP [63]. Subthreshold I_{NaP} generated in the AIS increases neuronal excitability, while I_{NaR} following AP contributes to after-depolarization and promotes repetitive firing, except in CA3 pyramidal cells where resurgent Na^+ channels are nonexistent [63, 66]. In hippocampal pyramidal cell dendrites, sodium channel, distributed uniformly in the apical trunk, support AP backpropagation, nonlinear synaptic integration, and dendritic Na^+ spike generation [67, 68].

Calcium channels. High-voltage activated calcium channels comprise L-, N-, P/Q, and R-type channels, while low-voltage activated calcium channels include T-type channels

[63, 68]. The distal dendrites of CA1 pyramidal neurons have high densities of T- and R-type Ca_vs, whereas, in apical dendrites, there is an abundance of L- and N-type channels [68]. Ca_v channels play a vital role in neuronal signaling by transforming electrical signals into changes in the cytoplasmic $[Ca^{2+}]$ [63, 64]. During depolarization, Ca_v channels are activated, causing the channels to conduct Ca^{2+} into the cytoplasm, thus raising the intracellular $[Ca^{2+}]$. The influx of Ca^{2+}, therefore, modulates the cellular processes such as regulation of Ca^{2+}-dependent channels, triggers neurotransmitter release, and stimulates intracellular signaling enzymes and gene expression. Ca_v channels also influence the AP generation, shape, and firing patterns.

Potassium channels. Potassium channels are classified into different families: voltage-gated (K_v), calcium-activated (K_{Ca}), inward-rectifying (K_{ir}), and 2-pore (K_{2P}) channels [63]. Transient rapidly activating and inactivating subthreshold current (I_A) carried by K_v4 and K_v3 channels delay AP initiation and slows down the firing frequency [63, 68]. Overall, K_v channels regulate neuronal excitability by controlling the AP initiation threshold, the AP repolarization, and limiting neuronal firing frequency. On the other hand, Ca^{2+}-activated potassium channels (K_{Ca}) have Ca^{2+} sensors that activate potassium channels in response to Ca^{2+} influx. In CA1 pyramidal neurons, A-type K^+ channels are distributed somatodendritically in an increasing manner, while in other neurons such as layer V pyramidal cells, these channels are distributed uniformly [68]. The increasing somatodendritic distribution of these channels create a 'shock absorber' that limits the spread of backpropagating AP.

HCN channels. HCN channels belong to the Kv channel superfamily [69]. However, these channels provide specializations that make them crucial in neuronal excitability. HCN channels include HCN1-4 subunits, in which HCN1 and HCN2 are the most abundant in the CNS [63]. HCN channels are partially open at rest and get activated during membrane hyperpolarization, in contrast with most voltage-gated channels activated by membrane depolarization [63, 68, 69]. The depolarizing current I_h counteracts both membrane hyperpolarization and depolarization [63].

2.4.2/ Membrane Potential and Action Potential

The membrane potential is fundamental in neuron signaling and brain functions [70]. The ionic charges in the extra- and intracellular fluid results in a potential difference in the impermeable membrane separating them [71]. Electrical signaling is mediated by the rapid changes in the membrane potential through ionic charge redistribution regulated by the opening and closing of ion channels [60, 71]. In neuronal signaling, the principal carrier of information is the sequence of electrical signals called action potentials (APs) (Figure 2.5), usually initiated in the AIS and distributed to diverse neurons via synapses [70, 72]. The temporal pattern of AP firing thus forms the basis of neural coding [70].

As mentioned earlier, VGCs plays a vital role in regulating neuronal excitability, the ability of the neuron to create rapid increase and decrease in membrane potential in response to a stimulus. Figure 2.6 shows the transition between states of the VGCs and the flow of ions in response to the membrane potential increase. At rest, when the neuron does not receive stimulus from synaptic inputs, VGCs are closed, and the membrane potential is measured to be -70 mV (Figure 2.5) due to the concentration gradient between the

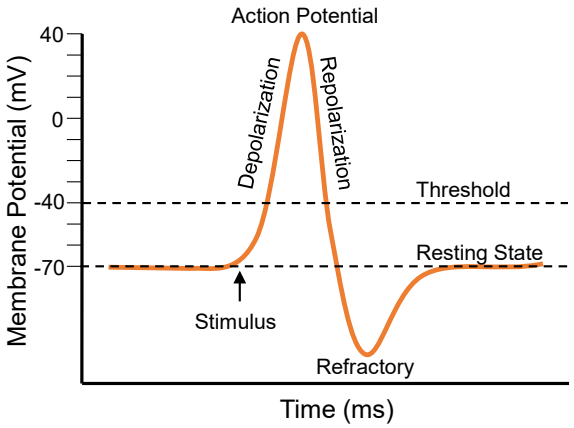

Figure 2.5: Action potential generation. An excitable neuron has two critical membrane potential levels: the resting potential and threshold potential. At rest, the ionic strength between the extra- and intracellular area sets the membrane potential to -70 mV. When a stimulus reaches a neuron compartment, it depolarizes the membrane, and if this stimulus is strong enough to produce a membrane potential higher than the threshold, a rapid increase of membrane potential to 40 mV occurs; thus, an action potential is generated. After reaching the AP peak, the membrane potential rapidly decreases during repolarization. During the refractory period, the voltage-gated channels are inactive. However, there are leakage channels and some K_v channels that are still open, causing a hyperpolarization until the membrane potential returns to the resting state.

Na^+ and K^+ ions in the intra- and extracellular spaces (Figure 2.6a) [58, 73, 74]. Depolarization begins in the arrival of a stimulus, which opens Na_v channels allowing Na^+ ions to penetrate the intracellular space making the membrane less positively charged (Figure 2.6b) [58, 73, 74]. There is a greater influx of Na^+ ions while a lesser efflux of K^+ ions resulting in a more positive membrane potential [61]. The influx of Na^+ further augments the membrane depolarization, consequently increasing the opening probability of other Na_v channels [58]. The further increase of membrane potential above a critical threshold generates an action potential [58, 70]. The membrane permeability for Na^+ becomes maximum, and the membrane potential for Na^+ reaches equilibrium at +40 mV (Figure 2.6c). At this point, a further increase in depolarization inactivates the Na_v channels and augments the opening probability of K_v channels [58, 73]. The neuron becomes more negatively charged as the K_v ions leave the cytosol until further augmentation of repolarization inactivates the K_v channels [58]. The point wherein the membrane potential is more negative than the resting potential is called hyperpolarization [74]. Both channels, Na_v and K_v, require a recovery period before the next activation. During the refractory period, VGCs are closed; however, some leakage channels are still open, allowing the flow of ions until the membrane potential recovers back to the resting potential, at -70 mV [73]. Fundamentally, the neuron loads Na^+ ions during depolarization and loses K^+ ions during repolarization. The proportion of intracellular K^+ ions and extracellular Na^+ ions is adequate to generate a sequence of thousands of APs [58]. This process, however, is energy-consuming for the brain; the neurons have ion equilibrium recovery proteins Na^+, K^+ - ATPase, whose activity requires almost half of the brain energy.

2.4.3/ ELECTRICAL EQUIVALENT

A cell membrane section can be represented by an equivalent nonlinear electrical circuit comprising active and passive components, such as resistance or conductance, capaci-

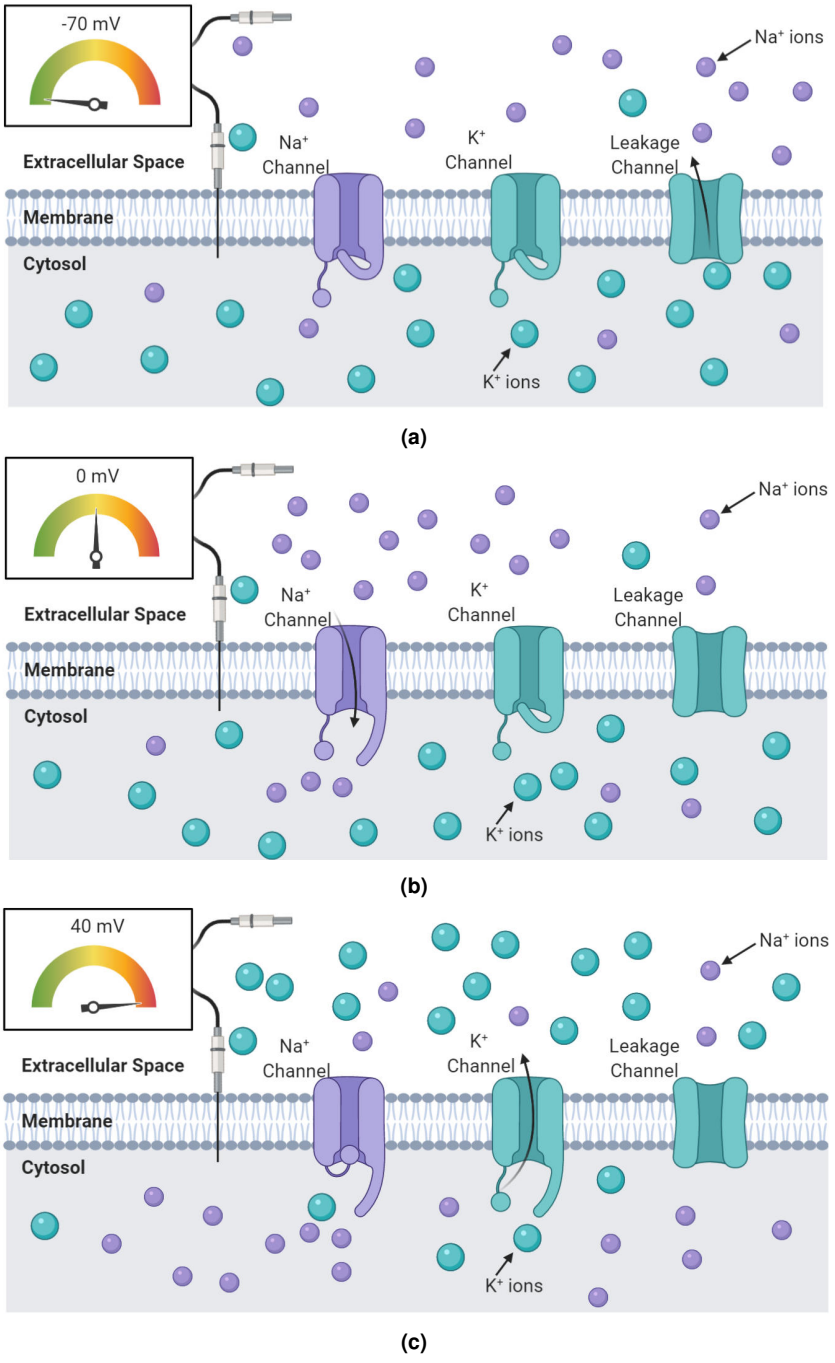

Figure 2.6: Neuronal membrane during action potential generation. (a) The Na_v and K_v channels, when the neuron is at rest, the membrane potential has a negative potential at -70 mV. The VGCs are closed; however, some open leakage channels allow K^+ ions to the extracellular space. (b) During depolarization, Na_v channels open, and the influx of Na^+ ions into the cytosol further increasing the membrane potential above the threshold. (c) Then, at peak depolarization of 40 mV, the cytosol becomes rich in Na^+ ions. Rapid repolarization starts, and the Na_v channels get inactivated while K_v channels open and allow the flow of K^+ ions out of the cytosol. The cytosol becomes negatively charged, and the membrane potential recovers back to its resting state.

tance, and voltage source [75]. Here, we describe the equivalent circuit of the AIS where AP is generated and whose membrane compartment in Figure 2.7a gives a neurophysiological model equivalent to a nonlinear electric circuit in Figure 2.7b, first described by

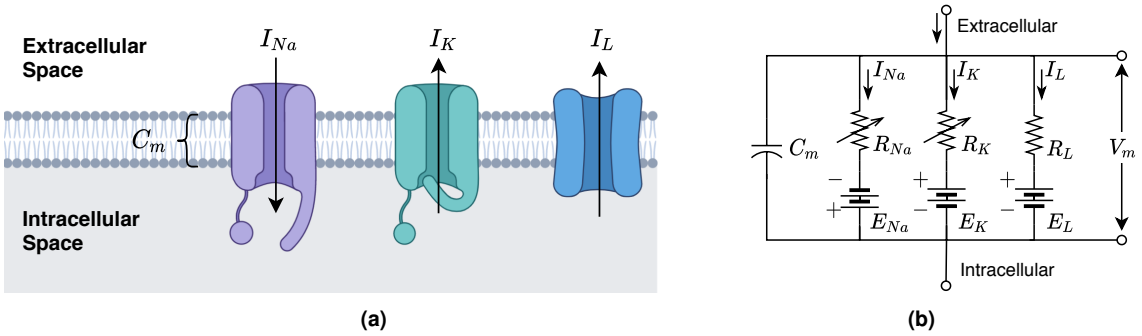

Figure 2.7: The neuron membrane and its equivalent circuit. (a) The neuron membrane which separates the cytoplasm and the extracellular fluid forms a capacitance C_m. The membrane retains potential due to the flow of currents (I_{Na}, I_K, and some leakage I_L) through the ionic channels. (b) Therefore, the membrane can be described as an electric circuit whose membrane potential V_m is the difference between the ionic charges in the extra- and intracellular space. A specific ionic channel is equivalent to resistor R in series with a battery representing the reversal potential E.

Hodgkin and Huxley [76, 77]. The voltage across the membrane, V_m, is the potential difference between the extracellular, v_o, and intracellular medium, v_i. At rest, the membrane potential is $V_m = -70$ mV, considering that the extracellular medium is the ground (0 mV) [61, 74, 75]. The membrane potential then fluctuates due to the Na^+, K^+, and leakage (remaining ions such as Ca^{2+} and Cl^-) ions flowing through the channels [75, 78].

The neuron resembles two plates of electrical conductors (the cytoplasm and the extracellular fluid) separated by an insulating material (the lipid bilayer); thus, the membrane forms a linear capacitive property implying that the ions move through the ion channels and not directly through the membrane C_m [61, 74, 75, 78]. Membrane specific **capacitance** is approximately equal to 0.7–1.0 μF/cm^2 [74, 78, 79]. As a consequence of the capacitance, the change in membrane potential follows an exponential time course. For the circuit in Figure 2.7b, the time constant is modeled as $\tau = R_{Th} \times C_m$ where R_{th} is the Thevenin resistance formed by the passive ion channels [74]. For a typical neuron, τ ranges from 1 to 20 ms, and at 5τ, the response is within the 1% of steady-state.

Sodium and potassium channels are passive components because they only allow specific ions to pass through the channel [74]. As shown in Figure 2.7b, a passive ion channel is modeled as a resistor in series with a battery [75]; a resistor because it resists the movement of electrical charge through the channel and a battery for the electromotive force that drives the ions through the channel [74]. In relation to the membrane resistance, **conductance** measured in Siemens (S), therefore, describes the ease in which ions flow through channels. Consider a specific ion channel with a conductance G'; the total conductance in the compartment is therefore proportional to the number of that specific channel, N; thus, $G = N \times G'$. Conductance is a linear function that varies with the ion concentration, so even the channel permeability is high, $G = 0$ if there are no available ions on either side of the neuron membrane [74, 78]. In the conventional model of the AIS equivalent circuit (Figure 2.7b), the total membrane conductance G_m is equal to the sum of the parallel conductances from Na^+ (G_{Na}), K^+ (G_K), and some leakage (G_L) ion channels.

There is an electromotive force for each specific channel called a **reversal potential** (also called Nernst potential) created by a concentration gradient and is represented by

a battery. The reversal potential is the equilibrium potential; the static difference in V_m wherein no current flows [71, 74, 75]. The reversal potential for Na^+ is higher while the reversal potential for K^+ is lower than the resting potential of the neuron, causing an influx of Na^+ ions during depolarization and efflux of K^+ during hyperpolarization [75]. The leakage current, commonly associated with other remaining ions such as Cl^- ions, is small compared to I_{Na} and I_K [78]. Essentially, when an external current I_{ext} is applied to stimulate the membrane in Figure 2.7, the Kirchoff's current law indicates that [74, 80]

$$I_{ext} = G_K\,(V_m - E_K) + G_{Na}\,(V_m - E_{Na}) + G_L\,(V_m - E_L) + C_m\frac{dV_m}{dt}. \tag{2.1}$$

2.5/ Neuron Models for Membrane Potential

Computational models are utilized to describe the fluctuations in the membrane potential and the shape of the AP, depending on the ionic channel distribution. In theoretical and computational neuroscience, there are various models ranging from **single-compartment** to **multicompartment** neuron models. The series of seminal studies in the squid giant axon performed and published by Hodgkin and Huxley in the 1950s paved the way to neuronal modeling [76, 81–83]. Using voltage-clamp experiments, Hodgkin and Huxley recorded ionic currents and voltage-gated conductances in the AIS, whose physiology is analogous to a single cylindrical structure. Thus, the Hodgkin-Huxley (HH) model became the basis of subsequent single-compartment neuron models for AP [77]. Following the studies of Hodgkin and Huxley, Wilfred Rall then provided profound insights into the cable properties of dendritic trees and developed the technique for modeling the current flow in neurons [84]. The dendritic tree was divided into compartments defined by their homogeneous activities and distinct hyperpolarization or depolarization [72, 84]. Input to the first compartment generates a corresponding output, which is directed to the next compartment. This technique revolutionized modern multicompartment modeling [77].

The selection between single- or multicompartment models generally depends on the modeling objective and complexity. A single-compartment model is isopotential and usually neglects the spatial dimension of the neuron [62, 85]; however, such a model is useful but straightforward enough to describe the membrane dynamics. Multicompartment models are made up of linked single-compartments that differ in ionic densities. Both models are useful in neuroscience study depending on the range of problem complexity: multicompartment models for problems requiring detailed neuron morphology and single compartment models for simplicity [62].

This section focuses on the membrane potential and AP generation, specifically in the AIS, of single-compartment models. These models include the biologically-inspired models (quantitative), starting from the Hodgkin-Huxley, where AP generation results from the model dynamics to integrate-and-fire (IF) models where spiking occurs when the voltage exceeds a threshold, and to some model variations that qualitatively describe neuron spiking [85].

2.5.1/ Dynamic-based Biophysical Neuron Models

Models formulated from biophysical data usually use similar formulism to describe the membrane potential V from the summation of ionic and applied currents I, and I_{app}, respectively, and with additional equations for ionic channels activation rates [62]. Then, these parameters are incorporated into a single-compartment (or multicompartment) neuron models whose membrane potential follows a time-dependent first-order differential equation:

$$C\frac{dV}{dt} = -\sum_{j=1} j^N I_j - I_{neighbors} \tag{2.2}$$

where the current form neighboring compartments $I_{neighbors} = 0$ for single-compartment model and I_j stands for the current flowing through several different ionic channels types, N [80, 86]. In an instance that an external current stimulus I_{ext} is applied to the membrane, the membrane potential becomes

$$C\frac{dV}{dt} = I_{ext} - \sum_{j=1}^{N} I_j \tag{2.3}$$

following Kirchoff's current law. Applying Ohm's law, the current intensity flowing through a specific channel I_j is equal to the product of the difference between the membrane potential and the reversal potential E_j and the conductance g_j of the corresponding channel, and is given by

$$I_j = g_j\left(V - E_j\right). \tag{2.4}$$

There are a wide range of neuron models developed from these equations.

2.5.1.1/ Hodgkin-Huxley Model

The HH model became a reference for a several model variations. Neuron models of HH-type usually vary in terms of the nature and properties of VGCs and still maintain the spiking behavior generated by the intrinsic dynamics of the neuron [80, 85]. The HH formulism also turned out to accurately reproduce the AP waveform across different types of neurons [70]. It provides a detailed description of ion channel dynamics and uses physiological parameters, the main advantage of the HH model [86]. Aside from a whole-cell model, the HH model can be expanded into local differential equations to model the dynamics in an individual compartment in a multicompartment model [78].

Ion Channels Gating Schemes. Markov chain models usually describe the transition between states of VGCs; however, structure-function investigations suggest that for almost all VGCs, HH-like kinetics are specific approximations of the channel behavior [60, 87]. The standard equation of a time- and voltage-dependent j-type channel conductance, g_j, is

$$g_j = \bar{g}_j a_j^{p_j} b_j^{q_j}, \tag{2.5}$$

where $\bar{g}_j$ is the maximum conductance of channels in the open state [60, 86]. The gating variables a_j and b_j characterize the probability of opening the activation and inactiva-

tion gates, where p_j and q_j are the numbers of activation and inactivation gates per ion channel [86]. During membrane depolarization, activation gates open gradually while inactivation gates close, in turn, modulating the conductance behavior as a voltage-function [75, 86]. Hodgkin and Huxley determined that for a Na_v channel, the number of activation gates $p_{Na} = 3$ and an inactivation gate $q_{Na} = 1$, while for potassium channel, there are for activation gates ($p_K = 4$) and zero inactivation gate ($q_K = 0$) [60, 86]. It can be interpreted that, for K_v channels, K^+ ions can flow through the channel when four identical particles occupy a certain region of the membrane [76]. The opening of the activation and inactivation gates are defined by gating variables moving from the off- to the on-state and back, with a voltage-dependent rate [76]. The transition rates $\alpha(V)$ determines the ion transfer from outside to inside, and $\beta(V)$ which determines the ion transfer in the other direction [60, 76]. The following are the conductance equations for Na_v and K_v gating schemes (at 6.3 °C) [60, 81]. The voltage- and time-dependent equation for Na_v channel conductance, g_{Na}, follows

$$g_{Na}(V,t) = \gamma \rho_{Na} A m^3(V,t) h(V,t) \tag{2.6}$$

where γ_{Na} is the single-channel conductance, ρ_{Na} is the channel density per area A and where $\bar{g}_{Na} = \gamma_{Na}\rho_{Na}A$ is the maximum Na^+ conductance [60, 75]. The forward and backward transitions rates in 1/ms for m and h are established as

$$\alpha_m = \frac{0.1\,(-V-45)}{\exp\left(\dfrac{-V-45}{10}\right)-1},\ \beta_m = 4\exp\left(\frac{-V-70}{18}\right), \tag{2.7}$$

$$\alpha_h = 0.07\exp\left(\frac{-V-70}{20}\right),\ \beta_h = \frac{1}{\exp\left(\dfrac{-V-40}{10}\right)+1},$$

where the membrane potential V has a unit in mV [60, 76, 88]. Likewise, the K_v channel conductance is

$$g_K(V,t) = \gamma_K \rho_K A n^4(V,t), \tag{2.8}$$

where $\bar{g}_K = \gamma_K \rho_K A$ is the maximal conductance for four identical activation variables n, with forward and backward transition rates given below [60, 75, 76, 78, 88].

$$\alpha_n = \frac{0.01\,(-V-60)}{\exp\left(\dfrac{-V-60}{10}\right)-1},\quad \beta_n = 0.125\exp\left(\frac{-V-70}{80}\right) \tag{2.9}$$

The gating variables have delayed first-order kinetics modeled by the differential equation

$$\frac{dx}{dt} = \alpha_x\,(1-x) - \beta_x x, \tag{2.10}$$

where $x = m, n$, and h [61, 75, 76, 78, 88]. The gating variables are dimensionless functions normalized between 0 to 1 to represent the relative number of open channels [75, 78, 80]. Refer to Figure 2.8a for the gating kinetics of m, h, and n, during the course of a single AP in Figure 2.8b. The rapid recruitment of Na_v channels (m) at the threshold outpaced the delayed activation (n) of K_v channels, resulting in an all-or-one event [70].

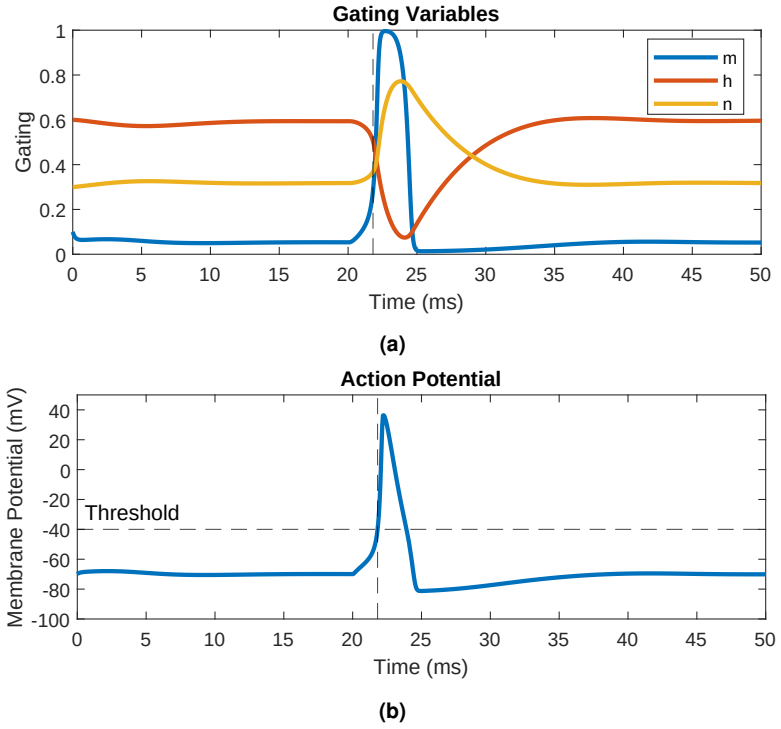

Figure 2.8: The kinetics of gating variables during an AP modeled using the Hodgkin-Huxley formulism. (a) The gating variables m and h represent the activation and inactivation of Na_v channels, while n represents the activation of K_v channels. (b) When the AP crosses the threshold after stimulation at $t = 20$ ms, a rapid increase in depolarization results from the m kinetics outpacing the n kinetics. During AP, h gates are closed.

Action Potential Generation. Returning to the equivalent circuit in Figure 2.7b and rearranging Equation 2.1, we obtain the Hodgkin-Huxley model following a nonlinear system of ordinary differential equations [76, 78].

$$C\frac{dV}{dt} = I_{app} - \bar{g}_{Na}m^3h\,(V - E_{Na}) - \bar{g}_K n^4\,(V - E_K) - \bar{g}_L\,(V - E_L)\,, \tag{2.11}$$

Here, I_{app} (in μA/cm^2) is applied to the membrane either from external stimulation or neighboring compartments. Table 2.1 shows the range of HH model parameters measured experimentally [89]. The shape of the AP depends on the conductance distribution in the AIS. Figure 2.9 illustrates a train of action potential showing different levels of excitability with varying I_{app} intensity. At the first I_{app} pulse of 2 μm/cm^2, the HH model is non-excitable. When $I_{app} = 5.82$ (second pulse), the model becomes excitable. Even a small increase of applied current (third pulse at $I_{app} = 5.83$) results in a large difference in the dynamics of the HH membrane. The membrane potential then oscillates for larger current intensity (from the fourth to the sixth pulse at $I_{app} = 6.10, 6.105$, and 10). Here, it is noticeable that the AP firing frequency and spiking are dynamic with respect to the membrane current.

2.5.1.2/ OTHER DYNAMIC-BASED MODELS

Based on the HH model, Morris and Lecar, in the 1980s, suggested a 2-dimensional conductance-based model by invoking the fast dynamics of Ca_v conductance with respect

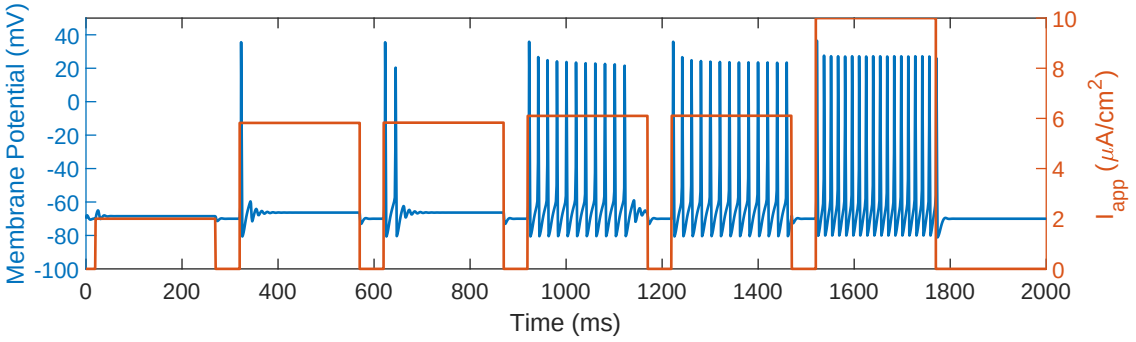

Figure 2.9: Action potential train with different levels of excitability. The HH model parameters are as follow: $\bar{g}_{Na} = 36$ ms/cm^2, $\bar{g}_K = 120$ mS/cm^2, $\bar{g}_L = 0.3$ mS/cm^2, $E_{Na} = 45$ mV, $E_K = -82$ mV, and $E_L = -59.40$ mV [88]. The excitability and firing rate of the AP (blue) depend on the intensity of the applied current I_{app} (red). For $I_{app} = 2\ \mu$A/cm^2, the cell is nonexcitable. From $I_{app} = 5.82\ \mu$A/cm^2, the model becomes excitable. Then further increase from $I_{app} = 6.10$ to $10\ \mu$A/cm^2, the AP shows oscillatory characteristics.

to the other variables [86, 90]. The principal equation describes the membrane potential V, dependent on the instantaneous Ca_v activation (I_{Ca}), delayed K^+ (I_K), and passive leakage (I_L) currents flowing through the membrane, while the second equation describes the slower activation current of the K_v channel, the same as in the HH model [86, 90–95].

The next model, called the FitzHugh-Nagumo (FHN) model, is a combination of the works of FitzHugh on ion channel dynamics of nerve cells and Nagumo on spatially-extended systems [96–98]. It is also a 2-dimensional model based on dividing the currents according to their time scale, turning the neural activity from four state-variables to only two [86, 99]. Going back to the HH model, where V and m evolve in similar time scales during an AP, while n and h also have similar and slower time scales, it is logical to lump these variables into a single variable V (for V and m) for "excitation" and ω (for n and h) for "recovery" [96, 100–102]. The FHN model ignores the Na^+ activation variable and replaces it with an equilibrium value [103].

2.5.2/ Threshold-based Neuron Models

In this subsection, we present the commonly-used neuron models that simulate the fundamental dynamics of the neuron and do not require a full description of ion transport.

Table 2.1: Hodgkin-Huxley model parameters.

Parameter	Description	Values		
		Min	Max	Mean
C	Membrane capacitance, μF/cm^2	0.80	1.50	0.80
$\bar{g}_{Na}$	Sodium channel conductance, mS/cm^2	65	260	120
$\bar{g}_K$	Potassium channel conductance, mS/cm^2	26	49	34
$\bar{g}_L$	Leak channel conductance, mS/cm^2	0.13	0.50	0.26
E_{Na}	Sodium channel reversal potential, mV	+30	+54	+44
E_K	Potassium channel reversal potential, mV	−79	−74	−76
E_L	Leak channel reversal potential, mV	−61	−43	−54

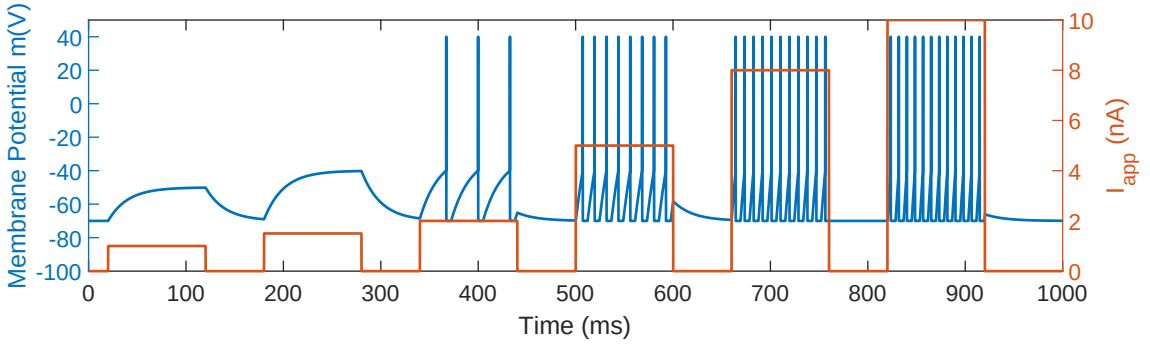

Figure 2.10: Action potential firing regime of a leaky integrate-and-fire neuron. The shape of the AP does not follow the shape of the AP of a biological model but depends on the membrane potential crossing the threshold (at −40 mV) for AP generation. However, the firing characteristics resemble that of a HH neuron wherein the it increases with further augmentation in the injected current I_{app}. The LIF model, here, has the following intrinsic parameters: $C = 1$ nF, $V_{th} = -40$ mV, $V_R = -70$ mV, $\tau_m^L = 20$ ms, $\tau_{ref} = 5$ ms [104, 105].

These models have a predefined threshold for AP generation and are often used in simulating large neural networks because of their low dimensionality and low computing power requirement.

2.5.2.1/ Integrate-and-Fire Model

The integrate-and-fire (IF) model could be considered an approximation of the HH model or a phenomenological description of AP generation [85]. It generates an AP in terms of a single variable, the membrane potential [106, 107]. However, the IF model only describes the subthreshold dynamics, as the AP generation is an extrinsic mechanism [86, 107]. When the membrane potential reaches the threshold, only then that an AP spikes. It uses a deterministic reset mechanism to return the membrane potential to the resting potential [108]. Since the IF model is an approximation, it does not present the dynamic mechanism, shape, and duration of an AP [86].

The IF model has several variants, where the original model is called the *leaky* integrate-and-fire (LIF) model [85]. The neuron is *leaky* because the membrane potential decays with a characteristic time constant, and if this decay is disregarded, the model becomes a *perfect integrator*. Once the membrane potential reaches the threshold, it generates an AP using a *firing* mechanism [107]. The subthreshold membrane potential is a first-order linear differential equation in time (t) and is given as

$$\begin{aligned} C\frac{dV}{dt} &= I_L(t) + I_{app}(t), \\ &\text{if } V(t) > V_{th} \text{ then } V(t) \leftarrow V_R \end{aligned} \tag{2.12}$$

where V is the membrane potential, C is the membrane capacitance, I_L is the current leaking through the membrane, and I_{app} is the injected current. The leak current is governed by

$$I_L(t) = -G_L\left[V(t) - E_L\right], \tag{2.13}$$

where E_L is the leak reversal potential and G_L is the constant leak conductance described as $G_L = C/\tau_m^L$, and τ_m^L is the time constant of the leaky membrane. Once V crosses the

threshold V_{th}, it diverges to infinity for AP firing (this can be set to the peak amplitude of the AP). The membrane potential then returns to the resting potential V_R ($V_R = E_L$) and stays in the refractory state for a time period of τ_{ref} [104–111]. The LIF model parameters are independent of the neuron dynamics and can be determined by a direct method [107]. Figure 2.10 shows the dynamics of the membrane potential of the LIF neuron, whose firing frequency increases with an increase in the injected current intensity.

Generalizations of the LIF model were developed to deal with its drawback. Here, we present a brief description of the IF model variants. These variants still follow the same firing mechanism and include changes on the membrane potential equation from linear to nonlinear or a second equation, an adaptation process, to the system. The IF models provide a simple approach for simulating a spiking neuron and displaying high computational efficiency and tractability, making it advantageous in both theoretical and computational [86, 110].

Quadratic Integrate-and-Fire Model. The *quadratic* integrate-and-fire (QIF) model is the most straightforward generalization of the LIF model. It is dynamically equivalent to a HH model with a constant current near the rheobase (the minimum stimulation current resulting in an AP) and approximates the qualitative behavior of the frequency-current (f-I) curve of a biological neuron [85, 112, 113]. The QIF model obeys

$$C\frac{dV}{dt} = \frac{G_L}{2\Delta_T}(V - V_R)^2 - I_0 + I_{app} \tag{2.14}$$

where for an applied external current, I_{app}, below I_0, the model exhibits both stable and unstable points. When $I_{app} > I_0$, the fixed points merge, then the membrane potential destabilized, and the neuron fires regularly [114, 115]. The parameter Δt is the spike shape factor that quantifies the sharpness of the AP initiation [106, 114]. The QIF model is ideal for very low spiking frequency [113].

Exponential Integrate-and-Fire Model. Current-voltage analysis of the HH model revealed a linear-plus-exponential dependence of the membrane potential on the ionic currents [116]. Assuming that the Na_v channel activation is instantaneous and neglecting its inactivation, the I_{Na} is described exponentially [117]. Therefore, the *exponential* integrate-and-fire (EIF) model includes an exponential approximation of I_{Na} and is equivalent to the HH model for fluctuating applied current [85]. The EIF model current-voltage (I-V) curve comprises a linear component in the subthreshold region and a sharp exponential rise above the threshold [118].

$$C\frac{dV}{dt} = -G_L\,(V - E_L) + G_L\Delta_T e^{\frac{V-V_{th}}{\Delta_T}} + I_{app}, \tag{2.15}$$

where $G_L\Delta_T e^{\frac{V-V_T}{\Delta_T}}$ is the spike generating current [106, 114, 118]. For pyramidal neurons Δ_T is typically equal to 1 mV.

Adaptive Integrate-and-Fire Model. Biologically speaking, the flow of specific ions during the opening and closing of channels modifies the intracellular concentration of that ion

and continues until the membrane potential decays back to the resting potential, thus a dynamically varying threshold [119]. Therefore, adaptation describes the instantaneous discharge rate in response to a sustained injected current, causing the firing rate to decay to a steady-state [120]. In the *adaptive* integrate-and-fire (AIF) model, the spike threshold is not constant as in the standard LIF; instead, the threshold $\theta(t)$ increases by α' after an AP and then decays exponentially to an asymptotic level θ_0 with a time constant τ_θ [109, 121]. In this case, the adaptation process is dependent on the firing history. The adaptive threshold $\theta(t)$ follows

$$\frac{d\theta}{dt} = \frac{\theta(t) - \theta_0}{\tau_\theta}, \tag{2.16}$$

where $\theta = V - V_R$, and if $V(t) > V_{th}$, then $V \rightarrow V_R$ and $\theta \rightarrow \theta + \alpha'$, where α' is usually equal to 0.1 mV [122, 123]. Studies on cortical pyramidal neurons revealed the presence of spike frequency adaptation mechanism, suggesting that IF models with adaptation can predict the firing rate of the neuron [124].

Adaptive Exponential Integrate-and-Fire Model (AdEx). The *adaptive exponential* integrate-and-fire model, generally called AdEx, is an extension of the EIF combined with an adaptation process [85]. In this case, it employs a spike-triggered current adaptation mechanism rather than an adaptive threshold [117, 123]. The AdEx model with an additional hyperpolarizing adaptation current is given as

$$\begin{aligned} C\frac{dV}{dt} &= -G_L(V - E_L) + G_L\Delta_T e^{\frac{V - V_{th}}{\Delta_T}} - I_{ad} + I_{app}, \\ \tau_{ad}\frac{dI_{ad}}{dt} &= a(V - V_R) - I_{ad}, \end{aligned} \tag{2.17}$$

where τ_{ad} is the time constant of the adaptation current I_{ad}, and a is a constant parameter [117, 125]. After an AP firing, V resets to V_R, whereas I_{ad} increases by a value b [117, 125]. When the neuron is at rest and I_{app} increases slowly to a critical current, the membrane potential destabilizes, resulting to the repetitive firing [117]. One advantage of the AdEx model is that the parameters can be fit with biological cell recordings [126].

2.5.2.2/ Other Threshold-based Models

The Izhikevich model is similar to the QIF with an adaptation process [85]. It also describes the subthreshold activity of the neuron, spikes up to a cut-off amplitude, and contains a recovery variable that accounts for the lumped K^+ activation and Na^+ inactivation currents [127]. The Izhikevich model is a system of two ordinary differential equations consisting of fast activation variable for the membrane potential, slow membrane recovery variable, and a resetting mechanism.

Fast-slow properties of the model help it simulate different types of oscillatory activity and spiking-bursting oscillations necessary for qualitatively reproducing a wide range of neuronal dynamics [86, 128]. This model is suitable for extensive network simulations because of its simplicity, computational efficiency, and biological plausibility [92, 129, 130].

2.6/ Signal Transmission Through Axons

Action potentials initiated in the AIS propagate along the axon proper to the axon terminals. During propagation, an AP undergoes a series of decay and regeneration as it travels through the alternating myelinated axon segments and nodes of Ranvier. Subtle changes in the myelin structure result in significant conduction velocity changes, critical to neural circuit functioning, and timely delivery of information in the CNS.

2.6.1/ Myelinated Axon Structure

Myelination is the process in which the plasma membranes of oligodendrocytes (a type of glial cells) ensheath the axons in the CNS with laminated layers of insulating materials as shown in Figure 2.11a [131–133]. These layers are compacted, forming periodic unexcitable myelinated axon segments, and unmyelinated gaps called nodes of Ranvier along the axon (Figure 2.11b). The myelin segment length tends to be similar along an axon rather than between individual axons. The nodes of Ranvier, which are approximately 0.3-1 μm long, are the unmyelinated regions (area free of myelin sheath) of the axon in contact with the extracellular matrix, thus allowing entry of Na^+ ions through Na_v channels [131–135]. Voltage-gated Na^+ channels are localized in the axonal membrane of the nodes of Ranvier with densities between 700 and 1200 per μm^2, enabling the regeneration of AP [100, 136]. The K_v channels are localized and segregated from the Na_v channels in the nodes of Ranvier, and are involved in AP repolarization [137].

2.6.2/ Saltatory Conduction

The interaction between the glial cell and the axon is essential for successfully transmitting the AP from the AIS to the axon terminal. The myelin sheaths inhibit ionic current conduction in the internodal region, therefore acting as an insulator. The signal passively and rapidly flows down through the myelin segment rather than across the axonal membrane [131, 133]. Depolarization only occurs in the nodes of Ranvier due to the high-density VGCs and their direct access to the extracellular space. Conduction through the alternating patterns of myelinated axon and nodes of Ranvier is therefore discontinuous, where AP from the AIS appears to 'jump' from node to node. This conduction is called **saltatory conduction** (Figure 2.12), an efficient process because only the small regions of the axon are depolarized (rather than the whole axonal length), thus enhancing the overall axon conduction [47, 79, 100, 132, 138, 139].

Saltatory conduction is rapid and cost-effective. Action potential propagation along the myelinated axon is 100-fold faster than along the unmyelinated axon as the oligodendrocytes reduce the charge needed for depolarization (1/100th of that the entire axonal length) [79, 131, 132, 140]. Also, saltatory conduction requires less energy to restore $[Na^+]$ gradient following AP generation in the node of Ranvier because of limited passive leaks and reduced current loss in the small nodes [79, 100]. Besides, myelinated axons are 50 times thinner than unmyelinated axons, allowing the brain to pack millions of axons [100].

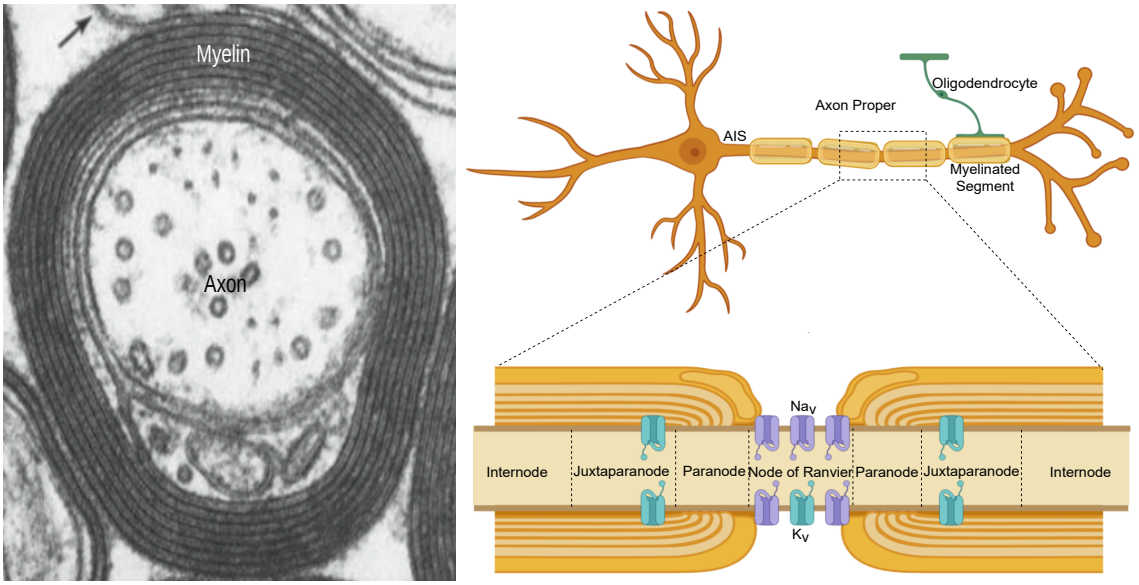

Figure 2.11: Myelinated axon structure. (a) The electron micrograph of an axon from a dog CNS shows the multiple layers of myelin sheaths [66]. (b) Oligodendrocytes wrap the axon with its plasma membrane creating myelin sheaths that insulate the axon segment. In between these myelin sheaths are the bare gaps called nodes of Ranvier, which have high expression of Na_v channels allowing Na^+ ions entry from the extracellular space through the axon membrane. The myelin sheaths are glued onto the axon membrane in the paranode regions, which inhibit current flow between the myelinated axonal segment and the nodes of Ranvier. Juxtaparanode regions are those axonal parts under the compacted myelin sheaths extending to the internode, where K_v channels are predominant. The internodes are directly under the compacted myelin sheaths and express low densities of VGCs.

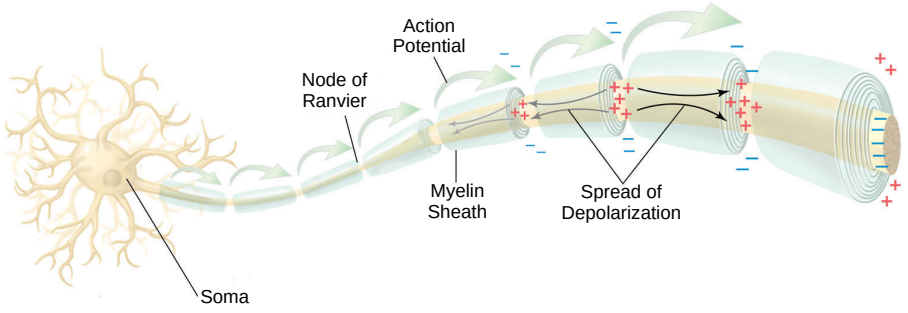

Figure 2.12: Saltatory conduction allows the AP initiated from the AIS to rapidly propagated down the axon terminal. The myelinated segment insulates the axonal membrane inhibiting ion flux from the extracellular space. Therefore, AP flows down the myelinated axon segment rather than across the membrane. Current flowing out the myelinated segment depolarizes the consecutive node of Ranvier, which has a high density of Na_v channels. Thus, the AP seems to jump from one node to the next. (The image was extracted from Rogers [141].)

2.6.3/ Electrical Model of Myelinated Axon

The axon is comparable to a transmission line where the nodes consist of leaky capacitors and voltage-sensitive ion channels (following the HH mechanisms) connected in parallel with the subsequent nodes by the internodal resistances and capacitances, as shown in the distributed circuit in Figure 2.13. The biological cable consists of two plates of conductors: the extracellular fluid and the intracellular fluid (axoplasm) [79, 132]. The

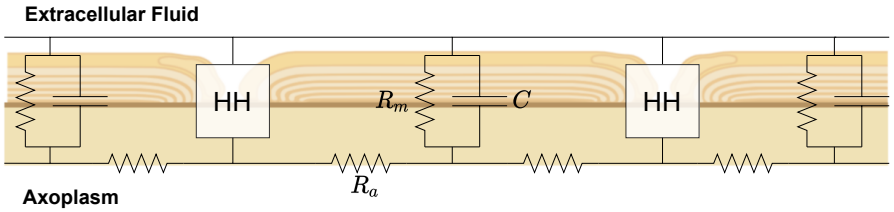

Figure 2.13: Myelinated axon equivalent circuit. The nodes of Ranvier follow the HH mechanisms for AP generation, and are connected in parallel with the subsequent nodes via the distributed circuit of the internodes. The myelinated axon is equivalent to a biological cable with two parallel conductors, the extracellular fluid and the axoplasm. The resistance of the extracellular fluid is negligible compared to the axoplasmic resistance (R_i). The parallel conductors then create a stray capacitance (C) while the myelin sheath provides a resistance (R_m) from ionic fluxes.

axoplasmic resistance (R_a) is high because of the conductivity of the inside fluid and the small cross-sectional area of the axon, thus cannot be disregarded. The resistance of the outside conductor is relatively lower than R_a because of the larger volume of the extracellular fluid and is assumed to be negligible. Furthermore, capacitance C occurs due to the two parallel conductors separated by a thin axon membrane (~7 nm), while a high membrane resistance R_m results from the insulation by the myelin sheath.

Generally, the resistance of a volume conductor is given as $R = \rho L/A$, where ρ is the resistivity (an intrinsic property of the material describing the opposition to electric current flow), L is the conductor length, and A is the cross-sectional area. The internal resistance R_a depends on the axon radius (r), therefore

$$R_a = \rho_a \frac{L}{\pi r^2}, \tag{2.18}$$

where ρ_a is the resistivity (Ω-cm) of the axoplasmic fluid, L is the internodal length, and r is the axon radius [132, 142]. The membrane resistance is dependent on the surface area of the membrane, thus

$$R_m = \frac{\rho_m}{2\pi r}, \tag{2.19}$$

where ρ_m is the membrane resistivity in Ω–cm^2 [142]. The internode then exhibits a capacitance

$$C = 2\pi r L C_m, \tag{2.20}$$

where C_m is the membrane capacitance per unit area.

2.6.4/ The Cable Equation

The AP initiated in the AIS enters the first myelinated segment, where the AP exhibits delay and decay. The current flowing from the other end of the segment must be enough to regenerate the AP in the node, as in saltatory conduction. The signal propagation along the myelinated segment, with respect to time and segment length, is often described by the cable model consisting of resistive and capacitive properties. The spatiotemporal cable model is a second-order differential equation that describes the membrane potential $v(x,t)$ as

$$\frac{r}{2\rho_a}\frac{\partial^2 v}{\partial x^2} - C_m\frac{\partial v}{\partial t} - \frac{v}{\rho_m l} = 0, \tag{2.21}$$

where v is the electrotonic potential (the difference between the membrane potential, and the resting potential) at time t, l is the membrane thickness, and x the location of v along the myelinated segment [143, 144]. In order to include the influence of distributed VGCs, such as K_v channels in the internode, the cable model is extended to

$$\frac{r}{2\rho_a}\frac{\partial^2 v}{\partial x^2} - C_m\frac{\partial v}{\partial t} - \frac{v}{\rho_m l} + \frac{G(v)}{2\pi r} = 0. \tag{2.22}$$

The parameter $G(v)$ is the charge generation function that describes the ionic exchanges within the segment and is equal to βv where $\beta \geq 0$. Bogatov et al. [143] presented an approximation of the cable model in Equation 2.22 and showed the changes in AP shape with distance traveled from the point of initiation and the propagation time.

$$v(x,t) \approx e^{-\frac{x\sqrt{\gamma}}{\lambda}} v_0\left(t - \frac{\tau x}{2\lambda\sqrt{\gamma}}\right), \tag{2.23}$$

where three constants parameters emerge: (1) γ (in mm) is the length constant which determines the maximum distance the AP can travel without considerate attenuation, (2) τ in (ms) is the time constant which is the maximum propagation time before the signal decay, and (3) γ (from 0 to 1) is the constant of distributed AP that describes the ionic exchanges within the segment. The term $-x\sqrt{\gamma}/\lambda$ describes the voltage decay while $\tau x/(2\lambda\sqrt{\gamma})$ is the time delay that the input v_0 experiences as it gets further away from the initiation site. The parameters are given as

$$\lambda = \sqrt{\frac{rl\rho_m}{2\rho_a}}, \quad \tau = l\rho_m C_m, \quad \text{and} \quad \gamma = 1 - \frac{\beta l\rho_m}{2\pi r}. \tag{2.24}$$

Length and Time Constant. The length constant and time constant govern the spread of AP from the initiation site to the adjacent node of Ranvier. The length constant determines the distance in which the signal can travel that still results in nodal membrane depolarization, and the time constant describes how long the capacitance delays the depolarization [139]. The myelin sheath serves two purposes in promoting signal propagation and conduction speed [79, 131, 135, 139]. First, it increases the effective axonal membrane resistance, lengthening the electrical space constant that promotes signal spread. Second, it lowers the effective membrane capacitance, decreasing the time constant so that less charge is needed to enter the node for depolarization. The time constant τ tends to increase with an increase in R_m. However, the decrease in C_m counteracts this effect; thus, τ remains almost constant [79]. Along the internode, the voltage decay is exponential (Equation 2.23). If λ is relatively short, the signal amplitude rapidly falls as a function of distance, and if it is shorter than the cable length, the signal will be insignificant [79]. Also, because of the high membrane capacitance, the membrane cannot charge immediately upon the arrival of the stimulus. The time it takes to charge one node depends on the charging time of the preceding internode [100].

Propagation Velocity. The propagation velocity depends on the interrelated factors, such as the axon diameter, the myelin thickness relative to the axon diameter, the internodal length, the length constant (λ), the time constant (τ), the local current intensity,

VGCs, and the threshold potential [79, 100, 131, 139, 145]. Therefore,

$$\theta \propto \frac{\lambda}{\tau}. \tag{2.25}$$

Substituting λ and τ, the propagation velocity becomes

$$\theta \propto \frac{1}{C_m}\sqrt{\frac{r}{R_m R_i}}. \tag{2.26}$$

Therefore, the larger the axon diameter, the lower the longitudinal resistance (R_m), the greater the local current flows along the internode. If myelination reduces C_m, then θ increases proportionally [79]. If the threshold (V_{th}) shifts to a more positive voltage, it will take longer for the node to spike; thus, the propagation velocity becomes slower. Considering the internode distance as constant, the *g*-ratio (the ratio between the axonal diameter and the sum of the axonal diameter and myelin sheath thickness) has a value of 0.6-0.7 for maximum conduction velocity [131].

2.7/ CONCLUSION

Information is initially stored as short-term memory in the hippocampus. Then, the hippocampus communicates with the prefrontal cortex to convert the short-term into long-term memory. Fundamental to the hippocampus processes is the neuron network called the trisynaptic circuit, where the information flows from the DG (input layer) to CA3, to CA1 subfields (hidden layers), and finally to the entorhinal cortex (output layer). Thus, the hippocampus inspired numerous research to understand its processes further and mimic them for applications in biomedical engineering and artificial neural networks (ANN).

Central to the hippocampal processes is the cellular elements called the pyramidal neurons. We presented its biological structure, morphology, and intracellular component. We then showed that the neuron membrane separates the extracellular fluid and the cytoplasm and plays a significant role in signal generation. The membrane consists of ion-specific channels regulating ion transport, such as Na^+, K^+, Ca^{2+}, and leakage ions, from and into the intracellular space. The intracellular concentration changes create a potential difference in the membrane that is essential for neuron signaling. We illustrated the influence of these ion channel dynamics on the neuron membrane using an equivalent electric circuit comprising the passive and active mechanism.

The instant that the membrane potential reaches a certain threshold, an AP is generated. This AP is considered the main information carrying-signal in the neuron and is generally generated in the AIS. The shape of the AP depends on the ionic channel distribution. The Hodgkin-Huxley model is the first model to describe the AP generation in the neuron. This model is recognized as biologically accurate since it details the dynamics of the necessary ion channels. Several neuron models were developed since then. Here, we presented the commonly used models and gave an example of the AP shape and spiking patterns resulting from increasing applied current intensity. Neuron models are divided into two categories based on the mechanism of spike initiation. AP generation can be dynamic-based, such as the HH, M-L, and FHN model, where the threshold is intrinsic in

the system. Models, such as the IF-type and Izhikevich models, initiate spikes when the membrane potential increases beyond an explicitly defined threshold.

Axons act as a transmission line that directs APs generated in the AIS to the neighboring neurons through synaptic endings, typically without significant AP changes and delays. Axonal excitability and signal transmission along the axon proper are challenging to study because the small axonal size poses difficulties in conventional electrophysiological recordings. However, recent studies on axons argued that axons modify the shape and firing patterns of APs, and determine how APs propagate along the axonal arbor, thus contributing to neural circuit functions. In this chapter, we have discussed the AP initiation in the AIS via the opening and closing of voltage-gated ion channels. The AP generation presented in this chapter follows a single-compartment model, that is, the AIS compartment.

In the following chapter, we present the information transfer from one neuron to another via the synapse. We also discuss the conversion of multiple incoming signals in the dendritic tree into a single AP.

3

Neurotransmission and Neural Coding

3.1/ Introduction

Neurotransmission is the process in which one neuron communicates to another neuron by releasing neurotransmitters into the synaptic space. The axon terminal of a presynaptic neuron transmits signals to its postsynaptic dendritic spine counterpart via the synapse chemically rather than electrically. The intracellular [Ca^{2+}] fluctuations play an essential role in converting the APs into chemical signals for presynaptic vesicle release of neurotransmitters, such as glutamate (Glu^{-}). Neurotransmitters then open neurotransmitter-specific receptors in the dendritic spines of spines, such as α-amino-3-hydroxy-5-methyl-4-isoxazolepropionic acid (AMPA) and N-methyl-D-aspartate (NMDA) receptors. These receptors are active mechanisms that induce membrane potential increase in the spine head.

The postsynaptic neuron receives thousands of synaptic inputs, be it excitatory or inhibitory inputs, from myriads of presynaptic neurons via its dendritic tree. These simultaneous inputs travel along the dendritic arborization to the soma while inducing changes in the membrane potential along their path, activating passive and active dendritic mechanisms. These mechanisms influence how the neuron processes the incoming signals and encodes information. The point neuron is the classical conceptual model of neural coding, wherein all inputs have the same influence on somatic depolarization. The soma integrates the synaptic inputs, and when the summation reaches a certain threshold, the soma generates an AP. The point neuron hypothesis, though conventionally used, is instead an oversimplified representation of neural computation and coding, as it disregards the local processes in the dendritic trees and the location of synaptic activation. Current studies suggest that the complex dendritic morphology creates independent computational subunits, compartments that perform individual operations separate from other dendritic branches or subunits. However, a comprehensive understanding of how neurons integrate the synaptic inputs, perform computations, and codes information into a single spike train is still lacking.

In this chapter, Section 3.2 describes the influence of APs and ER on the fast and slow Ca^{2+} dynamics. Section 3.3 is about neurotransmission. It illustrates the neurotransmitter release process and modes and describes the Glu^{-} dynamics in the synaptic cleft. Section 3.4 deals with signal propagation by describing the dendritic spines, the synaptic inputs that target them, and the resulting dendritic depolarization. It also illustrates

the dendritic membrane potential changes as the synaptic inputs travel along the dendritic arbor and the activation of passive and active dendritic mechanisms along the path. Lastly, Section 3.5 presents the transformation of synaptic inputs into somatic output. It describes the dendritic information processing, the processes the signals undergo before reaching the soma, and the computational schemes the neuron utilizes. It also presents dendritic abstractions and neural coding schemes at the single neuron level.

3.2/ Presynaptic Calcium Dynamics

Intracellular Ca^{2+} is an important secondary messenger that controls various cellular activities, such as in synaptic transmission [146–148]. The timing of fluctuations in the presynaptic Ca^{2+} concentration ($[Ca^{2+}]$) is crucial for triggering neurotransmitter release and improving synaptic plasticity [147, 149]. Various mechanisms control the presynaptic Ca^{2+} dynamics, including the voltage-dependent Ca^{2+} channels (VDCCs) along the cell membrane and the ER.

This section focuses mainly on the Ca^{2+} dynamics along the axon and specifically in the axon terminals. Cells not only exhibit compartmentalization of special proteins (ion channels) but also inorganic molecules such as Ca^{2+} ions [150]. The synaptic terminals display large $[Ca^{2+}]$ compared to the adjacent axonal segments, likely due to the nonuniform Ca^{2+} channel distribution [151]. Calcium signaling is both temporal and spatial. Cells can increase or decrease their $[Ca^{2+}]$ in different locations and with different timescales to target specific functions [146].

3.2.1/ Signaling Pathways

The series of intracellular biochemical reactions and diffusion, shown in Figure 3.1, forms signaling pathways wherein Ca^{2+} is a multifunctional secondary messenger [152]. Calcium is a unique secondary messenger in that Ca^{2+} influx can be derived from the opening of voltage-dependent ion channels or the Ca^{2+} released from the ER through Ca^{2+}-sensitive, Ca^{2+}-permeable channels. Here, we divide the intracellular signaling pathways into two timescales: the fast Ca^{2+} dynamics derived from the VDCCs, and the slow Ca^{2+} dynamics derived from Ca^{2+} stores.

3.2.1.1/ Voltage-dependent Calcium Influx

In the axon terminals, membrane depolarization controls Ca^{2+} signals [151, 153, 154]. Action potentials trigger Ca^{2+} influx to the cytosol from the extracellular space by opening voltage-dependent Ca^{2+} channels (VDCCs), which are voltage-sensitive membrane pores [147, 149, 153, 155]. Refer to Chapter 2 for the characteristics and subunits of VDCCs. All VDCC types are distributed in the neuron compartments, where P/Q-type and N-type channels are mainly responsible for Ca^{2+} influx in the presynaptic areas [155]. In the human brain during repetitive APs within a few hundreds of microseconds, approximately 10,000 Ca^{2+} ions enter the axon terminals or approximately a 500 nM-10 μM increase in

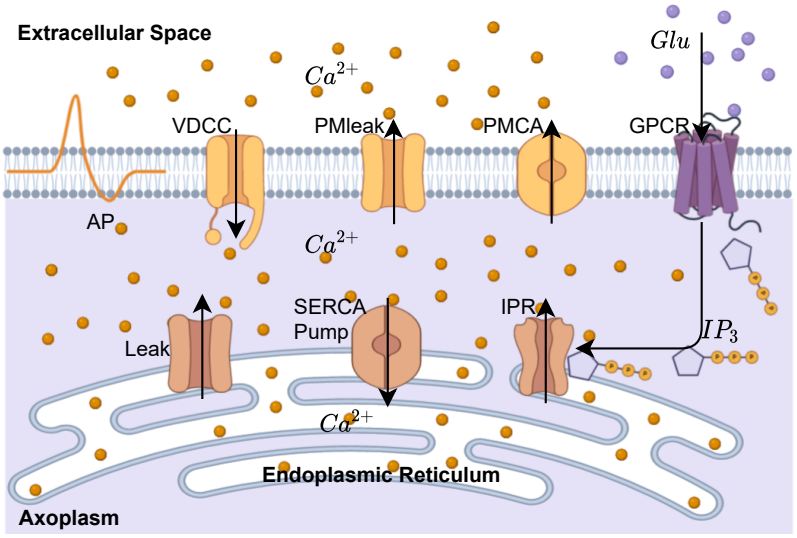

Figure 3.1: Calcium signaling pathways showing the influx and efflux of Ca^{2+} ions in the intracellular space (cytoplasm or axoplasm). The signaling pathways can be classified into two based on the Ca^{2+} signaling timescales. First is the fast Ca^{2+} influx from the extracellular space to the cytoplasm (axoplasm), derived from the opening voltage-sensitive Ca^{2+} channels (VDCCs) upon the arrival of APs. Surplus Ca^{2+} ions are pumped back to the extracellular space via plasma membrane leak channels (PMleak), and plasma membrane Ca^{2+} ATPase (PMCA) pumps to avoid cell toxicity due to high [Ca^{2+}]. Second is the slow Ca^{2+} influx from Ca^{2+} stores (endoplasmic reticulum). This influx includes an additional pathway for inositol-3-phosphate (IP_3). Extracellular molecules, glutamate (Glu^-), for example, impinge G-protein coupled receptors (GPCRs), which leads to the production of IP_3 molecules in the cytoplasm. IP_3 molecules diffuse and bind with IP_3 receptors (IPRs), which open the receptors for Ca^{2+} release from the ER. Excess Ca^{2+} ions are pumped back to the ER through sarco-endoplasmic receptor Ca^{2+} ATPase (SERCA) pumps, resulting in intracellular Ca^{2+} oscillations. The ER also has leakage channels that allow Ca^{2+} flow to the cytoplasm to avoid depletion of intracellular [Ca2+].

transient [Ca^{2+}] is elicited [151, 156]. The Ca^{2+} influx is driven by the 70 mV electrical gradient and a 20,000-fold concentration gradient, given that 50 nM intracellular and one mM extracellular [Ca^{2+}] [156]. When the Ca_v channels close, the Ca^{2+} ions diffuse in the intracellular space diminishing the [Ca^{2+}] in the microdomain, leaving a residual [Ca^{2+}] of 100 nM to 1 μM. High intracellular [Ca^{2+}] is detrimental to the cell. Therefore, excess cytosolic Ca^{2+} is removed from the cytosol to the extracellular space by plasma membrane Ca^{2+} (PMCA) pumps and plasma membrane leakage channels (PMleak) [155].

3.2.1.2/ Calcium Influx from Calcium Stores

One of the main contributors to the cytosolic Ca^{2+} oscillations is the ER. The smooth ER compartments are distributed throughout the neuron, extending to the axon and synaptic sites [150]. The smooth ER is a Ca^{2+} source, which stores internal [Ca^{2+}] of three to four orders of magnitude larger than in the cytosolic [Ca^{2+}] at resting condition [148, 152]. The ER releases Ca^{2+} via two types of channels. The first type is passive leakage channels that release Ca^{2}+ depending on the [Ca^{2+}] gradient between the cytosol and the ER. The second type is the Ca^{2+} release through inositol-3-phosphate (IP_3)-gated channels, or IP_3 receptors (IPR) [148, 152, 155]. The IP_3 signaling pathway starts from the extracellular molecules, such as glutamate (Glu^-), impinging the G-protein coupled receptors (GPCRs) on the cell membrane leading to the production of IP_3 molecules [157]. The IP_3

molecules then bind with the IPRs, which open to release Ca^{2+} to the cytosol [146]. As mentioned, high cytosolic [Ca^{2+}] is toxic to the cell. Therefore, following a rapid [Ca^{2+}] transient, excess cytosolic Ca^{2+} is pumped back to the ER via the sarco/endoplasmic reticulum Ca^{2+} ATPase (SERCA) pumps that results in a repetition of Ca^{2+} release and uptake cycle [146, 148, 155]. On the other hand, the ER leakage channel allows Ca^{2+} to enter the cytosol to ensure that the cytosolic [Ca^{2+}] will not decrease to 0 [88].

3.2.2/ Modeling Calcium Dynamics

The following dynamics and models describe the intracellular Ca^{2+} dynamics within a single compartment, where the external [Ca^{2+}] is held constant at resting conditions. The change in [Ca^{2+}] in a compartment is attributed to the fast kinetics of AP and the intracellular molecular events generating Ca^{2+} change. The total [Ca^{2+}] in the compartment, c_i, is equal to the summation of the [Ca^{2+}] due to AP, c_{fast}, and the intracellular transient [Ca^{2+}], c_{slow}, and is described as

$$\begin{aligned} c_i &= c_{fast} + c_{slow}, \\ \frac{dc_i}{dt} &= \frac{dc_{fast}}{dt} + \frac{dc_{slow}}{dt}. \end{aligned} \tag{3.1}$$

3.2.2.1/ Fast Calcium Dynamics

A set of ordinary differential equations describe the intracellular Ca^{2+} dynamics resulting from the time-dependent membrane potentials. In the following models, the Ca^{2+} influx in a single compartment (with homogeneous extracellular space) is related to the model geometry. The fast Ca^{2+} dynamics, c_{fast}, through voltage-dependent calcium channels (VDCCs), is governed by the construction-destruction formula [88, 147, 149, 158],

$$\frac{dc_{fast}}{dt} = -\frac{I_{Ca}A}{z_{Ca}Fv_c} + J_{PMleak} - \frac{I_{PMCA}A}{z_{Ca}Fv_c}. \tag{3.2}$$

Here, A is the surface area of the compartment, z_{Ca} is the Ca^{2+} ion valence, F is the Faraday's constant, and v_c is the volume of the compartment. The I_{Ca} is the influx current density per membrane surface area through N-type VDCC, which is directly dependent on the membrane potential V. The I_{PMCA} is the efflux current density per membrane surface area caused by ATP-driven PMCA and is dependent on the intracellular [Ca^{2+}]. The Ca^{2+} leak efflux J_{PMleak} represents all remaining currents implicitly described in the model.

The ohmic current-voltage relation of the Ca^{2+} influx, I_{Ca}, consists of both the voltage-dependent current through a single open pore $I_{open}^{single\ channel} = g_{Ca}(V - V_{Ca})$ and the VDCC voltage-dependent opening probability m_{Ca} [147, 149]. Therefore, the electrochemical gradient over the membrane drives the $Ca^{2}+$ current through an open VDCC. The current surface density through the N-type VDCC is given as

$$I_{Ca} = \rho_{Ca} m_{Ca}^2 g_{Ca} (V - V_{Ca}), \tag{3.3}$$

where ρ_{Ca} is the N-type channel surface density, g_{Ca} is the single N-type Ca^{2+} open-pore

conductivity [88, 147, 158, 159]. The potential difference through the VDCC is relative to the Ca^{2+} reversal potential, V_{Ca}, and incorporates in the model the [Ca^{2+}] in the intracellular and extracellular space at rest. The Nernst equation determines the VDCC reversal potential,

$$V_{Ca} = \frac{RT}{z_{Ca}F} \ln\left(\frac{c_{ext}}{c_i^{rest}}\right), \tag{3.4}$$

where c_{ext} is the extracellular [Ca^{2+}] and c_i^{rest} is the intracellular [Ca^{2+}] at rest. The variable m_{Ca} is the opening probability of a single gate in a two-gate N-type Ca^{2+} channel that is only open when the two gates are open. The probability is time-dependent and modeled by a single exponential approximation so that

$$\frac{dm_{Ca}}{dt} = \frac{\left(m_{Ca}^{\infty} - m_{Ca}\right)}{\tau_{m_{Ca}}}, \tag{3.5}$$

which may be related to experiment using data for the average number of open channels in an ensemble of channels [147, 149]. The probability m_{Ca} approaches its asymptotic value, m_{Ca}^{∞}, with a time constant $\tau_{m_{Ca}}$ [147]. The voltage-dependent m_{Ca}^{∞} is a sigmoidal function given by the Boltzmann function,

$$m_{ca}^{\infty} = \frac{1}{1 + e^{\frac{V_{m_{Ca}} - V}{k_{m_{Ca}}}}}, \tag{3.6}$$

approximated the dependence of m_{Ca}^{∞} on V fitted to the whole-cell current of an N-type Ca^{2+} channel. Here, $V_{m_{Ca}}$ is the half-activation voltage, and $k_{m_{Ca}}$ describes the steepness of the asymptotic opening probability m_{Ca}^{∞} [88, 147, 149, 158, 159]. In presynaptic axon terminals, the Ca^{2+} influx during a single AP has approximately 1 ms and 60 ms of a fast rise and slow decay time constants, respectively [151]. The proteins such as PMCAs actively transport Ca^{2+} ions through the membrane against the electrochemical gradient using the ATP molecules energy, and whose kinetics are different from pores (e.g., VDCCs) [147]. The protein structure limits the PMCA kinetics to a maximum rate [147, 149]. The Ca^{2+} current due to PMCA, I_{PMCA} is best described by the Hill function

$$I_{PMCA} = v_{PMCA} \frac{c_i^2}{c_i^2 + K_{PMCA}^2}, \tag{3.7}$$

where v_{PMCA} is the maximum Ca^{2+} current via PMCA and K_{PMCA} is the [Ca^{2+}] at half of v_{PMCA} [88, 149].

Then, J_{PMleak} in is the leak from the extracellular space into the compartment and is added to ensure that the [Ca^{2+}] will not decrease to 0, in that

$$J_{PMleak} = v_{leak}\left(c_{ext} - c_i\right), \tag{3.8}$$

where v_{leak} is the maximal [Ca^{2+}] and c_{ext} is the external [Ca^{2+}] [88].

3.2.2.2/ Slow Calcium Dynamics

The slow Ca^{2+} dynamics, c_{slow}, is attributed to (1) the release of Ca^{2+} from the ER triggered by the production of intracellular messenger IP_3, by the binding of the extracellular Glu^- molecules and the Glu^- receptors, and (2) the SERCA pump that pumps Ca^{2+} back into the Ca^{2+} depot [88, 158, 160, 161].

The IPR kinetics are central to IP_3-based Ca^{2+} signaling. The intracellular $[IP_3]$, p, is given as

$$\frac{dp}{dt} = v_g \frac{g^{0.3}}{k_g^{0.3} + g^{0.3}} - \tau_p (p - p_0), \tag{3.9}$$

where g is the extracellular $[Glu^-]$, p_0 is the resting $[IP_3]$, v_g is the maximum IP_3 production rate, k_g is the half-activation based on $[Glu^-]$, and τ_p is the IP_3 degradation constant [88]. The physiological range of $[IP_3]$ is between 0 and 5 μM [157].

The Li-Rinzel model describes the dynamical system governing the c_{slow} behavior [162]. The model assumes that the regulatory properties of the IPR provoke the periodic release of Ca^{2+} ions from the ER [157]. Under this hypothesis, intracellular calcium balance is determined by only three fluxes, corresponding to (1) a passive leak of Ca^{2+} from the ER to the cytosol (J_{leak}); (2) an active uptake of Ca^{2+} into ER (J_{pump}) due to action of SERCA pumps; and (3) a Ca^{2+} release (J_{chan}) that is mutually gated by Ca^{2+} and IP_3 concentrations (denoted by c_i and p, respectively) [157, 158]. Therefore,

$$\frac{dc_{slow}}{dt} = -J_{chan} - J_{pump} - J_{leak}, \tag{3.10}$$

describes the slow Ca^{2+} dynamics [88, 158, 160, 161, 163].

The Ca^{2+} current flowing out of the ER-mediated by IPR channel is relative to the $[Ca^{2+}]$ gradient between the cytosol and the ER whose permeability is relative to the IPR permeability, $r_C = c_1 v_1$, times the open channel probability [157]. The open channel probability is based on a gating model of the IPR subunit, assuming three binding sites: one for IP_3 and two for Ca^{2+} (including one activation and one inactivation site). Let m_∞ be the IP_3 binding probability, n_∞ is the Ca^{2+} activation, and q is the Ca^{2+} inactivation probability. Experimental data suggest a third power for the probabilities, thus

$$J_{chan} = r_C m_\infty^3 n_\infty^3 q^3 (c_i - c_{ER}), \tag{3.11}$$

where the opening probabilities

$$m_\infty = \frac{p}{p + d_1}, \text{ and } n_\infty = \frac{c_i}{c_i + d_5}, \tag{3.12}$$

are direct functions of intracellular $[IP_3]$ and $[Ca^{2+}]$, respectively, and where v_1 is the maximum IP_3 receptor flux, d_1 is the IP_3 dissociation constant, and d_5 is the activation Ca^{2+} dissociation constant [88, 157]. The concentration in the ER, c_{ER}, is relative to the slow calcium dynamics and is described as

$$\frac{dc_{ER}}{dt} = -\frac{1}{c_1} \frac{dc_{slow}}{dt}, \tag{3.13}$$

where c_1 is the ratio between the ER volume and the compartment volume [88]. For isolated cell model where Ca^{2+} fluxes across the membrane (fast Ca^{2+} dynamics) are neglected, the average free [Ca^{2+}] (c_0) is conserved [157]. Thus c_{ER} is equivalent to

$$c_{ER} = \frac{c_0 - c_i}{c_1}. \tag{3.14}$$

Assuming fast IP_3 binding and Ca^{2+} activation, the IPR gating kinetics is described by an ordinary differential equation with a dimensionless variable q that represents the inactivated IPRs by intracellular Ca^{2+},

$$\begin{aligned} \frac{dq}{dt} &= \alpha_q (1 - q) - \beta_q q, \\ \alpha_q &= a_2 d_2 \frac{p + d_1}{p + d_3}, \\ \beta_q &= a_2 c_1, \end{aligned} \tag{3.15}$$

where a_2 is the inhibitory Ca^{2+} binding constant, and d_3 is also an IP_3 dissociation constants [88, 157].

Intracellular Ca^{2+} oscillations can also be due to the activity of SERCA pumps drawing Ca^{2+} ions back to the ER. The Ca^{2+} pump rate is an instantaneous function of intracellular [Ca^{2+}] and expresses a Hill function with a Hill constant of 2.

$$J_{pump} = v_3 \frac{c_i^2}{k_3^2 + c_i^2}, \tag{3.16}$$

where v_3 is the maximal Ca^{2+} uptake rate of SERCA and k_3 is the SERCA Ca^{2+} affinity [88, 157].

The passive Ca^{2+} leakage current, J_{leak}, is relative to the [Ca^{2+}] gradient across the ER membrane and the maximum Ca^{2+} leakage rate from the ER to the cytosol.

$$J_{leak} = r_L (c_i - c_{ER}), \tag{3.17}$$

where $r_L = c_1 v_2$, and v_2 is the Ca^{2+} leak rate constant.

The Ca^{2+} influxes J_{chan} and J_{leak} can be grouped into J_{rel}.

$$\begin{aligned} J_{rel}(c_i, q, p) &= J_{chan}(c_i, q, p) + J_{leak}(c_i) \\ &= \left(r_C m_\infty^3 n_\infty^3 h_\infty^3 + r_L \right) (c_{ER} - c_i). \end{aligned} \tag{3.18}$$

Thus, J_{rel} becomes a function of cell parameters described by

$$J_{rel}(c_i, q, p) = \left(r_C m_\infty^3 n_\infty^3 h_\infty^3 + r_L \right) \times (c_0 - (1 + c_1) c_i). \tag{3.19}$$

Therefore, the intracellular [Ca^{2+}] balance equation is

$$\frac{dc_i}{dt} = -J_{rel}(c_i, q, p) - J_{pump}(c_i). \tag{3.20}$$

The Ca^{2+} dynamics equilibrium occurs when both the intracellular Ca^{2+} level and the fraction of inactivated IPR are constant, that is $dc_i/dt = 0$ and $dq/dt = 0$ [157]. During stimulation, cytosolic [Ca^{2+}] tends to fluctuate, also referred to as Ca^{2+} oscillations [148]. In the Li-Rinzel model, Ca^{2+} oscillations are related to the IP_3 levels; the stability in Ca^{2+} levels occurs either during low or high [IP_3] [157].

3.3/ NEUROTRANSMISSION

What is the importance of Ca^{2+} concentration and oscillations in the axon terminal? One consequence of the Ca^{2+} influx in the presynaptic terminal is the initiation of **synaptic transmission**, the process in which one neuron communicates with another. The accumulation of AP-evoked transient Ca^{2+} triggers synaptic vesicle exocytosis, therefore releasing neurotransmitters into the synaptic cleft. Synaptic neurotransmitters enter the postsynaptic neuron through the receptors in the spine head, causing membrane depolarization due to **excitatory neurotransmitters** or temporary hyperpolarization due to **inhibitory neurotransmitters**. The neurotransmitter presented here is of excitatory type, specifically glutamate (Glu^-). Therefore, synaptic transmission is the interplay between the electrical and chemical dynamics of the neurons.

The **synapse**, the basic neurotransmission unit, is a complex physiological structure that connects the axon terminal or bouton of the presynaptic neuron with the dendritic spine head of the postsynaptic neuron [164, 165]. The synapse serves as an intercellular junction whose intersynaptic space is approximately 15 nm between the bouton and the spine head [165]. Neurotransmitters are chemical messengers, molecules used by the neurons to transfer information to targeted cells. In the presynaptic neuron, these neurotransmitters are stored in **vesicles**, membrane-bound organelles synthesized in the soma [164, 166]. Cargos, such as neurotransmitters, are packaged into these vesicles for transport to the active zones located in the axon terminals through a microtubule-dependent process. A **quantal size** corresponds to a single synaptic vesicle [167]. Synaptic vesicles are classified according to their propensity to fuse with the plasma membrane [165]. The **readily releasable pool** (RRP), which is less than 5% of the total synaptic vesicles, fuse in response to an AP [165, 168]. In hippocampal synapses, the docked synaptic vesicles belong to the RRP. **Docked vesicles** are those vesicles fastened to the plasma membrane near the active zone [169]. The **reserved pool**, which comprises 10-60% of the total vesicles, restock the RRP to maintain neurotransmission [165]. Therefore, the RRP and reserved pool form the recycling pool of synaptic vesicles. The rest of the synaptic vesicles belong to the **resting** or **dormant pool**, which is highly invulnerable to synaptic activity. The resting pool may contribute to spontaneous neurotransmitter release or may act as reserved synaptic vesicles.

3.3.1/ NEUROTRANSMITTER RELEASE PROCESS

Figure 3.2 shows the neurotransmission process, from the AP-triggered Ca^{2+} influx to vesicle fusion and priming with the axon terminal membrane to neurotransmitters diffusing into the synaptic space. Neurotransmission begins with the arrival of APs in the

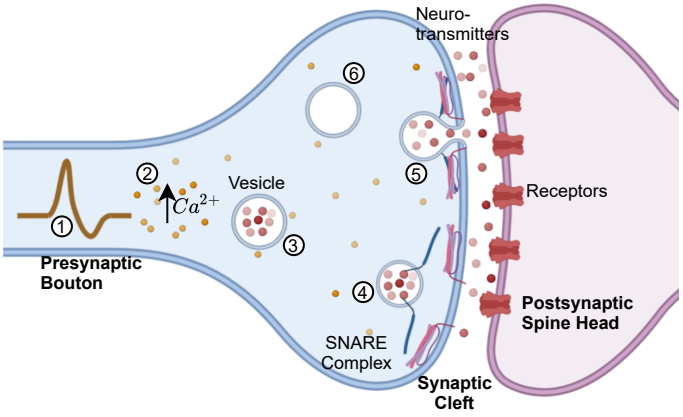

Figure 3.2: Calcium-triggered neurotransmitter release. Synaptic transmission occurs chemically via the presynaptic release of neurotransmitters from the axon terminal or bouton into the synaptic cleft and followed by the neurotransmitter uptake of the postsynaptic counterpart through the receptors in the spine head. (1) The arrival of APs in the axon terminal activates the VDCCs in the active zone, (2) increasing intracellular [Ca^{2+}]. (3) Calcium ions bind with the neurotransmitter-containing vesicle Ca^{2+} sensors. (4) With sufficient bounded Ca^{2+} ions, Ca^{2+} sensors activate and induce the fusion and priming of vesicles with the plasma membrane through the complex soluble N-ethylmaleimide-sensitive factor attachment protein receptors (SNARE) complex. (5) The vesicle and plasma membrane fuse together, creating an opening in the membrane for neurotransmitter release into the synaptic cleft. (6) Empty vesicles return in the circulation to replenish their vesicular neurotransmitters through endocytosis.

axon terminal, briefly opening VDCCs in the active zone, causing a rapid influx of highly-localized, transient Ca^{2+} ions [164, 164, 165, 167, 168, 170]. Intracellular Ca^{2+} ions bind with the vesicular Ca^{2+} sensors. The kinetic binding schemes between the vesicular sensor and intracellular [Ca^{2+}] differ depending on the release mode, the level of [Ca^{2+}], and synaptic plasticity [171]. In this study, there are five cooperative, low-affinity Ca^{2+}-binding sites where five Ca^{2+} ions must bind with vesicular Ca^{2+} sensors to induce docking. The kinetic model governing the Ca^{2+} binding to the Ca^{2+} sensors is given as

$$X \underset{\beta}{\overset{5\alpha c_i}{\rightleftarrows}} X(c_i)_1 \underset{2\beta}{\overset{4\alpha c_i}{\rightleftarrows}} X(c_i)_2 \underset{3\beta}{\overset{3\alpha c_i}{\rightleftarrows}} X(c_i)_3 \underset{4\beta}{\overset{2\alpha c_i}{\rightleftarrows}} X(c_i)_4 \underset{5\beta}{\overset{\alpha c_i}{\rightleftarrows}} X(c_i)_5 \underset{\delta}{\overset{\gamma}{\rightleftarrows}} X(c_i)_5^*, \tag{3.21}$$

where X is the Ca^{2+} sensor with no Ca^{2+} bound, $X(c_i)_1$ to $X(c_i)_5$ correspond to the Ca^{2+} sensors with one to five Ca^{2+} bound, $X(c_i)_5^*$ is the isomer of $X(c_i)_5$ ready for release, α and β are the Ca^{2+} association and dissociation constants, respectively, and γ and δ are the Ca^{2+} independent isomerization constants [172]. With sufficient bounded Ca^{2+} and [Ca^{2+}] elevation of $\sim$10 μM [173], Ca^{2+} sensors activate, inducing docking and then priming synaptic vesicles with the axon terminal membrane [164, 167, 168, 174]. During priming, the soluble N-ethylmaleimide-sensitive factor attachment protein receptors (SNARE) fusion complex starts to form in the synaptic vesicles and SNAREs syntaxin 1 and on the plasma membrane [164, 165, 169, 175]. The SNARE complex space is limited [175]; thus, there are two docked vesicles at the active zone [88]. The SNARE fusion complex pulls together the vesicle and the plasma membrane, effectuating the opening and expansion of the pore for exocytosis. The pore opening and neurotransmitter release are either Ca^{2+}-triggered mediated by Ca^{2+} sensors or by spontaneous release [170, 174]. After neurotransmitter release, the SNARE complex disassembles, and the empty vesicle leaves the terminal and reenters the vesicle circulation for endocytosis [166, 174]. The released neurotransmitters rapidly diffuse from the axon terminal and bind to dendritic

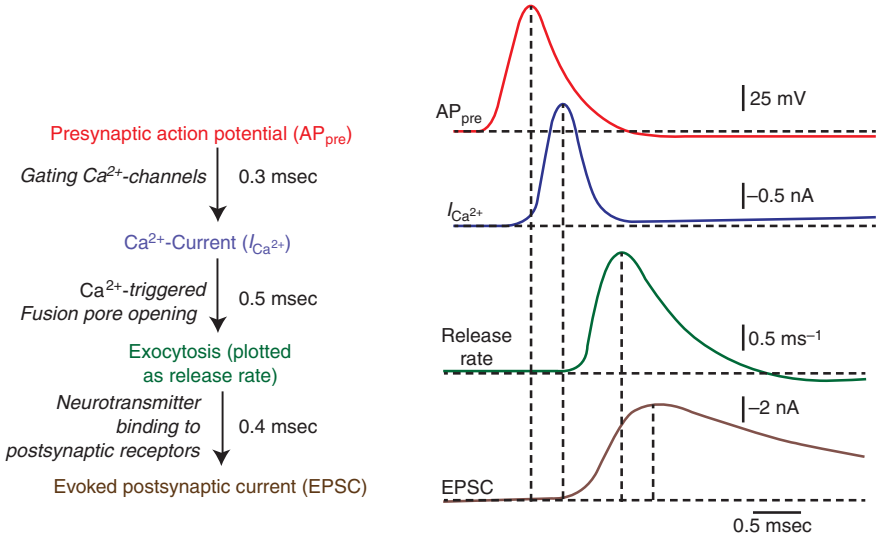

Figure 3.3: Neurotransmission time course. A single neurotransmission cycle, starting from the arrival of AP, to Ca^{2+} influx and binding with synaptic vesicles, to vesicle and plasma membrane fusion, and opening of pores for neurotransmitter release transpires within a few milliseconds. (Image was extracted from Südhof [170].)

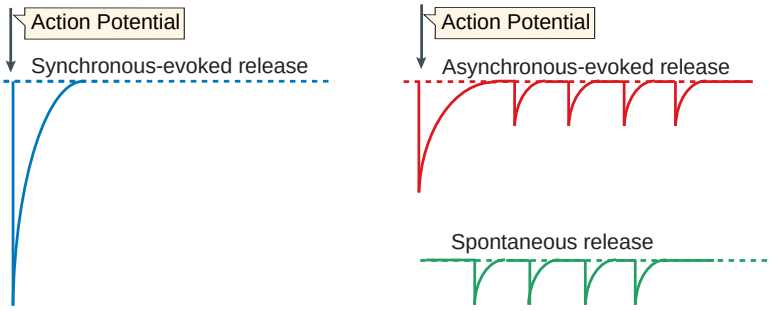

Figure 3.4: Modes of neurotransmitter release. Synchronous release occurs during the rapid Ca^{2+} influx upon the arrival of AP. Asynchronous release occurs and persists even after the arrival of the last AP. Spontaneous release is regulated by Ca^{2+} fluctuations but is independent of neuronal activity. (Image was extracted from Kavalali [169].)

receptors that induce postsynaptic membrane potential changes [165]. The success of synaptic transmission, therefore, is dependent on (1) the number of readily releasable vesicles, the [Ca^{2+}] in the presynaptic bouton, and (3) the Ca^{2+} coupling and vesicle fusion [167]. The neurotransmitter release process occurs within milliseconds upon arrival of an AP [175]. The neurotransmission time course is presented in Figure 3.3.

3.3.2/ Modes of Neurotransmitter Release

Molecular and electrophysiological data revealed diversity in synaptic vesicles, in turn, in presynaptic exocytotic fusion machinery, giving rise to multiple modes of neurotransmitter release: synchronous, asynchronous, and spontaneous release (Figure 3.4). These modes are influenced by the AP arrival or by transient [Ca^{2+}].

3.3.2.1/ SYNCHRONOUS RELEASE

The synchronous release is the predominant mode of neurotransmitter release in most synapses, accounting for >90% of release at low-frequency stimulation [164, 168]. Synchronous neurotransmitter release is time-locked with the arrival of AP in the axon terminal and induced by the rapid Ca^{2+} influx, which is closely associated with Ca^{2+} mediated fusion of synaptic vesicles [164, 165, 174]. In the presynaptic Ca^{2+} nanodomains, Ca^{2+} sensors respond quickly to Ca^{2+} entry, have low Ca^{2+}-affinity, and fast off-rate [168]. Vesicle fusion occurs in less than a millisecond after an AP invades the axon terminal. These properties are exceptionally vital for neuronal communication, which requires **fast neurotransmission** [165, 168]. The axon terminal must generate and maintains the RRP of vesicles for fast exocytosis.

Tsodyks-Markram Model. The **Tsodyks-Markram Model** (TMM) [176] is the classical phenomenological model that describes the time evolution of available vesicles and dynamically changing release probability [164, 174]. The arrival of AP at time t_{AP} induces a fraction of total vesicles in the RRP, R, to release their neurotransmitter content, where the total amount of neurotransmitter for release, E, is contained in this fraction of readily releasable vesicles (Equation 3.22).

$$\begin{aligned} \frac{dR}{dt} &= -\frac{R}{\tau_f} + R_0\,[1-R]\sum_{AP}\delta(t-t_{AP}), \\ \frac{dE}{dt} &= \frac{E_F - E}{\tau_d} - q_r, \end{aligned} \tag{3.22}$$

where τ_f controls the rate of decay of R, τ_d controls the rate of replenishment of vesicles, R_0 denotes the increment of R due to the arrival of AP, E_F is the total neurotransmitter in the vesicles after replenishment, and $\delta(\cdot)$ is the Dirac delta function. The variable q_r is the neurotransmitter release rate, described as

$$q_r = R(t_{AP}^+)E(t_{AP}^-)\sum_{AP}\delta(t-t_{AP}), \tag{3.23}$$

where t_{AP}^+ and t_{AP}^- correspond to when an AP begins and ends, respectively.

Tsodyks Model. The **Tsodyks Model** [177] is an extension of the TMM. In this case, instead of computing the amount of neurotransmitters in the readily releasable vesicles, the model postulates the probability of neurotransmitter release. Upon the arrival of AP at t_{AP}, the probability of neurotransmitters available for release (u_S) increases by a factor u_0 (release probability at rest), while the readily releasable neurotransmitter (x_S) decreases by a fraction

$$r_S(t_{AP}) = u_S(t_{AP}^+)x_S(t_{AP}^-), \tag{3.24}$$

that corresponds to the fraction of effectively released neurotransmitter. In between APs, neurotransmitter resources are reintegrated at a rate of $1/\tau_d$ while u_S decays to zero at a

rate of τ_f. The probabilities are given as

$$\begin{aligned} \tau_f \frac{du_S}{dt} &= -u_S + \sum_{AP} u_0 \left(1 - u_S\right) \delta \left(t - t_{-AP}\right) \tau_f, \\ \tau_d \frac{dx_S}{dt} &= 1 - x_S - \sum_{AP} r_S \delta \left(t - t_{AP}\right) \tau_d. \end{aligned} \tag{3.25}$$

The synapse is "at rest" when $u_S \rightarrow 0$ and $x_S \rightarrow 1$, which occurs during the AP onset is much larger than the synaptic time scales τ_d and τ_f. In this case, the probability of AP-evoked neurotransmitter release from the presynaptic bouton is equal to u_0 [178].

3.3.2.2/ Asynchronous Release

There are also some cases wherein synaptic transmission occurs even after the last AP. Synaptic vesicles fuse and release neurotransmitters asynchronously, and the amount of neurotransmitter that is released can be quite large [164, 165, 167, 168, 174]. This release may occur and persists for tens to hundreds of milliseconds after the end of stimulation, a single or a series of APs. The neuron type, presynaptic terminal capacity, intrinsic molecular attributes of the neurotransmitter release machinery, and prior activity history are some conditions that influence this particular mode of release. The asynchronous release is stochastic, and the level and duration are regulated by the Ca^{2+} entry and from sustained moderate- to high-frequency stimulation.

3.3.2.3/ Spontaneous Release

Almost in all neurons, spontaneous mini-releases occurs even when the presynaptic membrane is not depolarized, in that it is independent of neuronal activity [165, 168, 170, 174]. Confocal or two-photon microscopy with single-cell electrophysiology in the hippocampal CA1 area suggests that the spontaneous fluctuations of intracellular Ca^{2+} also regulate this mode of release [155, 165, 170]. The significance of spontaneous release is still under debate, though it may implicate synaptic stabilization, long-term synaptic plasticity and may prevent loss of dendritic spines [168].

Unlike in synchronous release, where the synaptic neurotransmitter can be computed directly in response to AP, the spontaneous release is dependent on the state of vesicles ready to be released. Given two docked vesicles in the active zone, the number of vesicles ready to be released spontaneously, f_r, can have values of [0, 0.5, 1] for [0, 1, 2] releasable vesicles. The probability, f_r, is a stochastic process; therefore, the fluctuation in f_r is a Poisson process whose rate, λ, is dependent on the intracellular [Ca^{2+}], c_i,

$$\lambda(c_i) = a_3 \left(1 + \exp\left(\frac{a_1 - c_i}{a_2}\right)\right)^{-1}, \tag{3.26}$$

where a_1 is the [Ca^{2+}] at which λ is halved, a_3 is the slope factor of spontaneous release rate λ, and a_3 is the maximum spontaneous release rate. Tewari et al. [88] modified the

TMM to make the vesicle fusion f_r-dependent.

$$\begin{aligned} \frac{dR}{dt} &= \frac{1}{\tau_{rec}} - f_r \cdot R, \\ \frac{dE}{dt} &= -\frac{E}{\tau_{inact}} + f_r \cdot R, \\ I &= 1 - R - E, \end{aligned} \tag{3.27}$$

where R is the fraction of releasable vesicles in the presynaptic terminal, E is the fraction of effective vesicles in the synaptic cleft, I is the fraction of inactive vesicles undergoing recycling, and τ_{inact} and τ_{rec} are the time constants of vesicle inactivation and recovery. Once a vesicle is released, either synchronously or spontaneously, the release process remains inactivated for 6.34 ms.

3.3.3/ Synaptic Glutamate Dynamics

The most abundant neurotransmitter in the human brain (80-90% of the neurons) is glutamate (Glu^-), which excites virtually every neuron (80-90% of synapses) for fast excitatory neurotransmission [179, 180]. In the hippocampus, Glu^- is the principal mediator for memory formation and retrieval. The hippocampus comprises mainly glutamatergic synapses: the entorhinal cortex to DG, DG to CA3, and between pyramidal cells from CA3 to CA1 regions. There are only a few mmol/l of Glu^- in the cytosol; instead, Glu^- is concentrated in the synaptic vesicles with 60-250 mmol/l of [Glu^-] per vesicle. A glutamatergic vesicle has an inner radius of ~17 nm and a volume of $2{\times}10^{-20}$ liters. Therefore, a [Glu^-] of 100 mmol/l (~$6{\times}10^{22}$ molecules per liter) would yield 1200 molecules of Glu^- in each vesicle.

In the Tsodyks model in Equation 3.25, assuming that the total vesicular [Glu^-] is Y_T, the released Glu^- into the synaptic cleft is equal to the

$$Y_{rel}(t_{AP}) = \varrho_c Y_T r_S(t_{AP}), \tag{3.28}$$

where ϱ_c represents the ratio between vesicular and synaptic cleft volumes [178, 179]. The time course of synaptically released Glu, Y_S , is modeled by a first-order degradation reaction of characteristic time τ_c,

$$\tau_c \frac{dY_S}{dt} = -Y_S + \sum_{AP} Y_{rel}\delta(t - t_{AP})\,\tau_c. \tag{3.29}$$

There are two vital quantities for the spontaneous release model: n_v, which is the number of docked of vesicles, and f_r, which is the release probability updated during every arrival of AP at time t_{AP} [174]. Therefore, the total amount of neurotransmitter released, with a small time delay, during a single AP is $T_(t_{AP}) = n_v(t_{AP})f_r(t_{AP})$. Upon synaptic release, Glu^- must rapidly exit the synaptic cleft, usually diffusing to the extrasynaptic space for astrocytic reuptake [181]. The synaptic cleft must regulate its [Glu^-] to prevent overactivation of neuronal glutamate receptors, which leads to excitotoxicity [179–181]. Therefore, in order to include the synaptic glutamate clearance, synaptic [Glu^-], g, time course is

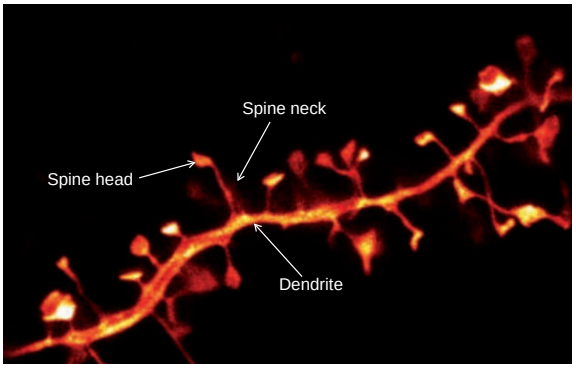

Figure 3.5: Stimulated-emission-depletion image of a spine-covered dendrite recorded from a living neuron of a hippocampal slice. (Image taken from de Souza [184].)

modified into

$$\frac{dg}{dt} = n_v g_v E - g_c g, \tag{3.30}$$

where E is the effective fraction of Glu^- in the synaptic cleft (Equation 3.27), g_v is the vesicular [Glu^-], and g_c is the rate of Glu^- clearance by neuronal or astrocytic reuptake [88]. Using these dynamics, synaptic [Glu^-] ranges from 0.24 to 11 mM and last 2 ms.

3.4/ Signal Propagation along the Dendritic Arborization

In the mammalian brain, a neuron typically receives 10^3 to 10^4 synaptic information formed on the dendritic tree, which processes electrical information locally and globally within a millisecond timescale [182, 183]. The complex morphology of neurons has fascinated neuroscientists since Cajal published his drawings of brain cells. Decades of experimental and computational work have shown that neurons performed sophisticated computations through the complex and diversified biophysical and electrical dendritic compartments. Studies on neuronal morphology, especially in varying and constant dendritic properties, attempt to elucidate the information transmission and signal processing in neurons.

3.4.1/ Synaptic Inputs via Dendritic Spines

The dendrites of pyramidal neurons are covered with small protrusions called **dendritic spines** (Figure 3.5), emanating from the dendritic surface [182, 183, 185]. The dendritic spines form the primary site of synaptic information contacts, mostly from (~95%) excitatory neurons and some from inhibitory interneurons. Figure 3.5 shows a dendritic segment recorded using a stimulated-emission depletion (STED) microscope. Spine distribution is low on dendrites less than 40 μm from the soma, then increases to a maximum within 40-130 μm from the soma, gradually decreasing toward the distal dendrites [186].

3.4.1.1/ Dendritic Spine Structure and Functions

Dendritic spines are composed of a small spherical spine head (<1 μm in diameter) and a narrow spine neck (~1 μ in diameter and ~1 μm in length) [182, 183, 185, 187]. Structural studies on dendritic spines using electron microscopy or super-resolution light microscopy showed that the dendrites of pyramidal neuron have a variety of spine shapes classified as stubby- (short and stubby necks with an unclear distinction between the neck and the head), thin- (long necks correlated with smaller heads), and mushroom-type (big and spherical head connected to a thick neck. Mature dendritic spines often have a mushroom shape. The dendritic head accommodates a synapse while the spine neck connects the spine to the dendritic shaft [187]. The spine neck separates the head from the main dendritic branch, acting as a diffusion barrier and compartmentalizing biochemical signaling [182, 183].

The dendritic spines serve as the postsynaptic contacts in cooperation with the presynaptic counterparts from presynaptic axon terminals. Excitatory contacts tend to terminate on spine heads rather than directly on the dendritic shafts, implying that the spines have an important functional role, or else the excitatory contacts could directly couple with the dendritic shafts [187]. Dendritic spines have a distinctive feature called **postsynaptic density** (PSD), an electron dense region packed with signal transduction machinery that acts as the receiving site of synaptic transmission [45, 183]. The PSD is linearly related to the dendritic geometry (largest in mushroom-shaped and smaller in thin or stubby spines) and sensitivity of spines to Glu^{-} [45]. Another example of the structural-functional importance of dendritic spines is the one-to-one relationship between the number of dendritic spines and excitatory synapses [188]. In addition, the morphological and biophysical characteristics of spines support synaptic plasticity by providing biochemical isolation and chemical compartmentalization distinct from the dendritic shaft [182, 185, 187].

3.4.1.2/ Excitatory and Inhibitory Synaptic Inputs

The dendritic spines accommodate excitatory synapses while inhibitory synapses directly target the dendritic shaft (Figure 3.6). Ligand-gated channels, also called receptors, are abundant on the postsynaptic sites. When the synaptic signaling chemical (ligand) binds to the specific site on the receptor, it opens and allows ion flow through the channel [21]. The most common types of receptors located at the postsynaptic membrane are the glutamate-gated AMPA and NMDA receptors mediating fast excitatory synaptic transmission and GABA-gated (γ-aminobutyric acid) $GABA_A$ (GABA A-subtype) receptors for inhibitory transmission [21, 189]. These receptors are named after their selective agonists. Glutamate binds with both AMPA and NMDA receptors; however, AMPA only binds with AMPA receptors (and NMDA with NMDA receptors).

In glutamatergic synapses, AMPA and NMDA receptors coexist in the same postsynaptic site [21]. AMPA-receptors are permeable to both Na^+ and K^+ ions, while NMDA receptors are permeable to Na^+, K^+, and Ca^{2+} ions. The Na^+ current influx through the AMPA-channel and the NA^+ and Ca^{2+} current fluxes through the NMDA channel cause an excitatory postsynaptic potential (EPSP). The activation of AMPA receptors results in the accumulation of positive ions into the intracellular space, resulting in a rapid and large depolarization. NMDA receptors also mediate excitation; however, they mediate weak

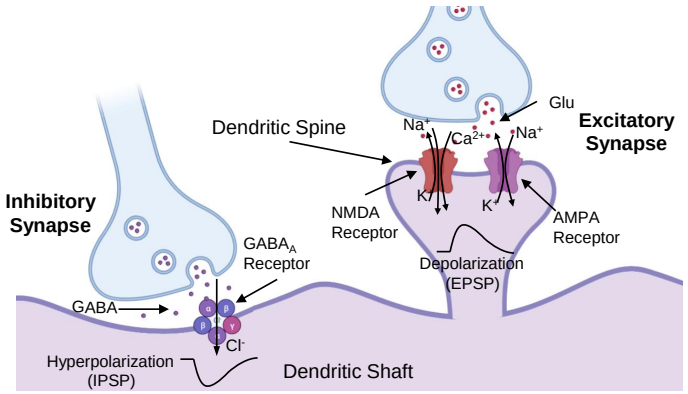

Figure 3.6: Excitatory and inhibitory synapses. A synapse can be excitatory or inhibitory, depending on the neurotransmitter in the synaptic cleft. In the excitatory synapse, the axon terminal of the presynaptic neuron makes contact on the dendritic spine of the postsynaptic neuron by releasing excitatory neurotransmitters such as Glu. In contrast, in the inhibitory synapse, the axon terminal makes contact directly on the dendritic shaft and releases inhibitory neurotransmitters such as GABA. Synaptic Glu activates the NMDA and AMPA receptors on the spine head, allowing the flow of Na^+, K^+, and Ca^{2+} ions through the channels. These current fluxes result in membrane depolarization or EPSPs. When synaptic GABA molecules activate the $GABA_A$ receptor, Cl^- current flux from the synaptic cleft through the membrane, creating hyperpolarizing potential or IPSP.

but more sustained depolarization, unlike AMPA receptors. Magnesium ions block or clog the NMDA channel at resting state, preventing other ions from flowing freely. During depolarization after AMPA receptor activation, the Mg^{2+} block separates from the NMDA receptor allowing the flow of inward ionic current. Therefore, there NMDA receptor is both a ligand-gated and voltage-gated channel.

GABAergic synapses mediate fast inhibitory transmission, with reversal potential close to the resting potential [21, 190]. GABA is an amino acid synthesized from Glu^- and is the major inhibitory neurotransmitter in the CNS [21]. The GABA receptor activation results in the influx of Cl^- causing a hyperpolarization or an inhibitory postsynaptic potential (IPSP). This hyperpolarization inhibits the depolarizing effects of excitatory synaptic inputs in the same dendritic compartment [185]. Hippocampal pyramidal neurons construct GABAergic synapses with interneurons. Pyramidal dendrites have an excitatory to inhibitory synapses ratio of 12:1 [186].

3.4.1.3/ Excitatory Postsynaptic Potentials

The small spine structure creates an electrical asymmetry caused by the very high spine resistance (R_{sp}) connected to a relatively low-resistance dendrite via an intermediary spine neck resistance (Figure 3.7a) [185, 187]. The cable theory also describes the electrical consequence from each spine compartment (head and neck), which helps analyze the EPSP propagation from the spine head to the dendritic shaft. As shown in Figure 3.7b, the dendritic head, neck, and dendritic shaft are separate compartments represented by a resistance-capacitance (RC) circuit. The transient synaptic conductance, g_{syn}, the electromotive force due to the ion influx from the synaptic area, the membrane capacitance (C_{head}, C_{neck}, and $C_{dendrite}$), and membrane resistance ($1/g_{head}$, $1/g_{neck}$, and $1/g_{dendrite}$) are the main parameters that determine the EPSP time course and amplitude [182, 187, 191]. The electromotive force (or the driving force) is the difference between the membrane potential and the synaptic reversal potential ($V_{spine} - E_{syn}$) [192]. The spine

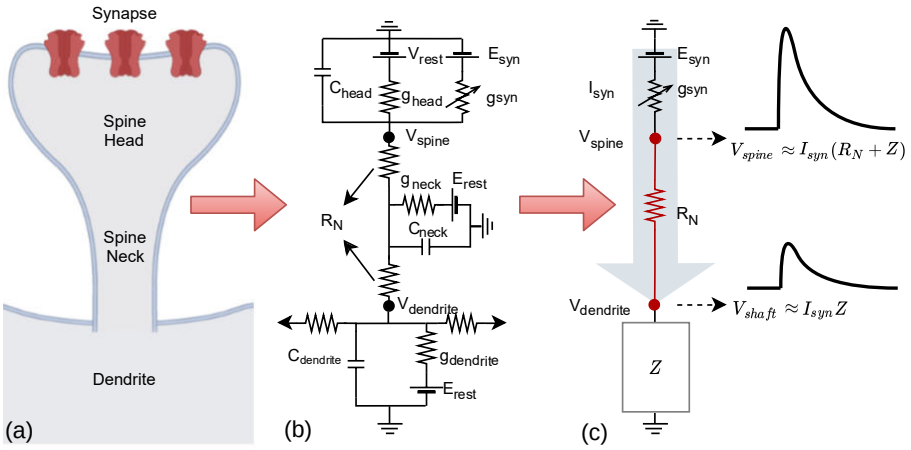

Figure 3.7: Electrical equivalent of a passive dendritic spine. (a) The large head and slender neck divide the spine into two separate compartments. (b) A resistance-capacitance circuit represents each compartment. (c) Due to the small size of the spine, the membrane resistance ($1/g_{head}$) and capacitance (C_{head}) become negligible, and the EPSP in the spine depends mainly on the change in synaptic conductance ($gsyn$). The narrow diameter of the spine neck also results in a large neck resistance R_N, eliminating the influence of the membrane resistance ($1/g_{neck}$) and capacitance (C_{neck}).

(head and neck) is so small that it has negligible membrane resistance and capacitance (Figure 3.7c) [185]. The spine behaves like a sealed cable whose overall resistance R_{sp} is larger than the dendritic compartment. However, according to Popovic et al. [193], this does not directly apply to all spines in the dendrites, especially in the proximal primary dendrite with large diameter and larger regions devoid of spines. Here, the EPSP amplitude is mainly dependent on high dendritic impedance Z and not on low R_{sp}.

Applying Ohm's law to the electrical circuit equivalent of the dendritic spine (with the spine head connected to a narrow spine neck) in Figure 3.7b, the excitatory synaptic input, V_{syn}, is described as

$$V_{syn} \approx I_{syn} R_{sp} \approx I_{syn} (R_N + Z) \approx I_{syn} R_N, \tag{3.31}$$

where I_{syn} is the synaptic current due to the ions flowing through the open channels, and R_{sp} is the spine resistance [88, 182]. The spine resistance is the sum of the spine neck resistance, R_N, and the dendritic impedance Z (Figure 3.7c) [182, 194]. The EPSP is dependent mainly on the spine neck resistance, R_N, whose resistance is so much greater than the dendritic of spine head resistance; therefore, the influence of Z becomes negligible [182, 195]. In addition, the small surface area of spines also provides negligible membrane conductance and capacitance. Electron microscopy measurements suggest that R_N ranges from 1 MΩ to 1 GΩ [182, 185], while measurements from voltage imaging with genetically encoded voltage indicators (GEVIs) estimates R_N to be 101 ± 95 MΩ [196]. The spine neck resistance, R_N, is determined by

$$R_N = \frac{4\rho l}{\pi d^2}, \tag{3.32}$$

where l is the spine neck length, ρ is the cytoplasmic resistivity, and d is the diameter [182, 197]. With the passive spine membrane mechanism, the change in the membrane

potential is generated by summating of all EPSP contributions of the receptors.

$$\begin{aligned}\tau_m \frac{dV}{dt} &= V_{rest} - V + V_{ampa} + V_{nmda}, \\ &= V_{rest} - V - R_N \left(I_{ampa} + I_{nmda}\right),\end{aligned} \tag{3.33}$$

where V is the EPSP in the spine, and τ_m is the membrane time constant [88, 178].

Dual-exponential function. During neurotransmission, the current flowing through the synaptic receptor is described as

$$I_{syn} = g_{syn}\left(V - E_{syn}\right), \tag{3.34}$$

where syn can be either AMPA or NMDA receptors. Here, g_{syn} is the synaptic receptor conductance, V is the membrane potential, and E_{syn} is the excitatory receptor reversal potential equal to 0 mV [198, 199]. The temporal dynamics of g_{ampa} is modeled using a dual-exponential formulation given as

$$g_{ampa}(t) = \bar{g}_{ampa}\alpha\left[e^{-\frac{t}{\tau_{2ampa}}} - e^{-\frac{t}{\tau_{1ampa}}}\right], \tag{3.35}$$

where $\bar{g}_{max}$ is the maximum conductance, α is chosen so that the maximum value of g_{ampa} matches the $\bar{g}_{ampa}$, $\tau_{1_{ampa}}$ is the rise time constant equal to 0.2 ms, and $\tau_{2_{ampa}}$ is the decay time constant equal to 2 ms [200–202]. A single AMPA receptor conductance has an estimated value of 9 pS [182, 203]. Note here that $\bar{g}_{ampa}$ is the collective conductance of AMPA receptors in the spine head (the mean number of receptors is 82) [182]. Furthermore, the NMDA receptor conductance is also modeled using a dual-exponential function with external [Mg^{2+}] and membrane potential dependence.

$$g_{nmda}(t) = \bar{g}_{nmda}\frac{\alpha\left[e^{-\frac{t}{\tau_{2nmda}}} - e^{-\frac{t}{\tau_{1nmda}}}\right]}{1 + \frac{[Mg^{2+}]}{3.57}e^{-0.062V(t)}}, \tag{3.36}$$

where $\bar{g}_{nmda}$ is the maximum g_{nmda} conductance, $\tau_{1_{nmda}} = 2$ ms, $\tau_{2_{nmda}} = 86$ ms, [Mg^{2+}] is the external Mg^{2+} concentration and V is the local membrane potential in mV [200, 204–206]. If both AMPA and NMDA receptors contribute to the response, [Mg^{2+}] is set to 1 mM, while when AMPA receptors are blocked, the [Mg^{2+}] is equal to 50 μM [200]. The total synaptic conductance, G_{syn}, due to AMPA and NMDA receptors is estimated to be $\geq$1 nS [182].

Receptor gating function. In order to take into account the receptor opening, the synaptic currents are modified into

$$I_{ampa} = g_{ampa}m_{ampa}\left(V - E_{ampa}\right), \text{ and} \tag{3.37}$$

$$I_{nmda} = g_{nmda}m_{nmda}B(V)\left(V - E_{nmda}\right), \tag{3.38}$$

where m_{ampa} and m_{nmda} are the gating variables of AMPA and NMDA receptors, respectively, and $B(V) = 1 + [Mg^{2+}]e^{-0.062V(t)}/3.57$ [88, 195, 199, 204]. In this simplified model, the synaptic receptor conductances are dependent on the neurotransmitter concentration

in the synaptic cleft and follow the HH-type formulism. The gate activation is governed by

$$\begin{aligned} \frac{dm_{ampa}}{dt} &= \alpha_{ampa} g \left(1 - m_{ampa}\right) - \beta_{ampa} m_{ampa}, \text{ and} \\ \frac{dm_{nmda}}{dt} &= \alpha_{nmda} g \left(1 - m_{nmda}\right) - \beta_{nmda} m_{nmda}, \end{aligned} \tag{3.39}$$

where α_{ampa} and α_{nmda} are the forward rates (1.1 μM^{-1} and 72 mM^{-1}, respectively) while β_{ampa} and β_{nmda} are the backward rates (190 s^{-1} and 6.6 s^{-1}, respectively), and g is the [Glu^{-}] in the synaptic cleft.

Instantaneous Jump and Exponential Decay. Fourcaud-Trocmé [114] used a more simplified model of synaptic inputs where at the arrival of the synaptic spike at time t_k, the V_{syn} jumps instantaneously to a maximum value J_{syn} (in mV) and then exponentially decays with a time constant τ_N. The model is given as

$$\tau_N \frac{dV_{syn}}{dt} = -V_{syn}(t) + J_{syn} \delta(t - t_k) \tau_m \tag{3.40}$$

where $\delta(\cdot)$ is the Dirac-delta function. Then, De Pitta and Brunel [178] modified this model to make V_{syn} dependent on the time course of synaptic neurotransmitters, g. The model becomes

$$\tau_N \frac{dV_{syn}}{dt} = -V_{syn}(t) + \hat{J}_{syn} \zeta g(t) \tau_N, \tag{3.41}$$

where ζ is the synaptic transmission efficacy from 0 to 1, and $\hat{J}_{syn}$ is the instantaneous jump given as

$$\hat{J}_{syn} = \frac{J_{syn}}{\varrho_c Y_T \tau_N}. \tag{3.42}$$

The parameter ϱ_c is the ratio between the vesicle and synaptic area volumes ($\varrho_c = 0.005$), and Y_T is the total vesicular [Glu^{-}].

3.4.2/ Synaptic input propagation through Dendrites

The high neck resistance, R_N, can significantly decrease the synaptic signal amplitude from the spine head to the dendritic shaft (Figure 3.7c) [182, 187]. Therefore, the activation of an excitatory synapse should produce a membrane potential greater amplitude than the voltage of the dendritic shaft where the spine is attached [45, 185]. The significant voltage drop from a single spine head to the dendritic shaft also limits the influence of the spine on its neighbors. However, dendritic voltage, produced during clustered synaptic activation or backpropagating APs (bAPs) and dendritic spikes, transmits reliably into spines altering the membrane potential of the spine. These dendritic voltages enter the spine head without significant attenuation, whereas EPSP amplitude decreases as it propagates to the dendrite. This electrical behavior is a consequence of multiple impedance mismatches between the spine and dendritic compartments. Even though an EPSP in a spine is quite large, the resulting EPSP in the soma is very small due to the dendritic morphology and the passive and active dendritic mechanism.

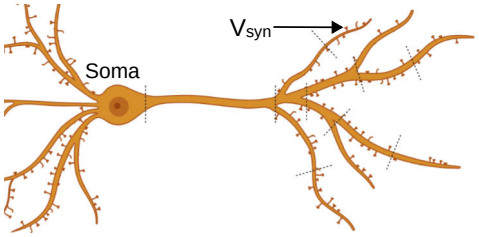

(a) Dendritic arborization.

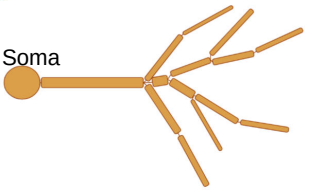

(b) Dendritic compartments.

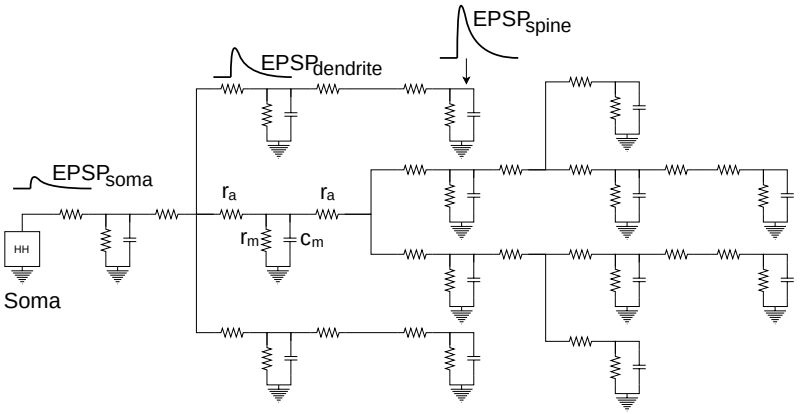

(c) Distributed circuit.

Figure 3.8: Compartmentalization in a passive dendritic tree. The dendritic arborization of a pyramidal neuron in (a) is divided into multiple compartments as shown in (b) approximately determined by the dendritic segments diameter and length and bifurcation points. The passive compartments are represented by the RC circuit (r_m is the membrane resistance and c_m is the membrane capacitance) and are connected to the next compartment via the axial resistance r_a. The activation of V_{syn} in (a) results in an EPSP in the dendritic spine in (c). The EPSP significantly attenuates as it enters the dendritic compartment and travels along the dendritic segment. Therefore, the EPSP reaching the soma is so much smaller compared to the synaptic input.

3.4.2.1/ Passive Dendrites

The dendritic arborization creates a more complex multicompartmental equivalent circuit (Figure 3.8). In his series of studies in the 1960s on modeling passive dendrites, Wilfrid Rall identified three important dendritic properties [207–210]. The dendritic compartment consists of axial resistance (r_a), membrane resistance (r_m), and membrane capacitance (c_m) (Figure 3.8c). In an elementary compartment, the current injected leaks across the membrane and decreases as it travels down to the next compartment through r_a, resulting in a continuous voltage drop to the soma [191, 211]. Therefore, the driving force flowing through r_m decreases with distance from the soma. The membrane capacitance, c_m, temporarily stores charge, which delays signal propagation. Overall, these passive properties attenuate the signal and slow down its time course.

3.4.2.2/ Active Dendrites

Passive cable models are only a first approximation to the physiological properties of neurons since the dendritic tree is not purely passive. The dendritic membrane expresses ionic conductances attributed to the heterogeneous distribution of VGCs, which can coun-

teract the influence of the passive mechanisms [187, 212, 213]. In CA1 pyramidal neurons, Na_v channel conductance tends to be constant at ~115 pS/m^2 from 0-100 μm distance from the soma [214]. A-type K_v and HCN channels have higher densities in distal apical dendrites than in soma or proximal dendrites [45]. T-type Ca_v channels increase moderately while L- and N-type Ca_v channels have relatively constant density [214]. In CA3 dendrites, Na_v channel conductance has a gradient decrease from 60 pS/m^2 near the soma to almost no conductance at 200 μm away from the soma, restricting the Na_v channel distribution in the proximal dendrites. A-type K_v channel seemed to be nonexistent or minimal along the dendrites because its hyperpolarizing effect of high-density K_v could inhibit somatic bursting.

In this case, the dendritic tree becomes excitable [185]. For active dendrites, active conductances are added to the equivalent circuit wherein the specific channel conductance is relative to the dimensions of the compartments (similar to the compartmentalization in axons presented in Section 2.6). The cable equation in discrete form for a compartment k is, therefore,

$$C_k \frac{dV_k}{dt} = \sum_l \gamma_{l,k} (V_1 - V_k) - I_{ionic,k}, \tag{3.43}$$

where k and l are index compartments, C is capacitance, V is the membrane potential, γ is the coupling conductance between the connected compartments, and the summation corresponds to the overall compartments l connected to compartment k [215]. The ionic current $I_{ionic,k}$ is the total ionic membrane current impinging synaptic inputs and ion influxes through VGCs. The distributed active conductances amplify synaptic activity by activating local dendritic spikes [216]. Compared to passive dendrites, active dendrites exhibit more location-specific activities [212]. Therefore, an active neuron can perform synaptic input transformations into AP, an event that usually requires multiple passive neurons.

3.4.2.3/ DENDRITIC MECHANISM

In addition to the complex structure is the distribution of synaptic inputs. Inputs may arrive at different spine heads synchronously or asynchronously. **Clustered** synaptic inputs arrive at a spatially restricted zone in the dendritic segment while **distributed** inputs spread along the dendritic arbor [182]. Bloss et al. [216] showed that a single axon of CA3 neuron projects clustered synapses in distal, not in proximal, dendrites of CA1 pyramidal neurons. The impact of individual synaptic inputs is generally weak to cause somatic spiking; however, the synchronous and clustered synapses on a dendritic branch produce local spikes that can nonlinearly influence somatic spikes [212].

What happens to the neuron dynamics if the dendrites contain both passive and active mechanisms? The complex structure of the dendritic arborization and the nonuniform expression of VGCs have a profound effect on signal propagation and processing by producing dendritic events (Figure 3.9), such as filtering, dendritic spikes, and backpropagation, that contribute to the activity-dependent refinement of neuronal circuitry.

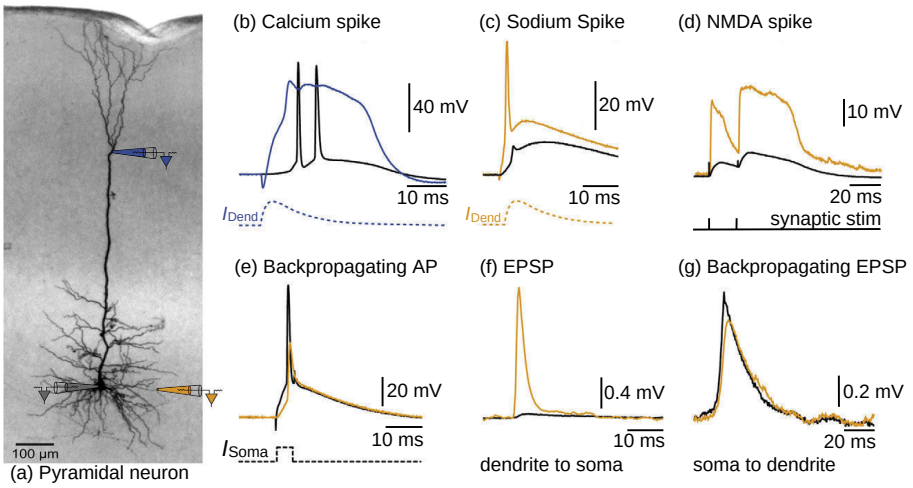

Figure 3.9: Dendritic mechanisms. (a) The electrodes (gray, orange, and blue) positioned at the soma, basal and apical dendrites of a biocytin stained layer 5 pyramidal neuron measure the membrane potential at the mentioned compartments. The dendritic tree expresses various VGCs distributed non-uniformly, activating localized dendritic spiking at separate dendritic compartments. These dendritic spikes (namely (b) Ca^{2+} spike, (c) Na^{+} spike, and (d) NMDA spike) are named after the main VGCs that are activated during the dendritic events. (e) Backpropagation occurs when the somatic AP propagates back to the distal dendrites. (f) Due to the passive dendritic properties, synaptic EPSP amplitude diminishes as it travels along the dendrite, causing a weak influence on somatic depolarization. (g) However, an EPSP evoked near the soma can propagate well to the distal end of the dendrite. (Image was adapted from Larkum and Nevian [212].)

Dendritic Filtering

As explained previously, the resistance-capacitance electrical equivalent of a compartment acts as a filter.The ratio between neck conductance and synaptic conductance (g_{neck}/g_{syn}) determines the amount of electrical filtering in the spine. [187]. Then, the EPSP in the dendrites is larger than the recorded somatic EPSP due to dendritic filtering (Figure 3.9f) [191]. Because r_i increases with distance from the soma, and c_m also increases with dendritic diameter, distal EPSPs have lower amplitude than proximal EPSPs (Figure 3.9g) [211]. Dendritic filtering accounts for the larger EPSPs along the dendrites than in those recorded in the soma [191]. The dendrites have other mechanisms for counteracting the effect of dendritic filtering, that is, through the active properties of VGCs. The ion influx through the opening of Na_v channels along the dendrites increase the EPSP amplitude by replacing the ions lost during propagation, while efflux due to K_v channels reduces the filtering effect of c_m by charging and discharging the membrane [211]. Also, the compound influence of clustered synapses minimizes dendritic filtering [216].

Dendritic Spikes

Dendrites are also excitable, like the AIS but with a higher threshold, and could generate dendritic spikes [185]. Few clustered synapses activated synchronously produce dendritic depolarization that is large enough to activate VGCs along the dendritic membrane [185, 212, 217]. These weak dendritic spikes do not reliably propagate throughout the dendrites and can be locally restricted within the dendritic branch where the spikes were

produced. Balind et al. [218] and Kim et al. [219] showed that CA3 pyramidal neurons efficiently produce local Na^+ and NMDA spikes and widespread Ca^{2+} spikes upon clustered synapses.

The name of dendritic spikes is mainly based on the dominant channels activated during the event (though varieties of channel-types can influence dendritic spiking).

1. **Na^+ spikes**.

   Sodium spikes (Figure 3.9c) are the fastest and relatively brief dendritic event similar to a somatically-evoked AP, resulting from fast Na_v channel kinetics [185, 191, 212]. High-amplitude local depolarization triggers Na^+ spiking, which implies that Na^+ spikes require synchronous activation of clustered synapses. Two-photon glutamate uncaging on radial oblique CA1 dendrites suggest that at least 20 synaptic inputs can trigger a local Na^+ spike [190]. In addition, the activation of NMDA receptors also contributes to an influx of Na^+ ions [185, 191, 212]. Even though Na^+ spikes tend to be highly confined and do not propagate reliably out of the branch, this dendritic event can be triggered in most dendritic regions and can still contribute to somatic spiking. The resulting depolarization can be large enough to activate other VGCs and NMDA receptors distributed along the dendrites.

2. **Ca^{2+} spikes**.

   Strong synchronous excitatory synaptic inputs initiate Ca^{2+} spikes (Figure 3.9b) [185, 191, 212, 220]. In contrast with Na^+ spikes, calcium spikes tend to be generated in specific dendritic locations, especially in the distal apical dendrite, which exhibits high-density VDCCs. Calcium spikes have a longer duration, causing plateau potentials as a consequence of slow Ca_v channel kinetics [185]. Calcium spikes tend to change the spiking behavior of the neuron to bursting mode, allowing dendrites in the distal tuft to communicate with the soma [212, 220].

3. **NMDA spikes**.

   Voltage-sensitive NMDA receptors activate dendritic NMDA spikes (Figure 3.9d) [185], most prominent in basal dendrites [212, 221]. NMDA spikes are highly restricted to the synaptic input sites due to the Glu^--dependence of NMDA receptors, thus not propagate to dendritic regions void of NMDA receptors [185, 190, 222]. If sufficient NMDA receptors are activated, regenerative spikes occur even if a small number of Na_v and Ca_v channels are active [185]. The regenerative activation is due to the voltage-dependent relief of Mg^{2+} blocks [212]. NMDA spikes are also longer than Na^+ spikes and produce plateau potentials, lasting from 20 to hundreds of milliseconds [190, 212, 223].

Dendritic spikes contribute to synaptic integration. Though not propagating actively, dendritic excitability still delivers enough charge to the axon and influences AP generation [185]. For example, the summation of dendritic spikes activated in multiple dendritic branches allows neurons to perform coincident detection. Dendritic spikes also mediate local communication by activating channels that allow dendrite to release substances, such as neurotransmitters. Dendritic spikes also increase synaptic strength, thus regulating synaptic plasticity.

Backpropagating Action Potentials

The AP generated in the axon can propagate back into the soma and then to the dendrites (Figure 3.9e and Figure 3.9g) via the transient increase in dendritic membrane potential, [Ca^{2+}] elevation through VDCCs, and interaction with NMDA receptors [45, 212]. Backpropagating APs signal the state of the soma back to the synaptic input sites. In addition, bAPs adds to the arriving synaptic activity where the increase in membrane depolarization activates VDCCs [211, 224]. Moreover, bAPs lessen the Ca^{2+} spiking threshold, resulting in a localized increase in [Ca^{2+}] that influences some Ca^{2+}-dependent synaptic plasticity [212, 220]. The amplitude of bAPs flowing through the dendrites varies with respect to the distance of the compartment from the soma [212, 225]. Potassium channel activation, heterogeneous Na_v channel distribution, inhibition, and neuromodulation control the extent of backpropagation. Theoretically, passive dendritic cables impair bAPs in thin basal dendrites. Backpropagating APs often decay entirely before reaching the distal dendrites of CA1 pyramidal neurons [216] due to the minimum distribution of Na_v channels along the distal dendrites.

3.5/ Dendritic Information Processing

A single neuron must transform these inputs into an appropriate somatic output train to process the information carried by the multiple synaptic inputs. For example, in the CA3 network, neurons process the patterned synaptic inputs to generate and consolidate information coding [226]. Individual neurons utilize the passive and active mechanisms such as filtering, dendritic spikes, ligand-gated or voltage-gated nonlinearities to control the transformation of incoming synaptic inputs into somatic output trains. One of the long-lasting questions in neuroscience is how exactly the neuron processes the various incoming synaptic signals into information. In this subsection, we discuss the current advances in dendritic computation studies, the biophysical mechanisms controlling the transformation of inputs into somatic firing, the operations the dendrites perform, and the dendritic abstraction describing the overall neuron model.

3.5.1/ Synaptic Integration

Postsynaptic currents flow through the dendritic arbor, integrate at the bifurcation points, or converge in the soma. Then, the soma converts the incoming signals into somatic depolarization, and if the resulting amplitude reaches a certain threshold, the soma generates an AP. The sequence of action potentials, even the subthreshold depolarizations, contains the processed information. The process of converting the synaptic inputs into somatic output is called **dendritic integration**, an intrinsic computation dependent on the location and number of activated synapses, the active and passive properties of the dendrites, and the spiking history.

Synaptic Integration in Passive Dendrites. In passive dendrites, the EPSP from a single synapse is insufficient to cause an AP [185]. Therefore, multiple inputs, clustered or distributed, must impinge the cell via the complex morphology of the dendritic arborization. The passive properties of the dendrite allow the neuron to integrate the EPSPs in a nonlinear manner. Because passive dendrites have low-pass filtering characteristics, the EPSPs arriving at the soma may be 100-fold attenuated compared to the EPSPs at the spine head [227]. Therefore, the main effect of the passive dendritic properties is dendritic filtering. Synaptic integration also varies with input location [190]. Based on the cable theory, the passive dendritic tree inflicts spatiotemporal distortion between distal and proximal inputs. Without compensatory mechanisms, distal synaptic inputs are significantly attenuated and delayed [228].

Synaptic Integration in Active Dendrites. Nonlinear dendritic integration improves the computational capacity of neurons [191]. It provides compensation and counteracts the filtering effect of the passive properties. Active synaptic EPSPs nonlinearly sum due to the current flowing through the synaptic conductance, reducing the driving forces [190]. As mentioned earlier, the spatial distribution of synaptic inputs significantly affects synaptic integration. Detecting temporally correlated and spatially segregated synaptic inputs (synapses located on separate dendritic branches) poses some difficulties for the neuron, as these inputs, especially those from the distal apical tuft, are heavily attenuated as they propagate down to the soma. Therefore, the neuron reacts more effectively with clustered inputs, a group of synaptic inputs that are spatially restricted within a dendritic segment, a branch, or a group of branches. Clustered synapses may produce large local depolarization, which activates nonlinear dendritic mechanisms that trigger regenerative spiking. Besides, dendritic spiking and VGCs distributed along the dendritic length also result in nonlinear integration of synaptic inputs [225]. The activation of Na_v channels amplifies the amplitude of subthreshold EPSPs in a multiplicative manner [190, 195]. Moreover, synaptic NMDA receptors provide an essential mechanism for the nonlinear amplification and integration of synaptic inputs.

3.5.2/ DENDRITIC OPERATIONS

The influence of the summation of synaptic inputs (input) to the resulting membrane depolarization at the soma (output) is quantified by defining the corresponding input-output (I/O) relationship [191]. In the I/O quantification process, the **expected** membrane depolarization (input) is the compound EPSP or arithmetic sum of individual EPSPs resulting from the simultaneous activation of excitatory synapses. The **observed** depolarization is the resulting depolarization, for example, at the soma (Figure 3.10). The resulting I/O relationships are comparable to mathematical functions that the neuron performs.

Neurons utilize different combinations of these dendritic operations for computations and signal encoding. These dendritic operations, as shown in Figure 3.10, can be (1) linear where the observed depolarization is equal to the expected depolarization, (2) supralinear where the observed depolarization is above the expected depolarization, and (3) sublinear where the observed depolarization is less than the expected depolarization [185, 191, 229]. It is important to note that different dendrites generate different IO curves

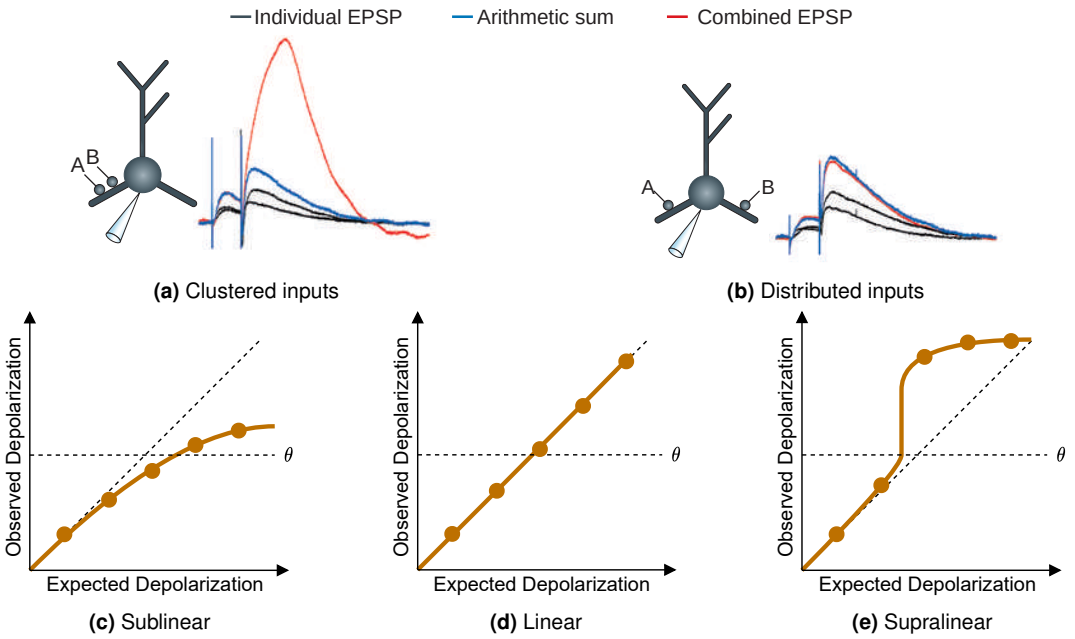

Figure 3.10: Input-Output transformation and dendritic operations. The input-output relationship between the arithmetic summation of the individual EPSPs (expected depolarization) and the resulting somatic depolarization (observed depolarization) from the combined effect of the individual EPSPs describes of the dendritic operation the neuron can perform. (a) The synaptic inputs that are clustered or target synapses on a restricted spatial location produce a nonlinear influence on somatic depolarization. (b) Distributed synaptic inputs, those inputs targeting different branches, perform linear summation in the soma. In this case, the arithmetic sum of EPSPs equals the measured depolarization in the soma. (Images were taken from [190].) (c) When the resulting somatic depolarization always results in a lower amplitude than the input summation, the dendritic operation is sublinear. (d) Linear operation occurs if the somatic depolarization consistently equals the input summation. (e) The dendrite performs supralinear integration when the output depolarization exceeds the input summation.

according to the number of simultaneous inputs targeting multiple locations in the cell and the biophysical mechanisms under consideration [206].

Sublinear. Excitatory synapses summate sublinearly in passive dendrites (Figure 3.10c) [225, 229]. The magnitude of sublinearity is dependent on the distance between synapses, where the depolarization experience by one synapse is dependent on the distance of the other activated synapses [185]. If two synapses are closer to each other, they strongly influence the individual driving force, and their summation is sublinear. Therefore, if the synapses are clustered, inputs are integrated sublinearly due to reduced driving force and membrane shunting [190]. However, clustered inputs are less efficient at triggering an AP than when inputs are scattered or distributed along the dendritic tree [191]. Sublinear operations primarily account for passive dendritic properties; however, some studies suggest that active dendritic properties also influence sublinearity [191]. Potassium channel activation can also provoke sublinear summation by producing hyperpolarization that decreases the membrane potential. Neuronal excitation from clustered inputs may be prevented through sublinear integration by providing a mechanism for input saturation [230].

Linear. Linear integration occurs when the arithmetic sum of the individual EPSPs produces a peak response equal to the actual peak depolarization (Figure 3.10d) [206]. Both the distributed and clustered synaptic inputs evoke linear summation in hippocampal pyramidal neurons [229]. Linear summation occurs when synaptic inputs are distributed over the dendritic tree due to the passive dendritic properties [190]. Gasparini and Magee [231] found that highly distributed or asynchronous synaptic inputs targeting the dendritic arbors of CA1 pyramidal neurons perform linear integration. This operation results in variable AP rate and timing and depends on the number of incoming inputs. In clustered inputs, activation of nonlinear dendritic conductances – such as NMDA receptors, Na_v channels, and Ca_v channels – can increase EPSPs during synaptic activities, while K_v conductance dampens them [190, 229]. A balance between these active conductances underlies linear summation of clustered synaptic inputs of culture pyramidal cells, compensating the sublinearity due to the reduced driving force and shunting from the passive properties.

Supralinear. Studies on dendrites showed that active dendritic properties are the main contributors to nonlinear integration, primarily in supralinear integration (Figure 3.10e) [191]. Makara and Magee [226] performed two-photon imaging and glutamate uncaging on CA3 pyramidal neurons to characterized the synaptic integration in thin dendrites. The results showed that synchronous synaptic inputs in thin dendrites are nonlinearly integrated with a supralinear fashion. Coactivation of a sufficient number of synaptic inputs in a dendritic branch activates NMDA receptors results in supralinear summation of excitatory synaptic inputs greater than expected [191, 195, 226, 229, 232]. Signal amplification mediated by NMDA receptors can activate Na^+ spiking, further increasing the peak depolarization that drives the somatic spiking. Using paired-pulse stimulation protocol, Gomez et al. [206] showed that the increase in NMDA conductance after the first spike triggers local dendritic spikes, thus resulting in a strongly supralinear integration, even if the temporal window between succeeding synaptic inputs is more than 100 ms. When synaptic input arrives synchronously and spatially clustered, the dendritic compartment receiving the clustered input produces a highly nonlinear integration that leads to an AP output that is extraordinarily precise and invariant.

Furthermore, a neuron can also perform more complex computations by utilizing the dendritic properties and background noise and combining the previously discussed dendritic integration [229].

Boolean Operations. The neuron can also perform basic Boolean operations – such as **AND**, **OR**, and **AND-NOT** –, which are also influence by the synaptic locations and spike threshold [185, 191]. These simple Boolean operations can be combined to perform more complex computations [225]. Neurons can implement an AND operation using inputs from multiple dendritic branches. The AND operation is equivalent to **coincidence detection** wherein two simultaneous and different groups of synaptic inputs are directed to different dendritic branches. Hippocampal CA3 neurons also perform OR operations. The soma initiates APs from DG inputs at the primary apical dendrite or neighboring CA3 neuron collateral connections near the soma [185]. Neurons implement logical AND-NOT operations using inhibitory synapses place between the soma and excitatory input [185, 190].

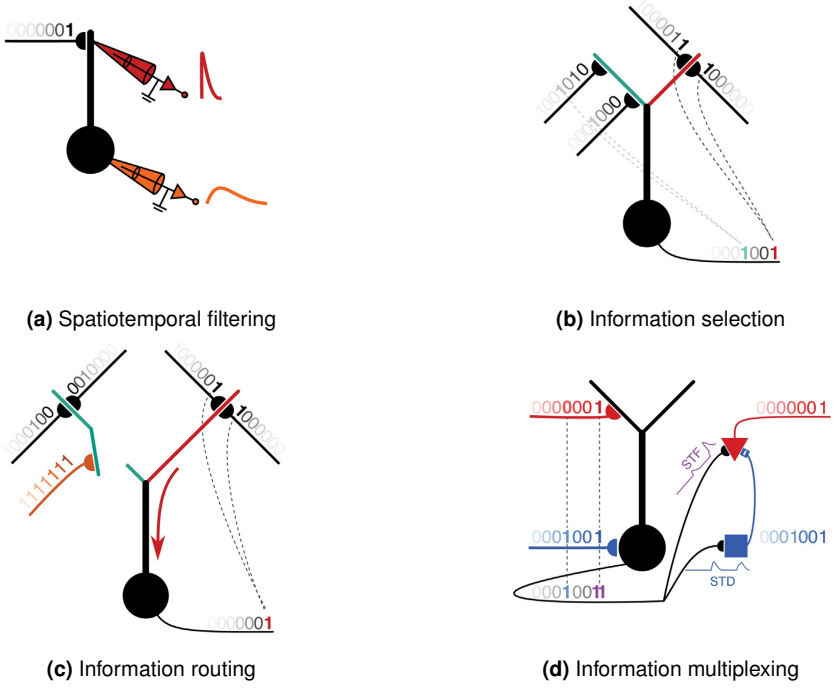

(a) Spatiotemporal filtering

(b) Information selection

(c) Information routing

(d) Information multiplexing

Figure 3.11: Classes of dendritic information processing. The binary inputs (0 and 1) represent the activation of synapses within a time window. (a) Synaptic inputs targeting the distal synapse evoke a local EPSP (red), which propagates down to the soma with considerable attenuation and delay (orange). (b) Coincident inputs from different branches can cause somatic spiking, while single inputs not communicated to the soma are still crucial for local processing. (c) Information routing is comparable to having a switch along the propagation path. Routing is usually performed by inhibitory signals (orange) vetoing the flow of EPSP between the distal branch and the soma. (d) Two input trains targeting different poles of the cell are encoded via multiplexing. The somatic spike (purple) constitutes two signals (one red and one blue) reaching the soma simultaneously. The multiplexed information can be decoded by short-term facilitation (STF) and short-term depression (STD). Image was taken from Payeur et al. [233].

Dendritic Arithmetic. Neurons perform simple **addition** by summing spatiotemporal inputs to react the spiking threshold [185, 190]. On the other hand, if inputs are inhibitory, the summation hyperpolarizes the membrane [225], which can be thought of as **subtraction**. **Multiplication** is the simplest nonlinear operation [230]. In the case of binary inputs, an AND operation can be considered as multiplication [185]. If either input is zeros, then the output is also zero. This operations describes **coincidence detection** [230]. Neurons may also perform **division** via shunting inhibition which scales down the membrane depolarization in proportion with the strength of the EPSPs, in accordance with Ohm's law [185, 190, 230].

3.5.3/ Dendritic Information Processing

The dendritic operations determine the resulting somatic depolarization and the somatic activity from the barrage of spatiotemporal synaptic inputs. The dendritic morphology, however, is a more complicated matter. Theoretically, dendritic integration does not only occur in the soma but anywhere throughout the dendritic tree. How does the neuron merge the diversified inputs into a single spike train? The definite answer is still about to be discovered as technology advances. However, current studies suggest the following

classes dendritic processes that can allow the soma to consolidate information.

Spatiotemporal filtering The dendritic tree attenuates and lowpass filtered a distal synaptic input as this signal spreads to the site of initiation and propagates down to the soma (Figure 3.11a) [230, 233]. It follows that due to dendritic filtering, distal synaptic inputs have a smaller influence on somatic firing [191]. The location-dependent attenuation and filtering combined with linear summation allow the dendrites to perform spatiotemporal filtering, which then tunes the input delays to give rise to selectivity.

Information Selection From multiple synapses activated simultaneously, only a small portion of these inputs are communicated to the soma Figure 3.11b [230, 233]. Due to **pooling**, information such as the origin of the synaptic inputs is lost during transmission. One solution is compartmentalization. Compartmentalization preserves the information that would otherwise be lost during pooling; however, it may also decrease the amount of information that reaches the soma. This dilemma can be solved if nonlinear mechanisms select a part of the information and transiently amplifies the information-containing signal for transmission to the soma. Furthermore, local information not communicated to the soma is still significant in local processes such as plasticity.

Information Routing Information routing is a process in which the dendritic subunits modify the flow of signal en route to the soma for information relay (Figure 3.11c) [233, 234]. One mechanism in which information is routed to the soma is via feedforward inhibition, where inhibitory synapses act as a binary switch that either allows or vetoes the propagation of signals [233]. The location of inhibitory synapses along the dendritic tree determines the signal route, a pathway-specific gating [235, 236]. Wilmes et al. [235] also showed that bAPs and Ca^{2+} spikes also enable signal switching.

Information Multiplexing Information multiplexing by neurons is a current concept in dendritic information processing (Figure 3.11d). The notion from theoretical studies is that the neurons can represent multiple inputs into one spiking output by harnessing its dendritic mechanisms [233]. Sardi et al. [237] performed different types of experiments on neuronal cultures and suggested that a neuron functions as a collection of independent threshold units. The compartmentalization allows the neuron to process local dendritic information independent from sibling dendrites. Wybo et al. [238] suggested that signals from distal branches arriving at the proximal dendrites do not merge; instead, they are superimposed from one another. The signal from one independent subunit is then transmitted to the soma through the dendritic arbor, acting as a multiplexer cable [239]. Metaphorically speaking, Payeur er al. [233] suggested that the dendritic arbor resembles a telegraph office, where incoming messages are first filtered, then selected for transmission, routed to the destination where the messages are summarized or encoded for future communication.

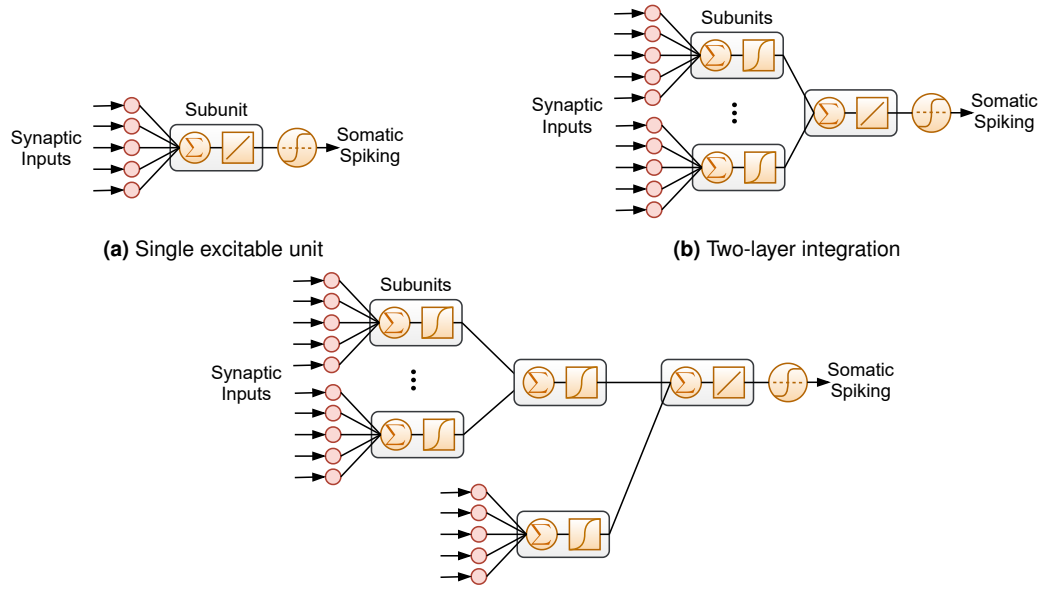

(a) Single excitable unit

(b) Two-layer integration

(c) Anisotropic threshold unit

Figure 3.12: Neuronal computational schemes. (a) The classical view describing neuronal computation is a single excitable unit. The neuron exhibits synaptic democracy; the synaptic inputs have an equal influence on the somatic depolarization regardless of synapse location in the dendritic tree. The soma linearly summates the inputs, and if the summation reaches a certain threshold, the soma generates an AP. (b) The two-layer computational scheme has one layer of functional subunits corresponding to dendritic trees and performing its specific nonlinear transformation. The subunit outputs are then transmitted to the soma for a global linear summation and somatic spiking. (c) An individual dendritic compartment exhibits independent processing of synaptic inputs and separate IO transformation. The compartmentalization creates multiple layers of integration with specific nonlinearity, comparable to a network whose architecture is determined by the dendritic morphology. Then, the soma integrates and multiplexes the incoming signals from the subunits for somatic depolarization.

3.5.4/ Computational Schemes

Decades of experimental studies used the conventional computational scheme, wherein the neuron acts as a **single electrical excitable threshold unit** or, in classical terms, a **point neuron** [237]. In the classical view of dendritic integration in CNS neurons, excitatory and inhibitory signals from the dendritic tree are channeled to the soma for linear summation (Figure 3.12a). Linear integration governs the transformation of weighted inputs into somatic output [228]. When the linear summation reaches a certain threshold, the soma generates an AP in an all-or-none manner [237, 240, 241]. This model is also known as the **integrate-and-fire** model introduced by Lapicque [242]. The point neuron hypothesis, where the whole dendritic tree is nonetheless considered as a single compartment, allows **synaptic democracy**; the synapses have equal ability to influence somatic depolarization [228]. It indicates that the synapses must be propagated and integrated neutrally for synaptic democracy to function [241] and that the soma acts as a **global** summing unit.

Another scenario is based on nonlinear integration and also consists of a single central excitable cell [237]. The computational scheme is a two-stage integration process, where the first layer consists of the independent dendritic compartments acting as separate thresholding functional subunits (Figure 3.12b) [243], and the group synaptic inputs within

the compartment interact with each other [237, 240, 244]. The assumption that dendrites are divided into subunits is based on the spatially restricted dendritic spiking [232]. The local nonlinear synaptic integration output is added to the somatic summation, and an AP is produced only if the summation crosses the threshold for spiking [237, 240, 244].

In the two-stage mode of integration, clustered synaptic inputs directed at a single or a group of distal dendrites could initiate a nonlinear response transmitted to the proximal compartments for global linear summation. Polsky et al. [232] provided the first experimental support for the two-layer network model of Poirazi et al. [243], wherein Polsky et al. [232] showed that the same branched inputs integrate sigmoidally, while between-branch inputs summed linearly. The researchers then identified the mechanism allowing pyramidal neurons to function as a two-layer network [245]. Two-stage integration can also significantly increase the computational power and spiking response of the neuron over that of the point neuron by introducing nonlinear operations between clustered synapses, thus increasing the number of nonlinear operations the neuron can perform and allows the implementation of a spatiotemporal coding scheme [228, 241, 246].

The most recent computational scheme is based on the neuronal capability of performing locally restricted computations. Sardi et al. [237] suggested that the neuron functions as an **anisotropic threshold unit** (Figure 3.12c) divided into independent excitable subunits or compartments that can be a dendrite or a part of the dendritic tree. Each compartment collects its anisotropic signals and performs its IO transformation process; thus, the inputs are independent of other threshold units. Then, Ujfalussy et al. [239] provided a quantitative approach for describing IO transformation in neurons and suggested that each subunit has its nonlinearity and transmits its output to the proximal subunit via multiplexing signals in parallel processing channels with different time constants. The hypothesis on multiple thresholding units was further supported by Wybo et al. [238] by devising a formulism that characterized the dendritic arborization to an impedance-based tree graph, revealing that the dendritic topology may indeed consist of multiple independent functional units.

The development of neuronal computation schemes, from a point neuron perspective to multiple independent excitable units, implies that a single neuron performs even more complex computations. Modeling studies suggest that neurons, by internal compartmental processes and independent synaptic transformation, can perform functions usually attributed only to neural networks. Independent subunit computations also suggest that neurons can perform branch-specific learning [238].

3.5.5/ Mathematical Models for Neural Coding

Neural coding is the process in which the neuron encodes the afferent spike trains into a single information-carrying output for communication to postsynaptic neurons. Analytical models are used to approximate and represent dendritic operations and neuronal computations to examine the experimental predictions and implement such operations in neural circuits. Biophysical models contain large parameter space, but the succeeding simplified models give us deep insights into neuron processes and computations, particularly in neural coding.

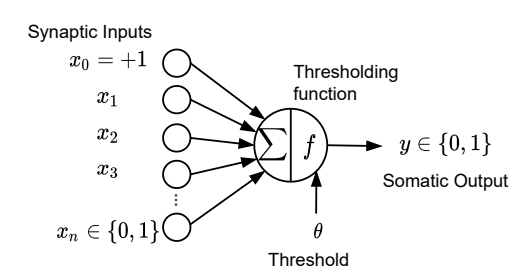

(a) McCulloch-Pitts model

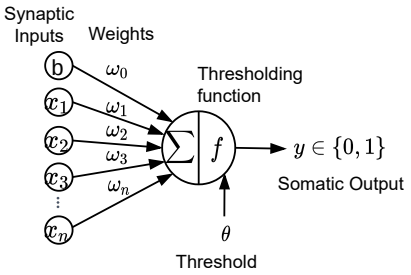

(b) Perceptron

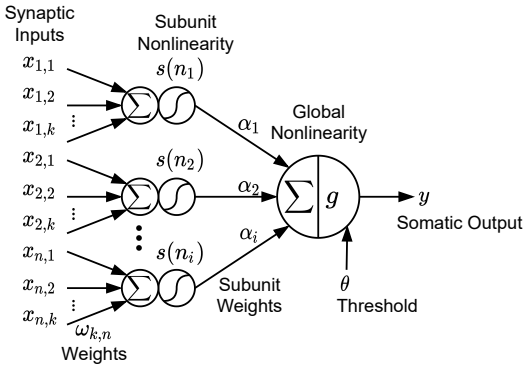

(c) Two-layer neuron model

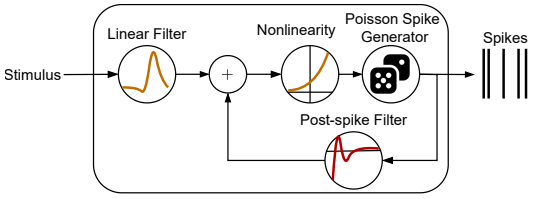

(d) Generalized Linear Model

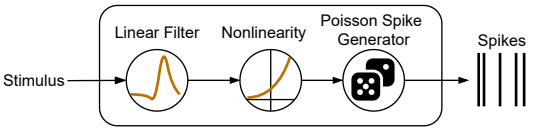

(e) Linear-Nonlinear Poisson spiking model

Figure 3.13: Neural coding schemes. (a) The first model depicting neural coding is the McCulloch-Pitts neuron model, where synaptic inputs, x_n, are binary, either 1 or 0 for active and inactive inputs, respectively. Inputs are linearly integrated, and when the summation is above a threshold, θ, the neuron produces an output equal to 1, and 0 otherwise. (b) The perceptron is an extension of the McCulloch-Pitts model. Here, the inputs x_n, which can be real values, are multiplied to arbitrary synaptic weights, ω_n, representing the strength of influence of the synaptic inputs to the neuron spiking. The thresholding function(activation function or nonlinearity), f, nonlinearly transforms the input summation into somatic output. Also, when the nonlinear summation is above the threshold, θ, the neuron produces binary 1. (c) The model by [243] is similar to a two-layer network of perceptrons. Each dendritic subunit has an independent linear summation of inputs and local nonlinearity. The output of each subunit is multiplied to the corresponding subunit weight, α_n, before reaching the soma for global summation and thresholding function, g. (d) Generalized linear models (GLMs) are point processes that model the stochastic properties and history-dependence of neuron spiking. The nonlinearity function transforms the convolution of the outputs of the linear and the post-spike filters to produce stochastic output spiking via the Poisson process. (e) Lastly, the Linear-Nonlinear Poisson (LNP) model is a class of GLM without the post-spike filter. In this case, the neuron spiking is purely stochastic due to the inhomogeneous Poisson process and independent from the previous spiking activity.

McCulloch and Pitts Model

McCulloch and Pitts suggested a binary **point neuron** model [247], which became the most dominant conceptual model for single neuron computation [189, 229] (Figure 3.13a). McCulloch and Pitts neuron model consists of binary inputs (0 and 1), a summing operation for the inputs, a thresholding function, and a binary output. Synapses have a value of 1 when active and 0 when inactive and are multiplied with their corresponding positive

weights (for excitatory inputs) that correspond to the synaptic strengths. The weighted inputs are summed together, and if the sum is greater than the somatic threshold, the soma will spike. The soma gives a value of 1 if the sum is above the threshold and 0 otherwise. Given the sum $g(\mathbf{x})$ of the input vector $\mathbf{x}$,

$$g(x_0, x_1, x_2, x_3, ..., x_n) = g(\mathbf{x}) = \sum_{i=1}^{n} x_i, \tag{3.44}$$

where n is the number of synaptic inputs and $x_n \in \{0, 1\}$, the soma generates an output y only if g is above the threshold for spiking, θ [247]. Therefore,

$$y = f(g(\mathbf{x})) = \begin{cases} 1 & \text{if } g(\mathbf{x}) \geq \theta \\ 0 & \text{if } g(\mathbf{x}) < \theta \end{cases}. \tag{3.45}$$

Linear summation and threshold adjustment allow the neuron to perform logical operations such as AND or OR operations but not XOR [189, 191]. Numerous studies, especially in neural information processing and neural networks, adapted the McCulloch and Pitts model because of its simplicity. However, biologically speaking, the model oversimplified neural processing. It disregards the fundamental spatiotemporal characteristics of neurons, the morphology of the dendrites, the stochasticity of synaptic inputs, and the history-dependence of somatic spiking [229].

Perceptron

Rosenblatt [248], inspired by the McCulloch and Pitts model and the theoretical studies of Donald Hebb in plasticity, developed a neuron model called a **perceptron** (Figure 3.13b). Rosenblatt [248] modified the McCulloch and Pitts scheme by extending the input values into real values (not only binary) and by adding arbitrary weights in the inputs. Let $g(\mathbf{x}, \mathbf{w})$ be the weighted sum of inputs $\mathbf{x}$,

$$g(\mathbf{x}, \mathbf{w}) = \sum_{i=1}^{n} x_i \omega_i + b, \tag{3.46}$$

where n is the number of inputs and b is the biasing constant. Instead of immediately deciding if the soma spikes or not, the summation is then passed through the nonlinearity for transformation. The nonlinearity acts as a thresholding or activation function, in that when the transformed sum is above the threshold θ, the soma spikes. Therefore, the somatic spiking is governed by

$$y = f(g(\mathbf{x}, \mathbf{w})) = \begin{cases} 1 & \text{if } g(\mathbf{x}, \mathbf{w}) \geq \theta \\ 0 & \text{if } g(\mathbf{x}, \mathbf{w}) < \theta \end{cases}. \tag{3.47}$$

The output still produces 1 for summation greater than the threshold and 0 otherwise. Inputs have different and adjustable weights; thus, removing synaptic democracy, in that some synapses can have a greater influence on the somatic spiking over the others. Adjusting the synaptic weights and thresholds enables the neuron to learn and perform more powerful computations [229]. Point neuron models can also accommodate various output nonlinearities. Compressive nonlinearity, such as **logarithmic**, produces an IO

curve that is sublinear [232]. For expansive nonlinearity, such as **quadratic** or **exponential** function, the input summations always exceed the linear summation; thus, the IO relationship is always supralinear. In a **sigmoidal** nonlinearity, the output ranges from supralinear to sublinear depending on the stimulus intensity.

Two-Layer Neuron Model

Even though the point neuron model is widely used, the assumption that the neuron has only one integrative point where all excitatory and inhibitory inputs are combined oversimplify the neuronal functions [240]. Thus from a modern perspective, the point neuron is insufficient. The model disregards the location-dependent dendritic mechanisms and synaptic interactions.

Poirazi et al. [243] studied the IO transformation in realistic hippocampal CA1 pyramidal neurons and suggested that the neuron functions as a two-layer network (Figure 3.13c). The first layer consists of the subunits from the apical and basal dendrites, and the second layer is the global summation at the soma. Assuming binary inputs, the hypothetical subunit IO function, $s(n)$, can be expressed as

$$s(n_i) = s\left(\sum_{j=1}^{k} x_{n,j}\omega_{j,k}\right), \tag{3.48}$$

where $i = [1, 2, 3, ...]$ is the subunit number, and k is the net number of synaptic inputs in n. Therefore, the somatic output is defined as

$$y = g\left(\sum_{i=1}^{m} \alpha_i s(n_i)\right), \tag{3.49}$$

where α_i is the weight of the n_ith unit, m is the number of subunits in the neurons, and g is the global output of nonlinearity. The subunit nonlinearity is a sigmoidal function. The two-layer binary model is an extension of the point neuron model. Each nonlinear compartments have its IO functions with different thresholds, representing the threshold of dendritic nonlinearity. The output of the nonlinear compartments is linearly summed in the soma and compared with the spike threshold [191].

Jadi et al. [240] also introduced an augmented **two-layer model** (2LM) that consists of local dendritic integration processes and a global integration process. Local integration occurs within a subtree consisting of a uniform set of thin and unbranched dendrites emanating from a node. Based on cable theory, it is assumed here that communication within the dendritic subunit is efficient while communication between dendrites is relatively low.

Generalized Linear Models

Unlike the point and two-layer neuron models whose spiking occurs upon the summation reaches the threshold, Generalized Linear Models (GLMs) capture the stochastic

response of the neuron and mathematically represents the canonical physiological characteristics and dynamics of a neuron, such as spatiotemporal filtering, without explicitly modeling the influence of ion channels [233, 249–251]. The GLMs models serve as tractable mathematical models describing single-neuron spiking activity.

In systems neuroscience, the term GLM refers to autoregressive point process models [252, 253]. Each GLM has (1) a linear stimulus filter determining the stimulus preference of the neuron and, (2) a static nonlinearity that transforms the convolution of stimulus and other variables, (3) a stochastic spiking function whose spiking probability is based on its spiking history, and (4) a spike history function capturing the refractory and bursting property of the neuron (Figure 3.13d) [229, 250]. The stimulus filter describes the external input integration process, and the nonlinearity transforms the filtered stimulus to produce the conditional intensity of the Poisson spiking [253]. Neurons tend to increase their spiking probability if the cell has previously spiked. The post-spike filter captures the history-dependence of the spiking activity and adds the response as input to the static nonlinearity [229, 253, 254]. Unlike the deterministic HH and IF modes, GLMs are stochastic due to Poisson spiking.

Linear-Nonlinear Poisson Model

The Linear-Nonlinear Poisson (LNP) model is a particular case of GLM that approximates the arbitrary spiking neuron models [255]. The LNP model consists of the linear temporal filter (the L operation), a static nonlinearity (the N operation), and the Poisson process (the P operation) (Figure 3.13e) [229, 255, 256]. In contrast to GLMs, LNP models have no spike history filter [253, 257]. Therefore, the timing of individual output spike is statistically independent [258].

First, the temporal filter linearly convolves the stimulus. The temporal filter here corresponds to the response of the neuron to a small and sharp input current The static nonlinearity then transforms the output of the convolution to an instantaneous firing rate. The feedback process in the GLM was simplified into a single nonlinearity corresponding to the average of the neuron, with a static input and background noise. Then, the heterogeneous Poisson process generates the spikes a fixed time window. The Poisson point process means that the distribution of spike counts within a time window must have a Poisson distribution [258]. Both the temporal filter and the static nonlinearity can be analytically approximated in several 1 or 2 variable spiking neuron models, such as the LIF, generalized integrate-and-fire (GIF), and generalized exponential models (GEM) [229].

Hierarchical model

As depicted beforehand, the dendritic arborization is complex, that a point process cannot fully describe the neuronal information processing. Since dendrites have independent subunits, the processes can be modeled using a hierarchy of cascaded linear-nonlinear (hLN) processes [106]. Ujfalussy et al. [239] developed an hLN neuron model wherein the dendrites are subdivided into subunits. The inputs to each subunit are linearly integrated and then fed to a nonlinearity, representing the spatiotemporal processes of the individual

subunit. The outputs of the subunits are then linearly combined with other subunits belonging to the mother subunit. The process continues until the signals reach the soma for global integration and somatic spiking using GLM. Because of compartmentalization due to localized active mechanisms, the neuron becomes similar to multilayer perceptrons, with nonlinear (e.g., sigmoidal) hidden units [229, 232, 244]. The multilayer architecture can be utilized to perform routing, information selection, and multiplexing [233].

3.6/ CONCLUSION

Neuronal communication and computation is a more multifaceted process than previously suggested, and the functional implications of single neurons to neuronal networks are thought-provoking. This chapter illustrated and presented the interaction between the electrical, biochemical, and physiological characteristics of neurons that control information processing and communication. Also, the neuronal computation are associated with mathematical models and showed the progression of neuronal models from single point process to multiple layer process.

The presynaptic Ca^{2+} dynamics, accompanied by the IP_3 dynamics, chiefly mediate neurotransmission. In the axonal compartments, the total intracellular $[Ca^{2+}]$ is the summation of Ca^{2+} ions acquired via Ca^{2+} influx through VDCCs during APs generation and via the slow Ca^{2+} fluxes to and from the ER. One of the consequences of intracellular $[Ca^{2+}]$ fluctuations is the release of neurotransmitters from presynaptic vesicles into the synaptic cleft, a cycle of vesicle fusion, neurotransmitter release, and replenishment. Therefore, the arrival of AP to the axon terminal followed by the increase of $[Ca^{2+}]$ and the time course of the neurotransmitter release process is indicative of the overall Glu^{-} time course. Here, we presented the models for stochastic (mainly evoked by the level of $[Ca^{2+}]$) and deterministic (evoked by the arrival of AP) neurotransmission.

Chemical synaptic signals are converted back to electrical signals when neurotransmitters activate the postsynaptic receptors, such as AMPA and NMDA receptors on the dendrites. What are the functional consequences of spines and the implications of the intricate dendritic trees to neuronal computations and processes? It is still difficult to answer precisely, though, with the advances in neuroimaging and measurements, researchers discovered that the dendrites are not just receptive surfaces but are essential for neurons to perform more complex computations. Here, we discussed synaptic input propagation from the dendritic spine head, the spine neck where it is significantly attenuated, and into the dendritic shaft where it is integrated with other inputs. The input signals do not directly propagate to the soma; instead, the signals undergo different changes due to the passive and active properties of dendrites. Highly localized dendritic mechanisms indicate that the dendritic tree must not be considered a point process; instead, it comprises computational compartments performing independent processes. These processes can be linear and nonlinear integration, as well as arithmetic and Boolean operations. Furthermore, the neuron also filters, select, routes, and multiplex signals through its dendritic arborization. However, the exact comprehension of how the neuron performs these operations and functions is still lacking.

Overall, we demonstrated the course of signals from the synapse through the dendritic

tree to the soma for information consolidation in the form of somatic spiking. Numerous efforts have been made and are continuing in order to understand or replicate neuronal processing. From a point process of McCulloch-Pitts model to the addition of synaptic weights in perceptrons, to the two-layer neuron model of Poirazi et al. (2003), and the cascade and hierarchical GLMs and LNP models, the neurons seem to be capable of performing computations that are previously solely associated to neural networks.

Furthermore, recent studies suggest that brain computations are not only assigned to neurons. More researchers are remarking on the functions of astrocytes as computational units rather than just structural supports. This notion implies more complex neural networks than previously thought. The following chapter deals with astrocytes as computational units, their properties, and dynamics that influence neural processing.

4

Astrocytes as Computational Units

4.1/ Introduction

In the 1800s, it was thought that the brain contains no connective tissues until Rudolf Virchow argued against this notion. In his series of works in the 1950s, Virchow identified connective cellular elements penetrating the brain, filling the interstices among nerve cells and fibers, and separating nervous tissues from blood vessels [259–261]. He termed these cellular elements as **neuroglia** or *Nervenkitt*. Camillo Golgi and Ramón y Cajal supported Virchow's discovery when they highlighted that neuroglia and nerve cells form separate populations, the variety of glial shapes and forms, and the glial network [261, 262]. The term **astrocytes** came into view when by the end of the 19th century, Lenhossék used the word to refer to star-shaped glial cells, which, even though electrically silent, had significant functions as nerve cells [263].

From then on, an increasing amount of studies on astrocytes and their functionality emerged, especially as support structures to other cells and in maintenance, pruning, and remodeling of synapses during development, aging, and disease [8, 262]. However, it took another century for scientists to determine that astrocytes, though electrically silent, influence neurotransmission via the **tripartite synapse**, a well-established concept introduced by Araque et al. [4]. In addition, astrocytes create a distinct network through gap junction and communicate via gliotransmission. Emerging technologies in the last decades, therefore, challenge the neurocentric view of signal processing in the brain, as astrocytes release gliotransmitters that change the synaptic function and modulate synaptic activity.

This chapter takes a closer view of astrocytes as computational units in the hippocampus, their function in the tripartite synapse, the communication between astrocytes, and their influence in the neuron-astrocyte network. As the presynaptic neuron releases glutamate into the synaptic cleft, a portion of the [Glu^-] spills out of the cleft into the perisynaptic space, which is then sensed and removed from the extracellular space by the perisynaptic astrocytic process. The astrocytic Glu^- intake then mediates the intracellular Ca^{2+} oscillations, and almost similar to presynaptic Ca^{2+} activity, results in gliotransmitters release but with a timescale that is much longer than neurotransmitter release. At this point, gliotransmission can have pathways back to the presynaptic or the postsynaptic

neurons, influencing synaptic activities. Indeed, the addition of astrocytes in the synaptic activity creates a more complex neural circuit. Adding in the complexity is that astrocytes also form a separate network, where IP_3 diffusion via gap junctions with neighboring astrocytes mediates calcium wave propagation allowing astrocyte-to-astrocyte communication.

4.2/ Biological Structure and Functions of Astrocytes

Astrocytes belong to a non-neuronal heterogeneous group of cells in the CNS with an electrically non-excitable nature [262, 264, 265]. Glial cells are about 10 to 50 times more than neurons [266], and that astrocytes account for approximately 20-40% of the total number of brain cells [1, 267]. Indeed, the proportion of astrocytes between brain regions varies. In the cerebral cortex, the astrocyte-to-neuron ratio typically ranges around 1:2 and 1:3 [43, 268].

There are two types of astroglial in the brain whose distinct morphologies were revealed by Golgi staining: the protoplasmic astrocytes found in the gray matter and the fibrous astrocytes in white matter [9, 269, 270]. Protoplasmic astrocytes form complex arborizations, occupy large volumes by giving rise to numerous fine processes, and appear uniformly and roughly spherically distributed within the gray matter area. On the other hand, fibrous astrocytes have distinguishable little to moderate branching, exhibits long fiber-like processes, and are oriented longitudinally in the fiber-bundle (or axonal) plane [9, 271, 272].

Most of this research focuses on astrocytes of the protoplasmic type since these astrocytes establish close contact with the synapse [267], necessary for neuron- and gliotransmission.

4.2.1/ Morphological Complexity

Protoplasmic astrocytes have structurally compact core regions consisting of the soma, processes, and endfeet and complex spongiform peripherals (gliapil) formed by fine branches (Figure 4.1a) [5]. Their sponge-like morphology allows astrocytic processes to penetrate and reach compacted areas in the neuropil, comprising the synapses [9]. Astrocytic processes are further classified depending on their sizes and locations (Figure 4.1b). These processes can be a **branch** (the primary stem process), **branchlet** (the secondary or tertiary process), thinnest processes which make contact with the synapse called **leaflets** or **peripheral processes** or **perisynaptic astrocyte processes** (PAPs), and **end feet** that are specialized and polarized astrocytic structures in contact with blood vessels [267, 272]. Additionally, astrocytes have motile **microdomains** that expand and surround synapses [15].

In rodents, astrocytes have diameters of $\sim$40-60 μm with volumes in the order of 10^4 μm, while human protoplasmic astrocytes are $\sim$2.5 times larger in diameter and $\sim$16.5 times larger in volume [267, 271]. The number of neuronal cell bodies and dendrites that a single astrocyte creates contact with varies dramatically. Mature protoplasmic astrocytes

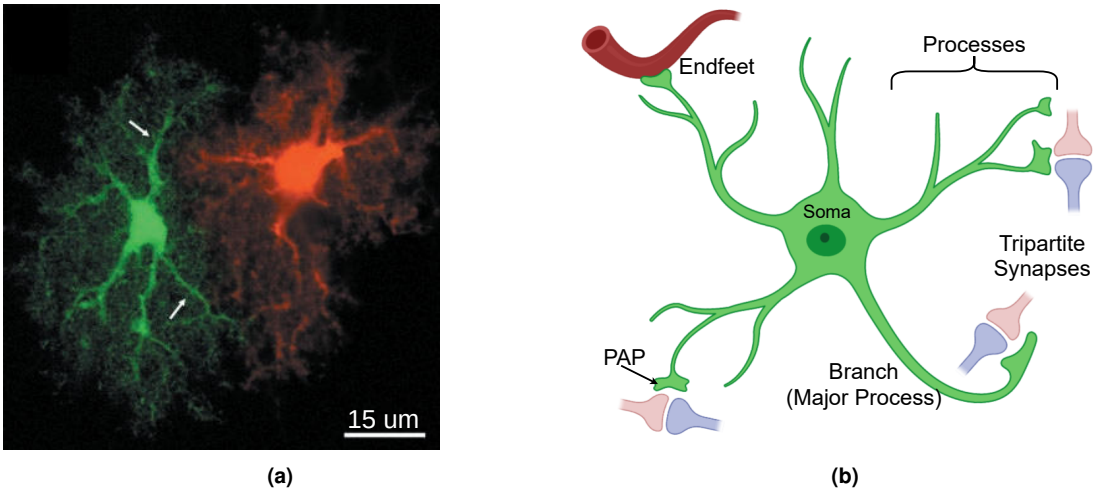

Figure 4.1: Morphology of a protoplasmic astrocyte. (a) An optical image of neighboring astrocytes in the CA1 region filled with different colored dyes showing separate anatomical domains. (Image taken was taken from Bushong et al. [273].) The morphological structure of the astrocyte consists of a soma (cell body) with protruding stem processes (*arrows*). (b) The major branches (stem processes) then bifurcate into smaller processes (i) forming the tripartite synapse, (ii) endfeet contacting the blood vessels, or (iii) gap-junctions connecting the neighboring astrocytes.

located in the hippocampus and cortex have more branch arborization than subcortical regions such as the hypothalamus [264]. In rodents, a single hippocampal astrocyte makes contact with ~100,000-140,000 synapses and one neuronal body; whereas, individual human astrocyte can cover ~2 million synapses with a synaptic density of ~1100 million synapses per mm^3, contacts 300-600 neuronal dendrites, and enwraps four to eight neuronal somata [9, 267, 273–275]. In the CA3 region, astrocytic processes fully enwrap the synapse prohibiting glutamate spillover, while in the CA1 region, astrocytic processes ensheath a portion of the synapse, partially covering 57-62% of the synapses in the CA1 stratum radiatum (synapse-containing region) [267, 276].

4.2.2/ Biophysical Characteristics

Like other cells in the mammalian body, astrocytes display complex molecular dynamics and cellular signaling and express abundant numbers of channels, transporters, and receptors necessary for providing homeostasis and synaptic functions. They express major ion channels such as K^+, Na^+, Ca^{2+} channels, and other non-selective channels such as anion and chloride channels, water channels, and transient receptor potential channels [277–279]. Astrocytes are traditionally considered electrically nonexcitable; they do not conduct APs. Even though astrocytic intracellular $[K^+]$ and $[Ca^{2+}]$ are somewhat similar to neurons, unlike neurons, astrocytes cannot generate membrane depolarizations due to higher $[Na^+]$ and $[Cl^-]$, yet maintain a more negative resting membrane potential between -85 to -90 mV, a consequence of the predominant K+ conductance [9, 15, 280]. Indeed, astrocytes do not fire APs and do not display excitatory/inhibitory postsynaptic potential-like activity [281]. However, astrocytes communicate with their neighboring astrocytes or influence synaptic transmission via chemical signaling through Ca^{2+}-mediated signals instead of electrical signaling in neurons. Therefore, astrocytes are also considered excitable cells based on their intracellular Ca^{2+} transients and oscillations [15].

Similar to neurons, astrocytes also express membrane transporters for ions, neurotransmitters, and other substances. Astrocytes have adenosine- and ATP-transporters such as Na^+/K^+-ATPase (Na^+/K^+ pump), Ca^{2+}-ATPase (PMCA), as well as Sarco/ER Ca^{2+}-ATPase (SERCA pump) on the ER membrane [282–284]. Notably, there are also secondary transporters such as glutamate transporters or excitatory amino acid transporters (EAATs), GABA-transporters, glycine transporters, NCXs, and others [285–288]. Among glial cells, astrocytes express the highest surface density of glutamate transporters (glutamate/aspartate transporter (GLAST) and glutamate transporter-1 (GLT-1)) of approximately 10,800 μm^{-2} (measured based on protein extracts from mature rodent hippocampal astrocytes) for Glu^- uptake [7, 9, 281, 289]. Human astrocytes have two prominent expressions of glutamate transporters called excitatory amino acid transporter 1 and 2 (EAAT1 and EAAT2, respectively) [281, 290]; EAAT1 and EAAT2 are human homologs of GLAST and GLT-1, respectively [291].

Ionotropic and metabotropic receptors (e.g., for Glu^-, GABA, serotonin, adenosine, ATP, and other typical neurotransmitters) coupled with secondary messengers allow astrocytes to sense neural activity and synaptically released neurotransmitters, as seen *in vitro* cell cultures and *in vivo*. Astrocytic Glu^- uptake is mediated by ionotropic glutamate receptors (iGluRs), such as AMPA- and NMDA type receptors, that directly regulate ion channel gatings and metabotropic glutamate receptors (mGluRs) from the family of GPCRs that, when activated, result in PLC- and IP_3-dependent intracellular $[Ca^{2+}]$ increase [9, 292–294]. The following sections further describe the functions of these transporters and receptors and their influence on glutamate-mediated astrocytic Ca^{2+} signaling.

4.2.3/ FUNCTIONS

A plethora of studies substantiate that astrocytes act as structural and metabolic supports essential for a healthy CNS. They maintain brain architecture, support neurodevelopment and migration, and regulate metabolism and hemodynamics [272, 281, 295]. Then, recent studies suggest that astrocytes also contribute to circuit information processing, especially in synaptic transmission in neural circuits [274]. This research focuses on their functional responsibilities in connection with neural information processing. The following are the primary functions of astrocytes, as suggested by Nedergaard and Verkhratsky [8].

Astroglial cradle. One of the primary functions of perisynaptic astrocytes is to create an **astroglial cradle**, structural support that works in two ways [8]. The first is creating a physical barrier that shields the synapse from the ”spill-in” of various extrasynaptic signaling events from neighboring non-neuronal cells. The second is preventing the ”spill-over” of neurotransmitters into the extracellular space [267]. Even though most cell types in the brain express glutamate transporters, astrocytes are the primary cells responsible for the uptake of synaptically released Glu^- and GABA. The PAPs rapidly remove these neurotransmitters to avoid synaptic excitotoxicity, which is detrimental to neurons [9, 285, 296].

Spatial precision of synaptic transmission. Because astrocytes serve as synaptic barriers, the dynamic changes in astrocytic coverage of synapses consequently modulate and keep the spatial specificity of synaptic transmission [8, 15]. By limiting the spill-over or spill-on of neurosignaling molecules, PAPs also limit the crosstalk between neuronal

elements, thus promoting input specificity during synaptic transmission. At the same time, the tight structural arrangement of neuron-astrocyte coupling allows astrocytes to sense specific synaptic activity and control the molecular signaling within the synaptic island, a group of synapses located within a single astrocytic territory [275, 297].

Synaptic strength modulation. Synapses with astrocytic processes coverage are larger than synapses consisting of the axon-spine interface alone [267]. This morphological characteristic hints that astrocytes might influence synaptic activities. Studies suggest that astrocytes participate in synaptic transmission by releasing gliotransmitters such as Glu^- which modulate the synaptic strength [298, 299]. In addition, astrocytes regulate extracellular levels and the diffusion of neurotransmitters via rapid glutamate uptake [271, 281, 299].

Global modulation of neural networks. The influence of astrocytes in synaptic transmission is not only restricted within the synaptic area. Astrocytic Ca^{2+} signals originating in the PAPs can propagate within the intracellular space, to the soma, or other PAPs; thus, affecting the $[Ca^{2+}]$ elevations in different compartments, and in turn, also influence the gliotransmitter release in neighboring synapses. Furthermore, Nedergaard and Verkhratsky [8] also suggested that astrocytes influence information processing by globally and tonically modulating neural networks. The morphological characteristics of astrocytes, such as extensive contacts with thousands of synapses and several neighboring astrocytes, enable them to listen and respond to other cellular elements. The range of neuron-astrocyte interactions expands into networks as astrocytes also release additional Glu^- to neighboring synapses resulting from intercellular Ca^{2+} wave propagation [15, 300].

The morphological and functional characteristics of astrocytes indicate that the complex bidirectional signaling between neurons and astrocytes, or among astrocytes, can potentially impact neural information processing. Though astrocytes perform diverse responsibilities, their exact role in these functions still needs further investigation.

4.3/ INTRACELLULAR DYNAMICS

Compared with their neuronal counterparts, astrocytes are electrically silent, where passive currents dominate the membrane conductance. However, astrocytes are chemically excitable in terms of the main signaling mechanism, the intracellular $[Ca^{2+}]$ oscillations [9, 271, 298]. Signaling molecules trigger intracellular $[Ca^{2+}]$ elevations in astrocytic microdomains (such as in PAPs) and in the soma [9, 299]. Let us consider a single-compartment astrocyte in Figure 4.2. Calcium ions, along with other signaling molecules such as Glu^-, IP_3, Na^+, and K^+, are located in the extracellular and intracellular spaces and can cross the astrocytic membrane [6]. Calcium ions are also stored in the ER, considered as a subcompartment separate from the intracellular space. There are two mechanisms responsible for Ca^{2+} oscillations: (1) the IP_3 triggered Ca^{2+}-induced Ca^{2+} release (CICR) from the ER driven by the mGluR activity, and (2) the entry of Ca^{2+} ions through the astrocytic plasma membrane that depends on the activities of GluTs and NCX [5, 6, 301].

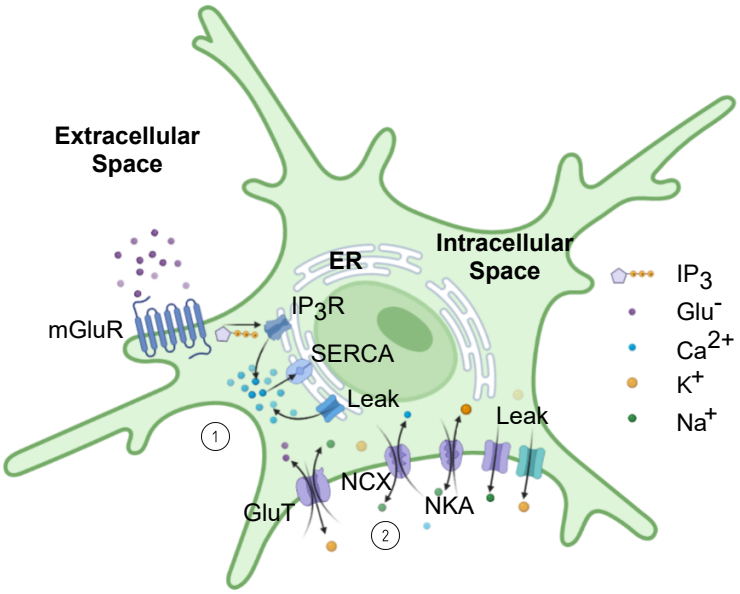

Figure 4.2: Astrocytic signaling mechanisms. Intracellular [Ca^{2+}] signaling in astrocytes have glutamate-mediated pathways that are mGluR- or GluT-dependent. (1) Glutamate from presynaptic terminals binds with astrocytic mGluR, which then triggers the production of IP_3 molecules. The second messenger IP_3 then binds to IP_3R on the ER membrane, opening the channel for Ca^{2+} release into the intracellular space. The SERCA pump and leakage channels on the ER membrane sustain intracellular Ca^{2+} oscillations by generating Ca^{2+} fluxes. (2) Extracellular Glu^- enters the intracellular space via the GluT, which simultaneously transports Na^+ and K^+ ions in and out of the cell. The Na^+ and K^+ gradients, caused by the transporters and leakage channels, activate the Na^+ efflux and Ca^{2+} influx between the intra- and extracellular spaces.

The main signaling mechanism of astrocytes is the Ca^{2+} signals from mGluR-dependent IP_3-sensitive ER, whose dynamics are illustrated in Figure 4.2(1) [6, 298]. Metabotropic GluRs from the GPCR family sense synaptic activities and influence Ca^{2+} mobilization from the ER, triggering intracellular astrocytic [Ca^{2+}] elevations [5, 265, 301, 302]. Neurotransmitter spill-over, specifically Glu^-, from the presynaptic terminals, activates astrocytic mGluRs. As a response, activated mGluRs then stimulate the PLC hydrolysis, which leads to the production of the second messenger IP_3 [6, 302]. The IP_3 molecules then bind with the IP_3Rs on the ER membrane, subsequently provoking the ER to release Ca^{2+} to the intracellular space. In order to sustain the nonlinear Ca^{2+} dynamics, Ca^{2+} stored in the ER must be replenished [303]. This is achieved by exchanging Ca^{2+} ions from the intracellular space to the ER by SERCA pumps. The ER membrane also contains leakage channels that prevent intracellular Ca^{2+} depletion. In this case, Ca^{2+} signaling is slower, peaking at three to ten seconds after initial stimulation [298].

The second pathway is GluT-dependent, as shown in Figure 4.2(2) [6]. Here, note that GluT has no direct influence on intracellular [Ca^{2+}] elevation. When the extracellular Glu^- molecule enters the GluT, it is accompanied by three Na^+ ions to the intracellular space and one K^+ to the extracellular space. The transient increase of intracellular [Na^+] drives the NCX to transport Na^+ out of the astrocyte while producing Ca^{2+} influx [304]. In this case, GluT indirectly increases the intracellular [Ca^{2+}]. In addition, Na^+/K^+ ATPase (NKA) breaks down energy from ATP, resulting in the three Na^+ ions efflux and two K^+ ions influx [305]. These intracellular [Na^+] fluctuations, with the influences of the Na^+ and K^+ leakages, allow astrocytes to drive multiple mechanisms for ion transports, such as the GluT.

Consider a single cylindrical compartment with the same intra- and extracellular volumes, the change of ion concentration in the intracellular space at any time t is equal to the summation of ionic currents multiplied by the ratio between the outer surface area, A, and the product of the Faraday's constant, F, and the volume, Vol, of the space where the ions are located [6]. Therefore,

$$\frac{d[ion]}{dt} = \frac{A}{F \cdot Vol} \sum I_{ion}, \tag{4.1}$$

where A and Vol are scaled by the length, l, of the compartment. Therefore, for a single compartment astrocyte whose intracellular volume contains the ER volume, the intracellular [Ca^{2+}] is determined by the Ca^{2+} entering the membrane through NCX and the Ca^{2+} ions exiting and entering the ER given as

$$\frac{d[Ca^{2+}]_i}{dt} = \frac{A}{F \cdot Vol} J_{NCX} + \frac{A\sqrt{r_{ER}}}{F \cdot Vol} \left(J_{IP_3R} - J_{SERCA} + J_{C_{ER}leak}\right), \tag{4.2}$$

where A is the surface area of the outer cell membrane, Vol is the intracellular volume, and $\sqrt{r_{ER}}$ is the factor that reduces the ER surface area in comparison with the intracellular space (r_{ER} is the ratio between the surface volume ratio of the compartment and the volume ratio between the ER and the intracellular space). Here, the flux J_{NCX} is the Ca^{2+} influx due to Na^{2+}/Ca^{2+} exchange, J_{IP_3R} is the Ca^{2+} influx due to the activation of mGluR, J_{SERCA} is the efflux due to SERCA pump, and $J_{C_{ER}leak}$ is the current leaking from the ER to the intracellular space. Furthermore, the amount of Ca^{2+} in the internal stores is determined by the Ca^{2+} fluxes entering and leaving the ER described as

$$\frac{d[Ca^{2+}]_{ER}}{dt} = \frac{A\sqrt{r_{ER}}}{F \cdot Vol \cdot r_{ER}} \left(-J_{IP_3R} + J_{SERCA} - J_{C_{ER}leak}\right), \tag{4.3}$$

where $A\sqrt{r_{ER}}$ and $Vol\sqrt{r_{ER}}$ are the surface area and the volume of the ER, respectively.

The properties of intracellular [Ca^{2+}] oscillations are different from neurons for their larger amplitude, longer duration, regular but infrequent occurrence, and are governed by the neuronal and astrocytic inputs [15]. Manninen et al. [306, 307] compiled a list of Ca^{2+}-mediated biophysical astrocytic models, presented the state-of-the-art, and compared computational modeling of astrocytes. One can consult their papers for more information on the advancement of astrocytic Ca^{2+} modeling. In that case, the following sections deal with the fundamental models describing the Ca^{2+} and IP^3 dynamics both in the dimensional and non-dimensional methods.

4.3.1/ Calcium and IP_3 Dynamics

4.3.1.1/ Reduced Li-Rinzel Model

As presented by Manninen [307], hundreds of models currently available are adaptations of the Li-Rinzel model [162], which is also a simplified version of De Young and Keizer [308]. The Li-Rinzel model assumes that the intracellular Ca^{2+} signaling is due to CICR from the ER to the cytosol, regulated by IP3Rs, the Ca^{2+} flux from the SERCA pump, and the ER Ca^{2+} leakage [157, 306]. See Figure 4.2(1). In addition, this model also

uses the closed-cell assumption, meaning that there is no Ca^{2+} flux across the astrocytic membrane [88], removing the influence of the GluT-dependent mechanisms. Calcium signaling is a consequence of the combined activities of the mGluRs on the astrocytic membrane and the IP_3Rs on the ER membrane and the active engagement of cytosolic Ca^{2+} and IP_3 ions [178].

IP_3 dynamics

Extrasynaptic Glu^- spilling over from the synaptic cleft, g, and the astrocytic Ca^{2+} both influence the production of IP_3 via G-protein link to PLC, while phosphorylation of IP_3 3-kinase (IP_3-3K) and inositol polyphosphate 5-phosphatase (IP-5P) degrade the [IP_3] [6, 10, 88, 157, 178]. The evolution of [IP_3] with time following the mass balance equation

$$\begin{aligned}\frac{d[IP_3]_a}{dt} &= J_{PLC\beta}\left(g,[Ca^{2+}]_a\right) + J_{PLC\delta}\left([IP_3]_a,[Ca^{2+}]_a\right) \\ &\quad - J_{3K}\left([IP_3]_a,[Ca^{2+}]_a\right) - J_{5P}\left([IP_3]_a\right),\end{aligned} \tag{4.4}$$

where $J_{PLC\beta}$ and $J_{PLC\delta}$ are the agonist-dependent and agonist-independent IP_3 productions mediated by phosphoinositide-specific PLCβ and PLCδ, respectively. The fluxes J_{3K} and J_{5P} cause IP_3 degradation mediated by IP_3-3K and IP-5P, respectively. Among these fluxes, PLCβ-mediated IP_3 production is dependent on the level of extracellular [Glu^-], $[Glu^-]_a$. The fluxes are described as

$$\begin{aligned}J_{PLC\beta} &= v_\beta \text{Hill}\left([Glu^-]_a^{0.7}, K_R\left(1+\frac{K_p}{K_R}\text{Hill}\left([Ca^{2+}]_a,K_\pi\right)\right)\right),\\ J_{PLC\delta} &= \frac{v_\delta}{1+\frac{[IP_3]_a}{k_\delta}}\text{Hill}\left([Ca^{2+}]_a^2,K_{PLC\delta}\right),\\ J_{3K} &= v_{3K}\text{Hill}\left([Ca^{2+}]_a^4,K_D\right)\text{Hill}\left([IP_3]_a,K_3\right),\\ J_{5P} &= r_{5P}[IP_3]_a,\end{aligned} \tag{4.5}$$

noting that $Hill(x^n,K)$ is the Hill function (sigmoid) equal to $x^n/(x^n+K^n)$ [6, 88, 178]. The constant terms v_β and v_δ are the maximal rates of IP_3 production by PLCβ and PLCδ, respectively, while v_{3K} and r_{5p} are the maximal degradation rate of IP_3 by IP_3-3K and IP-5P, respectively. The term k_δ is a constant inhibiting the $J_{PLC\delta}$ flux. Moreover, K_R is the Glu^- affinity of the GPCR (mGluR), K_p is the Ca^{2+}/Protein kinase C-dependent (PKC) inhibition factor, K_π Ca^{2+} affinity of PKC, $K_{PLC\delta}$ is the Ca^{2+} affinity of PLCδ, K_D is the Ca^{2+} affinity of IP_3-3K, and K_3 is the IP_3 affinity of IP_3-3K, respectively.

De Pitta et al. [178] approximated the IP_3 production based on the fraction of activated mGluRs rather than directly on g (synaptic Glu^- spilling to the extrasynaptic space). Glutamate from the presynaptic terminal spills and binds with mGluRs on the PAPs. Assuming that a fraction of synaptic glutamate binding with postsynaptic receptors is ζ, the fraction that spills out of the synapse to the PAP is therefore $1-\zeta$. The fraction of activated mGluRs, γ_A, is

$$\tau_A\frac{d\gamma_A}{dt} = -\gamma_A + O_A\left(1-\zeta\right)Y_S\left(1-\gamma_A\right)\tau_A, \tag{4.6}$$

where τ_A is the time constant of receptor deactivation, O_A is the agonist binding rate, and

Y_S is the synaptic [Glu$^-$] described in Equation 3.29. Then, $J_{PLC\beta}$ becomes $v_\beta \gamma_A$.

The [IP_3], in association with [Ca^{2+}], triggers the opening and closing of IP_3R channels on the ER membrane controlling the CICR mechanism for Ca^{2+} delivery into the intracellular space [6, 309]. The IP_3R channel is active when one Ca^{2+} and one IP_3 ion bind to two out of three IP_3R subunits [6, 310, 311]. The IP_3R channel becomes inactive when a second Ca^{2+} ion binds with the third subunit. Each IP_3R subunit in the cluster has a Ca^{2+} binding site for inactivation whose gating kinetics can be described by a dimensionless variable h_a [157, 162, 306], defined as

$$\frac{dh_a}{dt} = \frac{h_{a_\infty} - h_a}{\tau_h}, \tag{4.7}$$

where

$$\begin{aligned} h_{a_\infty} &= \frac{Q_2}{Q_2 + [Ca^{2+}]}, \\ \tau_h &= \frac{1}{a_2 \left(Q_2 + [Ca^{2+}]\right)}, \\ Q_2 &= d_2 \frac{[IP_3] + d_1}{[IP_3] + d_3}. \end{aligned} \tag{4.8}$$

The IP_3R gating variable in Equation 4.7 can be rewritten into

$$\frac{dh_a}{dt} = \alpha_{h_a} (1 - h_a) - \beta_{h_a} h_a, \tag{4.9}$$

where

$$\alpha_{h_a} = a_2 d_2 \frac{[IP_3] + d_1}{[IP_3] + d_3} \tag{4.10}$$

describes the opening rate of h_a and

$$\beta_{h_a} = a_2 [Ca^{2+}] \tag{4.11}$$

is the closing rate [88]. The terms a_2, d_1, d_2, and d_3 are the IP_3R binding rate for Ca^{2+} inhibition, the IP_3 dissociation constant, the Ca^{2+} inactivation dissociation constant, and the IP_3 dissociation constant respectively [6, 88, 157]. By adding a zero mean, uncorrelated, Gaussian white-noise $G_h(t)$ with covariance function described in Equation 4.12 to the rate of change of h_a, the Ca^{2+} flow through the IP_3R channel becomes stochastic.

$$\langle G_h(t) G_h(t') \rangle = \frac{\alpha_{h_a} + \beta_{h_a} h_a}{N_{IP_3}} \delta (t - t'), \tag{4.12}$$

where $\delta(t)$ is the Dirac-delta function, t and t' are specific times, the term $(\alpha_{h_a}(1 - h_a) + \beta_{h_a} h_a) / N_{IP_3}$ is the spectral density, and N_{IP_3} is the number of IP_3Rs in the cluster [88].

Moreover, each IP_3R also has two activation sites: one for IP_3 and another for Ca^{2+}. The gating kinetics for IP_3 activation is defined as

$$m_{a_\infty} = \frac{[IP_3]}{[IP_3] + d_1}, \tag{4.13}$$

while the gating kinetics for Ca^{2+} activation is given as

$$n_{a_\infty} = \frac{[Ca^{2+}]}{[Ca^{2+}] + d_5}, \tag{4.14}$$

where d_5 is the Ca^{2+} activation dissociation constant [88, 157]. Together, the gating kinetics m_{a_∞}, n_{a_∞}, and h_a represent the opening probability of the IP_3R cluster.

Ca^{2+} dynamics

Similar to the slow Ca^{2+} dynamics in neurons (presented in Chapter 3 Section 3.2), intracellular Ca^{2+} ($[Ca^{2+}]_a$) balance is primarily dependent on three fluxes [6, 88, 157, 178]; a passive Ca^{2+} leakage from the ER to the intracellular space (cytosol), $J_{C_{ER}leak}$, ER Ca^{2+} intake due to SERCA pumps, J_{SERCA}, and Ca^{2+} released from the ER to the cytosol based on the levels of $[Ca^{2+}]$ and $[IP_3]$, J_{IP_3R}, following the equation

$$\frac{d[Ca^{2+}]_a}{dt} = J_{IP_3R}\left([Ca^{2+}]_a, h, [IP_3]_a\right) + J_{SERCA}\left([Ca^{2+}]_a\right) - J_{C_{ER}leak}\left([Ca^{2+}]_a\right). \tag{4.15}$$

The ER releases Ca^{2+} by opening of IP_3R channels whose opening probability depends on three distinct gating processes described previously. The influx, J_{IP_3R}, is therefore proportional to the Ca^{2+} gradient and is also mediated by the IP_3Rs whose opening probability of channels has a power of three. Therefore,

$$J_{IP_3R}\left([Ca^{2+}]_a, h_a, [IP_3]_a\right) = r_C m_{a_\infty}^3 n_{a_\infty}^3 h_a^3 \left([Ca^{2+}]_{ER} - [Ca^{2+}]_a\right), \tag{4.16}$$

where the proportionality constant r_C is the maximal rate at which Ca^{2+} flows from the IP_3R cluster and $[Ca^{2+}]_{ER}$ is the Ca^{2+} concentration stored in the ER. The term $m_{a_\infty}^3 n_{a_\infty}^3 h_a^3$ characterizes the opening probability of the channel.

The Ca^{2+} current, J_{SERCA}, flowing through the SERCA pump is dependent on the intracellular $[Ca^{2+}]$. This influx assumes a Hill rate expression with Hill constant equal to 2, and given as

$$J_{SERCA}\left([Ca^{2+}]_a\right) = \frac{v_{ER}[Ca^{2+}]_a^2}{K_{ER}^2 + [Ca^{2+}]_a^2}, \tag{4.17}$$

where v_{ER} is the maximal Ca^{2+} uptake by the pump and K_{ER} is the SERCA Ca^{2+} affinity, which is the $[Ca^{2+}]$ at which the pump operates at half of its maximum capacity.

The Ca^{2+} leak $J_{C_{ER}leak}$ is proportional to the $[Ca^{2+}]$ gradient across the ER membrane, given as

$$J_{C_{ER}leak}\left([Ca^{2+}]_a\right) = r_L\left([Ca^{2+}]_{ER} - [Ca^{2+}]_a\right), \tag{4.18}$$

where r_L is the maximal rate of Ca^{2+} leakage from the ER. The Ca^{2+} current strength is proportional to the Ca^{2+} gradient between the ER and the intracellular space, ($[Ca^{2+}]_{ER} - [Ca^{2+}]_a$). The two influxes J_{IP_3R} and $J_{C_{ER}leak}$ can be combined into a single flux J_{rel},

$$\begin{aligned} J_{rel}\left([Ca^{2+}]_a, h_a, [IP_3]_a\right) =& J_{IP_3R}\left([Ca^{2+}]_a, h_a, [IP_3]_a\right) + J_{C_{ER}leak}\left([Ca^{2+}]_a\right), \\ =& \left(r_C m_{a_\infty}^3 n_{a_\infty}^3 h_a^3 + r_L\right)\left([Ca^{2+}]_{ER} - [Ca^{2+}]_a\right). \end{aligned} \tag{4.19}$$

Under the closed-cell assumption, the cell-averaged total free [Ca^{2+}], C_0, is conserved. The [Ca^{2+}] in the ER can also be expressed completely in terms of the astrocyte cell parameters, described as

$$[Ca^{2+}]_{ER} = \frac{\left(C_0 - [Ca^{2+}]_a\right)}{c_1} \Rightarrow [Ca^{2+}]_{ER} c_1 = C_0 - [Ca^{2+}]_a, \tag{4.20}$$

where c_1 is the ratio between the ER and cytosolic volumes. Therefore, the J_{rel} function can be rewritten as

$$J_{rel}\left([Ca^{2+}]_a, h_a, [IP_3]_a\right) = \left(r_C m_{a_\infty}^3 n_{a_\infty}^3 h_a^3 + r_L\right)\left(C_0 - (1 + c_1)[Ca^{2+}]_a\right). \tag{4.21}$$

Finally, the astrocytic Ca^{2+} in the intracellular space is

$$\frac{d[Ca^{2+}]_a}{dt} = J_{rel}\left([Ca^{2+}]_a, h_a, [IP_3]_a\right) - J_{S\,ERCA}\left([Ca^{2+}]_a\right). \tag{4.22}$$

Accordingly, the change in the intracellular [Ca^{2+}] results from the behavior and cooperation of four components: (1) the intracellular [Ca^{2+}], (2) the intracellular [IP_3], (3) the fraction of activated mGluRs, (4) the fraction of de-inactivated IP_3Rs.

4.3.1.2/ POSTNOV MODEL

Postnov et al. [312–314] developed a nondimensional and qualitative model, a generalized and simplified model describing the astrocytic Ca^{2+} and IP_3 dynamics. The synaptic coupling is described by a first-order differential equation

$$\tau_s \frac{dz}{dt} = (1 + \tanh(s_s(v_1 - h_s)))(1 - z) - \frac{z}{d_s}, \tag{4.23}$$

where the variable v_1 describes the presynaptic neuron fast variable and z is the synaptic activation that acts as the input to the postsynaptic neuron and the astrocyte, stimulating the IP_3 production. The time constant τ_s is the synaptic delay, and the constant terms s_s, h_s, and d_s control the activation and relaxation of z. Here, h_s is analogous to the AP activation threshold, wherein during $z < h_s$, the neuron is in the subthreshold region and the synapse is silent. As the v_1 increases beyond h_s, the synapse activates and z elevates. Upon reaching the peak value, $z \approx 1$, the synapse relaxes, and z inactivates. Once activated, the presynaptic neuron releases a neurotransmitter concentration, $[T]$, multiplied to an amplifying factor, a, exceeding zero, ($z = a[T]$). Because the model is nondimensional, the neurotransmitter concentration must be modified into

$$[T] = \frac{1}{1 + \exp(-(v_1 - \theta_S)/\sigma_s)}, \tag{4.24}$$

where v_1 is the membrane potential of the presynaptic neuron, θ_S is the half-activation voltage, and σ_s is the steepness of the sigmoid function.

The postsynaptic current input, I_{syn}, includes the combined influence of the presynaptic

neuron (z) and the astrocyte (δG_m) to the synapse.

$$I_{syn} = (k_s - \delta G_m)(z - z_0), \tag{4.25}$$

where, k_s describes the conductivity, δ is the fraction of G_m spilling into the synapse, and z_0 is the reference level during which the synapse is silent. Therefore, the total input to the postsynaptic neuron is the sum of I_{syn} and I_{ast}, the astrocyte-induced current G_m multiplied by the factor γ.

Ca^{2+} dynamics

Let c be the unitless description of [Ca^{2+}] in the cytoplasm given as

$$\begin{aligned}
\tau_c \frac{dc}{dt} &= c - c_4 f(c, c_e) + (r + \beta S_m), \\
\epsilon_c \tau_c \frac{dc_e}{dt} &= f(c, c_e), \\
f(c, c_e) &= c_1 \frac{c^2}{1 + c^2} - \left(\frac{c_e^2}{1 + c_2^2}\right)\left(\frac{c^4}{c_2^4 + c^4}\right) - c_3 c_e,
\end{aligned} \tag{4.26}$$

where c_e denotes the Ca^{2+} concentration in the ER, the constant parameters ϵ_c, τ_c together define the characteristic time for Ca^{2+} oscillations. The factor β controls the variable S_m, which defines the production of the secondary messenger IP_3, and r controls the initial state of Ca^{2+} oscillation. The nonlinear function $f(c, c_e)$ describes the Ca^{2+} exchange between the cytoplasm and the ER.

IP_3 dynamics

Let the slow astrocytic IP_3 dynamics be described by S_m defined as

$$\tau_{S_m} \frac{dS_m}{dt} = (1 + \tanh(S_{S_m}(z - h_{S_m})))(1 - S_m) - \frac{S_m}{d_{S_m}}, \tag{4.27}$$

where z is the synaptic activation that triggers the production of IP_3. The parameters τ_{S_m}, s_{S_m}, h_{S_m}, and d_{S_m} control the time scale, steepness of activation of the sigmoid function, threshold values, and the deactivation rate, respectively.

4.3.1.3/ HILL FUNCTION-BASED MODEL

Cresswell et al. [303] recently developed a simpler notation for Ca^{2+} fluxes, which also uses nondimensional models described by the Hill function

$$H_n(x, k) = \frac{x^n}{x^n + k^n}. \tag{4.28}$$

This model only contains two Ca^{2+} fluxes: J_r denotes the Ca^{2+} flux from the ER to the cytosol through IP_3R and J_p for the Ca^{2+} flux from the cytosol into the ER through SERCA pumps. Hill function was used due to the common characteristics of previous IP_3R models; the bell-shaped function of Ca^{2+}. Assuming a sufficient level of IP_3 and fast activation and slow inactivation of Ca^{2+}-sensitive IP_3R channels, the interaction between the cytosolic and ER Ca^{2+} pools creates a flux, J_r, described as

$$J_r\left(C_E, C_I\right) = H_2\left(C_E, 1\right) H_4\left(C_1, b_2\right), \tag{4.29}$$

where C_I and C_E are the nondimensional cytosolic and ER [Ca^{2+}], respectively. Here, b_2 is the half-activation value for C_I for the IP_3 channels. Then, the flux through SERCA pumps is a continuous model described as

$$J_p(C_I) = b_1 H_2(C_I, 1), \tag{4.30}$$

where b_1 is the maximum velocity of the reaction. The [Ca^{2+}] in the astrocytic process is given by

$$\begin{aligned} \tau_c \frac{dC_I}{dt} &= r + \sigma\xi_i + b_4\left(J_r - J_p\right) - C_I, \\ \epsilon_c \tau_c \frac{dC_E}{dt} &= -J_r + J_p. \end{aligned} \tag{4.31}$$

where C_I and C_E denote the intracellular and ER Ca^{2+}, respectively. The parameter r controls the intrinsic Ca^{2+} excitability in the PAP, $\sigma\xi_i$ denotes the stochastic neuronal input, b_4 is the ratio between the ER and the cytosolic volumes, τ_c is the time constant for Ca^{2+} variations, and ϵ_c is the timescale separation between the cytosolic and the ER Ca^{2+} pools.

4.3.2/ Local and Global Ca^{2+} Dynamics

Studies also suggest that astrocytes, like neurons, display compartmental dynamics. Calcium and IP_3 currents are confined within the astrocytic processes and the soma [9, 315], and diffuse to neighboring compartments, to different astrocytic processes, and even the whole cell [299]. These local astrocytic Ca^{2+} events can spread within the intracellular region by activating clusters of IP_3 receptors on the ER membrane or by astrocytic ligand-gated Ca^{2+} channels, transient receptor potential channels, and reverse operation of Na^+/Ca^{2+} exchanger (NCX), or by the activity of GPCRs within the perisynaptic regions [265, 302]. Calcium events can be classified as focal, expanded, or generalized depending on how the Ca^{2+} spreads.

Wu et al. [265] suggested that spontaneous Ca^{2+} events in single astrocytes, measured using two-photon imaging, have power-law distribution and that Ca^{2+} events may have scale-invariant properties. It means that Ca^{2+} spread in a single focal plane of astrocytes in the brain is a continuum rather than separated. However, Bindocci et al. [5] contradicted the results of conventional 2D imaging techniques (two-photon imaging) that assume that Ca^{2+} events in a single focal plane represent the whole-cell activity, given that astrocytes are highly three-dimensional. Therefore, they developed a three-dimensional Ca^{2+} imaging method and found transient and compartmentalized Ca^{2+} activities heterogeneously distributed within the astrocytic regions. Figure 4.3(left) is a 3D reconstruction

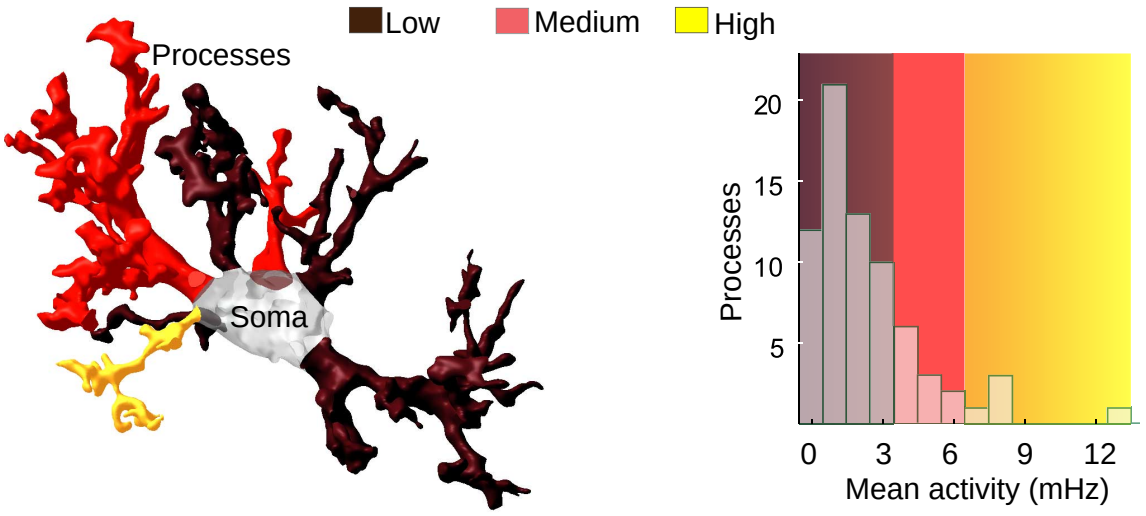

Figure 4.3: A three-dimensional reconstruction of hippocampal astrocyte by Bindocci et al. [5] showing heterogeneity in Ca^{2+} activities in each astrocytic process (left). The right side shows that an astrocyte has processes with different average activity ranging from low (0-3 mHz) to medium (3-6 mHz) and high (>6 mHz) levels.

of a hippocampal astrocyte *in situ*, while Figure 4.3(right) shows the average Ca^{2+} activity levels. Most of local mean Ca^{2+} activity in an astrocyte resides in the peripheral regions, while the soma is generally inactive. The results indicate the heterogeneity in Ca^{2+} activities in different astrocytic compartments, ranging from low to medium and to high activity levels. In addition, individual astrocytic processes also have alternating hot and cold spots distributed heterogeneously.

Furthermore, global Ca^{2+} events consist of multifocal Ca^{2+} activities starting from multiple peripheral regions, which spread to the soma rather than sweeping waves [5]. The astrocytic morphology and biophysics control the molecular diffusion from one region to another. In this case, the [Ca^{2+}] levels in an astrocytic process may increase even without neuronal inputs [9].

Compartmental Models

Global and local [Ca^{2+}] elevations in different astrocytic regions have specific spatial and temporal properties due to the complexity of the astrocytic morphology [316]. Consider, in Figure 4.4a, that the neuronal inputs in individual processes cause spatially distinct Ca^{2+} and IP_3 signals diffusing bidirectionally to the soma or other processes. Consider that the astrocytic processes and soma are separate compartments defined by their single point model with homogenized [Ca^{2+}] and where Ca2+ ions and IP_3 molecules diffuse between compartments (Figure 4.4b) [303].

Let (s) represent the soma compartment and (p_i) be the process compartment, where i is the astrocytic process number. The following system is derived from the Hill function-based Ca^{2+} dynamics of multicompartment astrocytes [303]. The variables $J_{IP3diff}$ and J_{Cadiff} are the amounts of IP_3 and Ca^{2+}, respectively, diffusing from the process, (p_i), to the soma, (s), and vice versa. Therefore, we extend the Ca^{2+} dynamics in the intracellular

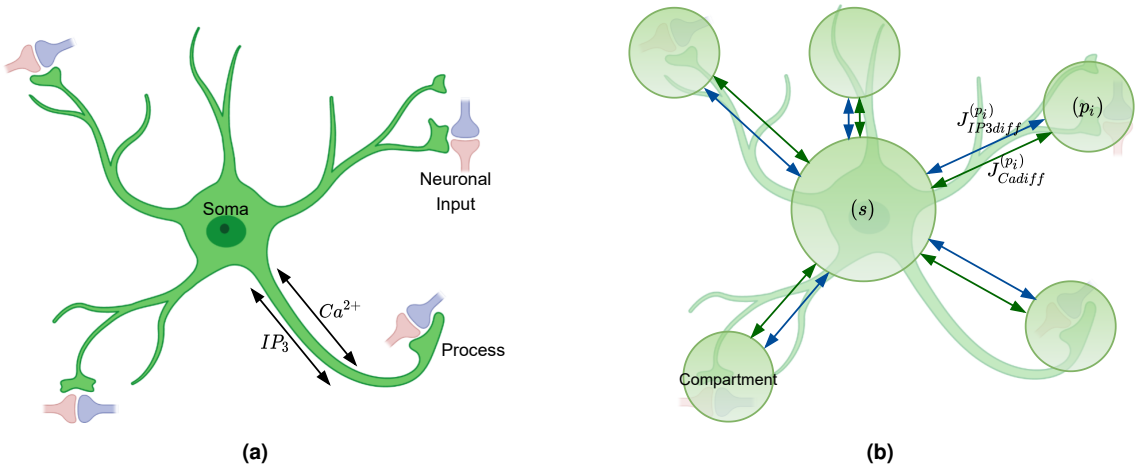

Figure 4.4: Dynamics in astrocytic compartments. (a) Calcium and IP_3 molecules diffuse from the processes to the soma to the neighboring processes bidirectionally. (b) Each astrocytic process and the soma are considered separate compartments consisting of distinct dynamics.

space, $[Ca^{2+}]_a$, into

$$\begin{aligned}\frac{d[Ca^{2+}]_a^{(p_i)}}{dt} &= J_{IP_3R}^{(p_i)} + J_{SERCA}^{(p_i)} - J_{CERleak}^{(p_i)} + J_{Cadiff}^{(p_i)},\\ \frac{d[Ca^{2+}]_a^{(s)}}{dt} &= J_{IP_3R}^{(s)} + J_{SERCA}^{(s)} - J_{CERleak}^{(s)} - \sum_{i=1}^{k} J_{Cadiff}^{(p_i)},\end{aligned} \tag{4.32}$$

where k denotes the number of compartments representing the astrocytic processes. The increase in somatic [IP_3] is independent of the synaptic input but on the Ca^{2+} diffusion. Therefore, the IP_3 dynamics in the processes and the soma become

$$\begin{aligned}\frac{d[IP_3]_a^{(p_i)}}{dt} &= J_{PLC\beta}^{(p_i)} + J_{PLC\delta}^{(p_i)} - J_{3K}^{(p_i)} - J_{5P}^{(p_i)} + J_{IP3diff}^{(p_i)},\\ \frac{d[IP_3]_a^{(s)}}{dt} &= J_{PLC\delta}^{(s)} - J_{3K}^{(s)} - J_{5P}^{(s)} - \sum_{i=1}^{k} J_{IP3diff}^{(p_i)}.\end{aligned} \tag{4.33}$$

In order to take into account the difference in volume between the processes, $V_{process}$, and the soma, V_{soma}, Cresswell et al. [303] considered the ratio

$$V_r = \frac{V_{soma}}{V_{process}} \tag{4.34}$$

Assuming that all astrocytic processes are homogeneous point processes with identical geometry, the somatic Ca^{2+} and IP_3 dynamics in the processes shown in Equation 4.32 are updated into

$$\begin{aligned}V_r\frac{d[Ca^{2+}]_a^{(s)}}{dt} &= V_{surf}\left(J_{IP_3R}^{(s)} + J_{SERCA}^{(s)} - J_{CERleak}^{(s)}\right) - \sum_{i=1}^{k} J_{Cadiff}^{(p_i)},\\ V_r\frac{d[IP_3]_a^{(s)}}{dt} &= V_{surf}\left(J_{PLC\delta}^{(s)} - J_{3K}^{(s)} - J_{5P}^{(s)}\right) - \sum_{i=1}^{k} J_{IP3diff}^{(p_i)},\end{aligned} \tag{4.35}$$

where V_{surf} is the surface volume equal to $V_r^{2/3}$ accounting for the increase in membrane area [303]. The increase in somatic volume, therefore, slows down the Ca^{2+} dynamics.

Ca^{2+} and IP_3 Diffusion

Calcium ions diffuse to the compartment of lesser concentration, from the process to the soma or vice versa, proportional to the difference between the [Ca^{2+}] of the two compartments, described by the equation

$$J_{Cadiff}^{(p_i)} = D_I \left([Ca^{2+}]_a^{(s)} - [Ca^{2+}]_a^{(p_i)} \right), \tag{4.36}$$

where D_I is the Ca^{2+} diffusion coefficient between the soma and the astrocytic process within the cytosol [303].

For short -distances, Fick's first diffusion law describes the intracellular IP_3 diffusion, such that

$$J_{IP3diff}^{(p_i)} = D_P \left([IP_3]_a^{(s)} - [IP_3]_a^{(p_i)} \right), \tag{4.37}$$

where D_P is the diffusion coefficient [300].

4.4/ GLIOTRANSMISSION

At the start of the 1900s, Jean Nageotte hypothesized that astroglials in the CNS also secrete signaling molecules, like neurotransmitters in neurons [317]. It took another one hundred years to experimentally confirm that astrocytes indeed release chemical transmitters, or **gliotransmitters**, that act as signaling mechanisms to neighboring neurons and astrocytes [318]. Thus the concept of **gliotransmission** began, substantiated by the discoveries that astrocytes sense and react to neurotransmitters, such as Glu^-, by altering their cytosolic Ca^{2+} [319, 320], and trigger astrocyte-neuron signaling via the gliotransmitter release [321]. In 1994 during the growth of Ca^{2+} imaging techniques, two separate studies by Nedergaard [321] and Parpura et al. [322] simultaneously demonstrated that Ca^{2+} dynamics in astrocytes could modify neuronal response by triggering delayed neuronal Ca^{2+} [298]. There is also a sudden increase in studies showing Ca^{2+} elevation in astrocytes as a response to downstream neurotransmitters, especially Glu^-. Astrocytes are then recognized to play active roles in neural communication [15].

Gliotransmission is the concept in which astrocytes, when activated, send signals to neighboring cells by releasing and regulating transmitters or modulators (gliotransmitters), allowing information transfer from astrocyte to neuron affecting synaptic activities [15, 275, 295, 322]. Gliotransmitters are neuroactive molecules such as Glu^-, ATP, GABA, and D-serine altering synaptic transmission and neuronal excitability [265, 275, 323]. Though neurons also release these molecules, these are called gliotransmitters based on their glial origins. There are at least two possible mechanisms of astrocytic signaling. The first is via the direct connection through gap junctions (astrocyte-astrocyte) [321]. Second is the indirect interaction utilizing astrocytic Glu^- release via Ca^{2+}-dependent exocytosis (astrocyte-neuron) [322], indicating a gliotransmission-based synaptic modulation [324].

The discovery of these interactions between neurons and astrocytes leads to the conception of the term 'synaptic triad' [325], which later became the so-called 'tripartite synapse' [4].

4.4.1/ TRIPARTITE SYNAPSE

The tripartite synapse concept describes the bidirectional signaling between neuronal synaptic elements and the astrocytic processes [299]. As the astrocytic process enwraps the synapse, it forms a third synaptic element, in addition to the two traditional elements, the presynaptic bouton and the postsynaptic spine head [318]. The neuron-dependent astrocytic excitation was first recognized in the hippocampus and cerebellum [15]. Then, most investigations on tripartite synapses were facilitated by scrutinizing the glutamatergic synapses in the hippocampal circuit, especially in the SC-CA1 region [302].

In the tripartite synapse model shown in Figure 4.5, the presynaptic neuron releases neurotransmitters into the synaptic cleft [8, 265]. Following the synaptic vesicle release, a fraction of these neurotransmitters spill over into the extrasynaptic space through passive diffusion, causing a decrease in the neurotransmitter concentration in the synaptic cleft [15, 281]. However, a high neurotransmitter concentration persisting in the extracellular space leads to prolonged activation of neuron receptors, a potentially neurotoxic effect [281]. The brain avoids this biologically toxic condition through astrocytic glutamate transporters. In effect, the neurotransmitter spill-over also facilitates the neuron-to-astrocyte information transfer [15]. The neurotransmitters diffusing into the presynaptic space bind with EAAT1 and EEAT2, whose binding rate is similar to ionotropic AMPA and NMDA receptors (i.e., $10^6 - 10^7$ M^{-1} s^{-1}) [281], and trigger the cytosolic [Ca^{2+}] elevation in the presynaptic astrocyte [8, 265]. When the intracellular [Ca^2+] increases beyond a certain threshold, neuron-dependent excitation occurs, and the astrocyte releases an additional amount of transmitters, such as Glu^- or ATP, into the extracellular space, triggering the delivery of specific messages to the neighboring cells (to neurons or even to astrocytes) through gliotransmission [8, 15, 265, 326]. These gliotransmitters can directly participate in synaptic activities by modulating the pre- and postsynaptic components.

Astrocytes in the hippocampus and the cortex show that they release Glu^-, ATP and D-serine, inducing neural excitation and inhibition modulating synaptic activity and plasticity [5, 9, 15, 302]. There are two pathways of gliotransmission relevant to synaptic modulation: astrocytic Glu^- mediation of extrasynaptic receptors at the (1) presynaptic boutons and (2) postsynaptic spines [327]. Researchers reported that the release of astrocytic Glu^- results in an increase or decrease of glutamate released from SC terminals of SC-CA1 synapses [302]. Also, in CA1 neurons, laboratory experiments where IP_3 molecules were uncaged to drive the astrocytic [Ca^{2+}] elevations exhibit increased spontaneous excitatory postsynaptic AMPA currents. These two pathways, therefore, provide feedforward and feedback interactions between the pre- and postsynaptic terminals [327]. The synaptic transmission, with the addition of the perisynaptic astrocytic process, becomes bi-directional rather than unidirectional.

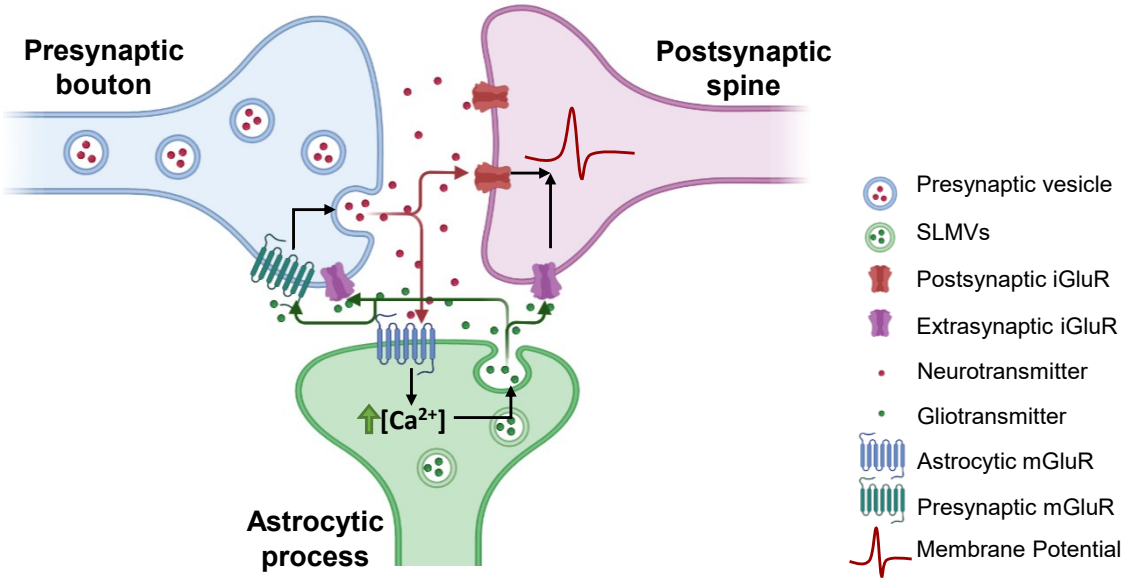

Figure 4.5: The tripartite synapse. The closed-loop interplay between the molecular and electrical dynamics in the tripartite synapse model is as follows. Upon the presynaptic vesicular release, a fraction of neurotransmitters bind with the postsynaptic ionotropic receptors (iGluRs), and the remaining fraction passively diffuses into the extrasynaptic space, binding to astrocytic metabotropic receptors (mGluRs). The binding activity triggers the production of IP_3 molecules, which then results in intracellular astrocytic $[Ca^{2+}]$ elevations. The neuron-dependent activation of the astrocyte occurs when its $[Ca^{2+}]$ exceeds a certain threshold, facilitating the release of gliotransmitters into the extracellular space. Astrocytes also consists of synaptic like microvesicles (SLMVs) containing gliotransmitters with a release mechanism similar to neurons. The released gliotransmitters diffuse in the extracellular space activating extrasynaptic iGluRs and mGlurs in the pre- and postsynaptic components. These additional transmitters (gliotransmitters) influence the synaptic vesicle release probability, indirectly modulating the synaptic activity. In addition, activation of postsynaptic iGluRs due to gliotransmitters adds to the postsynaptic potential. With this concept, information transfer becomes bidirectional rather than the unidirectional flow in the classical synapse.

4.4.2/ Gliotransmitter Release

Aside from opening anion channels, hemichannels, and ionotropic receptors on the membrane, the primary mechanism for gliotransmitter release is via the clear synaptic-like microvesicle (SLMV) release through Ca^{2+}-dependent exocytosis [15, 318, 328, 329]. This quantal release of vesicular transmitter content via exocytosis, typical with neurons discussed in subsection 3.3.1, is also observed in adult hippocampal astrocytes through fluorescence imaging. However, in contrast with vesicle-containing Glu^- from neurons, astrocytic Glu^- are not as tightly packed in SLMVs. Astrocytic SLMVs also express SNARE protein complex such as VAMP3 and transporters such as VGLUT1-3, equipping astrocytes of glutamate uptake, storage, and release. This subsection presents the models describing the gliotransmitter release process akin to the synaptic neurotransmitter release, starting from (1) the binding of Ca^{2+} ions to SLMVs for controlling the vesicular release probability, (2) the fusion of vesicles to the plasma membrane releasing a fraction of stored gliotransmitters, and finally, (3) the recycling process through endocytosis.

4.4.2.1/ GLIOTRANSMITTER RELEASE PROBABILITY

Bertram et al. [330] originally presented two-gate and four-gate neurotransmitter release processes. Then, Tewari and Majumdar [88] modified the release model and applied it to a three-gated gliotransmitter release model. In the model of Tewari and Majumdar [88], a possible gliotransmitter release occurs when three Ca^{2+} ions bind with the three independent sites ($S_1 - S_3$). Let C_a be the $[Ca^{2+}]_a$ in the release site, then

$$C_a + C_j \underset{k_j^-}{\overset{k_j^+}{\rightleftharpoons}} O_j, \quad j = 1, 2, 3 \tag{4.38}$$

where C_j denotes the closing probability of site j while O_j is the opening probability, and k_j^+ and k_j^- are the opening and closing rates of S_j, respectively. Since C_a is in μM, C_j and O_j here can be considered nondimensional and normalized $[Ca^{2+}]$ [330]. The vesicular release is a stochastic and dynamic process. The temporal evolution of the open gate O_j is a differential equation described as

$$\frac{dO_j}{dt} = k_j^+ [Ca^{2+}]_a - \left(k_j^+ [Ca^{2+}]_a + k_j^-\right) O_j. \tag{4.39}$$

Here, the opening (in μM^{-1} ms^{-1}) and closing rates (in ms^{-1}) are $k_1^+ = 3.7 \times 10^{-3}$ and $k_1^- = 4 \times 10^4$ for S_1, $k_2^+ = 2.5 \times 10^{-3}$ and $k_2^- = 1 \times 10^{-3}$ for S_2, and $k_3^+ = 1.25 \times 10^{-2}$ and $k_3^- = 10 \times 10^{-3}$ for S_3, respectively. The dissociation constants for gates S_1 to S_3 are 108 nM, 400 nM, and 800 nM. The time constants for gate closure ($1/k_j^-$) are 2500 ms, 1000 ms, and 100 ms. Then, the fraction of SLMVs ready for release, f_r^a, depends on the opening probabilities of the three sites and is given as

$$f_r^a = O_1 \cdot O_2 \cdot O_3. \tag{4.40}$$

4.4.2.2/ FUSION AND RECYCLING PROCESS

The fusion and recycling process of SLMVs is given by the system

$$\begin{aligned} \frac{dR_a}{dt} &= \frac{I_a}{\tau_{rec}^a} - \Theta\left([Ca^{2+}]_a - [Ca^{2+}]_a^{thresh}\right) f_r^a R_a, \\ \frac{dE_a}{dt} &= -\frac{E_a}{\tau_{inact}^a} + \Theta\left([Ca^{2+}]_a - [Ca^{2+}]_a^{thresh}\right) f_r^a R_a, \\ I_a &= 1 - R_a - E_a. \end{aligned} \tag{4.41}$$

where R_a is the fraction of readily releasable SLMVs inside the astrocytic process, E_a is the fraction of effective SLMVs in the extrasynaptic cleft, and I_a is the fraction of SLMVs undergoing endocytosis or re-acidification [88]. Θ is a Heaviside function with the threshold for release site activation equal to $[Ca^{2+}]_{thresh}$. The parameters τ_{inact}^a and τ_{rec}^a, respectively, are the time constants of inactivation and recovery of SLMVs.

De Pitta and Brunel [178] presented a deterministic approach of determining the fraction of released gliotransmitters based directly on the supply of $[Ca^{2+}]_a$ at any time t solely

rather than with the kinetics of Ca^{2+} binding to the SLMV. Considering that at time t_j, the $[Ca^{2+}]_a$ exceeds the $[Ca^{2+}]_a^{thresh}$, the astrocyte releases a fraction of gliotransmitters into the extrasynaptic space, $r_A(t)$, from the pool of readily available for release gliotransmitter resources, $x_A(t)$. The temporal evolution of $x_A(t)$ is defined by the set of equations

$$\begin{aligned} \tau_G \frac{dx_A}{dt} &= 1 - x_A - \sum_j r_A(t)\delta(t - t_j)\tau_G, \\ r_A(t) &= U_A x_A(t_j^-), \end{aligned} \tag{4.42}$$

where $\delta(\cdot)$ is a Delta function, τ_G is the Glu^- recycling time constant, and U_A is the resting Glu^- release probability ($0 < U_A < 0.9$). The residual Glu^- during recycling is reintegrated at a rate equal to $1/\tau_A$ (see Equation 4.6).

The astrocytic vesicular release is slow, attributable to the slow astrocytic Ca^{2+} dynamics, with an exocytosis rate of at least two orders of magnitude slower than in neurons [318, 331]. However, a small $[Ca^{2+}]_a$ increase of approximately 100 nM from the resting level is sufficient to induce gliotransmitter release [332].

4.4.2.3/ Extrasynaptic Glutamate Dynamics

The extrasynaptic Glu^- concentration, $[Glu^-]_a$, is governed by

$$\frac{d[Glu^-]_a}{dt} = n_a^v g_a^v E_a - g_a^c [Glu^-]_a, \tag{4.43}$$

where n_a^v is the number readily releasable pool of SLMVs, g_a^v is the $[Glu^-]$ within each SLMV, and g_a^c is the $[Glu^-]$ clearance rate due to diffusion and re-uptake by the perisynaptic astrocyte [88]. In their tripartite model, Tewari and Majumdar [88] assumed that there are 12 SLMV in the astrocyte and individual SLMV holds 20mM of Glu^-.

Also, De Pitta and Brunel [178] estimated the timecourse of extrasynaptic Glu^- as

$$\begin{aligned} \tau_e \frac{d[Glu^-]_a}{dt} &= -[Glu^-]_a + \sum_j G_{rel}(t)\delta(t - t_j)\tau_e, \\ G_{rel}(t_j) &= \varrho_e G_T r_A(t_j). \end{aligned} \tag{4.44}$$

At $t = t_j$, a quantal release event transpires, releasing Glu^- into the extrasynaptic space represented by G_{rel}, dependent on the total vesicular $[Glu^-]$, G_T, and the ratio between the volumes of the astrocytic vesicle and the extrasynaptic space, ϱ_e, with a clearance rate of $1/\tau_e$.

For nondimensional models such as the Postnov model [312], astrocytic Glu^- released depends directly on the intracellular astrocytic $[Ca^{2+}]$. Let G_m be the released astrocytic Glu^- mediator,

$$\tau_{G_m} \frac{dG_m}{dt} = (1 + \tanh(S_{G_m}(c - h_{G_m})))(1 - G_m) - \frac{G_m}{d_{G_m}}. \tag{4.45}$$

where the time constant τ_{G_m} is five times the synaptic variable time constant, τ_s (Equation 4.23). Note that the variable c is the dimensionless representation of the astrocytic $[Ca^{2+}]$, and h_{G_m} and d_{G_m} are control parameters.

4.4.3/ Synaptic Influence

Imaging studies of brain slices reported that astrocytic morphology changes spontaneously, revealing that the neuron-astrocyte interaction is also plastic [15, 298]. This subsection deals with the contribution of astrocytes in synaptic plasticity. First is its indirect control on the neurotransmitter release probability of the presynaptic neuron, and second is its modulating effect on the postsynaptic potential. By bidirectionally modulating both the pre- and the postsynaptic activities, astrocytes emerge as a computational unit rather than simple structural support.

4.4.3.1/ Synaptic Release Probability

Astrocytic Glu^- activates mGluRs located on the extrasynaptic membrane of presynaptic boutons, as shown *in situ* experiments at hippocampal synapses. In turn, extrasynaptic Glu^- is used as an input for PLCβ-mediated IP_3 production in the presynaptic neuron (see Equation 4.5) [88]. The increase of IP_3 production facilitates and modulates the neurotransmitter release probability lasting for tens of minutes [333], hinting that astrocytes can mediate long-term synaptic plasticity.

Below is a simpler model for neurotransmitter release probability, wherein the extracellular Glu^- binds with a fraction of extrasynaptically bound presynaptic receptors (γ_S), modulating the synaptic release probability u_0 [178]. Let

$$\tau_P \frac{d\gamma_S}{dt} = -\gamma_S + O_P\,(1-\gamma_S)\,[Glu^-]_a \tau_P, \tag{4.46}$$

where O_P and τ_P are the rising rate and the decay time of synaptic Glu^- release due to gliotransmission. Then, γ_S-dependent u_0 follows

$$u_0(\gamma_S) \approx U_0 + (\xi - U_0)\gamma_S, \tag{4.47}$$

where U_0 is the release probability at rest and $0 \leq \xi < U_0$, which represents the influence of gliotransmission to the delivered information.

4.4.3.2/ Slow Inward Current

Experiments use the whole-cell patch technique with selective astrocytic stimulation in parallel with EPSPs or IPSPs recordings to determine the impact of astrocytes in neural activity [298]. These experiments reveal that astrocytic Ca^{2+} triggers an increase in EPSP or IPSP frequencies or postsynaptic potential amplitudes [8, 298], detected by monitoring slow inward currents (SICs) activated by NMDARs containing subunit 2B (NR2B) [333–335]. These currents are kinetically distinct from EPSCs due to their large amplitude (19-477 pA), and slower rise (13–332 ms), and decay (72–1630 ms) time [15, 335–337].

The $[Glu^-]_a$-evoked SICs is modeled as

$$\begin{aligned} I_{SIC} &= g_{NR2B} h_{SIC} v_{post}, \\ \frac{dh_{SIC}}{dt} &= \frac{\sigma_a}{\tau_{SIC_1}} - \frac{h_{SIC}}{\tau_{SIC_2}}, \end{aligned} \tag{4.48}$$

where g_{NR2B} is the NR2B-containing receptor conductance, h_{SIC} is the extrasynaptic NMDAR gating variable, and v_{post} is the membrane potential of the postsynaptic spine [338]. Here, parameter σ_a regulates the gate opening dependent on Ca^{2+} activity of the astrocyte, where $\sigma_a = 0.4$ when $[Ca^{2+}]_a$ crosses its threshold and $\sigma_a = 0$ otherwise. The time constants τ_{SIC_1} and τ_{SIC_2} are the rise and decay times, respectively, of the extrasynaptic NMDARs, respectively.

De Pitta and Brunel [178] also presented SIC ($i_A(t)$) independent of the postsynaptic potential by an exponential difference given as

$$\begin{aligned} \tau_S^r \frac{di_A(t)}{dt} &= -i_A(t) + \hat{I}_A B_A(t) \tau_S^r, \\ \tau_S \frac{dB_A(t)}{dt} &= -B_A(t) + \hat{J}_A [Glu^-]_a \tau_S, \\ \hat{J}_A &= \frac{J_A}{\varrho_e G_T \tau_S}, \\ \hat{I}_A &= \frac{I_A((1/\tau_S) - (1/\tau_S^r))}{(\tau_S^r/\tau_S)^{(\tau_N/(\tau_N - \tau_S^r))} - (\tau_S^r/\tau_S)^{(\tau_S^r/(\tau_S - \tau_S^r))}}, \end{aligned} \tag{4.49}$$

where the parameters τ_S^r and τ_S are the rise and decay time constants of SICs. Here, $\hat{I}_A$ and $\hat{J}$ are scaling factors set so that SIC is maximum (equal to a constant value I_A) during astrocytic Glu^- release. Furthermore, J_A is the synaptic efficacy, and τ_N is the EPSC decay time constant.

4.5/ Calcium Wave Propagation

In the 1990s, laboratory experiments using cultured astrocytes demonstrated that astrocytes respond to stimuli by increasing their intracellular $[Ca^{2+}]$, which diffuse through the cell itself and then propagate through the astrocyte syncytium [9, 302, 319, 320]. From these results, researchers deduced that astrocytes could serve as a mechanism for long-distance information transfer, and their astrocytic Ca^{2+} events also convey information about local brain activity. As discussed in subsection 4.3.2, an astrocytic cell also exhibits Ca^{2+} oscillations in separate local and global regions. These Ca^{2+} responses may be (1) confined from distal processes, (2) within the single astrocytic cell, or (3) propagate to neighboring astrocytes, whose activities may also occur in the absence of neuronal signals [9, 15].

The continuous and gradual propagation of Ca^{2+} within the complex astrocytic network that causes a change in the intracellular $[Ca^{2+}]$ in a single or a group of astrocytes brought about by the calcium signals from the neighboring astrocytes forms the so-called **intercellular calcium waves** (ICWs) (see Figure 4.6) [300]. These ICWs propagate from one astrocyte to another in a coordinated manner and increase Ca^{2+} within the astrocytic net-

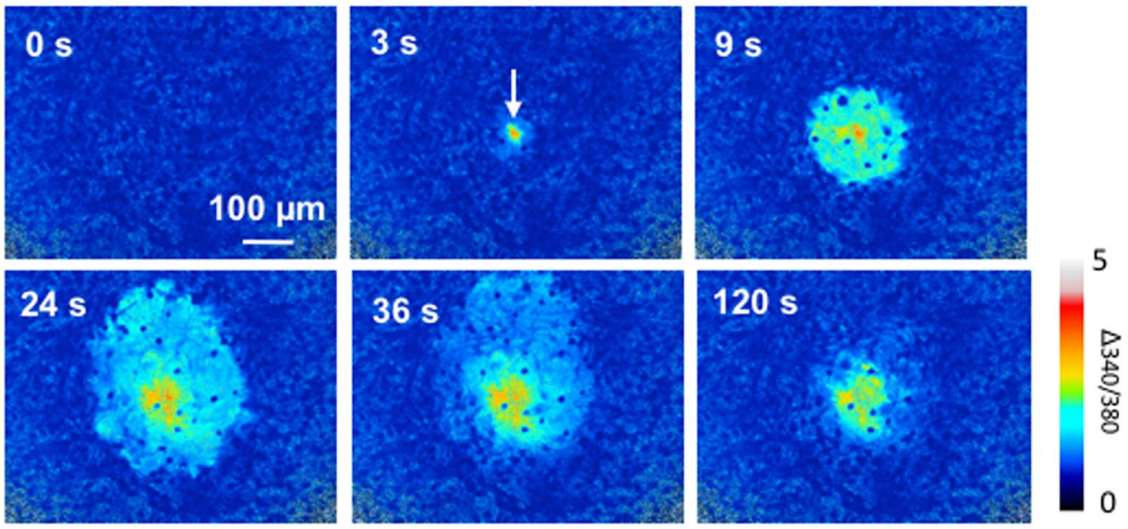

Figure 4.6: Astrocytic Ca^{2+} wave propagation from 0, 3, 9, 24, 36, and 120 seconds after mechanical stimulation (arrow), measured using Fura2 calcium indicator. The image was taken from Fuji et al. [339].

work, typically around 20-80 cells across a 200- to 600-mm-wide field, consistent with *in vivo* preparations [265, 298]. One of the main differences between neuronal and astrocytic signaling is their temporal scales, while AP-mediated conductance between neurons has a velocity of 10-100 m/s, astrocytic Ca^{2+} waves propagate at 4-20 m/s [8].

In this subsection, we illustrate the primary mechanism for ICW propagation between protoplasmic astrocytes, that is, via the gap junction. Through these gap junction connections (GJC), astrocytes can form a network and facilitate long-distance information transfer.

4.5.1/ Gap Junction Connection

The gap junction connections are the primary mechanism in which Ca^{2+} waves propagate between neighboring protoplasmic astrocytes in the gray matter [9, 271]. One of the main differences between astrocytes and neurons is that astrocytes are physically attached through connexin 43 hemichannels in their peripheral branches, allowing them to create a functional syncytium [9, 300, 307]. When these hemichannels are in the closed state, they are permeable to ions and small molecules; otherwise, when in the open state, they enable the passage of large hydrophilic solutes [15].

There are two experimentally verified routes for Ca^{2+} wave propagation, either via intracellular or extracellular diffusion [15]. First is the ICW propagation, mentioned previously and illustrated in Figure 4.7, involving the cell-to-cell diffusion of IP3 molecules through GJCs [340]. The IP_3 transport triggers the CICR mechanism of the coupled astrocytes, in turn triggering Ca^{2+} waves [265]. The second is through ATP release to the extracellular space [341]. In this study, we only consider the ICW as the fundamental mechanism for astrocytic communication.

Astrocytic Ca^{2+} propagation occurs in various modes, which can be spontaneous or

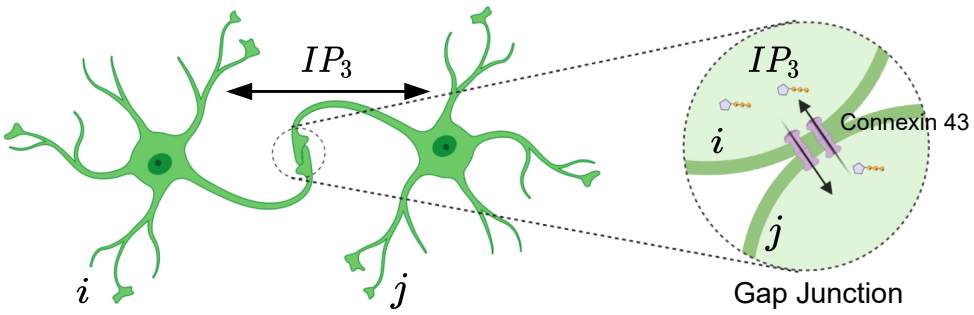

Figure 4.7: Intracellular communication between two coupled astrocytes i and j occurs via the exchange of IP_3 molecules through gap junction connections (GJCs) in the peripheries. Connexin 43 hemichannels physically connect the two astrocytes and facilitate the IP_3 diffusion between the two cells.

evoked and restricted to a small astrocytic network or within a hundred cells. Therefore, the actual operation in which Ca^{2+} spread is still vague. In its simplest form, IP_3 diffusion through GJCs can be modeled directly by the $[Ca^{2+}]$ gradient between the coupled astrocytes, comparable with the diffusion mechanism between compartments in a single astrocyte (Equation 4.37). Considering the astrocytes in Figure 4.7, let i be the astrocyte couple with astrocyte j. Then the exchange of IP_3 molecules between the two is modeled by

$$J_{ij} = D_{ij}\left([IP_3]_i - [IP_3]_j\right), \tag{4.50}$$

a linear relationship wherein D_{ij} is the diffusion coefficient [300].

In another case, to ensure that the intracellular supply of IP_3 within a single astrocyte will not deplete during gap junction communication, IP_3 diffusion between the coupled astrocytes can be modeled by a threshold-based function [342]. The IP_3 flux is

$$J_{ij} = -\frac{F_{ij}}{2}\left(1 + \tanh\left(\frac{|\,\Delta_{ij}I\,| - I_\theta}{\omega_{IP_3}}\right)\right)\frac{\Delta_{ij}I}{|\,\Delta_{ij}I\,|}, \tag{4.51}$$

where $\Delta_{ij}I$ is the astrocytic $[IP_3]$ gradient between astrocytes i and j, I_θ is the threshold gradient that triggers IP_3 diffusion, ω_I scales the rate in which J_{ij} decreases or increases in relative with $\Delta_{ij}I$, and F_{ij} establishes the maximum magnitude of J_{ij}.

4.5.2/ Astrocytic Networks

In the hippocampus, astrocytes exhibit heterogeneous coupling and network configuration (Figure 4.8) through GJCs [10], building dynamic communication between astrocytes as a response to various membrane receptor activation by extracellular Glu^- [271]. The anatomical domains of individual astrocytes cover non-overlapping or discrete territories accommodating local interactions with synapses and other astrocytes [15, 265]. Because of their separate territories, astrocytes appear to be interstitial, filling and tiling spaces between other cells [300]. Wallach et al. [10] provided an immunostaining image (see Figure 4.8a) of a cortical astrocytic network showing cells with exclusive territories and forming a lattice. This arrangement of astrocytes was also seen in fluorescent dyes of hippocampal astrocytes [15] and 3D confocal analysis and electron microscopy of protoplasmic astrocytes in the CA1 stratum radiatum shown in Figure 4.8b [273].

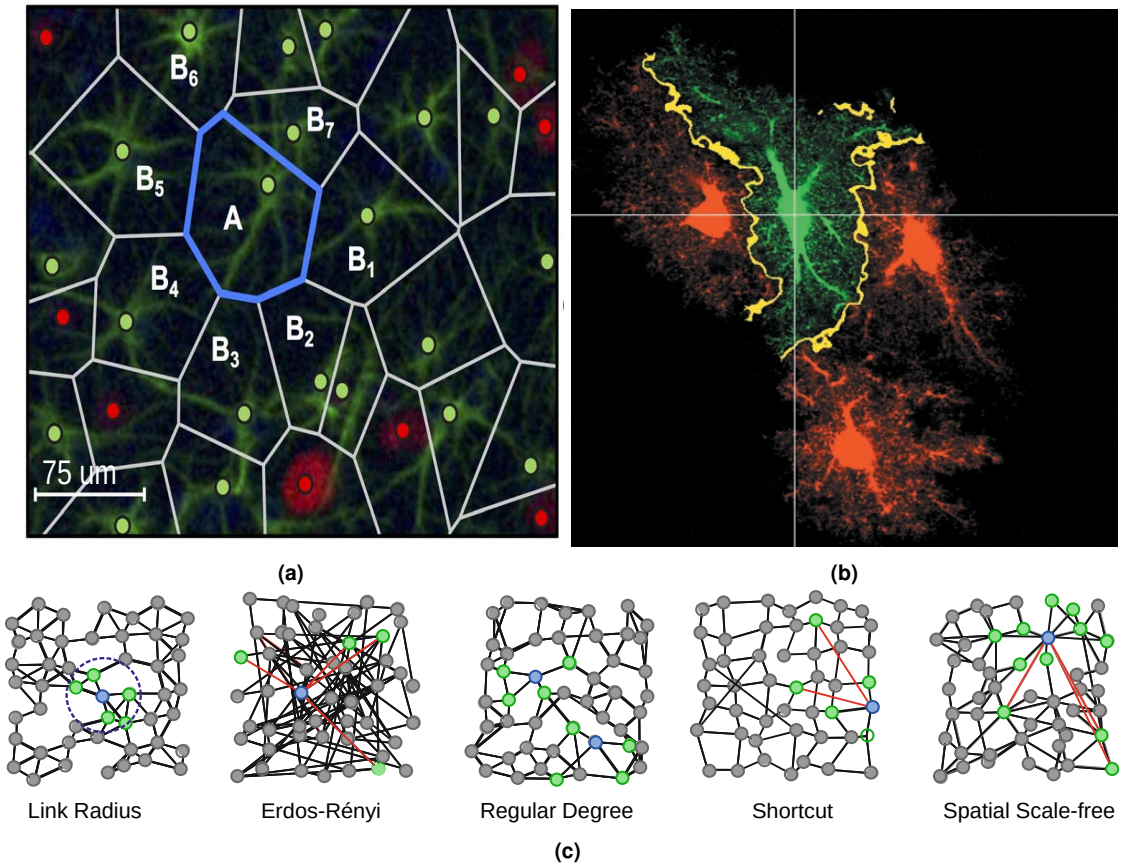

Figure 4.8: The anatomical domains of astrocytes form non-overlapping territories. (a) Wallach et al. [10] used the Voronoi tessellation to identify the extent of each astrocytic territory (*gray* and *blue* lines) on an immunostaining image composed of the astrocytes (green) and neurons (red) network. Here, astrocyte *A* is coupled to its neighboring astrocytes B_1 to B_7 through GJCs. (b) Confocal analysis of adjacent astrocytes in the CA1 region shows discrete regions of interaction (*yellow*) between astrocytic processes [273]. Models of Ca^{2+} wave diffusion can be visualized by simulating astrocytes connected in various topologies [300, 343]. An astrocyte under consideration (*blue*) connects to its neighboring neurons (*green*) within its boundary (*Link Radius*), any cell within the network (*Erdős*-Rényi), its nearest neighbors (*Regular Degree*), its nearest neighbors and random cells (*Shortcut*), and cells relative to its degree and distance (*Spatial scale-free*).

Network Topology

Astrocytes tile the brain spaces, and their network organization is diverse due to their heterogeneous morphology, flexible gap junction coupling, and the brain region [271, 340]. Houades et al. [344, 345] discovered that in the hippocampal stratum radiatum, astrocytes form a circular network; that is spherical in three-dimensional form. On the other hand, astrocytes positioned near the pyramidal cells layer form a somewhat elongated network parallel to the pyramidal layer.

One can develop a model of ICW with one- to three-dimensional astrocytic topologies, as shown by Lallouette et al. [300, 343]. One-dimensional astrocytic networks form cells connected in series or chains. For more intricate astrocytic connection in space shown in Figure 4.8c, the astrocytic organization can be:

1. strongly spatially constrained networks where an astrocyte attaches to all its neigh-

boring astrocytes within a specified radial constraint (e.g., *link-radius networks*),
2. completely spatially unconstrained random networks where an astrocyte connects to an arbitrary number of cells anywhere in the network, regardless of their distance (e.g., *Erdős-Rényi* network),
3. regular-degree network wherein the astrocyte connects to its k nearest neighbors,
4. shortcut networks originating from regular-degree networks with cell connections randomly rearranged independently of distance, and
5. spatial scale-free networks whose astrocytic connections follow a power-law distribution relative to the cell degree and distance.

General Framework

Each astrocyte in the network is a node whose somatic activation allows ICWs to jump from one cell to another through links of gap-junction [300]. Let i be an astrocyte in the network connected to a set of neighboring astrocytes $\aleph$. Its activity is modeled using the generic two-state vectors

$$\begin{aligned} \frac{d\mathbf{a_i}}{dt} &= \mathbf{F_i}\left(\mathbf{a_i}, \mathbf{s_i}\right) + \mathbf{D_i^a}\left(\mathbf{a_i}, \mathbf{a_j}, \mathbf{s} \mid \mathbf{j} \in \aleph_\mathbf{i}\right) \\ \frac{d\mathbf{s_i}}{dt} &= \mathbf{G_i}\left(\mathbf{a_i}, \mathbf{a_j}\right) + \mathbf{D_i^s}\left(\mathbf{s_i}, \mathbf{s_j}, \mathbf{a} \mid \mathbf{j} \in \aleph_\mathbf{i}\right), \end{aligned} \tag{4.52}$$

where $\mathbf{a}$ lumps the astrocytic $[Ca^{2+}]_i$, and $\mathbf{s}$ represents the Ca^{2+}-mobilizing signals responsible for regenerative Ca^{2+} propagation. The vector function $\mathbf{F_i}$ may also incorporate other components such as $[Ca^{2+}]$ of the ER and channel dynamics. Meanwhile, $\mathbf{G_i}$ corresponds to the second-messenger functions required in regulating $[Ca^{2+}]_i$. The constant terms D_i^a and D_i^s correspond to the chemical exchange between astrocyte i and its neighbors $j \in \aleph$.

4.5.3/ UAR Model

Lallouette et al. [300, 343] introduced a method of modeling calcium wave propagation in astrocytic networks, where astrocytes are considered nodes and GJCs are links. Lenk et al. [346] also utilized the discrete method for modeling Hill-functions-based astrocytic networks. The UAR model states that the probability that an astrocyte triggers Ca^{2+} wave propagation to neighboring astrocytes, or vice versa, depends on the state of the astrocyte S_a: $\mathbf{U}$ for the inactive or dormant state where the astrocyte is at rest (the dynamics of IP_3 and Ca^{2+} are in the subthreshold regions), $\mathbf{A}$ for the active state, and $\mathbf{R}$ for the refractory state during which the astrocyte cannot transmit Ca^{2+} signals. An astrocyte can be in one of these states at a time, and transitions between states are probabilistic depending on the propagation efficiency of coupled astrocytes.

Consider the coupled cells shown in Figure 4.9. From the biophysical perspective, the increase of $[IP_3]$ beyond threshold activates CICR resulting in a large Ca2+ spike ($\mathbf{U} \rightarrow \mathbf{A}$). The cell stays in the active state during the duration that the IP_3 flux coming into the cell via GJCs is sufficient to retain the CICR above the threshold. The cell deactivates and stays in the refractory state ($\mathbf{A} \rightarrow \mathbf{R}$) when the $[IP_3]$ and $[Ca^{2+}]$ drop below the threshold.

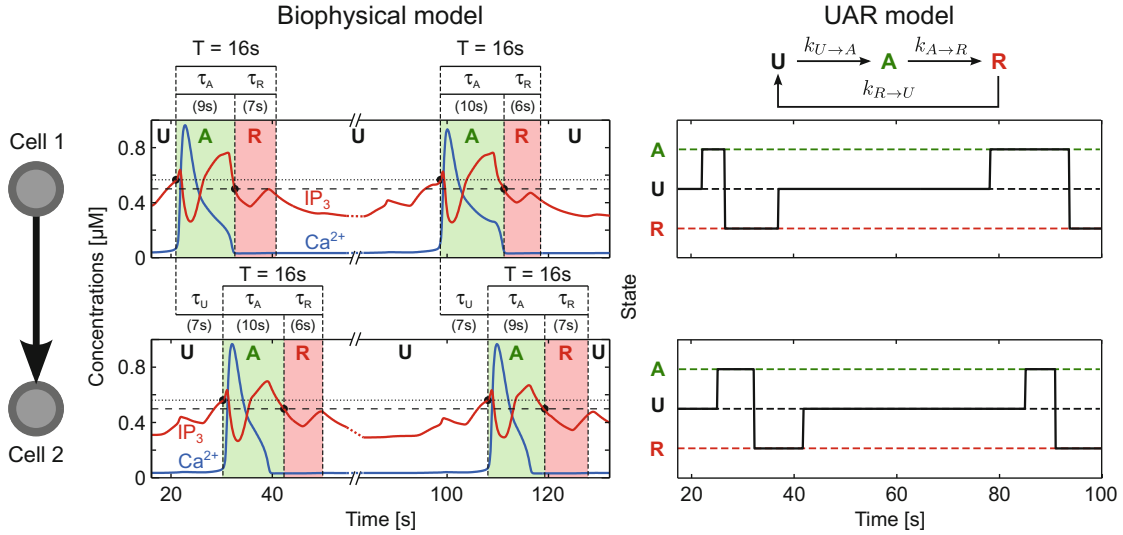

Figure 4.9: The UAR model [300, 343] describes the activity of an astrocyte during ICW propagation. Consider the coupled cells 1 and 2. During the **U** state, both cells perform in the subthreshold regions. Then, as Cell 1 gets activated, with simultaneous Ca^{2+} spiking, during the transition of $[IP_3]$ level beyond the threshold (*dotted lines*), it can supply Cell 2 with IP_3 via their GJC, which results in the activation of Cell 2. When both cells are in the **A** state, both cells are able to supply IP_3 to each other depending on the $[IP_3]$ gradient between the two cells. Once the $[IP_3]$ decreases below the threshold (*dashed lines*) at the same period that the $[Ca^{2+}]$ is in subthreshold level, the astrocyte becomes inactive and stays in the **R** state for some period. This activity is a continuous cycle and restarts when $[IP_3]$ goes beyond the threshold once again. The image was adapted from Lalloutte et al. [300].

The cycle repeats (from **U** to **A** to **R** and back to **U**) when both cells recover to their resting values.

Starting from the inactive state **U**, the rate of transition from inactive to active ($k_{\mathbf{U}\to\mathbf{A}}$) states also depends on the activities of the neighboring cells. The propagation efficacy or the ability of an astrocyte to supply IP_3 to neighboring cells is given as

$$\beta_a(t) = \begin{cases} 1/N_a^U(t) & \text{if } a \text{ is in the A state at time } t \\ 0 & \text{otherwise} \end{cases}. \tag{4.53}$$

Here, $N_a^U(t)$ is the number of astrocytes coupled to a that are not in the active state at time t. Then, the activation propensity of astrocyte a is computed using

$$\gamma_a(t) = \theta_a \sum_{b \in N_a} \beta_b(t_k) + \frac{\sum [Ca^{2+}]_{ija}}{N} \cdot M, \tag{4.54}$$

where $N(a)$ is the set of astrocytes connected to a and θ_a is the astrocyte activation threshold. The first term of the right-hand side is the dependency of activation propensity on the propagation efficiency of the neighboring astrocytes b, and the second term is the average $[Ca^{2+}]$ of local areas ija of astrocyte a. These local areas are the number of perisynaptic astrocytes forming excitatory connections with neurons (N is the number of excitatory connections) and then scaled by a factor M for their contribution to the activation propensity. The state of astrocyte a changes from **U** to **A** once the activation propensity is above the threshold θ_a. This threshold changes based on the number of neighboring astrocytes gap junction couples to astrocyte a and follows a linear relation

given by

$$\theta_a(n_a) = b_0 n_a + b_1, \tag{4.55}$$

where b_0 and b_1 are the slope and intercept of activation threshold. Therefore, the probability that the astrocytic state shifts from inactive to active state $k_{U\to A}$ at time t is

$$k_{U\to A}(t) = \begin{cases} 1/\bar{\tau}_U & \text{if } \gamma_a(t) > \theta_a(n_a) \\ 0 & \text{otherwise} \end{cases}, \tag{4.56}$$

which states that the astrocyte becomes active only if the accumulative IP_3 through GJCs exceeds the threshold of activation θ_a, where $\bar{\tau}_U$ is the activation transition.

The transition of astrocyte a from active to refractory ($\mathbf{A} \to \mathbf{R}$) and from refractory back to the inactive state ($\mathbf{R} \to \mathbf{A}$) is spontaneous, where

$$\begin{aligned} k_{(A\to R)} &= 1/\bar{\tau}_A, \\ k(R \to U) &= 1/\bar{\tau}_R, \end{aligned} \tag{4.57}$$

where the parameters $\bar{\tau}_A$ and $\bar{\tau}_R$ are the average time in which the astrocyte is active during ICW and the average refractory period, respectively.

4.6/ Conclusion

After decades of studies on the biophysical properties and functions of astrocytes, our perspective on astrocytes becomes expansive than ever, from a single passive cell whose primary function is structural support into a more complex cell for intercellular communication. In this chapter, we dealt with the functional characteristics of astrocytes, from their complex morphology, intracellular dynamics, to its ability to form networks through gap junctions and even through tripartite synaptic couplings. The morphological complexity of astrocytes, and more recent discoveries, its Ca^{2+}-dependent excitability, put astrocytes in a vital position in neural signaling.

In the tripartite synapse concept, an astrocyte is considered as the third active component for neural information processing. It integrates synaptic signals which activate receptors and trigger IP_3 and Ca^{2+} activities on its processes. In return, it controls the synaptic transmission by modulating either or both the pre- and postsynaptic activities, thus influencing short- and long-term synaptic plasticity, and ultimately, a broader network activity. Given that the presence of astrocytic processes results in larger synapses, tripartite synapses may function differently than those with synaptic coupling alone. One difference is that synaptic communications become bidirectional with astrocytes due to the lateral astrocyte regulation of synaptic signals. In addition, because an astrocyte enwraps thousands of synapses from separate neurons, it serves as a bridge communication between neurons without direct neuronal connectivity. This type of connection expands the astrocytic influence. It provides additional pathways for neuronal such as the intracellular Ca^{2+} signaling resulting in gliotransmission.

Furthermore, astrocytic influence is not confined within the synaptic areas alone — astrocytes, like neurons, form computational compartments. Different regions of astrocytes

exhibit transient and local Ca^{2+} activities, allow IP_3 and Ca^{2+} diffusion between neighboring compartments, and communicate with neighboring astrocytes through IP_3 exchange via gap junctions. These morphological connections enable Ca^{2+} wave propagation within a group of astrocytes or a more extensive network. However, the heterogeneity in astrocytic connections and the expression of GJCs still need further investigation; therefore, the exact mechanisms and the exact influence of ICW propagation in neuronal processing are still unclear.

With the ability of astrocytes to form a syncytium, neuron-astrocyte signaling is not only synapse- or cell-specific but also develops into a broader circuit-specific activity. What are the implications of these complexities on our understanding of neuronal signaling and neural network dynamics? If astrocytes can therefore influence the neuronal AP generation, how then can they affect network dynamics? In the following chapter, we delve into the neuron-astrocyte interaction by modeling tripartite synapse-specific activities and then expanding it into a small neuron-astrocyte network intercellular communication.

I

CONTRIBUTIONS

5

Modeling the Neuron-Astrocyte Interactions

5.1/ Introduction

In the hippocampus, the complex interconnections of neuronal elements control brain activities crucial for cognition and storage and memory functions by generating, modulating, and combining intrinsic and extrinsic signals nonlinearly. In Chapter 2 and Chapter 3, we discussed the information transfer between neurons via synaptic connections. A pyramidal neuron integrates the incoming signals, and upon reaching a certain threshold, generates an AP. It then encodes information into the spiking frequency and patterns of repetitive firing of the output signal, which is then sent to different brain regions through neuronal networks for signal processing and response generation. Recently, researchers hypothesized that hippocampal astrocytes impact contextual memory, especially in the CA1 region [338, 347]. As discussed in Chapter 4, astrocytes, though electrically passive, can influence synaptic transmission by sensing presynaptic activities and modulating extrasynaptic Glu^{-} which activates pre- and postsynaptic receptors. In this case, astrocytes play an active role in neuronal excitability and synaptic plasticity.

Even with experimental and computational studies, however, a coherent view on the functions of astrocytes in neuronal processes, apart from being structural and metabolic supports, is still lacking. One of the main reasons is the complex astrocytic morphology that spreads radially and creates myriads of leaflet processes throughout maturation [348, 349]. The influence of intracellular Ca^{2+} dynamics in the astrocytic processes on the synaptic transmission depends on the percentage of enwrapped synaptic volume and the size of the astrocytic processes. In addition, neuron-astrocyte interaction is not only constricted in the synaptic areas. Astrocytes also sense extracellular Glu^{-} from nonsynaptic sources [350] such as the neuronal bodies and nodes of Ranvier because an axon, as it bifurcates, can pass through several astrocytic domains [351]. As mentioned previously, neuron-astrocyte signaling is not only cell- or synapse-specific but circuit-specific as well. An inactive synapse can still be stimulated even in the absence of presynaptic inputs. Intracellular Ca^{2+} wave propagation activates astrocytic microdomains and allows the release of extrasynaptic Glu^{-} to inactive synapses, which triggers the opening of pre- and postsynaptic mGluRs. Consequently, the extent of astrocytic influence is more than a point process.

In this chapter, we focus on the computational models of the neuron-astrocyte intercommunications based on physiological processes. Here, we implement a bottom-up strategy: studying the electrical dynamics and molecular interplay between the tripartite synapse components, extending the model to incorporate the transient and localized astrocytic Ca^{2+} dynamics in a single astrocyte, and lastly, further expanding the interactions by modeling the Ca^{2+} wave diffusion in a small neuron-astrocyte network.

5.2/ Modeling the Tripartite Synapse Dynamics

With their sponge-like morphology, protoplasmic astrocytes in the gray matter establish non-overlapping and exclusive three-dimensional domain within their neuropilar volume [273, 348, 349, 352]. Three-dimensional confocal analysis and electron microscopy showed protoplasmic astrocytes in rat CA1 stratum radiatum form almost a spherical territory. In the human brain, the polyhedral domains of protoplasmic astrocytes are arranged repeatedly and uniformly in a 3D manner [351]. Within a single territory, an astrocyte can influence an average of four neurons, enveloping thousands of neuronal structures, including the neuronal soma, dendrites, synapse, and axons [273, 275, 349, 353]. According to Debanne and Rama [353], the spherical volume of an astrocyte in the hippocampus has an approximate diameter of 40 mm, suggesting that it can affect a population of axons. Furthermore, an axon, as it bifurcates, can pass through several astrocytic territories [351]. These imply that information transfer is not constrained within the synaptic area but occurs with all cellular elements within the astrocytic domain.

Through stimulations on ex vivo systems of CA3 pyramidal neurons of hippocampal slice cultures, Sasaki et al. [354] investigated the effects of Ca2+ uncaging of perinodal astrocytes near the unmyelinated axon (150 to 400 μm from the initial segment) on synaptic efficacy. However, physical evidence of direct contact between the node of Ranvier and the protoplasmic astrocyte is still lacking. Nonetheless, given that the soma and the unmyelinated axon release Glu^- and that the expression of astrocytic mGluRs varies, Glu^- released from these cellular elements may reach astrocytic compartments in proximity [355], thus influencing synaptic transmission. Besides, the morphological heterogeneity of astrocytes plays an active role in neuron-astrocyte interaction [356]. Studies suggest that leaflet processes extend towards the location with high glutamate concentration ($[Glu^-]$), predominantly in the synaptic area [357]. Since leaflets are fine processes that are not easily captured by light microscopy [267], it is possible that these processes are not only in contact with synapses but may also contact other neuronal elements where Glu- release occurs.

Numerous investigations concerning the role of astrocytes in neuronal activity have already been published [178, 307]. Manninen et al. [306, 307] collected, compared, and presented in their literature reviews the computational models of biologically-based astrocyte and neuron-astrocyte Ca2+ signaling and dynamics in single cells or networks. However, the gathered models only incorporate astrocytes, neuron-astrocyte synapses, and neuron-astrocyte networks, but none regarding nonsynaptic neuron-astrocyte signaling. Astrocytes can sense signals from nonsynaptic neuronal localities due to extrasynaptic transmission, the flow of transmitters released from the soma, axon, and dendrites occurring through exocytosis or spillover even in the absence of a postsynaptic counter-

part [350]. For example, localized receptors in the perinodal astrocytic area receive Glu-released from the neuronal nodes of Ranvier [358].

Given these current discoveries regarding astrocytic dynamics, it is about time to include such an astrocytic process in the tripartite synapse and synaptic information processing model. This section focuses on the molecular exchange that regulates transmission in a closed-loop system comprising the pre- and postsynaptic neurons and astrocyte. Our goal is to present the neuron astrocyte interaction as biologically plausible as possible and compare its dynamics with a system containing synaptic coupling alone [359]. The model presented by Tewari and Majumdar [88] described the biological processes in detail; with that, we used this as the basis of our study, along with other studies [158, 160, 360]. In their model, the AP originates from the AIS and reaches the presynaptic bouton without delay and voltage change. Also, their model focuses on the Ca^{2+} dynamics within the tripartite synapse domain. Hence, we extended their model and incorporated nonsynaptic neuronal and astrocytic elements that may also affect intracellular Ca^{2+} dynamics. Here, the extended model includes compartmentalization of cellular processes, and by doing so, it describes an intercellular relationship rather than a synapse-specific process. The proposed model of the tripartite synapse by Tewari and Majumdar [88] is therefore modified to include the propagation of AP along the axon, the molecular dynamics in the node of Ranvier for neurotransmitter release, the perinodal astrocytic processes for extrasynaptic signaling, and the compartmentalization of astrocytic Ca^{2+} dynamics via different Ca^{2+} store sites. Biophysical models demonstrate the electrical and chemical dynamics of the system and how compartmentalization in astrocytes contributes to information processing and synaptic plasticity. The results suggest that Ca^{2+} stores positioned on different astrocytic processes improve the synaptic efficacy by increasing intracellular astrocytic $[Ca^{2+}]$. However, the longer the $[Ca^{2+}]$ is above the threshold, the astrocyte can create an oversupply of Glu^{-} in the extrasynaptic area, which can cause excitotoxic effects to the neurons.

5.2.1/ Functional Model of the Tripartite Synapse (Spontaneous Release)

The tripartite synapse is modeled based on the pyramidal neurons and astrocytes in the hippocampal CA3-CA1 network. In this case, we focus on the tripartite area and extend the morphology to include the nonsynaptic components such as the axonal length, shown in Figure 5.1. The model comprises multiple compartments whose characteristics and dynamics are described subsequently. These are the (1) AIS for AP generation, (2) myelinated segments and (3) nodes of Ranvier for AP propagation via saltatory conduction, (4) perinodal astrocytic process sensing vesicular release from the node of Ranvier, (5) the presynaptic bouton for neurotransmitter release, (6) the synaptic area for neurotransmission, (7) the perisynaptic astrocytic process for gliotransmission, (8) the astrocytic soma for signal integration, and finally, (9) the postsynaptic spine head for EPSP. The presynaptic neuron generates APs at the distal end of the AIS, then propagates them along the myelinated segment, which causes signal decay, then to the node of Ranvier for signal re-amplification. During the axonal transmission, Ca^{2+} dynamics in the node of Ranvier results in the release of neurotransmitters into the perinodal area. The perinodal astrocyte then receives and utilizes these neurotransmitters for intracellular Ca2+ release.

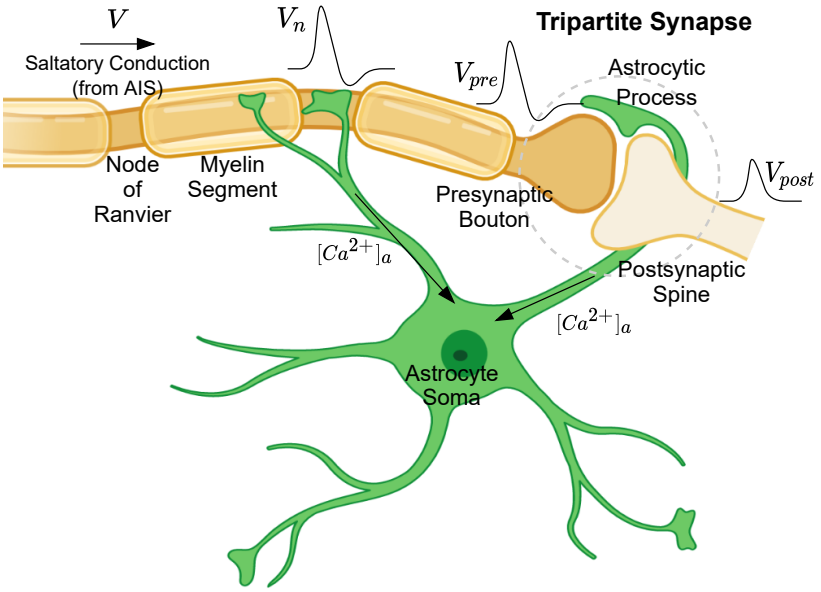

Figure 5.1: Tripartite synapse with perinodal astrocytic components. The morphology and the exclusive dynamics under consideration commence from the AP generation in the presynaptic AIS, V, propagating via saltatory conduction along the axonal length with alternating myelinated segments and nodes of Ranvier, V_n. Along the axonal length, the astrocytic process enwraps the node of Ranvier positioned within the astrocytic territory, developing a perinodal area for nonsynaptic molecular transmission. Another astrocytic process enwraps the synaptic area connecting the presynaptic bouton and the postsynaptic spine, thus forming the tripartite synaptic connection. The extracellular Glu^- sensed from the extrasynaptic and perinodal areas trigger the astrocytic $[Ca^{2+}]_a$ elevation for gliotransmitter release. Here, only the extrasynaptic process releases extrasynaptic Glu^- within the extrasynaptic area. Lastly, the postsynaptic spine head generates an EPSP, V_{post}, dependent on the excitatory synaptic input.

The pattern of AP attenuation and regeneration continues until it reaches the presynaptic bouton. From here, the tripartite synapse follows the dynamics described by the functional model in Figure 5.2. The presynaptic bouton membrane potential V_{pre} causes an increase in the $[Ca^{2+}]$, c_i, which influences the probability of neurotransmitter release, R_S. The released neurotransmitters in the synaptic cleft, specifically Glu^-, G_S, activate AMPA receptors on the postsynaptic spine head producing the excitatory synaptic current I_{ampa}, which increases the EPSP. Synaptic Glu^- also diffuses into the extrasynaptic area and activates mGluRs on the perisynaptic astrocytic process producing the second messenger IP_3, which activates IP_3Rs on the astrocytic ER enabling the influx of Ca_a^{2+}, J_{IP_3R} into the intracellular space, in addition to the Ca_a^{2+} leakage, $J_{C_{ER}leak}$. Part of the Ca_a^{2+}, J_{SERCA}, flows back into the internal Ca^{2+} store to maintain the molecular balance in the astrocyte. These three fluxes, J_{IP_3R}, J_{SERCA}, and $J_{C_{ER}leak}$, contribute to the intracellular Ca^{2+} oscillation. Assuming that the astrocytic soma integrates the transient Ca_a^{2+} from the astrocytic processes, the amount of intracellular Ca_a^{2+} influences the probability of gliotransmitter release, R_A, into the extrasynaptic area, increasing the extracellular $[Glu^-]$, G_A. This process creates a closed-loop, in the form of G_A as feedback to the presynaptic neuron: by activating presynaptic mGluRs and influencing the presynaptic $[IP_3]$, the c_i level increases. In turn, the astrocytic dynamics indirectly influence the neurotransmitter release process, thus affecting the activities of the postsynaptic neuron. Following is a more comprehensive description of each compartment and its processes.

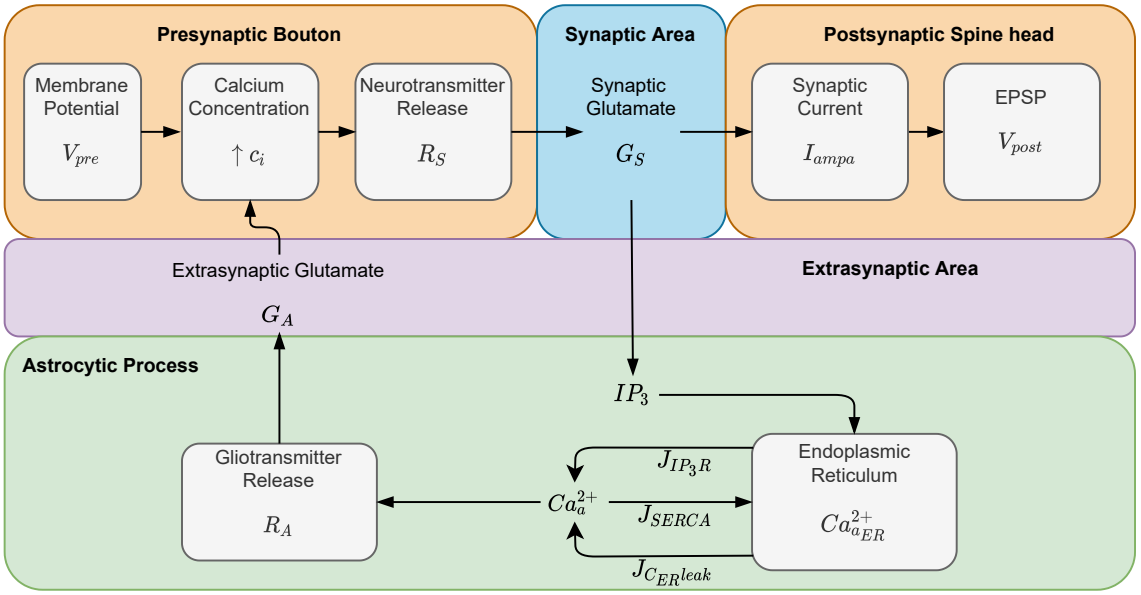

Figure 5.2: Tripartite synapse functional model. The tripartite synapse is the interaction between the cellular compartments (the presynaptic bouton, the postsynaptic spine head, and the astrocytic process) and areas (the synaptic area and the extrasynaptic area).

Axon Initial Segment

The AIS is the neuronal domain separating the axonal and somatodendritic compartments and is a critical site where AP is initiated and propagated bidirectionally (to the axon terminals and back to the soma) [361–365]. Electrical excitability occurs in this site due to the clustering of high-density voltage-gated channels, such as Na_v channels causing the AIS to obtain the lowest AP threshold within the neuron and K_v channels counteracting the Na_v channels by suppressing AP generation. Aside from these ionic channels, the location of the AIS plays a vital role in AP generation [154]. It is isolated from the soma, which makes it electrically compact, and its proximal distance from the soma optimizes the charge reaching its domain [364]. Multi-compartmental studies noted that AP initiates at the distal end of the AIS due to electrotonic isolation [362]. Here, the Hodgkin-Huxley model [76] in Equation 2.11 describes the membrane potential, V, and the AP generation in the AIS through the influx/efflux of Na^+ and K^+ ions. Refer to Table A.1 for the list of parameters and the corresponding values.

Myelinated Segments

The AP, generated at the distal end of the AIS, propagates along the first myelinated segment. Electrically, myelin sheaths have significantly high resistance and low capacitance. Furthermore, the ionic channel density along the myelinated segment is low, causing a passive voltage spread [139]. Here, the extended model of cable transmission in Equation 2.22 describes the signal propagation along the myelinated segment, V_m, considered a transmission line consisting of resistive and capacitive properties [143]. The characteristics of the myelinated segment are listed in Table A.2. The subscript m corresponds to the parameters exclusive to the myelinated segment. With the solution from Bogatov

et al. [143], the constant parameters such as the length constant, λ, the time constant, τ, and the constant of distributed AP, γ, were computed. These parameters describe the signal propagation along the myelinated segment. Because of the small capacitance and considerable resistance of the myelin [136], the length constant of the axonal cable is longer while its time constant is shorter than in unmyelinated segments [139].

Node of Ranvier

The current density at the distal end of the myelinated segment is the stimulus for regenerating the AP at the node of Ranvier. Electrophysiological studies showed that the node of Ranvier follows the spike frequency of the AP initiated in the AIS with ~100 μs delay [362]. The current density I_n flowing into the node from the myelinated segment is computed as the change in voltage over time [366] so that $I_n = CdV_m/dt$, where V_m is the voltage at the point in the axon where the myelin segment ends. Arancibia-Carcamo et al. [135] measured the node lengths of the myelinated axons. As a result, they found that the nodal length is consistent along an axon but differs between axons. The node length and the number of nodal Nav channels positively correlate, indicating a constant channel density. Also, the transmembrane inactivating Na+ and low-threshold K+ channels densities are higher in the node of Ranvier than in the soma and the AIS [132, 367, 368]. Therefore, there is a lower threshold of AP activation in this compartment [367]. In saltatory conduction, the AP amplitude, initiated in the AIS, diminishes as it propagates along the myelinated segment and intensifies at the node due to the voltage-gated mechanisms in the node. This activity repeatedly occurs until the AP reaches the axon terminals. In these compartments, the AP regeneration, V_n, also follows the Hodgkin-Huxley model in Equation 2.11 [81, 82] using channel conductances and reversal potentials specific in the node and input current $I_n = I_{app}$. Refer to Table A.3 for the corresponding parameters. Here, the subscript n indicates values exclusive to the node of Ranvier.

Perinodal Area

We considered the node of Ranvier and perinodal astrocyte as compartments due to their properties similar to the synapse; therefore, we have taken the perinodal area into account for the following reasons. First is the presence of vesicles containing neurotransmitters in the nodes. The soma packages these vesicles and transports them into the axon terminals to be captured by axonal varicosities. Uncaptured vesicles leave the terminal and re-enter circulation [166]. Second, in the central nervous system, the nodes are connected to perinodal astrocytes [136, 369], which occupy the space between myelinated segments in the axon and show biochemical characteristics when connected. Action potential influences the release of Glu^- from the unmyelinated section of the axon. This release is dependent on the $[Ca^{2+}]$ elevation attributable to AP and the ER extending throughout the axon [370, 371]. This nonsynaptic neurotransmitter release [372] influences the opening of Glu receptors in the perinodal astrocyte [358]. Lastly, while communication is classically known to occur at synapses, evidence shows that extrasynaptic transmitter release from the soma, axon, and dendrites occurs even without a postsynaptic counterpart via exocytosis or spillover [178, 350, 373]. The Ca^{2+} and Glu^- dynamics in the node, perinodal area, and perinodal astrocyte follow the presynaptic bouton and

astrocytic dynamics presented next. The biophysical properties and parameters related to the perinodal section are in Tables A.4, A.5, A.7, and A.7.

PRESYNAPTIC BOUTON

The increase in the intracellular [Ca^{2+}], c_i, in the presynaptic bouton (and also $c_{i,n}$ in the nodes of Ranvier) is the consequence of the interplay between the electrical (the fast Ca2+ activities due to the voltage-dependent increase in cytosolic Ca^{2+} upon the arrival of AP) and chemical dynamics (the slow Ca^{2+}-dependent release of Ca^{2+} ions from the ER) in the compartment. The Ca^{2+} dynamics in each compartment are also dependent on the dimension and shape of the compartment itself. Here, the intracellular Ca^{2+} dynamics follow the biological model in Subsection 3.2.2 (Modeling Calcium Dynamics). The construction-destruction formulism in Equation 3.2 describes the changes in c_{fast}, and the modified Li-Rinzel model [162] defines the dynamics of c_{slow}. Refer to Table A.4 for the parameters associated with the presynaptic neuron Ca^{2+} activities.

There are two conditions for triggering the release of neurotransmitters from the presynaptic bouton (or the node). First, the compartment releases Glu^- into the synaptic cleft when five Ca^{2+} ions bind to the Ca^{2+} sensor of the vesicle. The transition of the Ca2+ sensor from one state to another is computed using the Markov model for ionic channels. The arrival of AP, in correlation with the intracellular [Ca^{2+}], evokes the release [88, 178]. Second, the intracellular [Ca^{2+}] can also randomly provoke vesicular neurotransmitter release. Following the study of Tewari and Majumdar [88], two docked vesicles are present in the bouton; therefore, f_r, (with values 0, 0.5, and 1) represents the fraction of the ready vesicles out of the total number of docked vesicles in the bouton. See Subsubsection 3.3.2.3 (Spontaneous Release). In addition, based on the amount of intracellular [Ca^{2+}], the spontaneous vesicle release is also possible even in the absence of AP. In the study of Modchang et al. [374], comparing stochastic and deterministic approaches on vesicle release, the result suggested that in synapses with nanodomain, stochastic vesicle release algorithm is more accurate than deterministic approach. The modified TMM in Equation 3.27 describes the vesicular fusion and recycling process. The synaptic release is history-dependent; therefore, if the next incoming AP is in the order of these time constants, vesicles are neither replenished nor released. Whether evoked or spontaneous, the vesicle release process is history-dependent; that is, the process is inactive 6.34 ms after release the previous release, wherein the vesicles neither replenish nor release their neurotransmitter content [88, 178]. Lastly, Equation 3.30 describes the synaptic Glu^- dynamics, g. The parameters in the neurotransmitter release process and synaptic Glu^- dynamics are explicitly for CA3-CA1 synapse and are listed in Table A.5.

ASTROCYTE

Transient astrocytic [Ca^{2+}] (or [$Ca^{2+}]_a$) increases in response to synaptic activity and propagates within the astrocyte into the soma or nearby cells. The discovery of this Ca^{2+} wave suggests that astrocytes integrate and transfer signals [375]. In this model, the extrasynaptic and perinodal astrocytic processes are distinct compartments whose Ca_a^{2+} transients flow into the soma for integration and vesicle packaging. In the astrocyte,

Ca_a^{2+} oscillation is attributed to the CICR from the ER into the cytosol through IP3 receptors. Astrocyte responds to synaptic activity by changes in its global (somatic) and focal (perisynaptic and perinodal) Ca_a^{2+} elevations [316, 376]. Intracellular $[Ca^{2+}]_a$ transients can propagate along the process and into the soma, influence somatic $[Ca^{2+}]_a$ elevations. Subsequently, the overall summation of somatic and transient $[Ca^{2+}]_a$ leads to transmitter release [377]. However, biophysical mechanisms of astrocytic Ca^{2+} intracellular propagation are still insufficient [378], specifically if global $[Ca^{2+}]_a$ elevations result from the linear summation of transient Ca^{2+} [316].Therefore, we assumed that the total intracellular $[Ca^{2+}]_a$ is responsible for astrocytic vesicle release. Astrocyte dynamics is a stochastic process, and the total intracellular $[Ca^{2+}]_a$ is the summation of all the transient Ca_a^{2+}. Here, the biologically-based and modified Li-Rinzel model presented in Subsection 4.3.1.1 describes the astrocytic IP_3 and Ca^{2+} dynamics in the extrasynaptic and perinodal astrocytic processes, where the parameters and the corresponding values are presented in Table A.6.

Then, three Ca^{2+} ions must bind with three independent gates (S_1, S_2, and S_3) for possible gliotransmitter release, following the kinetic model and release probability presented in Subsection 4.4.2.1. Astrocytic vesicle fusion and recycling uses an essentially similar transmitter release process as the presynaptic neuron, described by the stochastic models in Subsection 4.4.2.2. Here, only the extrasynaptic process releases extracellular Glu^-, which is necessary for presynaptic IP_3 production. Extrasynaptic Glu^- dynamics is governed by Equation 4.43. Refer to Table A.7 for the parameters.

Postsynaptic Spine Head

Synaptic Glu^- then activates the postsynaptic firing. In this glutamatergic synapse, the excitatory synaptic input is due to the activation of clustered and localized AMPARs in the spine head. The passive postsynaptic membrane potential, V_{post}, is given as

$$\tau_{post}\frac{dV_{post}}{dt} = -\left(V_{post} - V_{rest}\right) - R_m I_{ampa}, \tag{5.1}$$

where V_{rest} is the postsynaptic resting membrane potential, R_m is the spine resistance, and I_{ampa} is the AMPAR current computed using the AMPAR gating function in Equation 3.37. See Table A.8 for the list of parameters and their corresponding values.

5.2.2/ Simulation and Analysis Method

We simulated the tripartite synapse dynamics in Matlab, implementing the Euler method with a time step $dt = 0.05$ ms for the system of differential equations numerical computation. In this model, there are 20 myelinated segments in the presynaptic axon [379], forming 41 compartments: one AIS, 20 myelinated segments, 19 nodes of Ranvier, and one presynaptic bouton. The AIS input is a pulse wave of 10 $\mu A/cm^2$ with a frequency of 5 Hz and a pulse width of 4 ms [10, 88]. In addition, there is one compartment for the postsynaptic spine head, one compartment each for perisynaptic astrocytic process and astrocytic soma, 0 to 2 perinodal astrocytic process/es, a synaptic area, perinodal area/s (0 to 2), and an extrasynaptic area.

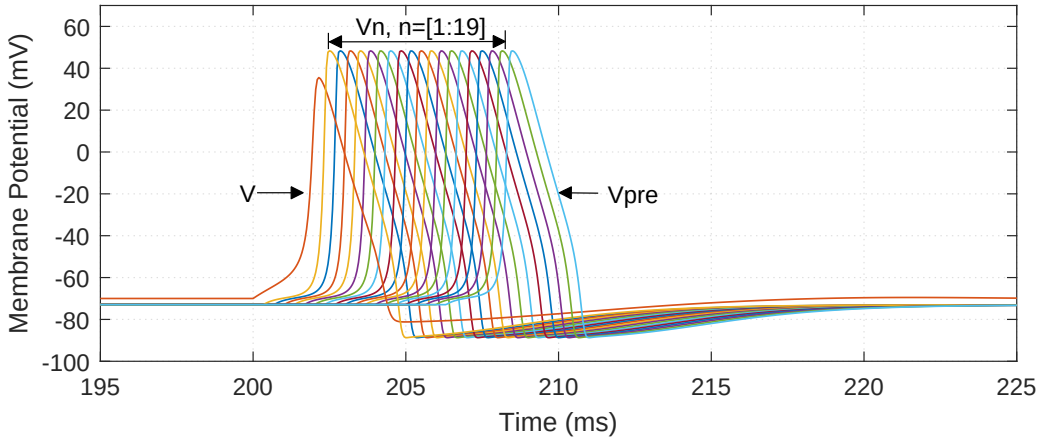

Figure 5.3: Signal propagation via axonal saltatory conduction changes the AP waveform and propagation delay. The stimulus at $t = 200$ ms generates an AP, V, in the AIS. Given the myelinated segment characteristics mentioned in Table A.2, the constant parameters are computed as $\gamma = 1$, $\lambda = 1.5076$, and $\tau = 0.3317$ ms. There is a 0.33 ms delay in AP arrival from the AIS to the first node of Ranvier, V_1. Therefore, it takes 6.66 ms before AP reaches the bouton, V_{pre}.

We previously addressed the electrical and chemical dynamics of a neuron-astrocyte interaction with nonsynaptic sources from external areas. To analyze the impacts of these sources, we simulated different neuron-astrocyte configurations: (1) tripartite synapse, (2) tripartite synapse with one perinodal source, and (3) tripartite synapse with two perinodal sources. Because of the stochastic nature of the dynamics, we simulated each configuration for 50-second simulation time and repeated the simulation 20 times.

The neurotransmitter release is a stochastic process that varies the postsynaptic membrane potential spiking pattern over time. The fundamental quantity in neural circuits that describes these variations is called synaptic efficacy or strength [380–382]. Synaptic efficacy determines the strength of the connection between the pre- and postsynaptic neurons with time, identified by the transferred mutual information based on the activity patterns of the input and output spike trains. We also used synaptic efficacy to identify the influence of astrocytic processes in synaptic transmission numerically, computed by obtaining the ratio of the number of successful postsynaptic spikes over the number of presynaptic spikes within a 5-second sliding window.

5.2.3/ Results

5.2.3.1/ Presynaptic Neuron Dynamics

Figure 5.3 shows the generated AP in the AIS (V) and the regenerated AP in the nodes (V_n where $n = [1, 19]$) and bouton, V_{pre}. Here, the voltage delay and attenuation resulted from the AP propagation across the myelinated segments. The change in amplitude from the AIS (peak amplitude of 36.53 mV) to the first node of Ranvier (peak amplitude of 46.56 mV) results from channel conductance increase in the nodes. Due to the increase in the voltage-gated channels and the changes in their reversal potential, the nodal Na^+ current amplifies the axosomatic AP and hyperpolarizes the AP voltage [365, 383].

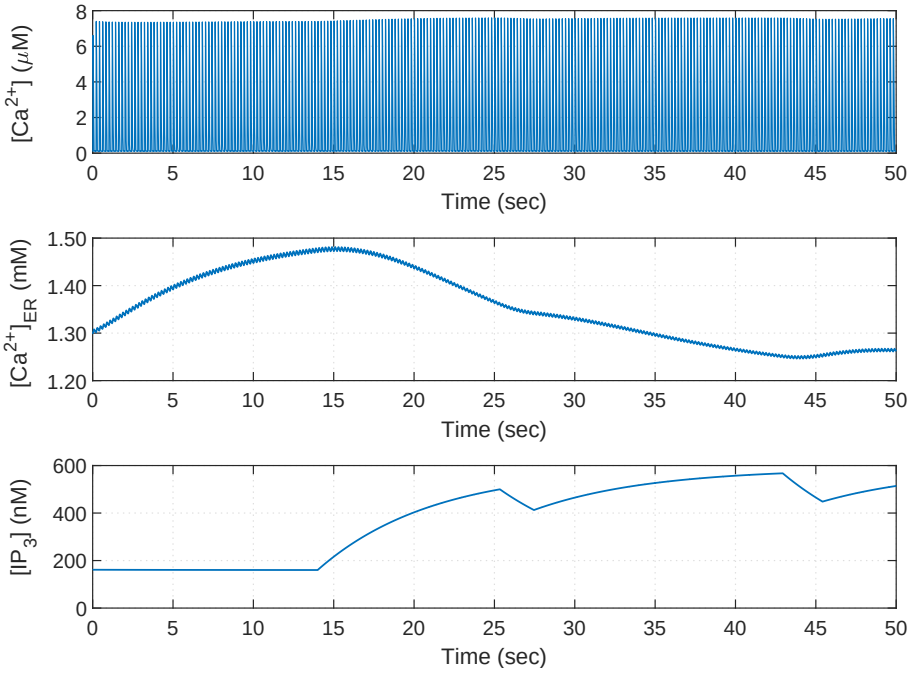

(a) Presynaptic Bouton

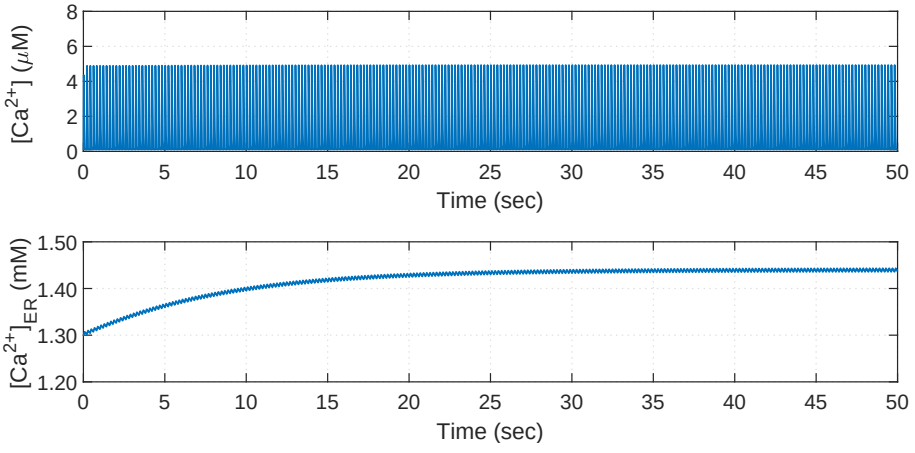

(b) 19th node of Ranvier

Figure 5.4: Calcium dynamics on the presynaptic bouton and node of Ranvier. (a) The total presynaptic bouton [Ca^{2+}], (c_i), oscillation has a frequency equivalent to the frequency of the incoming AP. The [Ca^{2+}] gradient between the intracellular space and the ER is relative to the increase and decrease of the [IP_3]. (b) Calcium oscillation in the node of Ranvier also happens simultaneously with the AP arrival to the node, however with lesser peak amplitudes due to the dimension of the node. Then, the $[Ca^{2+}]_{ER}$ stabilizes to 1.44 mM due to the absence of extracellular inputs triggering the increase of IP_3.

In this model, the astrocytic processes cover the synapse and the 19th node of Ranvier. As the AP propagates through the axonal length to the presynaptic bouton, it simultaneously triggers the [Ca^{2+}] elevations in the said compartments. In the presynaptic axon, the local calcium concentration combines the AP-evoked Ca^{2+} and the ER Ca^{2+} fluxes. As presented in Figure 5.4, intracellular Ca^{2+} fluctuations in the bouton (Figure 5.4a) and the 19th node (Figure 5.4b) exhibit probabilistic behaviors concurrent with the arrival of AP. The average peak amplitudes of [Ca^{2+}] in the bouton and node were 7511 nM and 4919 nM, respectively. With the same channel conductance and compartment-to-ER ratio, the difference between the amplitudes of bouton and nodal [Ca^{2+}] is the consequence

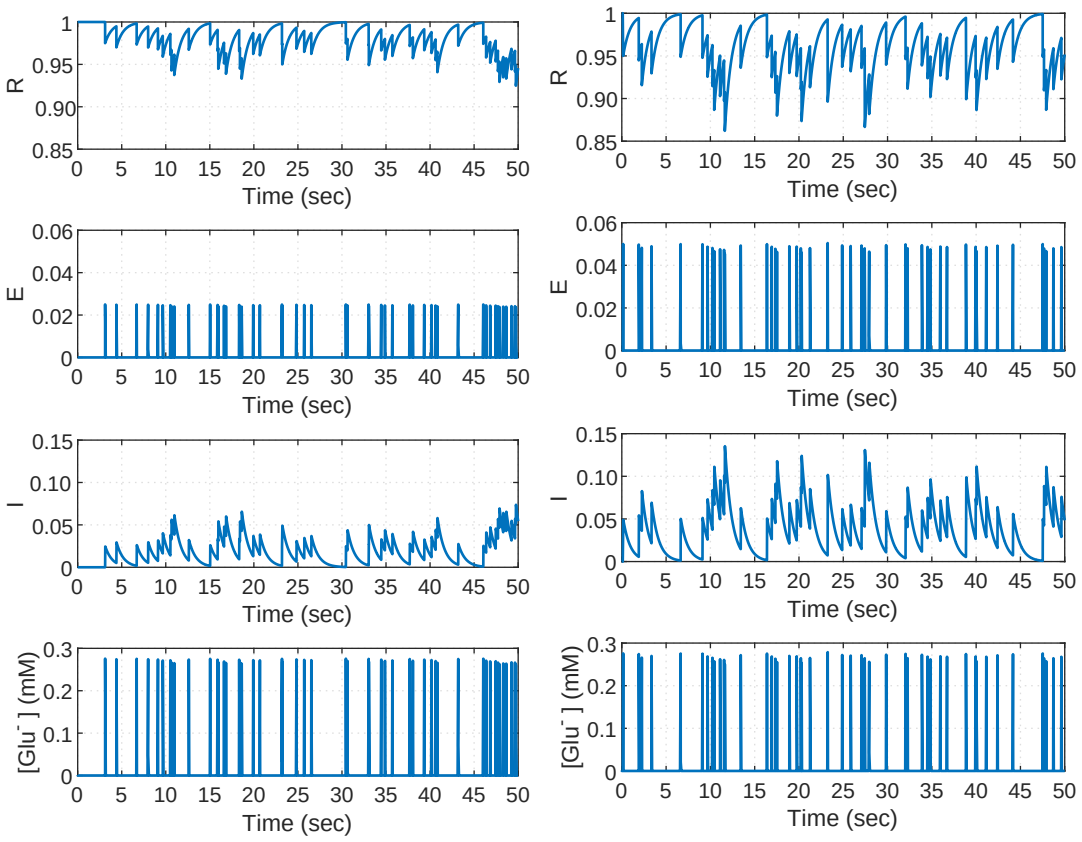

(a) Presynaptic bouton **(b)** 19th node of Ranvier

Figure 5.5: Synaptic and perinodal neurotransmitter release within a 50-second stimulation. The vesicle fusion and recycling process in the (a) presynaptic bouton and the (b) 19th node of Ranvier results in stochastic Glu^- spikes in the synapse and the perinodal area, respectively.

of the morphometric properties of the compartments. In addition, the intracellular $[Ca^{2+}]$ peak amplitudes are inversely proportional to the Ca^{2+} content of the ER. The activation of IP3Rs allows the release of Ca^{2+} from the ER to the intracellular space. Thus, Ca^{2+} ER shows an inverse activity of the IP3. The $[IP_3]$ concentration in Figure 5.4a is equivalent to the initial value (160 nM) from $t = 0$ to $t = 13.97$ sec. Note that the increase in $[IP_3]$ amplitude corresponds with the astrocytic gliotransmitter release shown in Figure 5.7. The perinodal activity does not involve extracellular gliotransmitter release; therefore, there are no fluctuations in the nodal $[IP_3]$ levels but rather increases from the initial concentration and stabilizes at 1.44 mM.

The internal Ca^{2+} dynamics in the presynaptic compartments determine the vesicle release probability resulting in either evoked or spontaneous Glu^- spiking activities. Refer to Figure 5.5. The fraction of readily releasable synaptic vesicle, R, in the presynaptic bouton fluctuates between 0.9249 and 1, resulting in stochastic and fractional vesicle release, E, into the synaptic cleft with an average peak amplitude of 0.0245, and a fraction of inactive vesicles, I, ranging from 0 to 0.0737 (Figure 5.5a). Therefore, the resulting synaptic $[Glu^-]$ in the synaptic cleft peaks at an average amplitude equal to 0.2705 mM. The perinodal coupling displays a different range of neurotransmitter release activities (Figure 5.5b). The perinodal R has a lower release probability, between 0.8621 to 1, a higher fraction of effectively released vesicle, E, with an average amplitude of 0.0484,

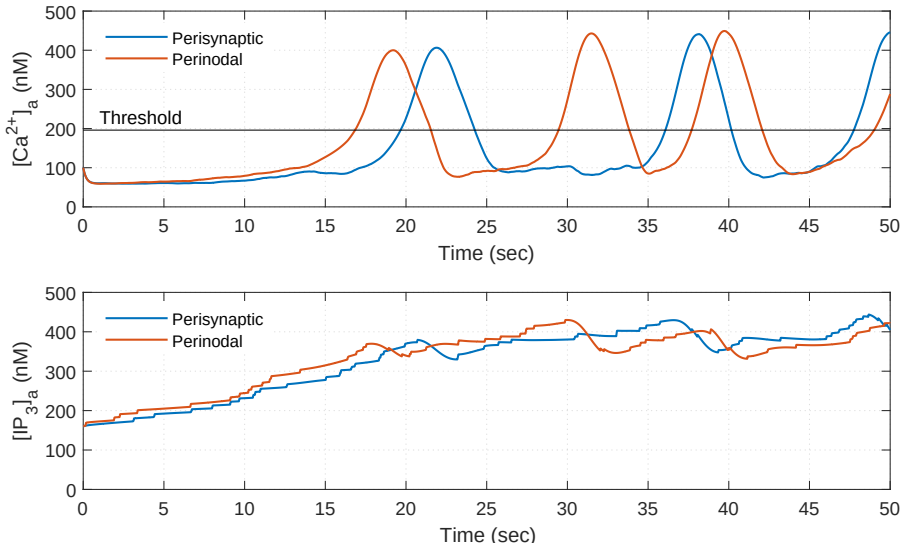

Figure 5.6: Transient $[Ca^{2+}]_a$ and $[IP_3]_a$ elevations in the perisynaptic (blue) and perinodal (red) astrocytic processes.

and a higher fraction of vesicles for recycling, $I \in [0, 0.1353]$. This phenomenon can be attributed to the absence of astrocytic Glu^- released into the node and the lower nodal $[Ca^{2+}]$. On the other hand, the perinodal area also shows similar Glu- activities (in terms of Glu^- spike peaks, with an average peak amplitude of 0.2670 mM). Glutamate spikes in both perinodal and synaptic areas are dependent on their neurotransmitter release probability. This asynchronous process results in 50 and 49 Glu^- spikes in the synapse and perinodal area, respectively, which is infrequent compared to the 5 Hz input spiking 250 times within the 50-second stimulation.

5.2.3.2/ Astrocytic Calcium Dynamics

Figure 5.6 shows the localized transient $[Ca^{2+}]$ elevations and the corresponding IP_3 dynamics in the astrocytic compartments. These transients are independent of each other, occur rapidly due to the individual Ca^{2+} stores [384], and are highly variable between cell subcompartments [385], with an independent local initial $[Ca^{2+}]_a$, according to the spatial Ca^{2+} quantification by Lopez-Caamal et al. [386]. The resulting Ca^{2+} dynamics coincide with the experimental studies using mouse hippocampus slices wherein patterns of transients and localized Ca^{2+} events with different sizes and durations were detected in a single astrocyte [265, 387]. Astrocytic Ca^{2+} oscillations show a much lower frequency compared to the oscillations exhibited by the presynaptic compartments. In addition, the increase in the $[IP_3]_a$ is concomitant with the synaptic neurotransmitter release while the $[Ca^{2+}]$ elevation creates a time window for astrocytic IP_3 level depression.

These Ca^{2+} waves can remain localized or propagate, as shreds of evidence showed that after initiation, Ca^{2+} waves spread within the cell [307, 388, 389]). Figure 5.7 displays the total intracellular $[Ca^{2+}]_a$ on which the vesicle fusion and recycling process depends. Vesicle synthesis in astrocytes depends on the sensitivity of the secretory apparatus to the intracellular Ca^{2+} [384]. The fraction of SLMVs available for release is maximum ($R_a = 1$) during subthreshold Ca^{2+} activities and minimum ($R_a = 0$) at Ca^{2+} peaks. The fraction

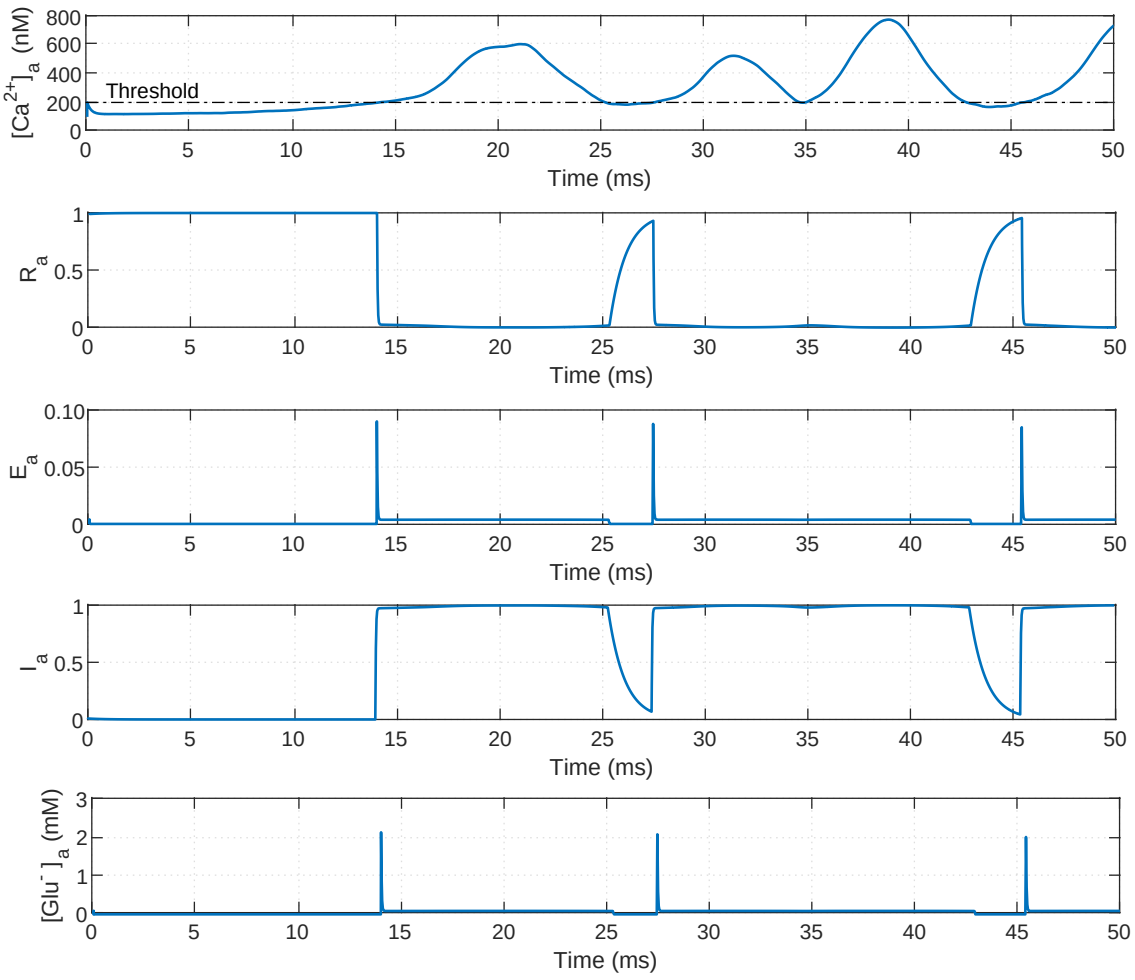

Figure 5.7: Extracellular gliotransmitter release process. The total intracellular $[Ca^{2+}]_a$ activates the SLMV fusion and recycling process (R_a, E_a, and I_a) in the perisynaptic astrocytic process, simultaneously triggering Glu_a^- spikes.

effectively released SLMVs, E_a into the perisynaptic area peaks simultaneously (average peak amplitude equal to 0.0867) with the drop in R_a. In addition, most of the released Glu_a^- undergoes the recycling process ($I_a \approx 1$). Once the $[Ca^{2+}]_a$ goes beyond the threshold, gliotransmitters are released. Going back to Figure 5.6, the second elevation of perinodal $[Ca^{2+}]_a$ causes the Glu_a^- release. Therefore, even when the synaptic area is silent, the astrocyte might modulate the synaptic transmission by processing signals from the extracellular matrix. However, prolonged delay in Glu^- release might also be possible. Consider only the perisynaptic Ca^{2+} dynamics; there should be a Glu_a^- release from $t = 36$ to $t = 40$ sec. However, with the additional perinodal $[Ca^{2+}]_a$, the total intracellular $[Ca^{2+}]_a$ just remained over the threshold, making the vesicle fusion and recycling slower.

Within the 50-second presynaptic stimulation, $[Ca^{2+}]_a$ crosses the threshold three times producing simultaneous Glu_a^- spikes. Notice that a fraction of total Glu_a^- stays in the perisynaptic area until the recycling process is over ($I_a \lesssim 1$) or $[Ca^{2+}]_a$ drops below the threshold. The extrasynaptic Glu_a^- serves as feedback to the presynaptic neuron activity and produces second messenger IP_3, as displayed by the fluctuations in $[IP_3]$ in Figure 5.4a. The ER then releases Ca^{2+} into the intracellular area, increasing the $[Ca^{2+}]$ elevation peaks in the presynaptic bouton.

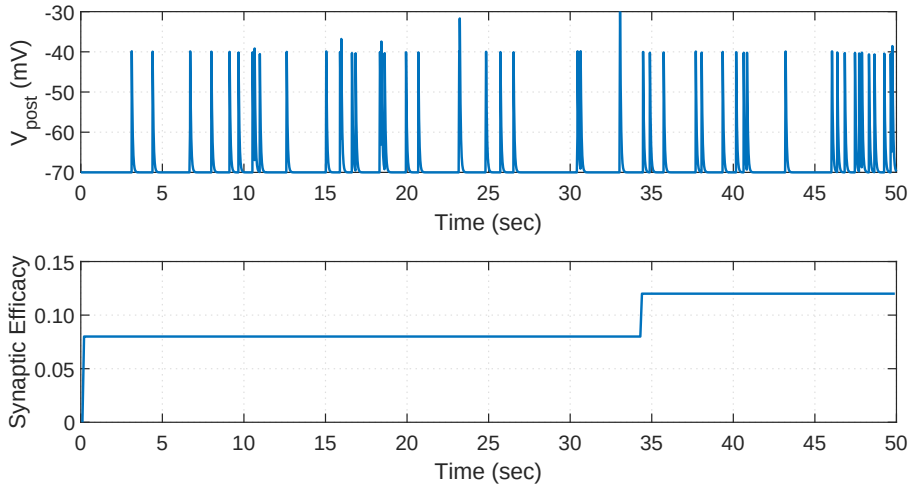

Figure 5.8: Postsynaptic membrane potential and synaptic efficacy. (a) The postsynaptic membrane potential of the dendritic head is dependent on the synaptic [Glu⁻]. The dendritic spikes coincide with the synaptic Glu⁻ spikes with an average peak amplitude of –39.57 mV. (b) The synaptic efficacy is stable when t is between 0 and 34 s at 0.08, then increases to 0.12.

5.2.3.3/ Postsynaptic Neuron Activities

The postsynaptic membrane potential spiking frequency is dependent on the amount and frequency of synaptic [Glu⁻]. Therefore, the sudden increase in synaptic [Glu⁻] results in a voltage spike in the postsynaptic spine head, as shown in the relationship between the [Glu⁻] in Figure 5.5a and V_{post} in Figure 5.8. A postsynaptic spike is successful when its peak driving force is less than or equal to the difference between the reversal and the resting potential $(E_{AMPA} - V_{rest})$ [197]. The increase in synaptic efficacy occurs at $t = 34$ sec, displayed by the higher number of spikes clustering with time, indicating increased postsynaptic activity [381].

5.2.4/ Discussion

Advances in neuron-astrocyte researches expand our observation of the complexity of brain processes. State-of-the-art imaging techniques challenge the present concept of the tripartite synapse, where information flows from the presynaptic to the postsynaptic component with astrocytic influences on plasticity. We extended the tripartite synapse model presented by Tewari and Majumdar [88] by incorporating nonsynaptic elements through axon-astrocyte interaction for the following reasons. (1) Information transfer is not only confined in the synapse and can be an intercellular process. Astrocytic mGluRs, distributed heterogeneously throughout the cell body, react to extracellular Glu⁻. A single protoplasmic astrocyte can, therefore, sense molecular signals from the neuronal elements within its domain. (2) The vesicular release also occurs in the soma, unmyelinated axon, and varicosities. Adjacent astrocytic processes sense these signals, in turn recognizing the activity of neighboring neurons or networks. (3) Compartmentalization of neuronal and astrocytic Ca^{2+} dynamics is probable. In the neuron, the cell morphology, the expression of ionic channels, the distribution of Ca^{2+} stores, and the behavior of AP means that intracellular [Ca^{2+}] varies across the neuron. Astrocytic Ca^{2+} dynamics, Sup-

ported by the ER, are transient and localized, indicating individual processes in each locality. With these, we presented a model of neuron-astrocyte interaction extending the tripartite synapse and incorporating saltatory conduction along the myelinated axon, nonsynaptic neurotransmitter release, perinodal astrocytic compartments, and integration of transient astrocytic $[Ca^{2+}]$ for gliotransmitter release.

5.2.4.1/ Tripartite Synaptic Transmission is More Than a Point Process

Previous models assumed that AP generated in the AIS reaches the axon terminals without delay or decay by considering the axon as one compartment. We showed that even though myelination promotes rapid conduction, signal delay still occurs. Besides, the AP waveform changes due to the different expression of ionic channels in the nodes and the AIS. Therefore, we considered the axonal length as a sequence of compartments representing the nodes and myelinated segments. By doing so, we were able to insert perinodal processes that are independent of the synapse.

At this point, we described information transfer within the tripartite synapse, originating from the AP generation in the AIS to the nodal $[Ca^{2+}]$ elevations during saltatory conduction, followed by the unmyelinated axonal and presynaptic bouton vesicular release triggering the Glu- dynamics in the perinodal and synaptic areas, respectively, to the activation of perinodal and perisynaptic astrocytic mGluRs, and finally, the astrocytic dynamics. Here, we presented the localization of astrocytic Ca^{2+} dynamics in the perisynaptic and perinodal compartments. The stochastic nature of neurotransmitter release and the spatial variation in extracellular $[Glu^-]$ surrounding the astrocyte determine transient astrocytic Ca^{2+} activities. Here, we assumed a linear summation of transient $[Ca^{2+}]$ in the soma that determines the $[Glu^-]$ in the perisynaptic cleft. As a result, the additional nonsynaptic Glu- sources boost the intracellular astrocytic $[Ca^{2+}]$, which improves synaptic efficacy. However, as the extrasynaptic $[Glu^-]$ increases indirectly, presynaptic Ca^{2+} stored in the ER will be depleted due to the frequent activation of presynaptic ER IP_3Rs. The results show that the extent of astrocytic influence on synaptic transmission is distributed within the astrocytic territory; thus, the astrocytic activities and computation can be considered as more than a point process. We recommend further biophysical investigation and model formulation on astrocytes viewed as a compartmentalized system, similar to neurons, rather than a point process.

5.2.4.2/ Nonsynaptic Elements Influence Synaptic Efficacy

We simulated the tripartite synapse dynamics for 50 seconds with an increasing number of nonsynaptic sources of Glu^- and then summarized the Glu_a^- activities in the perisynaptic area in Table 5.1. Configuration 0 is a tripartite synapse alone, Configuration 1 has one nonsynaptic source coupled with the 19^{th} node of Ranvier, and Configuration 2 is coupled with the 19^{th} and 18^{th} nodes of Ranvier. Here, the average Glu_a^- spikes show an inverse relationship with the number of Glu^- sources (therefore, also related to the total amount of sensed $[Glu^-]$). Gliotransmitter release becomes less frequent, and the period wherein Glu_a^- is available in the extrasynaptic area extends for a longer time window. This activity results from the amount of intracellular $[Ca^{2+}]_a$ staying above the $[Ca^{2+}]_a^{thresh}$ for

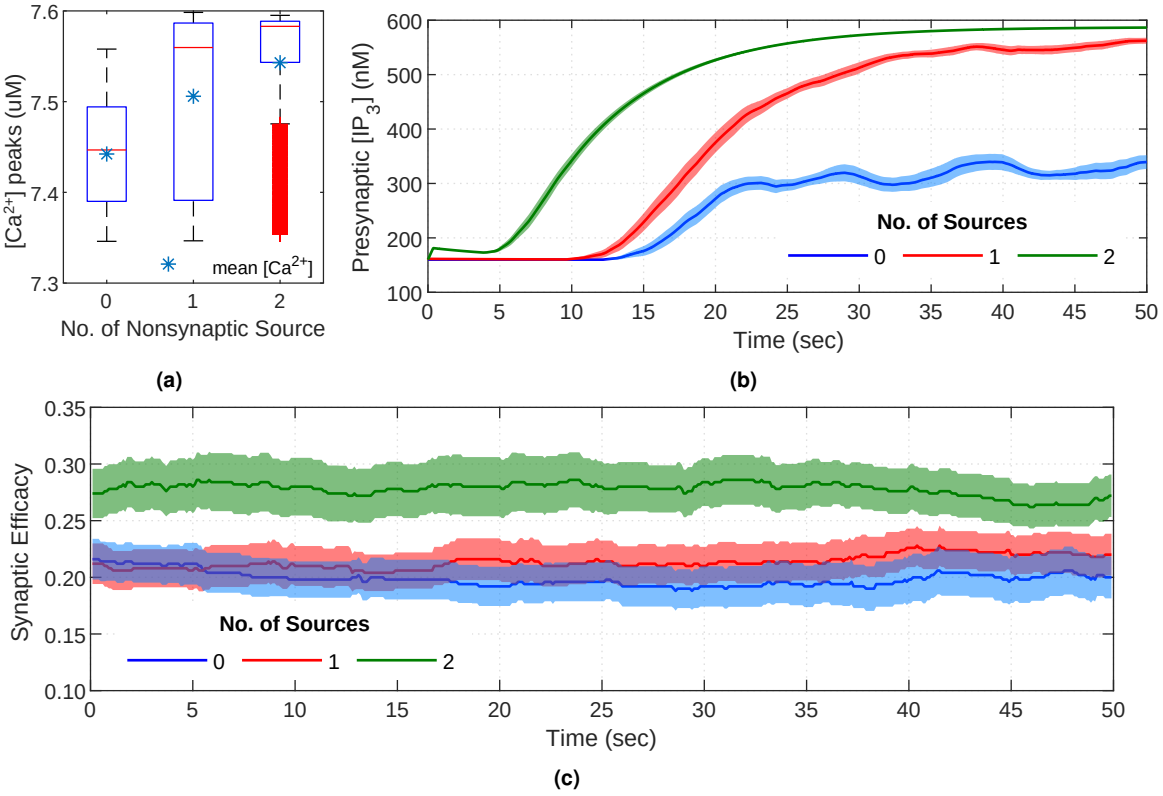

Figure 5.9: Influence of extrasynaptic glutamate to synaptic efficacy with increasing nonsynaptic sources (*blue* for 0, *red* for 1, and *green* for 2). (a) The boxplots show the range and mean of $[Ca^{2+}]$ peak amplitudes in the presynaptic bouton. As the amount of Glu_a^- the nonsynaptic sources sensed increases, the astrocytic $[Ca^{2+}]_a$ rises, increasing the presynaptic Ca^{2+} peaks. (b) Simultaneously, the Ca^{2+}- and Glu_a^-–dependent IP_3 reaches the equilibrium more progressively when the number of extrasynaptic sources, in this case, is maximum (*green line*). The solid line indicates the change of mean synaptic efficacy with time for the three model configurations, while the shaded area is the corresponding standard error. (c) The comparison of synaptic efficacy between the three configurations, computed per 5-ms sliding window, shows that synaptic strength is minimum with tripartite synapse alone (*blue*), and increases as the number of Ca^{2+} stores (located in the different locations, i.e., perisynaptic and perinodal astrocytic compartments) engages in intracellular Ca_a^{2+} integration.

a more extended period and denotes that the vesicle fusion and recycling process slows down. How does the extrasynaptic Glu_a^- activity influence the synaptic plasticity? In order to demonstrate this, we then analyzed the factors influencing synaptic plasticity directly linked with extrasynaptic Glu_a^-.

Table 5.1: Extrasynaptic glutamate activities.

No. of Non-synaptic Sources	Average No. of Glu_a^- Spikes (50-sec Stimulation)	Average Time Before First Spike (sec)	Average $[Glu^-]_a$ Peak (mM)	Average Period of $[Glu^-]_a$ elevation (sec)
0	3.40	14.40	1.7414	4.56
1	2.35	14.50	1.7955	11.85
2	1.05	6.05	2.1712	$\geq$ 44.04

In the presented tripartite synapse model, most of the factors affecting synaptic plasticity are components of the presynaptic terminal, such as the vesicle release probability and the number of available releasable vesicles. These factors are dependent on the presynaptic $[Ca^{2+}]$ elevations that are simultaneously affected by the extrasynaptic Glu_a^-. While in the postsynaptic side, the amount of synaptic neurotransmitters released into the synaptic cleft regulates the postsynaptic spiking activity. By taking the presynaptic bouton $[Ca^{2+}]$ into account, the mean presynaptic $[Ca^{2+}]$ peaks increase as the astrocytic $[Ca^{2+}]_a$ rises, as shown in Figure 5.9a. The ER of the presynaptic bouton utilizes the extrasynaptic Glu^- for Ca^{2+} release via the opening of IP_3Rs. Figure 5.9b shows the mean $[IP_3]$ for each configuration. Noting that the Glu_a^-directly influences the presynaptic IP_3 dynamics, the extended availability of extrasynaptic Glu_a^- causes the IP_3 to reach equilibrium. In Figure 5.9c, the mean synaptic efficacy per sliding time window for each configuration shows that the tripartite synapse alone exhibits the lowest synaptic efficacy and that the addition of perinodal Glu_a^- sources increases the synaptic strength. However, an extremely high concentration of intracellular $Ca^{2+}]_a$ leads to an abnormal extrasynaptic $[Glu^-]_a$ [390], as shown in Table 5.1, wherein Glu_a^- remains in the extracellular space for a prolonged period ($\geq$ 44.04 sec) which can cause neuro-excitotoxicity.

Based on the simulation results, the changes in the neuron-astrocyte dynamics during extrasynaptic transmitter sites have constructive and destructive implications for neuronal information processing. Neuron-astrocyte interactions support neural firing and synchronization and synaptic coordination [12, 391]. However, according to Deplanque [392], overload in Glu^- within the synaptic space causes detrimental excitotoxic effects to the postsynaptic spine head by exaggerating the activation of its receptors. The impairment of such glial-neuronal interaction (consisting of perinodal astrocytic components) may result in schizophrenia, as shown in the pathophysiological study conducted by Mitterauer [140]. Neurodegenerative diseases, such as Alzheimer's, are caused when astrocyte Ca^{2+} signaling is altered [393]. On the contrary, the inadequacy in Glu^- may cause the severity of Alzheimer's disease. Therefore, synaptic Glu^- insufficiency can be avoided during synaptic transmission by the additional extrasynaptic transmitter sites provided by the axon-astrocyte interaction. In that case, excessive Glu^- in the synaptic area exaggeratedly activates postsynaptic receptors damaging neurons.

5.2.4.3/ Astrocytes Form a New Level of Functional Integration.

Rossi [349] suggested that the intercellular coordination of elements within the astrocytic domain indicates a new layer of functional integration that does not entirely include synaptic networks. Here, we present a tripartite synapse model whose dynamics are not dependent only on the tripartite area. This model is not restricted to the perinodal astrocytic process and may be varied to represent perineuronal astrocytic processes, as neuron-astrocyte signaling is not only synapse-specific but cell- and circuit-specific as well [394]. If astrocyte influences thousands of neuronal elements within its territory, it suggests that the individual astrocytic processes in its branch and branchlets and its somata form a new level of functional integration. We recommend further biophysical investigation and model formulation on astrocytes viewed as a compartmentalized system, similar to neurons, rather than a point process.

We presented a model of intercellular communication between a neuron and astrocyte

that includes synaptic and nonsynaptic processes. In the current wave of research on astrocytic processes, conflicting views on gliotransmission, an artifact or reality, arise. Over the years, controversies regarding gliotransmission have emerged, whether it is a natural astrocytic process or a consequence of pharmacological stimulation [8, 395]. Fiacco and McCarthy [396] deduced that gliotransmission is not a physiological mechanism but the result of observing cultured astroglia in vitro; thus, it does not affect short- and long-term plasticity. Savtchouk and Volterra [295] contradicted the "negative" evidence on astrocytic Ca_a^{2+} waves, explaining that this concept is due to oversimplification of data collection techniques and presumptions on the interpretation of results. A century ago, Santiago Ramon y Cajal expressed that the real purpose of glial cells would only be known when a direct method of studying them is available [397]. Heterogeneity and complexity of astrocytic mechanisms lead to divergence in conclusions on the exact role of astrocytes in information transfer. Until researchers arrive at a coherent view, differences in perception imply that our current knowledge of astrocytic mechanisms is inadequate. Moreover, interaction between local $[Ca^{2+}]_a$ elevations and their propagation through the cell and astrocytic network is inconclusive. Future experimental and methodological advances will provide clarifications of these issues.

5.3/ Modeling Neuron-Astrocyte Network

Previously, we discussed the roles of astrocytes in synaptic information transfer and acknowledged that the heterogeneous properties of astrocytes could either improve or impair synaptic communication. In this section, we continue our analysis on the astrocyte syncytium, looking into the influence of astrocytes in a global perspective, that is, their functions in a neuron-astrocyte network. The main goal in this section is to develop a spiking network of neurons and astrocytes with varying connectivity, where astrocytes are connected via gap junctions and communicate through ICW propagation.

Then, what network architecture should we use if we implement a neuron-astrocyte network in image processing or deep learning applications? Depending on the intended output, how should astrocytes be connected to increase synaptic efficacy or improve network activity? In what specific applications can we employ astrocytes? We aim to unravel these questions at the end of this section; to relate and inspire artificial networks based on biological network processes.

5.3.1/ Calcium Wave Propagation Functional Model

5.3.1.1/ Tripartite Synapse (Synchronous Release) Model

In the extended tripartite synapse model (Figure 5.10), the astrocytic process modulates the presynaptic release probability and the postsynaptic potential via the SICs. This paradigm makes the tripartite synapse both a feedforward and feedback system. In this model, the Hodgkin-Huxley mechanism models the presynaptic bouton membrane potential, V_{in}, and action potential generation. Refer to Equation 2.11 and Table A.1. We employed the synchronous neurotransmitter release process, where the presynaptic bou-

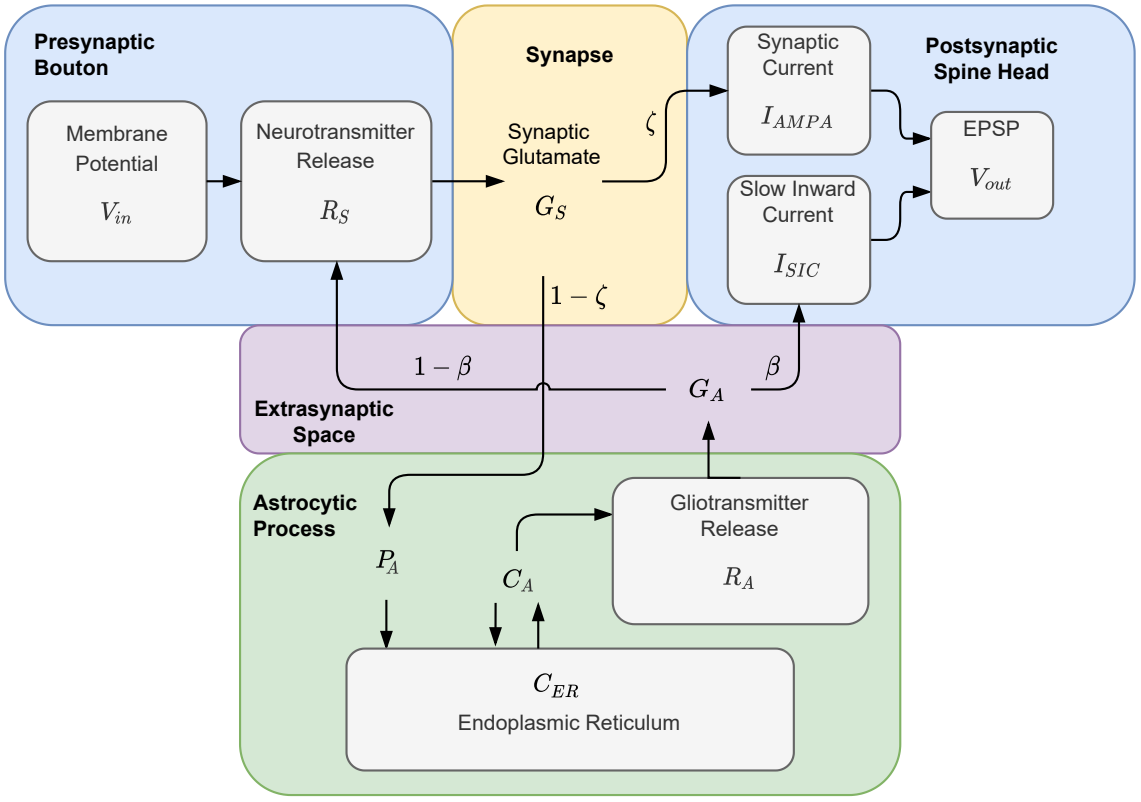

Figure 5.10: Tripartite synapse model with feedforward and feedback signaling pathways. The membrane potential (V_{in}) of the presynaptic neuron axon terminal, as well as the extrasynaptic glutamate concentration (G_A), set the amount of neurotransmitter release (R_S). Vesicles release neurotransmitters into the synaptic cleft each time an action potential arrives. A fraction, ζ, of synaptic glutamate (G_S) activates the postsynaptic spine head, and the astrocytic process receives the remaining fraction spilling out of the synaptic cleft. Synaptic glutamate interaction with mGluRs results in IP_{3_a} production, which subsequently results in CICR from the ER. Endoplasmic reticulum calcium reuptake occurs via SERCA pumps. In addition, $[Ca^{2+}]_a$ ions leak from the ER to the cytosol. An increase in the amount of cytosolic C_A above threshold results on the gliotransmission release. Gliotransmitters (G_A) activates iGluRs in the postsynaptic spine head and presynaptic bouton, with fractions equal to β and $1-\beta$, respectively. The sum of the slow inward current (I_{SIC}) due to G_A and the synaptic current (I_{AMPA}) current results in excitatory postsynaptic potential V_{out}.

ton releases synaptic glutamate simultaneously with the arrival of the AP. Here, we used the Tsodyks Model [177] described in Chapter 3 to compute for a fraction of effectively released neurotransmitters, R_S. This parameter sets the amount of Glu^- in the synaptic cleft. Given the vesicular [Glu^-] in the synaptic cleft, G_S, the total amount of released Glu^- in the synaptic cleft at time t_{AP} is G_{rel} [178]. Refer to Equation 3.29. The control parameter ζ sets the fraction of G_S that activates the AMPA receptors in the postsynaptic spine head and the amount of Glu^- spilling over to the extracellular spaces that activate astrocytic mGluRs.

The astrocytic IP_3 production follows a simple model depending only on the synaptic input [398], given as

$$\frac{dP_A}{dt} = \frac{P_0 - P_A}{\tau_{IP_3}} + r_{IP_3}(1-\zeta)G_S \tag{5.2}$$

where P_A is the astrocytic [IP_3] at time t. The astrocytic Ca^{2+} dynamics also follow the Li-Rinzel model [162] used in the previous section. Refer to Subsection 4.3.1.1 for the models and Table A.6 for the parameters. Here, the astrocytic gliotransmitter release

process is a deterministic approach, akin to the neurotransmitter release process, where gliotransmitters release is simultaneous with the crossing of astrocytic [Ca^{2+}] (C_A) above the Ca^{2+} threshold instead of the Ca^{2+}-binding with SLMV. This model by De Pitta and Brunel [178] described in Equation 4.42 models the amount of glutamate released into the extracellular space R_A. The control parameter β sets the amount of extrasynaptic Glu^{-}, G_A, diffusing to the extrasynaptic iGluRs on presynaptic and NMDARs on the postsynaptic membranes. The feedback amplifies the neurotransmitter release probability while the feedforward signal triggers the influx of SIC through NMDARS. Refer to Table A.9 for the set of parameters.

For excitatory synaptic currents, we consider the fast component of AMPAR-mediated EPSC and the slow dynamics of the NMDAR-mediated SIC. The synaptic voltage caused by I_{AMPA} is modeled by the instantaneous jump and exponential decay function originally presented by Fourcaud-Trocme [114] in Equation 3.40 and modified by De Pitta and Brunel [178] shown in Equation 3.41. Due to the presence of SICs, the synaptic input, v_S, is further extended into

$$\begin{aligned} \tau_N^r \frac{dv_S}{dt} &= -v_S + \hat{I}_S B_S \tau_N^r, \\ \tau_N \frac{dB_S}{dt} &= \frac{dB_S}{dt} = -B_S + \hat{J}_S \zeta G_S \tau_N, \end{aligned} \tag{5.3}$$

where τ_N^r and τ_N, respectively, are the rise and decay time constant of the EPSC, $\hat{J}_S$ is a scaling factor corresponding to the amplitude of the instantaneous jumps that causes the gating variable B_S to increase unitarily, and $\hat{I}_S$ is also a scaling factor that sets the increase in synaptic current equals I_S. These scaling factors are described as

$$\begin{aligned} \hat{J}_S &= \frac{J_S}{\varrho_c G_{S_T} \tau_N}, \\ \hat{I}_S &= \frac{I_S \left(\frac{1}{\tau_N} - \frac{1}{\tau_N^r} \right)}{\left(\frac{\tau_N^r}{\tau_N} \right)^{\frac{\tau_N}{\tau_N - \tau_N^r}} - \left(\frac{\tau_N^r}{\tau_N} \right)^{\frac{\tau_N^r}{\tau_N - \tau_N^r}}}. \end{aligned} \tag{5.4}$$

The voltage dependence of SIC is negligible, therefore the extrasynaptic input due to SIC, v_A, is modeled similarly with v_S but with different time scales. Refer to Equation 4.49. Note that G_A is multiplied to the control parameter β.

The postsynaptic membrane potential, V_{out}, is, therefore, the summation of the synaptic I_{AMPA} and extrasynaptic I_{SIC} inputs, and evolves as

$$\tau_m \frac{dV_{out}}{dt} = V_{rest} - V_{out} + v_S + v_A, \tag{5.5}$$

where τ_m is the membrane time constant equal to 40 ms and the resting potential $V_{rest} = -70$ mV. For the postsynaptic membrane potential, the parameters are in Table A.10.

5.3.1.2/ Astrocytic Network Model

We extend the intercellular communication beyond the tripartite synaptic area to model the ICW. We developed a network of astrocytes where the processes and soma are inde-

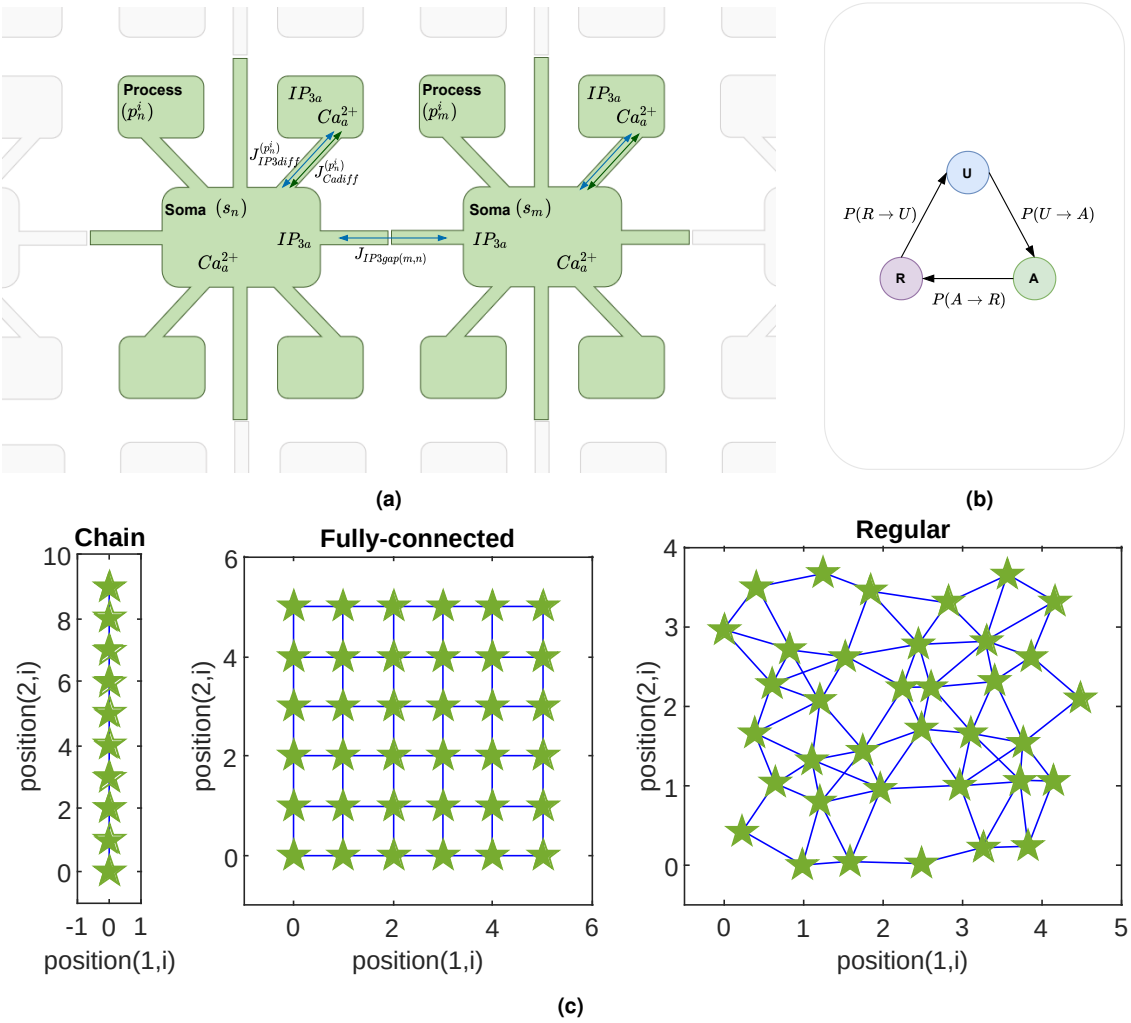

Figure 5.11: Astrocytic network model. (a) Each astrocyte is divided into compartments $p(i)$ denoting the astrocytic process where i corresponds to the process number and s_n (s_m) denoting the soma where n (m) corresponds to the cell number in the network. Intracellular calcium signaling occurs between processes and soma of individual astrocytes, while IP_3 signaling occurs both intra- and intercellularly (via gap-junction connections). (b) The shift between states of the astrocyte is a Markov process where P corresponds to the event that a cell changes its state. (c) The astrocytes (green stars) form a network via gap junctions (blue lines) with varying topologies: chain where each astrocyte is connected in series, fully connected where the astrocytes form a lattice, and regular where each cell is connected to its k nearest neighbor.

pendent compartments whose joint function is to integrate synaptic inputs via local and global Ca_a^{2+} oscillations and where astrocytic somas are connected with the neighboring astrocytes via GJCs to allow intercellular communication. Consider the astrocyte n in Figure 5.11a. Assuming homogenizations, the processes (p_n^i) and soma (s_n) are separate compartments that interact with the other compartments (neighboring processes or soma, and vice versa) via the Ca^{2+} and IP_3 diffusion along the branches. Here, i is the number of the astrocytic process and n is number of astrocytes in the network, while m is the number of astrocytes linked to n. Astrocyte n communicates with its neighbor m via the exchange of IP_3 molecules through the GJC. Therefore, the communication with astrocyte n causes an increase or decrease in [IP_3] in astrocyte m, affecting is intracellular Ca^{2+} oscillations. It is important to note that only the processes receive synaptic inputs triggering IP_3 production. Therefore, P_A in the soma from molecular diffusion between the

processes and the soma, and the IP_3 influx from GJCs. In addition, only the processes reaching a local C_A above threshold releases gliotransmitters into the input-specific extrasynaptic area.

There are two additional fluxes in the Ca^{2+} dynamics: (1) the $J_{IP_3diff}^{(p_n^i)}$ which is the amount of IP_3 diffusing from (p_n^i) to (s_n) or vice versa, and (2) the $J_{Cadiff}^{(p_n^i)}$ corresponding to the amount of Ca^{2+} also diffusing between the process and the soma. These fluxes are concentration gradients given as

$$\begin{aligned} J_{IP_3diff}^{(p_n^i)} &= D_P\left(P_A^{(s_n)} - P_A^{(p_n^i)}\right), \\ J_{Cadiff}^{(p_n^i)} &= D_C\left(C_A^{(s_n)} - C_A^{(p_n^i)}\right), \end{aligned} \tag{5.6}$$

where D_P and D_C, respectively, are the IP_3 and Ca^{2+} diffusion constants between the process and the soma.

The IP_3 flux through the gap junction, $J_{IP_3gap(n,m)}$ is described by the threshold function in Equation 4.51. The ability of the astrocyte to send or receive $J_{IP_3gap(n,m)}$ is stochastic, depending on its state and the states of its neighbors. We apply the Markov process to determine the state of the astrocyte and its probability, P, to shift from one state to another, depicted in Figure 5.11b. Refer to the UAR model in Chapter 4.5.3. Here, the astrocyte can only transmit signals in the active (A) state.

Let $P_A^{(p_n^i)}$ be the IP_3 and $C_A^{(p_n^i)}$ be the cytosolic $[Ca^{2+}]$ in the process compartment. Therefore,

$$\begin{aligned} \frac{dP_A^{(p_n^i)}}{dt} &= \frac{P_0 - P_A^{(p_n^i)}}{\tau_{IP_3}} + r_{IP_3}\left(1-\zeta\right)G_S + J_{IP_3diff}^{(p_n^i)}, \\ \frac{dC_A^{(p_n^i)}}{dt} &= -J_{chan}^{(p_n^i)} - J_{pump}^{(p_n^i)} - J_{leak}^{(p_n^i)} + J_{Cadiff}^{(p_n^i)}. \end{aligned} \tag{5.7}$$

Let $P_A^{(s_n)}$ be the somatic $[IP_3]_a$, the sum of all the fluxes flowing from the processes and the GJCs, and $C_A^{(s_n)}$ is the somatic $[Ca^{2+}]_a$ with additional fluxes from the processes.

$$\begin{aligned} \frac{dP_A^{(s_n)}}{dt} &= \frac{P_0 - P_A^{(p_n^i)}}{\tau_{IP_3}} - \sum_{i=1}^{k} J_{IP_3diff}^{(p_n^i)} + \sum_{m=1}^{j} J_{IP_3gap(n,m)}, \\ \frac{dC_A^{(s_n)}}{dt} &= -J_{chan}^{(s_n)} - J_{pump}^{(s_n)} - J_{leak}^{(s_n)} - \sum_{i=1}^{k} J_{Cadiif}^{(p_n^i)}. \end{aligned} \tag{5.8}$$

We also consider the ratio between the process and somatic surface areas to account for the impeding influence of larger somatic volume to Ca^{2+} flux [303]. By homogenization, we assume that all processes have the same dimension; therefore, the ratio V_r is equal to $V_{soma}/V_{process}$ and the surface volume ratio is $V_{surf} = V_r^{(2/3)}$. In this model,$V_r = 1.5$. The

somatic dynamics become

$$\begin{aligned} V_r \frac{dP_A^{(s_n)}}{dt} &= V_{surf}\left(\frac{P_0 - P_A^{(p_n^i)}}{\tau_{IP_3}}\right) - \sum_{i=1}^{k} J_{IP_3 diff}^{(p_n^i)} + \sum_{m=1}^{j} J_{IP_3 gap(n,m)}, \\ V_r \frac{dC_A^{(s_n)}}{dt} &= V_{surf}\left(-J_{chan}^{(s_n)} - J_{pump}^{(s_n)} - J_{leak}^{(s_n)}\right) - \sum_{i=1}^{k} J_{Cadiff}^{(p_n^i)}. \end{aligned} \tag{5.9}$$

Three types of astrocytic connectivity were considered (Figure 5.11c): (1) astrocytes are connected in series (chain), (2) astrocytes form a lattice (fully-connected), and (3) astrocytes are randomly connected with k nearest neighbors in the network where k is the degree of connection [293]. Overall, the shallow network comprises three layers of neurons: the HH presynaptic neuronal layer, the IF postsynaptic neuronal layer, and the astrocytic layer between the neuronal layers forming the tripartite synapses.

5.3.1.3/ Synaptic Efficacy

The postsynaptic neurons integrate the synaptic inputs, and when the summation of $V(t)$ exceeds the threshold (–40 mV), the neuron fires an action potential. Synaptic efficacy, ρ, here is another parameter defined as the coupling strength between the pre- and postsynaptic components. It determines the strength of communication between the neurons. We modified the synaptic efficacy equation from De Pitta and Brunel [178] so that the synaptic efficacy is dependent on the synaptic inputs and the spiking activity of the neuron. Let ρ be described by the first-order differential equation

$$\tau_\rho \frac{d\rho}{dt} = -\rho(1-\rho)(\rho_b - \rho) + \gamma_p(1-\rho)\Theta\left(V(t) - \theta_p\right) - \gamma_d \rho \Theta\left(V(t) - \theta_d\right), \tag{5.10}$$

where $V(t)$ is the input summation voltage of the presynaptic neuron, ρ_b is the boundary parameter, τ_ρ is the decay time constants, and γ_p and γ_d are the corresponding rate of increase and decrease in synaptic efficacy, respectively, when $V(t)$ exceeds the depression and potentiation thresholds, θ_d and θ_d, with $\Theta(\cdot)$ the Heaviside function. Synaptic efficacy strengthens the contribution of V_{out} for every successful postsynaptic spike. Refer to Table A.11 for the parameters.

5.3.2/ Simulation Method

The neuron-astrocyte network was simulated in MATLAB by performing numerical analysis of the systems of differential equations using Runge-Kutta with time step $dt = 0.5$ ms. In the simulation, we used the handwritten images from the modified National Institute of Standards and Technology (MNIST) database [16] instead of entirely random inputs. In this case, we can also visualize and make sense of the activity of the output layer. Each pixel corresponds to a presynaptic neuron, where each image is fed to the network for 200 seconds. Therefore, the presynaptic neuron receives a 5 Hz input current whose pulse amplitude varies from 0–10 μA/cm^2 proportional to the pixel intensity in grayscale and pulse width of 4 ms. The network was simulated for 200 continuous batches of 100

images each, 4000 seconds in total length.

The shallow spiking neuron-astrocyte network, therefore, consists of three layers: an input layer with 784 presynaptic HH neurons (equal to the number of pixels in an MNIST image), an output layer of 196 postsynaptic IF neurons linked to four distinct presynaptic neurons, and an astrocytic network creating the tripartite synaptic connections distributed equally to 196 astrocytes, in that each astrocyte has four process compartments connected to distinct synapses. Then, we simulated the network for the three types of astrocytic connectivity: chain, fully connected, and regular topology (maximum of five gap junction connections). Calculations were performed using HPC resources from DNUM CCUB (Center de Calcul de l'Université de Bourgogne).

5.3.3/ RESULTS

The following section presents the simulation results and analysis in a bottom-up approach, starting from the local tripartite synapse and astrocytic compartments, moving up to the single-cell activity, and finally to the network level.

5.3.3.1/ TRIPARTITE SYNAPSE DYNAMICS (SYNCHRONOUS RELEASE)

Figure 5.12 summarizes the dynamics of a single tripartite synapse compartment simulated for 20 seconds. The presynaptic bouton generates an AP pattern (V_{in}) with 5 Hz spiking frequency (Figure 5.12a). In the synchronous and deterministic model, the synaptic release probability, R_S, peaks simultaneously with the arrival of AP, whose peak amplitudes vary between 0.68 to 0.74 (Figure 5.12b). As a result, the synaptic [Glu$^-$], G_S, also fluctuates in accordance with the AP spikes, with an average peak concentration of 0.20 mM (Figure 5.12c).

Twenty-five percent of G_S diffuses to the astrocytic process and activates the astrocytic IP_3 production, as shown in Figure 5.12d. From the initial condition, $P_0 = 0.16\ \mu$M, and with a constant input frequency, P_A increases and saturates at a level equal to 0.45 μM. Figure 5.12e depicts the slow astrocytic calcium dynamics (C_A) in the process compartment. Note that the astrocytic IP_3 and Ca^{2+} dynamics shown here results from blocking the control factors D_P and D_C. The astrocytic process then releases extrasynaptic Glu$^-$ at the event that C_A crosses above threshold (0.197 μM) as shown in Figure 5.12f. Also, half of G_A (given that $\beta = 0.5$) modulates the presynaptic neuron activity by increasing R_S (Figure 5.12b) and, in turn, also modulates the synaptic Glu$^-$ activity (Figure 5.12c). It is noticeable that R_S and G_S increase following the astrocytic Glu$^-$ release.

A single postsynaptic spine head generates an excitatory input, shown in Figure 5.12g, with a peak amplitude of 3 mV through fast AMPARs activations controlled 75% of G_S ($\zeta = 0.75$). In addition, the astrocytic process indirectly modulates the postsynaptic activity, remarking that V_{AMPA} (v_S), peaks with G_A activity. The remaining half of G_A activates SIC in the postsynaptic spine head, generating a slow excitatory input V_{SIC} (v_A), as shown in Figure 5.12h, with a peak amplitude of 1 mV. The summation of these excitatory inputs leads to the postsynaptic spine head membrane potential shown in Figure 5.12i.

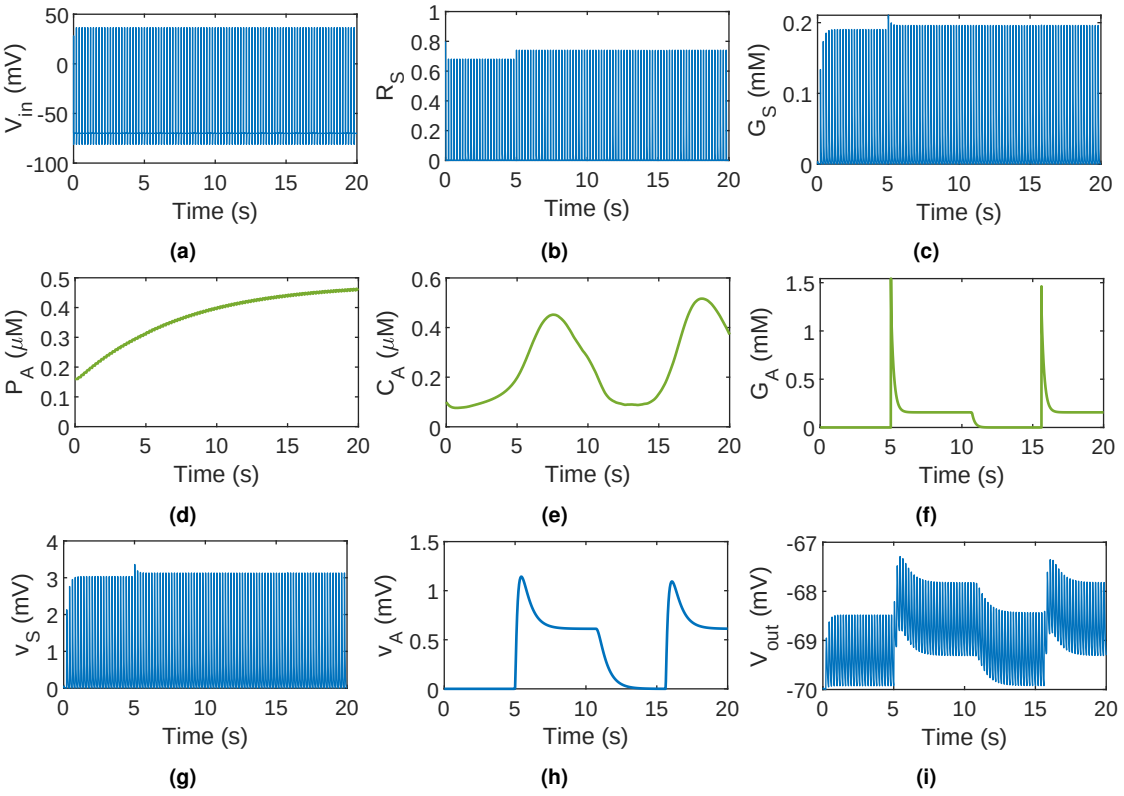

Figure 5.12: Tripartite synapse dynamics with synchronous neurotransmitter release, showing the interrelationships of the fundamental signaling mechanisms and pathways between the (a-c) presynaptic bouton, (d-f) astrocytic process, and (g-i) postsynaptic spine head.

5.3.3.2/ Calcium Wave Propagation

We extended the analysis from the tripartite synapse to the astrocytic cellular activity and changed the inputs to random frequencies based on the MNIST dataset. Four processes and the soma exchange signal via the Ca^{2+} and IP_3 diffusions (Figure 5.13a and 5.13b). Both the diffusion coefficients D_P and D_C are equal to 0.005, which maintains the dynamics between the soma and the processes, and subsequently sets the boundaries of P_A between P_0 and 0.5 μM to prevent oversaturation or depletion of the signaling molecules within a compartment. The somatic Ca^{2+} oscillation (Figure 5.13a) exhibits global events during the first and last spikes and independently local events from $t = 15$ to $t = 40$ seconds. Synaptic inputs stimulate IP_3 production exclusively in astrocytic processes; consequently, somatic P_A (Figure 5.13b) is entirely due to intracellular diffusion of IP_3 from the processes, or intercellular diffusion through gap junction connections. Intracellular Ca^{2+} oscillation then triggers the glutamate release activity that favors the synchronization of compartmental activities (Figure 5.13c).

All four neighbors of the astrocyte under consideration exchange IP3 soma-to-somatically through gap junctions. Figure 5.13d and 5.13e show the Ca^{2+} and IP_3 dynamics of the soma and its neighbors. The probability that the astrocytic state changes from inactive (U) to active (A) and then to refractory (R) depends on the Ca^{2+} dynamics of both the subcellular compartments and the somatic compartments of its adjacent cells (Figure 5.13f). The P_A level increases when the astrocyte is in the U and R states; the increase rate is

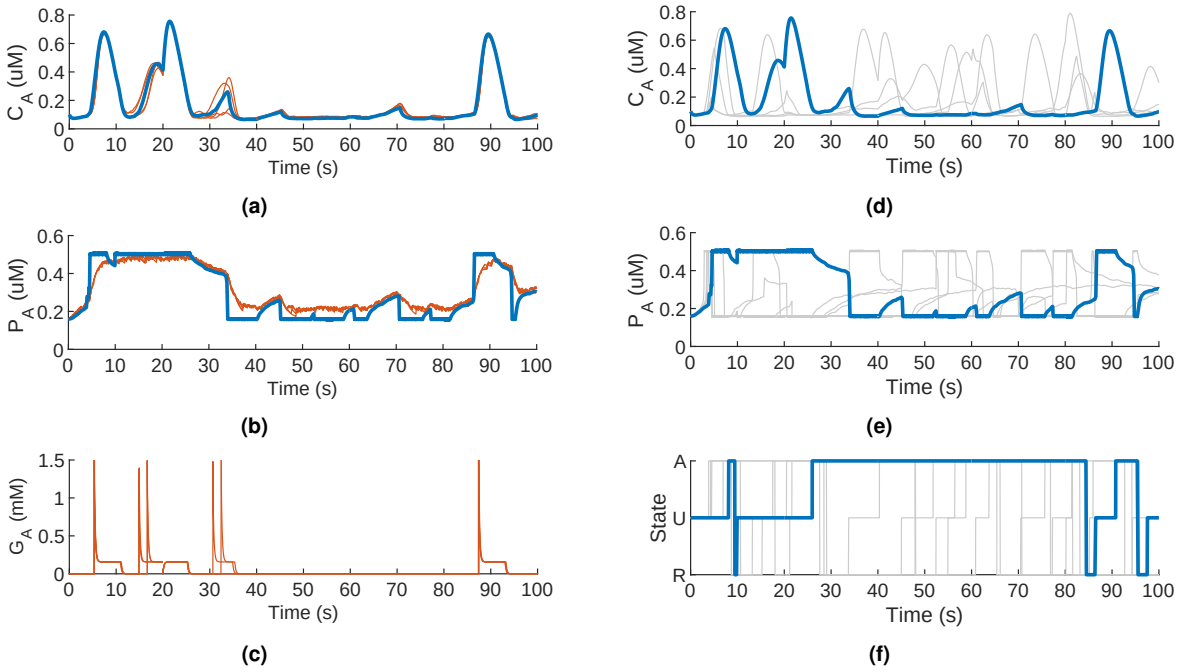

Figure 5.13: Intra- and intercellular activities in a single astrocyte. (a) Intercompartment molecular exchange between compartments leads to somatic (*blue*) and process (*red*) Ca^{2+} dynamics showing local and global events. (b) The somatic P_A increase is the summation of IP_3 fluxes from the astrocytic processes. (c) Astrocytic processes exhibit synchronous and asynchronous G_A spiking activity following the Ca^{2+} events. On the network level, (d) Ca^{2+} and (e) IP_3 dynamics of the soma (blue) are also dependent on the molecular concentration levels of its neighboring astrocytes (*gray*). (f) Whether the astrocyte can communicate with its neighbors depends primarily on its state.

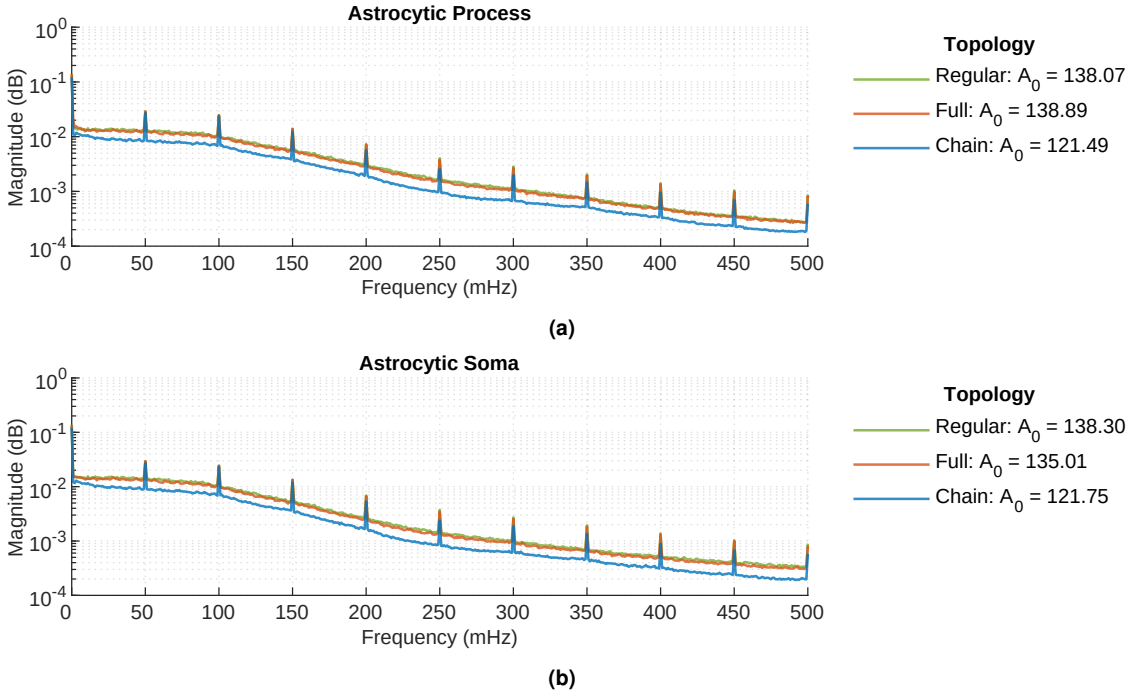

Figure 5.14: Spectral analysis of Ca^{2+} oscillation in (a) the processes and (b) somas.

maximal during the U state, where its gap junction connections permit IP_3 influxes. Inversely, the somatic Ca^{2+} and IP_3 levels drop in the A state as the astrocyte becomes readily available for IP_3 exchange.

We developed an astrocytic network model, a syncytium that operates as a singular system. We simulated the three network architectures with varying astrocytic topology (chain, full, and regular) for 4000 seconds. Next, we characterized the global (network level) astrocytic Ca^{2+} oscillations by converting the temporal responses of all the compartments into their corresponding frequency responses using Fast Fourier Transform (FFT). Figure 5.14 shows the comparisons between the process and soma Ca^{2+} spectra. The C_A levels fluctuate between frequencies from 0 to 500 mHz, with peak amplitudes at $f = [0 : 50 : 500]$ mHz. The magnitudes are steady at frequencies less than 100 mHz and start to decrease beyond that. In addition, the spectra suggest that the networks exhibit more Ca^{2+} activities in the processes than in the soma. Moreover, the astrocytic network with chain topology exhibits lower Ca^{2+} activity than the regular and full network topologies, particularly during steady-state at $A(0)$, whereas the full and regular networks have similar global activities.

5.3.3.3/ Astrocytic Glutamate Spiking Activity

Intracellular calcium wave propagation indirectly modulates the neural activity via astrocytic Glu^- spikes. Therefore, we examined the spiking behavior of the astrocytes under varying levels of connectivity. The raster plots in Figure 5.15a display the spiking pattern of the astrocytic processes during the initial 100 seconds of stimulation. Of the three networks, synchronous spiking activity is apparent primarily in the chain topology (notably at $t = [20, 40, 60]$ s) and least in the regular topology. Meanwhile, regular topology appears to have more frequent and dispersed spiking activity, in which processes at the extremities (process number $<$100 and $>$700) were active, unlike in the chain topology. Additionally, Figure 5.15b gives the number of spikes per second (equivalent to the number of Glu_A^--releasing astrocytic processes. The results support the previous expectation that series-connected astrocytes favor network synchrony, whereas the spike rate decreases in the full topology and is minimal in the regular connection.

To gain insight into the effect of ICW propagation in the network, we map the presynaptic input into astrocytic output. Figure 5.16 shows the average spiking rate of input and output per astrocyte in the network, given that the chain, full, and regular networks receive the same set of stimuli. The input pattern in Figure 5.16a reveals certain astrocytes that receive no presynaptic input. The IO comparisons show that the chain topology spiking distribution (Figure 5.16b) reflects the input pattern compared with the other topologies. On the other hand, the influence of ICW becomes more prominent in the full (Figure 5.16c) and most in the regular topology (Figure 5.16d), noting the increase in spike rate of those astrocytes with no presynaptic input. Therefore, the spikes in astrocytic processes, such as those found in the extremities (Figure 5.15a), result from intracellular Ca^{2+} diffusion and gap junction mediated IP_3 diffusion rather than neurotransmission. The spike rate distributions (Figure 5.16) suggest that the more gap junction connections an astrocyte has, the slower it will take for local C_A to reach the threshold, shown by the decrease in spike rates of those astrocytes initially receiving the presynaptic inputs.

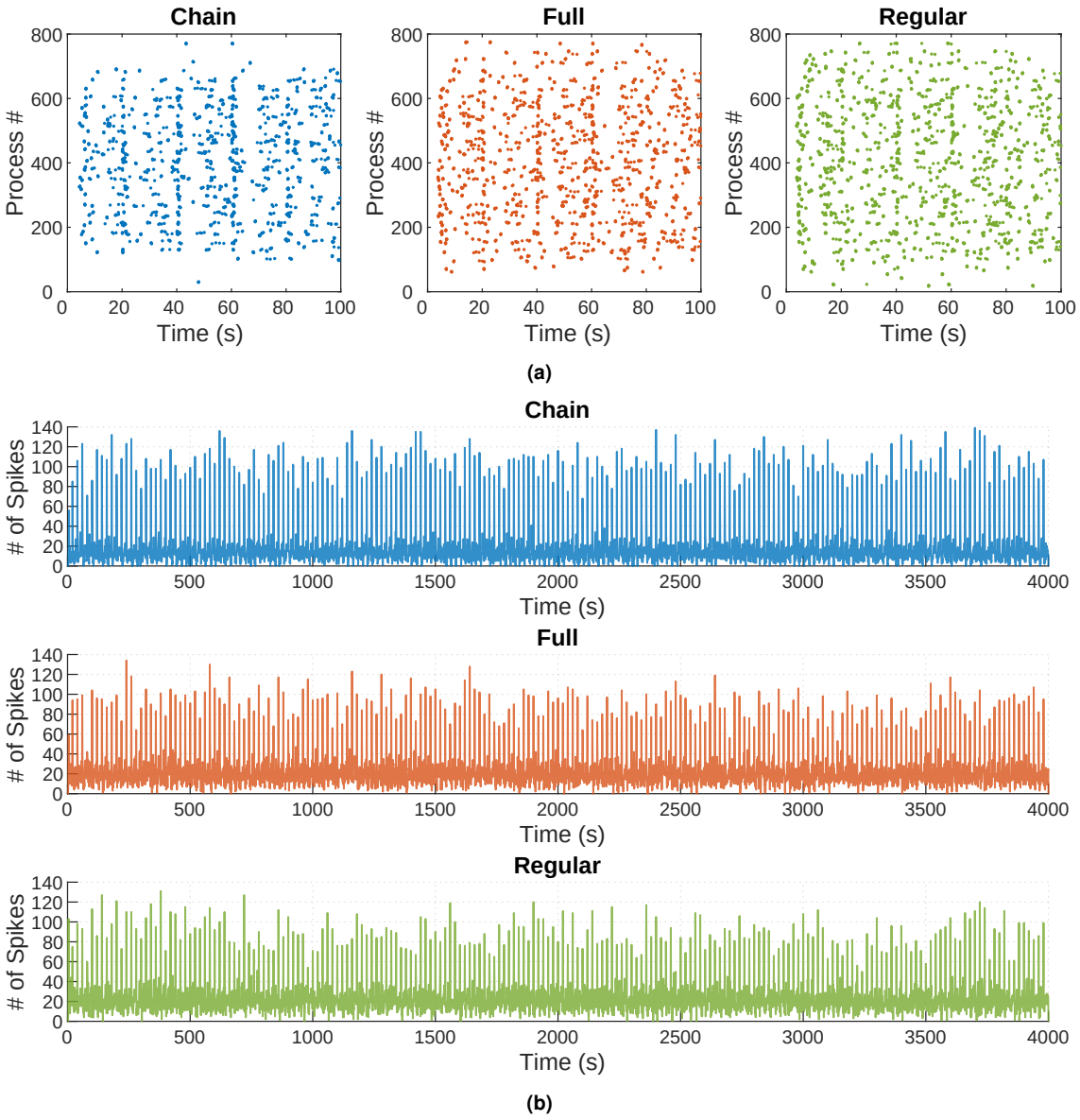

Figure 5.15: Astrocytic network spiking behavior. (a) The raster plots and (b) the Glu_A^- spikes per second graphs for the chain, full, and regular astrocytic network topologies suggest that the chain topology favors synchronous activity.

5.3.3.4/ Synaptic Release Probability and Efficacy

Extrasynaptic glutamate then modulates the neurotransmitter release probability. In the synchronous release process, the presynaptic bouton release Glu^- upon the arrival of AP. We also simulated a network without astrocytes while maintaining the neural network architecture. The deterministic release results in constant counts of synaptic Glu^- spikes in all topologies, though they differ in the spike amplitude, based on the activity and inactivity of the astrocytic process (except to the neural network). The synaptic release peak probability, R_S, changes from 0.685 to 0.745 upon iGluRs activation during gliotransmission. Given the same input pattern, the chain topology produces higher synaptic release probability, as presented in Table 5.2, indicating that 68.57% (out of 2.26×10^6) of synaptic

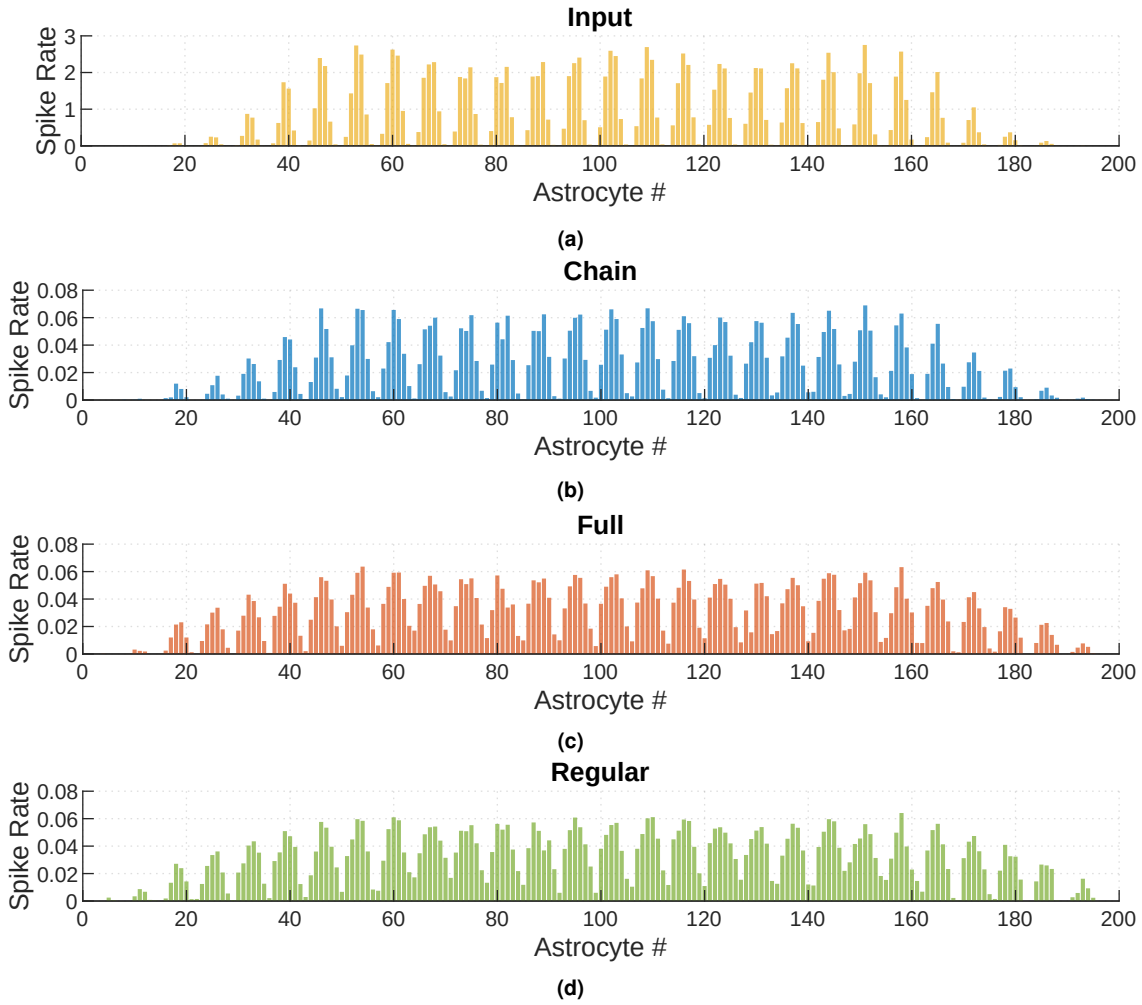

Figure 5.16: Comparison between the average spiking rates of the input and the astrocytes in the network.

release events are astrocytic Glu^{-}-mediated. It also reveals that even though more astrocytes get activated in the full and regular topologies (shown in Figure 5.16c and 5.16d), gliotransmission occurs in short durations.

Synaptic efficacy determines the strength of communication between the pre- and the postsynaptic components, computed by comparing the number of successful postsynaptic spikes over the number of presynaptic input spikes, where successful spikes are those $V_{out} \geq -50$ mV, per 20 second-time windows. We performed a two-dimensional correlation

Table 5.2: Synaptic release probability.

Topology	Counts (%)	
	Without Gliotransmission $R_S = 0.685$ (peak)	With Gliotransmission $R_S = 0.756$ (peak)
No Astrocyte	100	0
Chain	31.43	68.57
Full	32.48	67.52
Regular	32.56	67.44

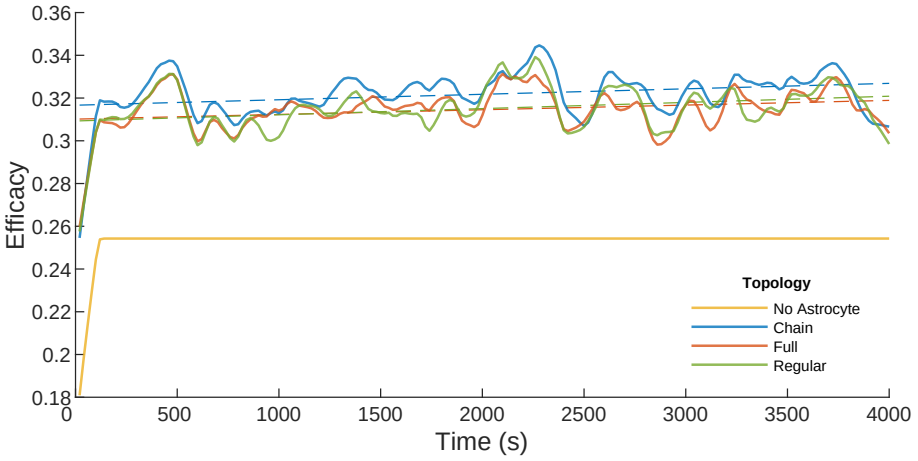

Figure 5.17: Average synaptic efficacies (*solid lines*) in networks with varying astrocytic topologies. The corresponding linear fits (*dashed lines*) indicate increasing efficacy with time.

between the input and output spikes using the `corr2` MATLAB function to get the efficacy curves shown in Figure 8. The curves indicate that neuron-astrocyte networks perform more reliable synaptic communication than neurons. Here, the synaptic efficacy of the neuron network (No Astrocyte) increases to and saturates at 0.254. Neuron-astrocyte networks exhibit higher but fluctuating efficacy. The chain topology also produces the highest efficacy, consistent with its synaptic release probability (Table 5.2) and spiking rate (Figure 5.15b). In addition, the linear fits indicate that the efficacy gradually increases with time (except in No Astrocyte topology).

5.3.4/ Discussion

We have developed spiking neuron-astrocyte networks with varying astrocytic topologies and analyzed its dynamics from the bottom up: from the subcellar compartments to the single cells and finally to the network level. The tripartite synapse with deterministic neurotransmitter release process is a feedforward and feedback system, where the presynaptic neuron creates input patterns with random frequency based on the pixel color intensity (in grayscale) of the input MNIST image. The postsynaptic output consists of fast and slow excitatory inputs from synaptic and extrasynaptic Glu^{-}. Fraction of synaptic Glu^{-} diffuses to the astrocytic processes. The process releases extrasynaptic Glu- which can modulate the presynaptic neuron release probability and the postsynaptic spine head membrane potential, creating closed-loop signaling pathways.

The proposed model differs from the previous models in that the proposed astrocytic cell dynamics are compartmentalized. The astrocyte performs integration of synaptic inputs in the processes, and the soma forms a new level of integration of Ca^{2+} molecules diffusing from the processes, rather than the commonly employed single point process. In addition, the astrocytic also communicates with its gap-junction connected astrocytes. Communication occurs based on the state of the astrocyte and not solely by the IP_3 gradient between the cells. The change of state, a Markov process, is highly stochastic and adds complexity to the direction of ICW propagation in the astrocytic network. Given the complexity of the model and the numerous variables involved, HPC resources allowed

us to observe the activity of every compartment in the network.

Extending the model to the network level, we simulated three networks with different astrocytic topologies: series connection, the full connection forming a lattice, and a regular connection forming a k-NN random network. The simulation results indicate that the astrocytic network topology though highly heterogeneous depending on its location in the brain is an essential factor in determining the function of the astrocytes in that network. The astrocytic connectivity indicates the distance a Ca^{2+} wave can travel and influence distant astrocytes in the network and, indirectly, the distant neurons. For example, in Figure 5.15 and Figure 5.16, ICW in chain topology travels slower due to the distance between astrocytes, resulting in confined communication between adjacent cells. Meanwhile, ICW in lattice and random networks influence numerous astrocytes, producing a more dispersed spiking activity as shown in the raster plots.

5.3.4.1/ Astrocytic Connectivity Driving Network Synchrony

There are two levels of synchronization in the proposed astrocytic network. The first one is at the cellular level, wherein the astrocytic processes release extrasynaptic Glu^{-} simultaneously, albeit they receive different presynaptic input patterns (Figure 5.13c). The synchronization is an effect of the IP_3 and Ca^{2+} intracellular diffusions, as shown in the global activity (all compartments have similar molecular levels) of the cell in Figure 5.13a and 5.13b. The second is the network level synchronization, wherein various astrocytes (adjacent or distant) simultaneously activate Glu_A^- spikes, as depicted in Figure 5.15. In this case, synchrony is a consequence of ICW propagations and the stochastic shift of astrocytic states.

One of the main functions of the astrocytic syncytium in neural activities is to maintain network synchronization [314, 399]. A single astrocyte enwraps numerous synapses of different neurons and can simultaneously modulate the postsynaptic neuron spiking activity during global Glu_A^- release. The simulation results suggest that the astrocytes connected in series generate a more synchronous activity than those connected in lattice or random, as shown by the average Glu_A^- spike rate in Figure 5.15b. One can hypothesize that the more gap-junction connected astrocytes, the greater the network synchrony; however, the results suggest the opposite. For chain topology with a maximum of two neighboring astrocytes, the ICW is restricted within these cells, and the compartmental $[Ca^{2+}]_A$ increase rate from active and inactive is fast. In contrast, the full and regular topologies have more neighboring astrocytes participating in gap junction mediated IP_3 exchange. Crossing the Ca^{2+} threshold takes longer for an astrocyte because it has more adjacent astrocytes to share its IP_3 content. The spectrum in Figure 5.14b shows that the chain topology has the lowest Ca^{2+} oscillation magnitude, supporting the assumption that the Ca^{2+} oscillation is restricted within a few cells. The Ca^{2+} level is lower because the astrocyte has fewer sources of IP_3, unlike in regular topology with a maximum of five GJCs, there is a sudden IP_3 influx once the astrocyte shifts to the U state (Figure 5.13f).

In summary, astrocytic chain topology in neuron-astrocyte networks improves network synchronization compared to the full or regular topology. Therefore, synchronization is dependent on the number of GJC mediating IP_3 exchanges and the distance of ICW propagation.

5.3.4.2/ Efficacy vs. Homeostasis

We quantified the synaptic efficacy with time by correlating the input and output spiking activity. It is evident in Figure 5.17 that the networks with astrocytes have a considerable improvement in communication strength over the neuron network alone. In addition, the levels of synaptic efficacy linearly increase with time, unlike in a neuron network that stabilizes at 0.254. This increase in efficacy corroborates our results discussed in the previous section, that astrocytes indeed support synaptic plasticity. Moreover, the chain network topology gives the highest efficacy of the three neuron-astrocyte networks, an effect attributed to the restricted ICW propagation between a few adjacent cells. Restricted ICW is evident in the average spiking rate shown in Figure 5.16a and 5.16b. Because of this restriction, IP_3 production and spiking activity of the astrocytes in chain topology significantly depends on the presynaptic spikes [300]. In addition, Vuillaume et al. [400] presented neuron-astrocyte network wherein astrocytes transform neural activity across multiple layers of neurons. It showed that the input activities are more correlated with the neuron networks than with astrocyte mediated neuron networks, which corroborates our results that neural activity in the proposed network is correlated with both the input and astrocytic activities.

Another function of astrocytic networks is homeostasis, where astrocytes prevent neurons from hyperactivity. In the case of full or regular network topology, ICW facilitates Glu_A^- release, even in the absence of presynaptic input, or weakens Glu_A^- release probability by lessening the amount of $[Ca^{2+}]_A$ in the astrocytic processes (through diffusion). The effect of ICW is noticeable in Figure 5.16c and 5.16d, where astrocytes receiving no input generate Glu_A^- spikes while those with high input rates show lower activity than in chain topology. Synaptic strengths of tripartite synapses from a single neuron are bounded in a mean efficacy. If a group of postsynaptic spine heads fires more frequently than others, astrocytes would slightly decrease the group activity and activate previously silent neurons via ICW propagation. Remarkably, the full and regular connections can best implement network homeostasis, credited to GJCs. The regular network activity in Figure 5.15b displays a dispersed astrocytic activity, indicating that neural modulation by astrocytes is widely spread in the network. Homeostasis is, therefore, necessary to maintain network stability.

In the proposed network architecture, the astrocytic heterogeneity posed a counteracting effect between efficacy (and synchrony) and homeostasis, where chain topology promotes higher efficacy while full or regular topology leads to network stability.

Therefore, whether to implement a chain, full or regular astrocytic topology entirely depends on the intended applications.

5.3.4.3/ Astrocytic Networks in Autoencoders

We used the MNIST dataset to visualize the output of the postsynaptic neurons rather than presenting a random set of spikes. Autoencoders in artificial intelligence is a type of neural network composed of an input layer encoder, a hidden layer compressor, and an output layer decoder that use unsupervised learning algorithm [401]. Gordleeva et al. [14] proposed a spiking neuron network to model working memory where the astrocytic

network promotes successful recall by modulating the synaptic connections. Though not explicitly termed, the biological model by Gordleeva et al. is equivalent to an autoencoder in artificial networks. Our proposed network architecture can also be employed as a sparsely connected autoencoder, where astrocytes help the postsynaptic spines to replicate the input signals.

Therefore, the functions of astrocytes in maintaining network synchronization, improving synaptic communication strength, promoting stabilization, and learning [402] are indicative of the potentials the astrocytes have in artificial intelligence implementations.

5.4/ CONCLUSION

Astrocytes are highly heterogeneous, with their diverse receptor expressions, complex morphology, and elaborate network connections, making the astrocytic dynamics challenging to predict. However, increasing studies support the notion that astrocytes are not just passive components but are integral components in brain computations. In this chapter, we studied the interaction of neurons and astrocytes from the ground up, from its tripartite coupling to neural modulation by ICW, and determined the possible functions of astrocytes in neural computing.

First, we focused on communication within the tripartite synapse, where we developed a detailed and biological model of the presynaptic bouton, postsynaptic spine head, and the astrocytic processes. The stochastic neurotransmitter release mediates the astrocytic processes, which forms a feedback signaling pathway through Glu_A^- that modulates the neurotransmitter release probability. The results suggest that the astrocytes indirectly modulate synaptic plasticity and increase the communication strength between the neuronal components. On the other hand, astrocytes can also impair synaptic communication due to the excitotoxicity resulting from the overactivation of neuronal receptors during a prolonged period of Glu_A^- released in the extracellular space.

We then extended the neuron-astrocyte interaction by widening the astrocytic territory by developing a neuron network for signal reconstruction using unsupervised learning mediated by astrocytic networks. We concluded that the heterogeneous connection of the astrocytic networks is not random at all but instead plays a significant role that depends on the function of the neural network. Astrocytic networks with chain topology can assist network synchrony and improve communication strength, while randomly connected astrocytes can promote network homeostasis via ICW propagation.

There are still some debates on whether astrocytes should be considered computational components, which can only be answered when leading-edge technology capable of measuring and analyzing the minute dynamics of subcellular components are available. Based on the advantages displayed by the astrocytes in our study, we continue to work under the notion that astrocytes are active components in brain processes and memory. In the following chapter, we extend our study on the neuron-astrocyte interaction by implementing a spiking network for image recognition and identifying the role of astrocytes in learning.

6

Neuron-Astrocyte Network for Image Recognition

6.1/ Introduction

Astrocytes influence neural communication on three levels. First is in the tripartite synapse compartment, where an astrocytic process via gliotransmission forms a closed-loop system consisting of a feedback pathway for modulating the presynaptic neurotransmitter release and a feedforward connection activating postsynaptic SICs. Second is the cellular level integration, where thousands of incoming presynaptic signals produce IP_3-dependent global and local Ca^{2+} elevations. During astrocytic activation, the astrocytic Glu^{-} release modulates the postsynaptic neurons coupled with the astrocyte, thus, promoting network synchrony. Lastly, at the network level, ICW propagation facilitates communication between astrocytes, allowing an astrocyte to modulate the synaptic activities of neurons not coupled with itself but with its neighboring astrocytes. The heterogeneity of the astrocytic morphology and gap junction connectivity either boosts or impairs synaptic communication, thus, affecting the whole network performance.

In the previous chapter, we proposed that different astrocytic topologies can be employed in neural networks to improve network performance by increasing synaptic efficacy, promoting synchronization through simultaneous firing, or maintaining network stability through homeostasis. Here, we develop a spiking neural network with astrocytic modulation to show that astrocytes assist memory formation and recognition. In AI, spiking neural networks or SNNs are considered the next generation of neural network that closely mimics neural processes where computations are event-based, rather than the previous generations using rule-based knowledge. However, one of the main challenges in simulating a biologically inspired neuron-astrocyte network is the computational complexity; it requires a longer simulation time using supercomputing resources than is necessary for a neuron network alone.

We develop an architecture derived from the baseline SNN for unsupervised MNIST classification designed by Diehl and Cook [403], then extend the architecture by integrating astrocytes into the network using the simplified Postnov astrocytic model [312, 313], which lessens the computational complexity while keeping the primary astrocytic functions. This study is one of the first attempts to utilize astrocytes in a spiking network for digit classification using the standard MNIST dataset. Interestingly, astrocyte-mediated SNNs display better network performance with an optimal variance-bias tradeoff.

6.2/ Spiking Neuron Astrocyte Networks: Biological to Artificial

The Spiking Neural Networks (SNNs), considered the third generation of neural networks, are becoming competitive with their Artificial Neural Network (ANN) counterparts due to their ability to capture brain dynamics [11, 404, 405]. Inspired by biological neural mechanisms, SNNs utilize spike-based signaling to perform brain-like computations, represent and integrate spatiotemporal information, communicate sparse and asynchronous signals, and process massive data in parallel. These properties, especially its temporal dimensions, make SNNs leading candidates for real-life applications and neuromorphic hardware implementations compared to other deep neural networks. As in real neural circuits, SNNs offer low-power consumption, analog computation, fast inference, online learning, and event-driven processing.

While models of SNNs closely mimic brain processes, there are some drawbacks. Training using benchmarks such as MNIST and ImageNet indeed yields a lower accuracy than ANNs, which can be attributed to converting the frame-based images into rate-coded information. Besides, there is a lack of training algorithms for spiking networks. Training SNNs means dealing with the asynchronous and discontinuous nature of spikes, making the application of current differentiable backpropagation techniques quite challenging [11]. In spiking neuron-astrocyte networks (SNANs), astrocytes were determined to promote neural synchrony [406], which can help in stochastic neural spiking. Another advantage of astrocytes in the neural network is their function in memory storage – in maintaining long-term hippocampal potentiation [407]. Our research explores these astrocytic properties and their functions in neural networks to develop a SNAN capable of recognizing images, an attempt to bridge brain-inspired computation and artificial networks.

The general aim of this study is to develop a SNAN architecture for image recognition purposes using an unsupervised learning scheme. First, we create a neural network incorporating astrocytes between neuronal networks using simplified neurons and astrocyte models. Then, we added an unsupervised learning algorithm for image recognition using spike-timing-dependent plasticity (STDP). Next, we train the network using inputs from the MNIST dataset to determine the hyperparameters (related to network architecture and learning) and optimize the network parameters (synaptic coupling strengths and firing thresholds), leading to the best network performance. Using the trained network, we then identify the accuracy of the network in predicting the output digits. Lastly, we analyze the influence of astrocytes on network performance. The results suggest that astrocytes indeed facilitate faster learning compared to SNN alone.

6.3/ Developing the SNAN Architecture

This section describes the tripartite synapse connection, the neuron and astrocyte layers, and the corresponding network architecture. In addition, it also includes the learning algorithm used in training the network, the simulation process, and the performance analysis method.

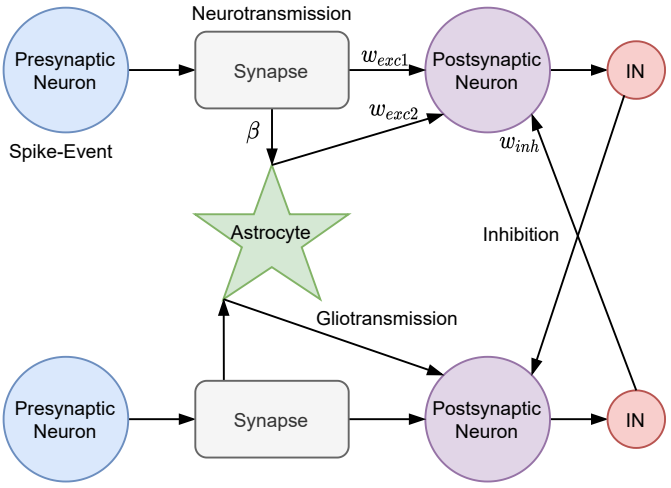

Figure 6.1: The tripartite synapse model consists of two layers of neurons and an astrocytic layer in between. The presynaptic neuron is a Poisson spiking neuron whose spike-based event modulates the postsynaptic neuron and the astrocyte. The postsynaptic layer consists of AIF neurons with lateral inhibitions from interneurons (IN). Therefore, the postsynaptic neuron receives three types of inputs whose strengths are defined by the synaptic weights w_{exc1}, w_{exc2}, and w_{inh} from the presynaptic neuron through neurotransmission, the astrocyte through gliotransmission, and inhibition from neighboring IN. The IN sense the spiking activity of the coupled postsynaptic neuron and relays it to the neighboring excitatory neurons. The astrocyte then integrates the synaptic inputs whose coupling strengths are controlled by β. Here, the model ensures that in a tripartite connection, the astrocyte modulates the postsynaptic neuron counterpart of its input neuron.

6.3.1/ Tripartite Synapse Model

The tripartite synapse shown in Figure 6.1 consists of a Poisson spiking presynaptic neuron whose output is coupled to the astrocyte and the postsynaptic neuron. Here, the Poisson spiking rate depends on the input image pixel intensity ranging from 0 for black to 31.875 Hz for white pixels – low enough so that the presynaptic inputs do not oversaturate the astrocytic dynamics and high enough to generate a postsynaptic spike. The postsynaptic neuron summates three types of inputs: (1) the fast excitatory inputs resulting from neurotransmission, (2) the slow excitatory inputs due to gliotransmission, and (3) the inhibitory inputs from the interneurons (IN). This adaptive integrate-and-fire (AIF) neuron is defined by

$$\begin{aligned} \tau \frac{dv}{dt} &= (v_{rest} - v) + g_{exc1}\,(v_{exc1} - v) + g_{exc2}\,(v_{exc2} - v) + g_{inh}\,(v_{inh} - v)\,, \\ \tau_x \frac{dx}{dt} &= -x, \quad x = g_{exc1},\, g_{exc2},\, g_{inh}, \end{aligned} \tag{6.1}$$

where v (in mV) corresponds to the postsynaptic neuron potential (see Integrate-and-Fire Model). The conductance (in nS) of the fast excitatory, slow excitatory, and inhibitory synapses are equal to the weight summations g_{exc1}, g_{exc2}, and g_{inh}, respectively, and where x defines their conductance decay through time t. The parameter v_{rest} is the membrane resting potential while v_{exc1}, v_{exc2}, and v_{inh} are the reversal potentials of the excitatory and inhibitory synapses. The constant parameters, τ and τ_x, are the time constants of the membrane potential and the synapses, respectively. When the AIF neuron membrane potential v crosses its spiking threshold θ, it generates a spike, then immediately resets to a level equal to v_{reset}, and remains here until the refractory period, τ_{ref}, ends. During training, the adaptive threshold increases by α' after a spike and decays following

Table 6.1: List of parameters of the postsynaptic neurons with lateral inhibition.

Parameter	Value	Description
Postsynaptic Excitatory Neurons		
v_{rest}	-65 mV	Membrane resting potential
v_{exc1}	0 mV	Fast synaptic input reversal potential
v_{exc2}	0 mV	Slow synaptic input reversal potential [338]
v_{inh}	-100 mV	Inhibitory synaptic reversal potential
τ	100 ms	Membrane time constant
τ_{exc1}	1 ms	Excitatory synapse (fast) time constant
τ_{exc2}	600 ms	Excitatory synapse (slow) time constant [338]
τ_{inh}	2 ms	Inhibitory synapse time constant
v_{reset}	-65 mV	Reset potential
v_{thresh}	-52 mV	Spiking threshold level
t_{ref}	5 ms	Refractory period
θ_0	20 mV	Spiking threshold offset
τ_θ	107 ms	Spiking threshold time constant
α'	0.05 mV	Increase in spiking threshold
Postsynaptic Inhibitory Neurons		
v_{rest}	-60 mV	Membrane resting potential
v_{exc1}	0 mV	Synapse reversal potential
τ	100 ms	Membrane time constant
τ_{exc1}	1 ms	Excitatory synapse time constant
v_{reset}	-45 mV	Reset potential
v_{thresh}	-40 mV	Spiking threshold
t_{ref}	2 ms	Refractory period

Unless otherwise stated, the parameters are taken from Diehl and Cook [403].

the exponential model

$$\frac{d\theta}{dt} = \frac{\theta - \theta_0}{\tau_\theta}, \tag{6.2}$$

where $\theta = v - v_{reset}$ and τ_θ is the time constant.

The postsynaptic neuron layer consists of lateral inhibition for maintaining homeostasis and signaling the postsynaptic neuron activity to its neighbors. Here, the postsynaptic neuron signals its spiking activity to the IN, and in return, the IN then inhibits the activity of the other neurons, generating competition among neurons. The interneurons follow the IF model in Equation 6.1 but without the adaptive property θ and the g_{exc2} and g_{inh} conductances, while g_{exc1} changes with respect to the postsynaptic neuron spiking activity. Refer to Table 6.1 for the list of parameters of the postsynaptic excitatory and inhibitory neurons.

The astrocyte function as a point process integrating the presynaptic inputs, following the simplified astrocytic model proposed by Postnov et al. [312, 313]. The synaptic coupling variable z spikes to 1, synchronous with the presynaptic neuron spiking, and

Table 6.2: Simplified astrocytic model parameters.

Parameter	Value	Description
Neuron-astrocyte coupling		
τ_S	10 ms	Synaptic delay time constant
s_S	1	Steepness of activation
h_S	0	Activation control
d_S	3	Relaxation control
IP_3 production		
τ_{Sm}	100 ms	Time constant
s_{Sm}	100	Steepness of activation
h_{Sm}	0.45	Threshold
d_{Sm}	3	Deactivation rate
Astrocytic Ca^{2+}		
ϵ_c	0.04	Characteristic time control
c_1	0.13	Ca^{2+} oscillation control parameters
c_2	0.9	
c_3	0.004	
c_4	$2/e_c$	
r	0.31	Ca^{2+} oscillation initial state
τ_c	600 ms	Time constant for Ca^{2+} oscillation

The parameters are taken from Postnov et al. [312, 313].

then immediately inactivates by decaying to 0, following the simplified model

$$\tau_S \frac{dz}{dt} = -\frac{z}{d_S}, \tag{6.3}$$

where d_S controls the relaxation of z and τ_S is the synaptic delay. The variable z triggers the astrocytic IP_3 production, S_m, (Equation 4.27) resulting in $Ca2^{2+}$ elevation, c, described by the system shown in Equation 4.26. The astrocyte then integrates the presynaptic signals from multiple synaptic connections, where β is the control parameter defining the magnitude of influence of the presynaptic neuron activity on the astrocytic Ca^{2+}. The modified Ca^{2+} model [313] is defined as

$$\tau_c \frac{dc}{dt} = c - c_4 f(c, c_e) + \left(r + \sum_{i=1}^{k} \beta S_{m_i} \right). \tag{6.4}$$

When the astrocytic $[Ca^{2+}]$, c, increases beyond the threshold, c_{thresh}, it triggers the release of extrasynaptic Glu^-, activating slow excitatory synapses of the coupled postsynaptic neurons. After the Glu^- spike, the astrocyte stays in the refractory period provided that c stays above the threshold. The astrocytic parameters are listed in Table 6.2.

6.3.2/ Network Architecture

The digit recognition process follows the network architecture presented in Figure 6.2. The process starts from the image preprocessing, where the input or sample image is

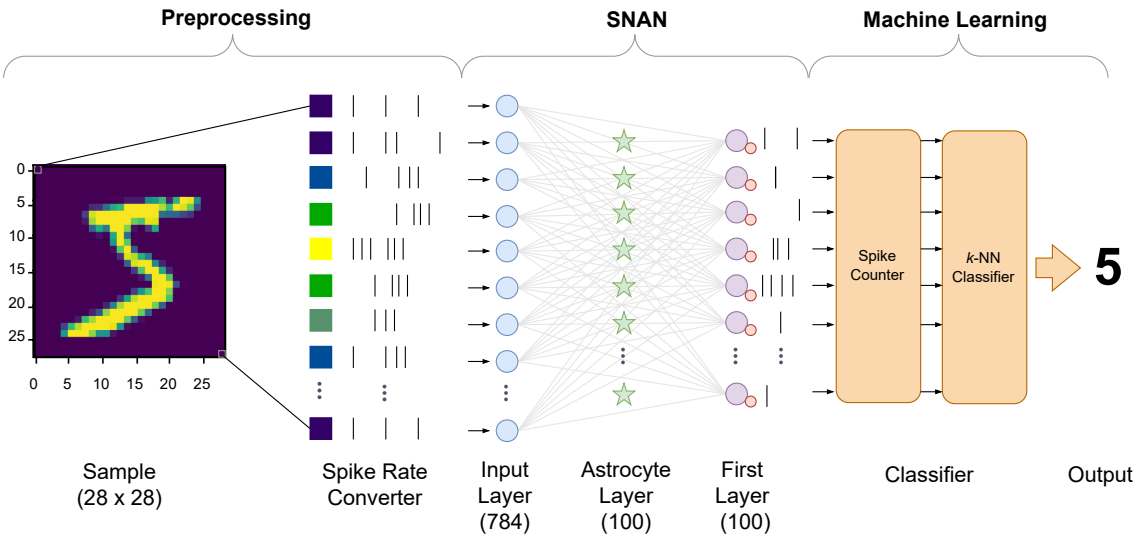

Figure 6.2: Network architecture for image recognition is a three-stage process comprising an input preprocessing unit, a SNAN learning unit, and a classifier unit.

converted into rate-coded signals, followed by unsupervised learning by the SNAN, and lastly, based on the SNAN output spike patterns, the machine learning (ML) model predicts the output digit. Given a sample digit from the MNIST dataset, a 28×28-pixel image of a handwritten digit is converted into a 784×1 vector of pixel intensities. One pixel intensity corresponds to the spiking frequency that drives a Poisson neuron in the input layer of the SNAN.

In the spiking network, 784 Input layer neurons form 78 400 fully connected (dense) synapses with the neurons in the First Layer. There is a 1:1 ratio between the number of excitatory and inhibitory neurons in the First Layer, where the forward connection (from the excitatory to the inhibitory) is a one-to-one topology. At the same time, the lateral inhibitions form 9900 inhibitory synapses, where an IN connects with all excitatory neurons in the same layer except with the one in the forward connection. The astrocytic layer between the two neuronal layers, also following a 1:1 ratio with the First layer neurons, forms the tripartite synapses by connecting with the synapses rather than directly with the input layer neurons. Because an astrocyte is coupled with the synapses, it can receive multiple presynaptic inputs from the same Input layer neuron and increase its influence on a First layer neuron by modulating multiple tripartite synapses coupled to that postsynaptic neuron.

In the machine learning unit, the spike counter converts the output spiking patterns of the First layer excitatory neurons into a vector of whole numbers corresponding to the number of spikes in each neuron. This vector gives the set of input features for the classifier. Our simulation analysis suggests that the cosine k-NN classifier using 5-fold cross-validation yields a faster and more accurate classification performance than the other available machine learning classifier. Then lastly, the network predicts the output from ten classes labeled from 0 to 9. This paradigm requires that the SNAN generates a stable spiking pattern for each input class for the network to recognize and differentiate each input pattern.

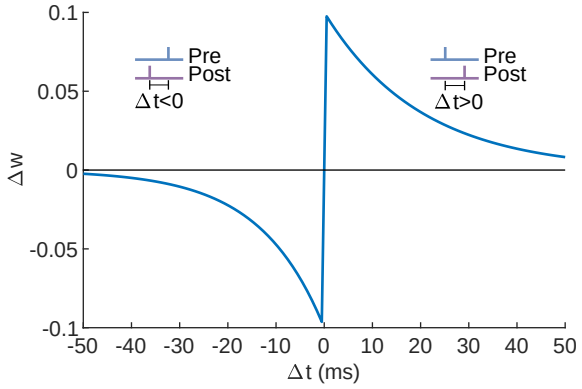

Figure 6.3: STDP curve. Synaptic plasticity, specifically the strengthening and weakening of the synaptic connection between two neurons, is relative to the temporal window between the pre- and postsynaptic spikes. (Parameters: $\tau_{pre} = \tau_{post1} = 20$ ms, $\tau_{post2} = 40$ ms, $\eta_{pre} = 0.1$, $\eta_{post} = -0.1$.)

6.3.3/ Spike-Timing-Dependent Plasticity

Learning between interconnected neurons (or neuron-astrocyte) occurs by strengthening or weakening their synaptic connections during neuronal activities. Donald Hebb proposed the concept of synaptic plasticity, suggesting that simultaneous and correlated spiking between biological neurons strengthens their synaptic coupling [408]. This form of synaptic plasticity prompted the Hebbian learning rule, one of the earliest algorithms used in training SNNs. Here, the synaptic weight increases when both the pre- and postsynaptic neurons are active and decreases otherwise [409]. However, one of the main drawbacks of the Hebbian learning rule is that synaptic weights are updated only when the neurons are coactive, causing a long period of synaptic weakening when the spiking activities between neurons are uncorrelated. A form of long-term plasticity called spike-timing-dependent plasticity (STDP) addressed the temporal issue in Hebbian plasticity [410–412]. Rather than correlated inputs driving the synaptic plasticity, the spiking activities of neurons within a temporal window define the direction of synaptic plasticity, and the relative timing between the pre- and postsynaptic firing determines the change in the synaptic weights. Therefore, the SDTP learning rule is suitable for training the SNAN due to the significant difference between the neuronal and astrocytic time scales.

The STDP curve in Figure 6.3 describes the increase or decrease in synaptic weight (Δw) relative to the arrival of the presynaptic spike and the generation of postsynaptic AP. If the presynaptic spike arrives before the postsynaptic spike ($\Delta t > 0$), the synaptic weight is updated following $w \rightarrow w + \Delta w$. Otherwise, the weight decreases when the postsynaptic neuron generates an AP before the presynaptic spike ($\Delta t < 0$), in that $w \rightarrow w - \Delta w$. However, biological neurons do not have memories of their spiking activities, and storing and comparing all the spike timing during simulation has rich computational cost. Therefore, we used a time-invariant and event-based STDP rule by adding pre- and postsynaptic traces, α_{pre} and α_{post}, eliminating the need to compute for Δt while still following the STDP curve (Figure 6.3) [413, 414].

In this STDP rule following Diehl and Cook model [403], the increase in synaptic weight includes a weight-dependent term so that during postsynaptic activation, the weight increases only after the presynaptic activation. Let the traces α_{pre}, α_{post1}, and α_{post2} decay

exponentially by

$$\tau_{pre}\frac{d\alpha_{pre}}{dt} = -\alpha_{pre}, \quad \tau_{post1}\frac{d\alpha_{post1}}{dt} = -\alpha_{post1}, \quad \tau_{post2}\frac{d\alpha_{post2}}{dt} = -\alpha_{post2}, \tag{6.5}$$

where τ_{pre}, τ_{post1}, and τ_{post2} are the decay constants equal to 20 ms, 20 ms, and 40 ms, respectively. On presynaptic activation, the weights are updated following the rule

$$w \rightarrow w + \eta_{pre}\alpha_{post1}, \tag{6.6}$$

while on the postsynaptic activation,

$$w \rightarrow w + \eta_{post}\alpha_{pre}\alpha_{post2}, \tag{6.7}$$

where η_{pre} and η_{post} are the pre- and postsynaptic rates, respectively. The excitatory-to-excitatory connections use the pre- and postsynaptic spiking weight update rules, while astrocyte-postsynaptic coupling only increases postsynaptic weights during astrocytic activation. Due to the significant time scale difference between neurons and astrocytes, the slow synapse conductance depletes to zero when the postsynaptic neuron fires continuously. Moreover, the excitatory-to-inhibitory and the inhibitory-to-excitatory Δw are constants equal to 17 and 10.4, respectively.

6.3.4/ Simulation Method and Performance Analysis

Neural simulators such as NEURON [17], NEST [415], and Brian2 [416] provide computational neuroscientists efficient tools to simulate and analyze large networks [417]. Here, we used the Brian2 simulator, in conjunction with the python programming language, as it explicitly describes models in a high-level form by writing the differential equations directly in the code, compared with other simulators. It allows us to efficiently model and to integrate astrocytes into the network.

The MNIST dataset [16] contains 60 000 training, 5 000 validation, and 5 000 test images. Each image is fed into the proposed network one at a time for 350 ms, followed by a resting time of 150 ms, to ensure that the network activity due to the previous image will not overlap with the new sample; therefore, one sample takes 500 ms to pass through the SNAN. The network continuously updates its weights via the STDP learning rule and the neuronal firing thresholds during training. We divide one epoch (containing all the training images) into batches of 1000 samples each and then normalize the weights after each batch. After each epoch, the validation set is fed into the network using the learned parameters.

We simulated different spiking network configurations to determine the hyperparameters that lead to optimum network performance: one SNN and three SNANs (SNAN,1, SNAN2, SNAN3). All networks have the same number of neurons and astrocytes (except in SNN), while the number of synaptic connections with astrocytic coupling increases from 10% to 60% (increment of 10%) of the total synapses, where each astrocyte receives the same number of presynaptic inputs. The set of hyperparameters is listed in Table 6.3. The simulations were performed using the high-performance computing resources from the Barcelona Computing Center and the Centre de Calcul de l'Université de Bourgogne.

Table 6.3: Set of hyperparameters per configuration.

Hyperparameters	SNN	SNAN1	SNAN2	SNAN3
$\eta_{exc1_{pre}}$	0.0001	0.0001	0.0001	0.0001
$\eta_{exc1_{post}}$	0.01	0.01	0.01	0.01
$\eta_{exc2_{pre}}$	-	0.000001	0.00001	0.000001
$\eta_{exc2_{post}}$	-	-	-	-
$w_{exc1_{max}}$	1	1	1	1
$w_{exc2_{max}}$	-	0.001	0.01	0.001
β	-	0.00005	0.00005	0.0001

Refer to Appendix E for more information regarding the computing resources specifications.

6.3.5/ PERFORMANCE ANALYSIS

The ML accuracy defines how well the system groups and distinguishes the spiking patterns generated by the SNAN from one class to another. Therefore, the classification performance of the ML unit depends on the extent to which the SNAN learned the rate-coded images. As the network evaluation metric, accuracy is the ratio between the number of correctly predicted outputs over the total number of inputs. During training, we determine the accuracy after each epoch. Then, using the learned parameters after each epoch, we feed the validation set into the network for prediction and compare the results with the training accuracy. Therefore, the parameters chosen for the test network simulations are the learned parameters of the epoch giving the maximum average accuracy between the train and validation sets.

6.4/ RESULTS

We simulated the spiking networks and set the SNN as the baseline of the SNAN activities. Here, we focus on the influence of astrocytes in network activities. The minimum numbers of neurons for conventional MNIST classification networks are 784 and 100 in the Input and First layers, respectively. Here, the number of astrocytes in all networks is equal to the number of First layer excitatory neurons (1:1 ratio); however, the number of synapses covered by astrocytes increases by 10% of the total number of Input to First layer synaptic connections. A higher number of neurons results in more synapses. Moreover, astrocytes create two more types of synaptic coupling (presynaptic neuron-to-astrocyte and astrocyte-to-postsynaptic neuron shown in Figure 6.1), resulting in a more complex network that requires prolonged simulations.

The SNAN design is a highly iterative process, requiring numerous trials before arriving at the possible set of hyperparameters shown in Table 6.3. The neuronal and neuron-to-neuron synaptic hyperparameters are consistent in all the networks. Based on our initial simulations, these parameters lead to regular neuronal spiking. The Poisson neuron changes its spiking rate every 500 ms. We also determined that the Poisson neuronal

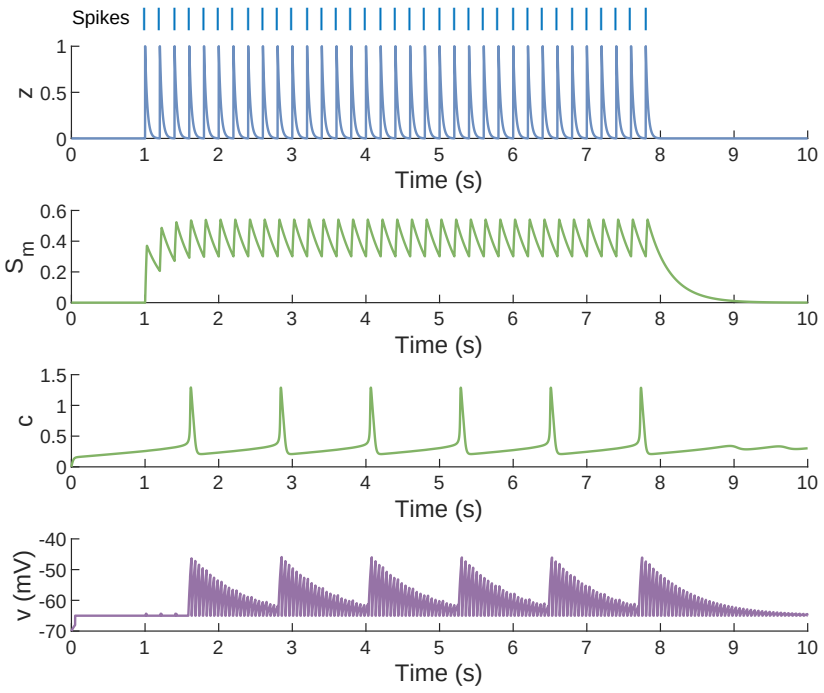

Figure 6.4: Sample tripartite synapse dynamics. The spikes represent the regular spiking activity of the input neuron that triggers the fluctuation of the synaptic coupling z from 0 to 1, which then activates the S_m signaling pathway. The parameter β controls the fraction of S_m influencing the astrocytic Ca^{2+} spiking. The postsynaptic membrane potential v is the summation of the excitatory signals from the presynaptic neuron and the astrocyte. (Parameters: $dt = 1$ ms, input spike rate $= 5$ Hz, $v_{rest} = -70$ mV, $\theta = -40$ mV, $c_{thresh} = 0.40$, $g_{e1} = 1$ nS, synaptic delay $= 9.62$ ms, $\beta = 0.006$, $\tau_c = 50$ ms, $g_{e2} = 1$ nS.)

firing rate lies between 0 to 32 Hz (proportional to the pixel intensity from 0 to 255) to prevent oversaturation of astrocytic S_m (IP_3 pathway) and avoid overexcitation of astrocytic Ca^{2+} dynamics, c.

6.4.1/ Tripartite Synapse Dynamics

Figure 6.4 is an overview of the activities of a single tripartite synapse without STDP and wherein the astrocyte only receives a presynaptic input and modulates one postsynaptic neuron. The presynaptic neuron generates 5 Hz and regularly spaced spikes. The synaptic coupling variable z increases to 1 simultaneously with the input neuron spikes and then exponentially decays back to 0, replicating the neurotransmitter release and recycling process. In addition, the IP_3 pathway (S_m) also increases and decays with z, and whose peak amplitudes stabilize at 0.54. The Ca^{2+} variable c generates spikes, upon crossing the 0.4 threshold, with a peak amplitude equal to 1.29 with a pulse duration of 58 ms. After activation, the astrocyte is in the refractory period provided that $c > 0.4$. A single fast excitatory synaptic input generates a postsynaptic spike, v, with -64.38 mV peak amplitude (first three spikes). In this example, the fast and slow excitatory synapse conductances and weights are equal to 1 nS and 1, respectively, creating the same strength of influence on the postsynaptic neuron. However, the combination of the neuronal and astrocytic inputs triggers a sudden increase in v up to -46.35 mV. Then, v decays to 0 while fluctuating, resulting from the fast activation of presynaptic input.

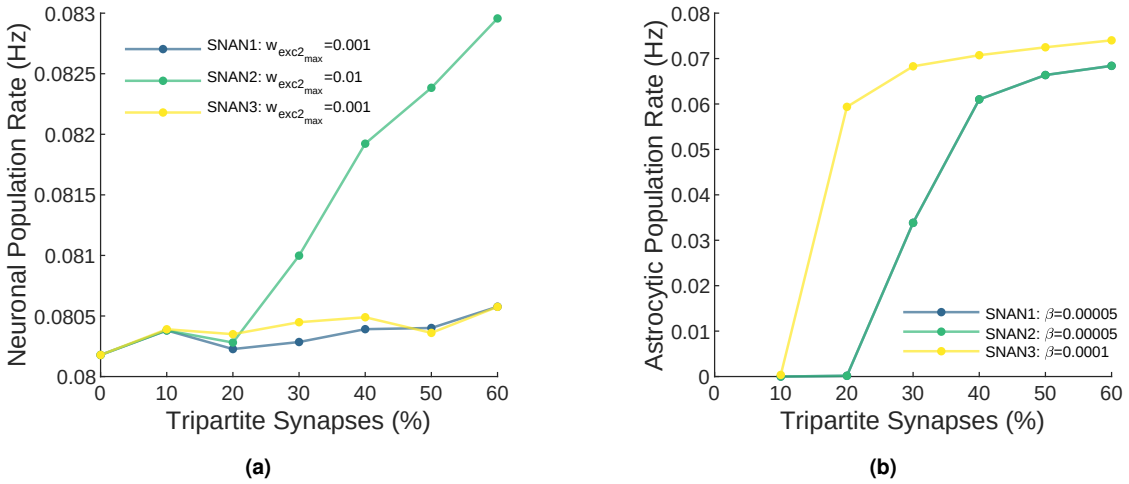

Figure 6.5: Population rates of (a) First layer neurons and (b) astrocytic layers with an increasing number of tripartite synaptic connections.

In the SNAN, astrocytes receive hundreds of inputs; therefore, the summation of slow synaptic weights must generate a conductance, g_{exc2}, low enough to not overexcite the postsynaptic neuron. In addition, the neuron-astrocyte coupling control factor β must be high enough to trigger astrocytic activation. We performed multiple simulations and determined the astrocytic hyperparameters in Table 6.3. Here, the astrocyte-neuron coupling, w_{exc2}, is updated upon the arrival of astrocytic input; however, there is no w_{exc2} update ($\eta_{exc2_{post}}$ is null) upon postsynaptic neuron spiking due to the significant time scales difference between the astrocyte and the neuron. If STDP is bidirectional, then the fast-spiking of the postsynaptic neuron can cancel the astrocyte-neuron coupling. High slow excitatory synaptic weights excite the First layer neurons that can cause erratic spiking patterns, suggested by the average spiking rates of SNAN2 in Figure 6.5a that grow with an extended number of tripartite connections. The astrocytic population rates of SNAN1 and SNAN2 (Figure 6.5b) have the same trend due to the similarity in β. For $\beta = 0.001$ and $\beta = 0.0005$ with 10% and 20% tripartite synapses, respectively, are inadequate to activate the astrocytes.

6.4.2/ Training Results

We trained the networks by presenting the entire 60 000 MNIST training dataset 25 times. The Table F.4 shows the approximate simulation runtime for training 25 times of input representations per configuration. Figure F.1 and Figure F.2 in Appendix F, respectively, show the synaptic weights of the input-to-first and astrocyte-to-first layer couplings of the SNN and SNANs (with 50% tripartite synapses) after 25 epochs. The patterns suggest which input neurons were inactive and strongly coupled with the first layer neurons. The synaptic weight evolution in Figure 6.6 show the ability of the First layer neurons to learn the representative inputs. Here, the 784 excitatory-to-excitatory synaptic weights vector of a neuron is rearranged to a 28×28 matrix. For example, the second neuron in the SNN learned the features of class "1", and the ninth neuron in SNAN3 initially learned class "8" features, then became strongly coupled with class "1" inputs. The receptive fields show that neurons in the three SNAN configurations learn almost the same features (3, 2, 0, 6, and 6), while the neurons in SNN learn differently.

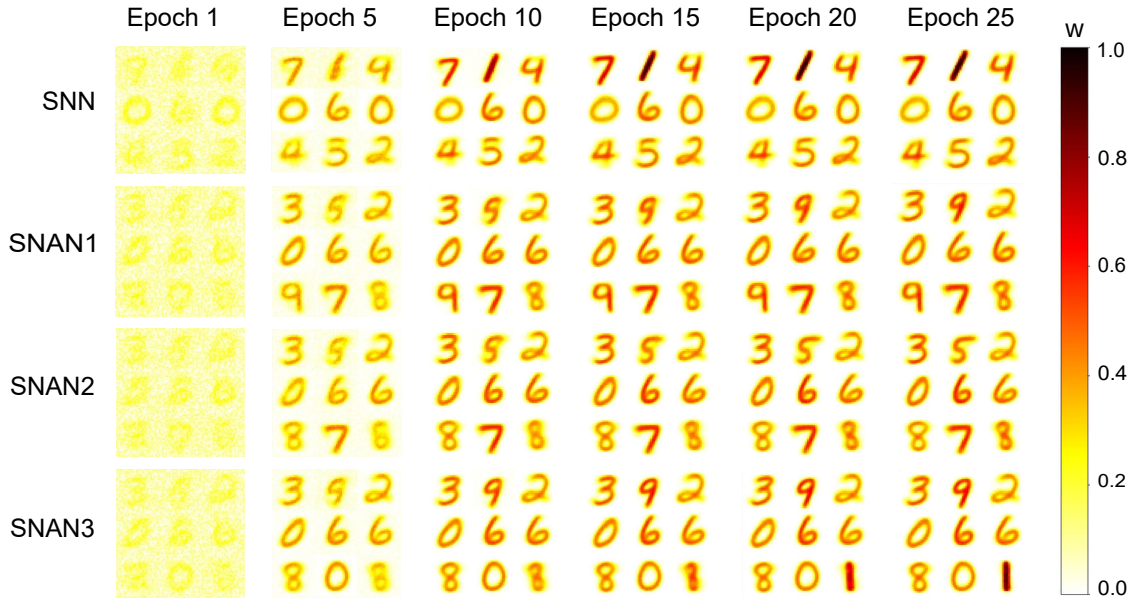

Figure 6.6: Receptive field evolutions for the nine First layer neurons of the SNN and SNANs with 50% tripartite synaptic components.

The classifier then predicts the output class based on the spiking patterns given by the SNAN per individual input. Figure 6.7 summarizes the change in training accuracy of each network configuration with increasing synapses covered by astrocytes. The curve with 0% tripartite synapses is the training accuracy of SNN, used as the reference in comparing the SNAN performance. The accuracy curves are the same during initial training, and the SNN gradually outperforms the SNANs. In SNAN2, it is noticeable that the rate of increase in the accuracy of SNN is maximum. However, starting from Epoch 13, the SNN performance decreases to a minimum and becomes stable at an average accuracy of 65.38%, and then all SNANs achieve higher accuracy than SNN. Figure 6.6 also indicates that SNANs with 50% tripartite synapses have higher performance in all network configurations, wherein the maximum accuracy is 69.94% at Epoch 13 for SNAN1, 69.76% at Epoch 25 for SNAN2, and 70.13% at Epoch 23 for SNAN3. From these results, SNAN3 with 50% tripartite synapses leads to maximum classification performance. It is also indicative that the SNAN produces spiking patterns easily categorized by the ML unit.

The validation accuracy curves in Figure F.3 of Appendix F, on the other hand, indicate the reverse – showing that the SNN best predicts the output class with maximum accuracy of 70.66% at Epoch 25. In SNAN1 (10%-50% tripartite synapses), the accuracy curves stabilize at an average level equal to 61.60%, almost 9% lower than SNN. In SNAN2, where the astrocyte-neuron synaptic coupling strength is a factor of 10 greater than SNAN1, the increase of tripartite connections to 50% and 60% results in a sudden decrease in validation accuracy, implying overfitting of the trained SNAN2 and that the introduction of unknown samples generates irregular spiking patterns. SNAN3 has the same coupling strength as SNAN1 but double the presynaptic-to-astrocytic coupling strength. In this case, the validation accuracy increases gradually but results in higher performance (for 20% and 30% tripartite synapses).

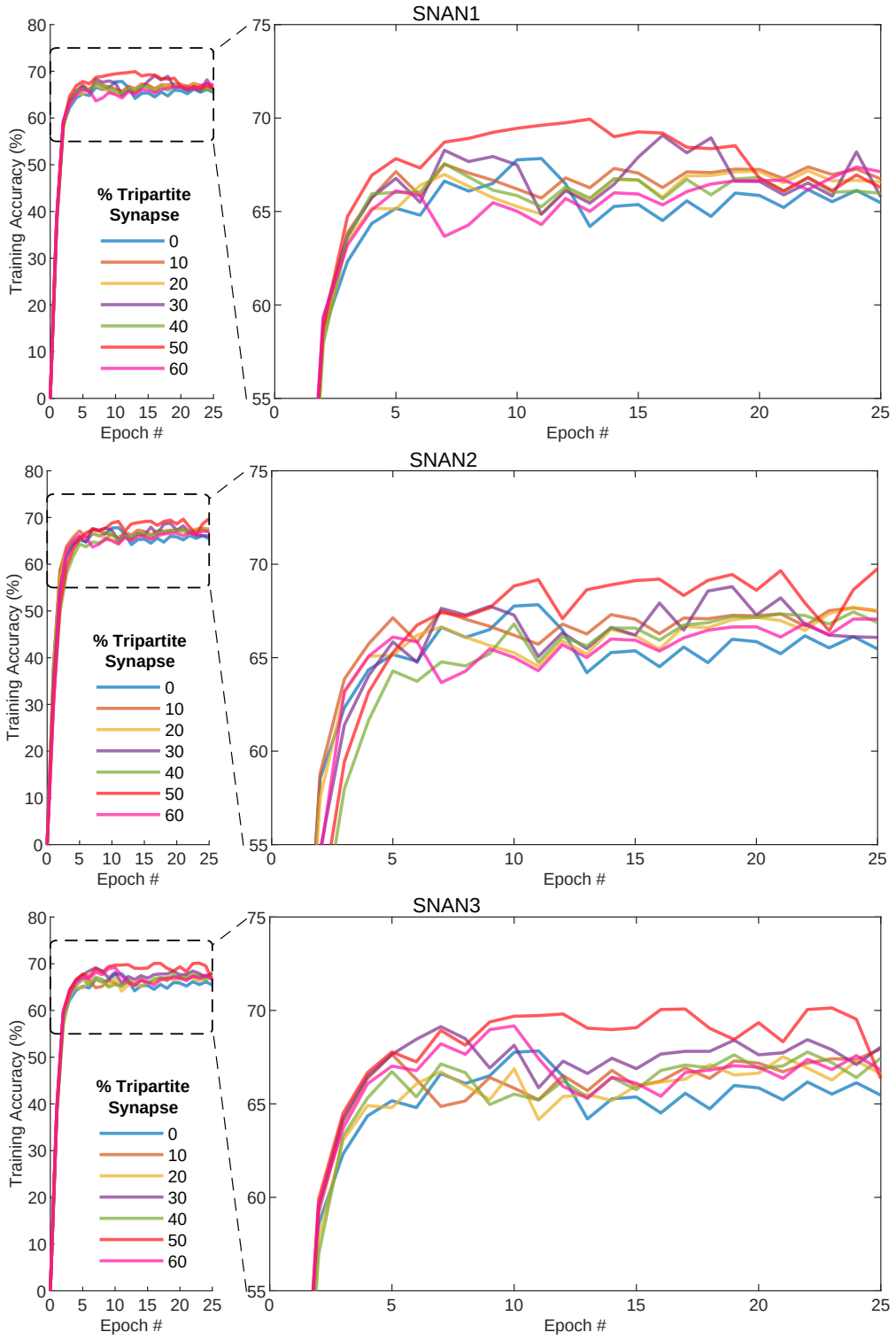

Figure 6.7: Training accuracy per network configuration with an increasing number of tripartite synapses as a function of the presented training epoch.

We chose the test network parameters from the train vs. validation accuracy graphs in Figure 6.8 to 6.10. Strikingly, the SNN network has a validation accuracy curve of 6% higher than the training accuracy, indicating underfitting. The increase of astrocytic coverage by up to 30% diminishes the difference between the train and validation accuracy of SNAN1 (Figure 6.8). A further increase to 60% results in considerable divergence between the accuracy curves. The same results are noticeable in SNAN2 (Figure 6.9); validation accuracy increases with more astrocytic-mediated synapses but drops significantly to 10% accuracy for 60% tripartite connections. However, SNAN3 validation accuracy, with slow astrocyte-to-neuron STDP, and stronger neuron-to-astrocyte coupling ($\beta = 0.001$), also shows a slower convergence with the training accuracy (Figure 6.10). The SNAN3 with 20% and 30% tripartite connections have comparable training and validation accuracy levels in all configurations. Also, for the given SNAN3 parameters with 40%-60% astrocytic mediated synapses, the network performance improves gradually, compared to the low validation accuracy in SNAN2 (Figure 6.9). These results are accordant with our results in Chapter 5, suggesting that astrocytes can either improve or impair network activities.

Variance is a metric describing the ability of the network to adjust and predict the output given a different input dataset [418, 419]. Here, low variance means that the training and validation accuracy is in the same low error region while ensuring that the training accuracy is higher than the validation (not overfitting). Bias describes the ability of the network to capture relevant features, determined by the difference between the predicted and actual values [420]. The SNN, in this case, displays underfitting (having a higher validation than training accuracy). Therefore, the test network parameters are from the epoch giving the best variance-bias tradeoff – with the low classification variance and bias [421].

The network parameters giving the optimal model complexity (balance between variance and bias) are the learned parameters after the epochs specified in Table 6.4. The SNN is optimal after ten times input presentations. SNANs achieve higher network performance and, in some instances, require less training. For example, it only takes seven iterations for SNAN1 with 40% tripartite connections to achieve an accuracy of 0.20% less than SNN, and nine iterations for SNAN3 with 60% tripartite connections to obtain 1.21% higher than SNN. In addition, for the same number of epochs, SNAN2 with 50% tripartite connections achieves 1.07% higher than SNN. The results in Table 6.4 suggest that astrocytes support neuronal memory formation and promote faster learning.

Table 6.4: Epochs of the network parameters with optimal model complexity.

% Tripartite Synapse	SNAN1		SNAN2		SNAN3	
	Train Accuracy (%)	Epoch #	Train Accuracy (%)	Epoch #	Train Accuracy (%)	Epoch #
0	67.76	10	67.76	10	67.76	10
10	67.30	14	67.30	14	67.94	25
20	67.12	19	65.90	12	66.65	20
30	68.94	18	66.34	12	68.41	19
40	67.56	7	67.45	24	67.45	25
50	69.26	15	68.83	10	66.36	25
60	67.13	25	67.07	24	68.97	9

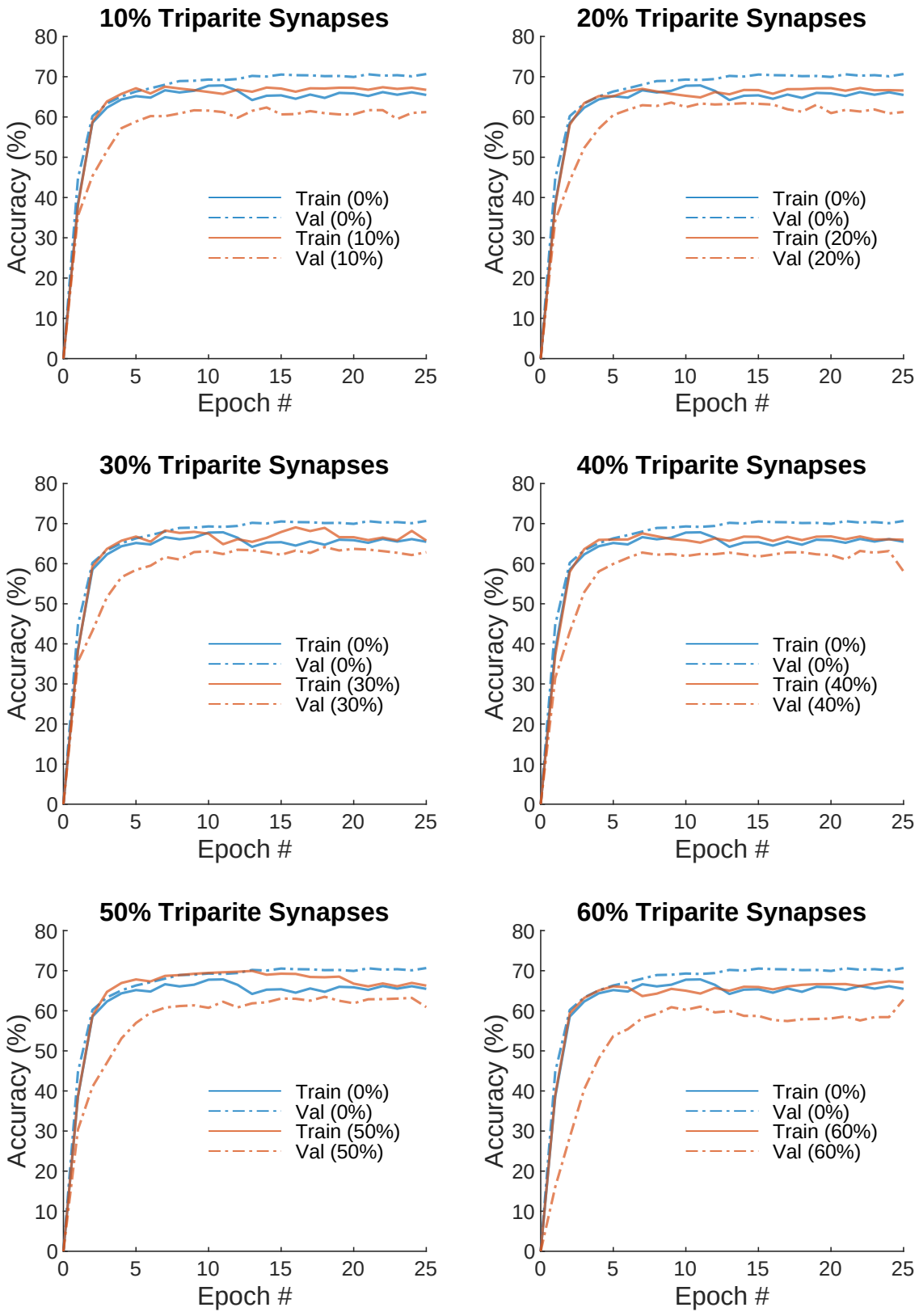

Figure 6.8: SNAN1 training (*solid lines*) and validation (*dashed lines*) accuracy for n% tripartite synapses. (Parameters: $\eta_{exc1_{pre}} = 0.0001$, $\eta_{exc1_{post}} = 0.01$, $\eta_{exc2_{pre}} = 0.000001$, $w_{exc1_{max}} = 1$, $w_{exc2_{max}} = 0.001$, and $\beta = 0.00005$.)

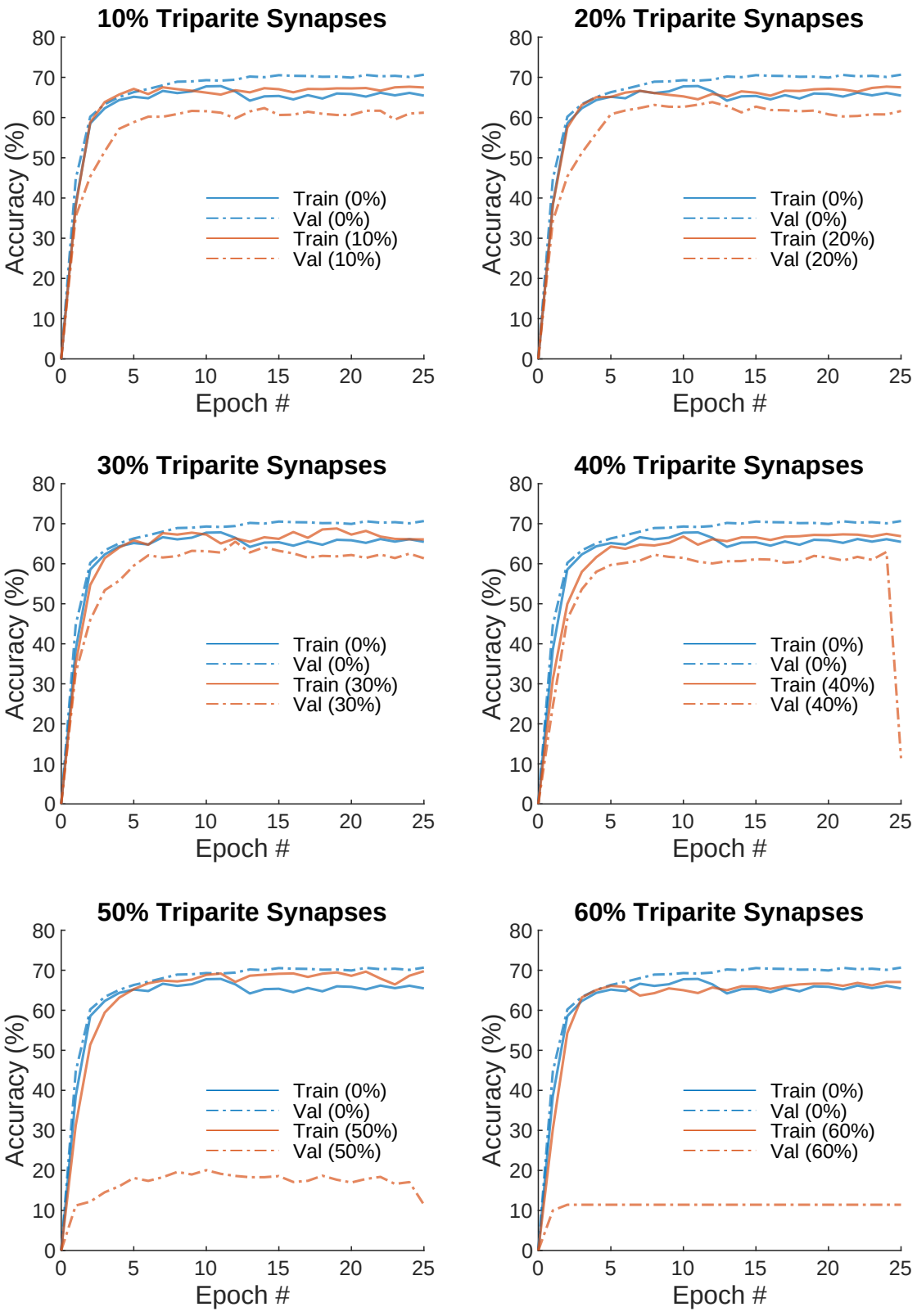

Figure 6.9: SNAN2 training (*solid lines*) and validation (*dashed lines*) accuracy for n% tripartite synapses. (Parameters: $\eta_{exc1_{pre}} = 0.0001$, $\eta_{exc1_{post}} = 0.01$, $\eta_{exc2_{pre}} = 0.00001$, $w_{exc1_{max}} = 1$, $w_{exc2_{max}} = 0.01$, and $\beta = 0.0005$.)

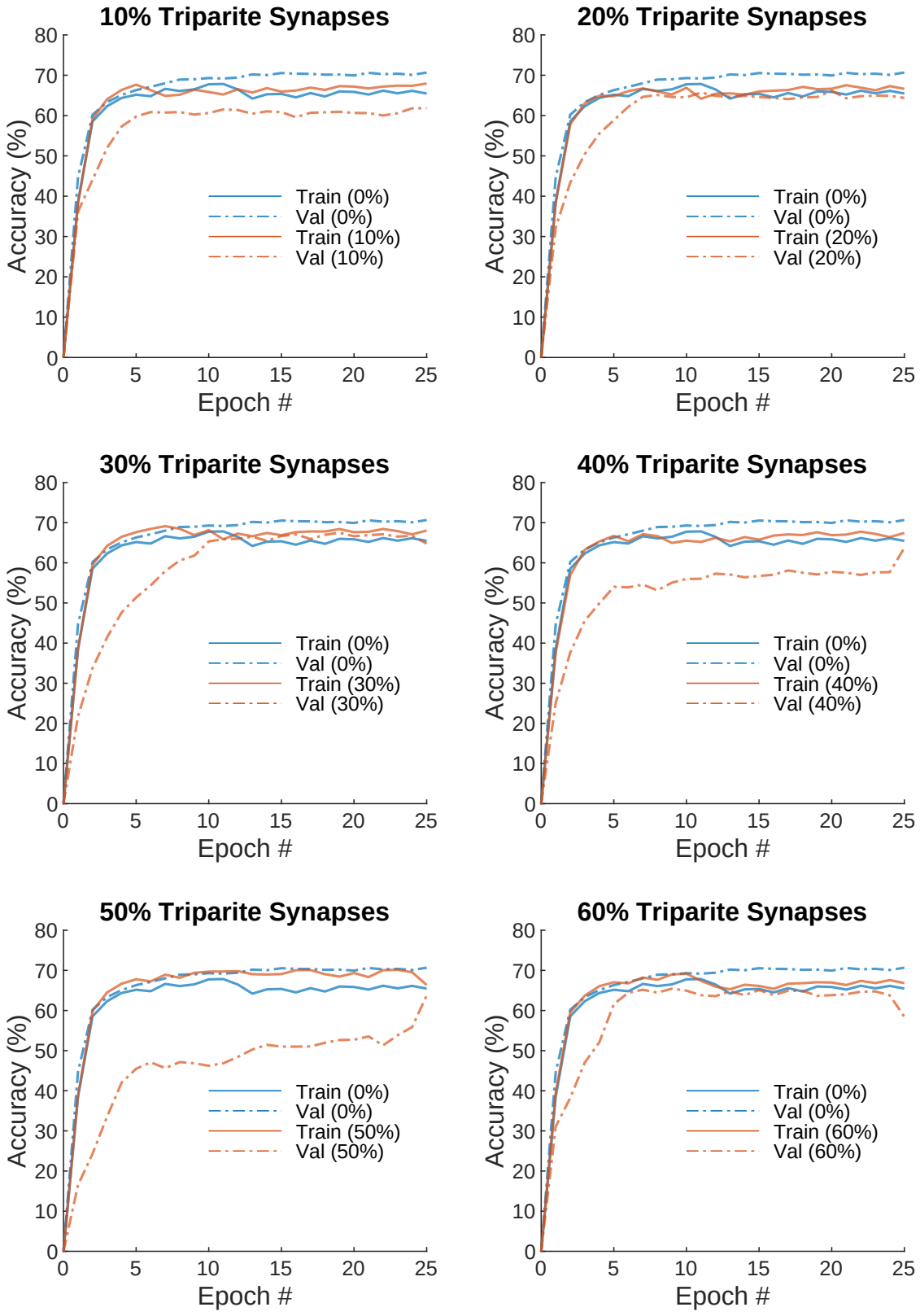

Figure 6.10: SNAN3 training (*solid lines*) and validation (*dashed lines*) accuracy for n% tripartite synapses. (Parameters: $\eta_{exc1_{pre}} = 0.0001$, $\eta_{exc1_{post}} = 0.01$, $\eta_{exc2_{pre}} = 0.000001$, $w_{exc1_{max}} = 1$, $w_{exc2_{max}} = 0.001$, and $\beta = 0.001$.)

6.4.3/ TEST RESULTS

We tested the network using the 5 000 test images from the MNIST dataset. The test simulations take an average of 0.41 s, 0.69 s, 0.88 s, 1.02 s, 1.33 s, 1.67 s, and 1.59 s for the networks with 0%, 10%, 20%, 30%, 40%, 50%, and 60% tripartite synaptic connections, respectively, to predict the class of a single test image. Then, Table 6.5 shows the resulting test accuracy per network configuration. The proposed SNN gives an accuracy of 82.46%, 0.44% less than the accuracy reported by Diehl and Cook [403] for their network with 100 First layer neurons. Of the neuron-astrocyte networks, the parameters of SNAN3 give the best network performance, with maximum accuracy of 75.28% for 30% tripartite connections. Indeed, the neural network displays higher prediction accuracy than the neuron-astrocyte networks. However, the neuron network also displays high bias and underfitting, given that the test accuracy is 14.17% greater than the training accuracy. It suggests the SNN network is not yet fully optimized and requires extended training for more than 25 epochs. Therefore, the astrocytes improve network performance, especially in the SNAN3, where there is an optimum variance-bias tradeoff.

The diagonals of the confusion matrices in Figure 6.11 shows the number of correctly predicted input class. Even though the SNN correctly predicted class ”0” more times than the SNAN, the SNAN still generates higher precision (92%) for the specified class, given that there are more instances that the SNN confuses the remaining input classes as ”0”. The SNAN precisely predicts input classes ”1” (93.70%) and ”3” (97.10%). Furthermore, The SNAN also displays higher recall for input classes ”4” (79.90%) and ”6” (95.60%), correctly predicting the input class and not confusing them with other classes. For other instances otherwise, the SNN displays higher precision and recall compared to the SNAN as expected. SNAN3 also predicts input classes ”1” and ”2” as ”8”. This prediction can be caused by the receptive field of the neuron showing combined features of ”1” and ”8”, for example, the ninth neuron in the SNAN3 shown in Figure 6.6. SNAN3 also confuses class ”9” as ”4” due to their similar vertical features. The neurons with receptive fields of ”9” spike at a high rate when the number ”4” is presented to the network.

Table 6.5: Test accuracy.

% Tripartite Synapse	SNAN1	SNAN2	SNAN3
0	82.46	82.46	82.46
10	65.46	65.46	66.80
20	67.54	66.44	71.96
30	68.94	69.98	75.28
40	67.26	67.32	70.26
50	68.56	21.66	72.44
60	71.20	11.28	71.96

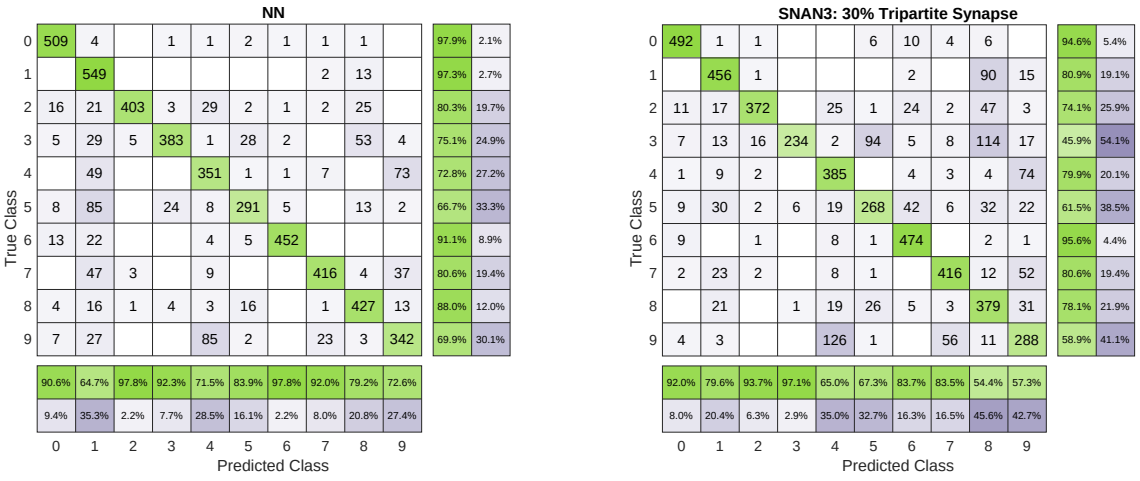

Figure 6.11: Confusion matrices for (a) SNN and (b) SNAN3 with 30% tripartite synapses. The precision and recall are displayed, respectively, below and on the right of the confusion matrix.

6.5/ DISCUSSION

We have developed a spiking neuron-astrocyte network for recognizing image features of the handwritten digits from the standard MNIST dataset and showed that astrocytic-mediated plasticity improves the network capacity to learn these features. Like neurons, astrocytes are active and integrative components described by the Postnov model [312]. The astrocytes were incorporated into the network based on the biological tripartite synapse coupling, where the astrocytes translate the spike events from the input layers and then transmit them, via spike events, to the first layer neuron; thus, the astrocytes create feedforward signaling pathways in parallel with the synaptic communication directions.

6.5.1/ TOWARDS THE DEVELOPMENT OF SNANS FOR DEEP LEARNING

Furthermore, we presented a hybrid network of spiking networks and machine learning, derived from the baseline SNN by Diehl and Cook [403], where the SNAN generates a spiking pattern specific to the input class and the k-NN classifier predicts the output class. Diehl and Cook [403] reported a classification performance of 82.90% for 100 first layer neurons. With our proposed baseline SNN, we acquired a relative value equal to 82.46%. Our analysis suggests that even though the baseline SNN has the highest accuracy, it displays underfitting caused by insufficient training iterations shown by the difference in training and validation accuracies (Figure 6.8-6.10). However, there was no validation set in the study of Diehl and Cook [403]. We reported a maximum test accuracy of 75.28% for the SNAN, displaying optimal variance and bias tradeoff.

Rastogi et al. [13] recently demonstrated SNAN designs using the MNIST dataset, where astrocytes modulate the presynaptic neuron release probability during faults when synaptic learning is stuck at zero. In this case, the astrocytes indirectly modulate synaptic activities. In our proposed network, astrocytes act as excitatory inputs to the postsynaptic

neurons with STDP ability. To our knowledge, the proposed neuron-astrocyte network is one of the first attempts to identify the potential of astrocytes in image classification using the standard MNIST dataset. Therefore, this study can serve as a baseline for evaluating future studies on astrocyte implementation in SNNs.

6.5.2/ Astrocytes Improve Network Performance

Our results suggest that astrocytes influence and improve three attributes of the spiking network: (1) faster learning, (2) variance and bias tradeoff, and (3) simplified network architecture. During training, the SNANs displayed higher accuracy than SNN (Figure 6.7), indicative of the ability of the network to stabilize its spiking activity quickly. Moreover, the SNANs achieved peak accuracy with fewer input set presentations (Table 6.4). These activities support the idea that astrocyte-mediated neuronal spiking aids in faster learning. For traditional SNN and artificial networks, increased neuronal connectivity equates to fast and precise learning. Therefore, the astrocytes and the corresponding tripartite synapse promote efficient learning by providing additional synaptic connections in parallel with the neuron-to-neuron couplings, thus strengthening the communication strength between neuronal layers. Also, as the neuron spikes more frequently, the spiking threshold increases, thus requiring more input eventually. Astrocytes, therefore, provide additional input for equalizing neuronal firing rate.

Second, networks with astrocytes balanced variance and bias, as shown in comparing the training and validation accuracies (Figure 6.8-6.10). The SNAN3 with 30% tripartite synaptic connections exhibits optimal variance and bias tradeoff, with higher training accuracy than SNN and comparable validation accuracy. These metrics ensure that the spiking patterns from the validation set matched the spiking patterns produced during training. The SNN displays underfitting, exhibited by a higher validation accuracy than training accuracy, conveying that the trained network has difficulty generalizing new data. Defining the SNAN architecture is a highly iterative process due to the heterogeneity of the astrocytes combined with the stochastic spiking activity. Therefore, the number of astrocyte-to-neuron synapses must be sufficient to influence the postsynaptic neuron spiking and low enough to avoid neuronal overexcitation resulting in erratic neuronal spiking patterns. These effects are noticeable in the networks with more than 30% tripartite connections (Figure 6.9), whose validation accuracies suddenly drop to minimum levels.

Lastly, we have developed a SNAN where astrocytes are point processes with simpler models (compared with the astrocytic networks presented in Chapter 5) while retaining the essential astrocytic dynamics. Interestingly, astrocytes can simplify the network architecture. An SNN achieves faster learning with increasing synaptic connections, which is maximum when neurons have dense synaptic connections. If the dense connection is insufficient, another solution is increasing the number of postsynaptic neurons. Saunders et al. [422] presented a network with 100 and 400 postsynaptic neurons and reported that the training accuracy increases from 67% to 70%, respectively. Therefore, for example, a network with 400 neurons creates 316 600 synaptic connections. The proposed SNAN3 with 30% tripartite achieved 75.28% accuracy with only 78 400 synaptic connections plus 47 040 (neuron-to-astrocyte and astrocyte-to-neuron synaptic connections) with only 200 integrating components (100 neurons and 100 astrocytes).

6.6/ CONCLUSION

We proposed a novel and simplified spiking neuron-astrocyte network for unsupervised learning using STDP, combined with k-NN classifier for image recognition. The input layer consists of Poisson spiking neurons translating the input image pixel intensity into spike events. The dense synaptic connections transmit the input activities to the 100 postsynaptic neurons. The postsynaptic neurons then learn the input features by changing their synaptic weights following the STDP algorithm. In these networks, astrocytes have three main functions: (1) create a new network layer for integrating and translating presynaptic inputs, (2) act as additional synaptic connections simplifying network architecture, and (3) modulate synaptic plasticity for faster learning. We have achieved a maximum of 75.28 % of classification performance for SNANs, ensuring an optimal balance between variance and bias. We showed that astrocytes improve network performance (depending on their topology within the network) and facilitate stable neuronal spiking.

One of the main challenges we faced during network design is the simulation costs, where simulations are restricted to series computation rather than in parallel. Indeed, the additional astrocytic components plus the neuron-astrocyte couplings require more extended simulation and computationally heavy programs. Instead of using the Li-Rinzel model, we opted for the Postnov model and simplified the corresponding code using the Brian2 simulator with high-performance computing resources. Researchers can also design and implement SNAN using neuromorphic systems or hardware to solve the series computation restrictions. One can also design SNANs where astrocytes communicate via gap-junction mediated ICW propagation.

The next chapter aims to further simplify the network architecture by investigating how a single neuron can analyze synaptic inputs (neuronal and astrocytic inputs the like) for faster integration and transformation. This chapter is also a part of our objective to bridge the biological processes and artificial intelligence by taking advantage of the computational capacity of neurons and astrocytes.

7

A Multilayer-Multiplexer Network Processing Scheme

7.1/ Introduction

Synaptic inputs entering the dendritic heads diffuse along the dendritic shaft and pass through a series of attenuation, amplification, filtering, and delay depending on the passive and active mechanisms in the dendritic compartments, as discussed in Chapter 3. We have shown that fast synaptic current via AMPARs activation and slow synaptic or inward currents via NMDARs activation triggered by synaptic Glu^{-} or astrocytic Glu_a^{-}, respectively, influence the information processing in a single neuron (Chapter 5) and, therefore, in a network (Chapter 6). Identifying the influence of the dendrites in a single input signal is a rudimentary process. However, the driving force of a single synaptic input is inadequate to influence a somatic spike. Therefore, multiple presynaptic cells (neurons and astrocytes) continuously bombard the dendrites with input signals, and this is where the dendritic computation gets complicated. During simultaneous synaptic activation, the driving force of an input signal combines with the driving forces of its neighboring synaptic inputs. The contribution of a signal depends on several factors: its distance from the points of entry of other inputs, the diameter and length of its dendritic compartment, the morphology of the dendrites, the distribution of active channels, and the somatic dynamics, as well [229, 423–426]. An AP is generated if the sum of the driving forces reaching the somatic compartment exceeds the spiking threshold. At this point, it is challenging to determine the influence of synaptic input on somatic depolarization or to identify the role of the dendrites in neuronal computation [233, 426, 427].

After decades of studies, developing a unified understanding of how dendrites integrate and transform synaptic inputs entering the dendritic arborization into information-carrying spiking patterns is still lacking. In addition, advances in neuronal studies suggest that a single neuron can perform integration functions previously associated only with neuronal networks. To bridge and employ biological processes with deep learning schemes, we developed an abstraction modeling neural input integration and described how we could employ such abstractions in deep networks. The abstraction includes synaptic input location-dependent voltage delay and decay, time-dependent linear summation, and dynamic thresholding function. The proposed dendritic abstraction can be used to create multilayer-multiplexer neurons that consider the spatiotemporal properties of the dendrites and with greater computational capacity than the conventional schemes.

7.2/ BIOLOGICAL TO ARTIFICIAL SYNAPTIC INPUT INTEGRATION

The pioneering studies of Rall in the 1960s [207, 428] paved the way for extensive research to determine the governing principles of dendritic integration [217], the crucial roles of dendrites in neuronal processing [429], and to create models or abstractions for improving the computational capacity of a neuron [430]. As discussed in Section 3.5, the biologically-inspired McCulloch-Pitts neuron model describes the dendritic integration process in its simplest abstraction [247]. The linear summation of weighted synaptic inputs passes through a nonlinear thresholding function that determines the spiking behavior of the neuron. The most recent dendritic abstraction extends the linear-nonlinear Poisson (LNP) called the generalized linear model (GLM). In GLMs, the convolution of inputs passes through a static nonlinearity and is then fed to a spiking mechanism for the instantaneous firing rate [229, 431]. For both abstractions, the thresholding function (also called activation or transfer function) in the McCulloch-Pitts model and the static nonlinearity in GLM serves as the quantified function for dendritic integration. Most dendritic abstractions suggest that the nonlinearity is a sigmoidal signal [239, 243, 432, 433], although it becomes increasingly implausible when fitted with biological data [240].The subthreshold nonlinearity consists of three divisions for inputs within the same branch: linear for weak signals, supralinear for intermediate signals, and sublinear for strong inputs [232]. Sigmoidal nonlinearity then becomes inaccurate when the dendritic parameters and input distribution change [191].

A widely used method for quantifying dendritic integration is the IO transformation, comparing the synaptic inputs and the corresponding response in the somatic depolarization [191, 211, 239]. However, the IO curves vary significantly depending on which parameter is under observation, such as dendritic morphology, synaptic topology, and properties, ion channels, or combinations. Therefore, the level of biological realism or the complexity of the neuron model used for investigation is crucial for determining the dendritic nonlinearity [429]. Another factor to be considered in quantifying the dendritic integration is how the synaptic inputs were injected. In modeling and physiological experiment, stimulation protocols commonly use unitary or paired-pulse inputs. [191, 226, 245]. However, such inputs limit the dynamic range of the dendrites. Because experimental recording and dendritic manipulation are challenging [429], the stimulation protocols and experiments on dendritic integration performed under simplified conditions *in vitro* or unobserved inputs *in vivo* do not conclusively describe the biophysical dynamics of the neuron [239]. Singh and Zald [434] introduced a static linear hook transfer function describing linear-nonlinear dendritic integration by performing IO transformation with the neuron model. However, the formulation of the transfer function sacrificed some dendritic properties due to the simplification of the dendritic morphology, removal of dendritic mechanisms, and application of a time-invariant function. Simplification or tuning of such properties can potentially bias the output [435].

Our goal here is two-fold: (1) formulate a thresholding function that captures the linear-nonlinear dendritic integration, both in the sub- and suprathreshold region, and (2) propose a dendritic abstraction that takes into account the spatiotemporal synaptic and dendritic dynamics. First, we created a CA3 pyramidal neuron model, which included most biophysical mechanisms distributed somatodendritically. Then, we simulated the model using *in vivo*-like synaptic inputs to reconstruct biophysical dynamics. We identified the synaptic input propagation along the dendritic length and formulated the corresponding

signal delay and attenuation model. Next, we proposed a method for IO quantification for continuous inputs. Based on the results of the IO-transformation, we formulated the dynamic nonlinear thresholding functions. We described the functional components of the dendritic abstraction, which considers the spatial specificity of the inputs and the interaction between the inputs and dendritic mechanisms. Using multiple regression analysis, we identified the thresholding function. The resulting threshold nonlinearity is a dynamic function dependent on the synaptic input amplitude and the number of activated synapses that capture the linear, supralinear, and sublinear dendritic integration processes in the subthreshold region. The proposed dendritic abstraction captures the spatiotemporal processes such as synaptic input attenuation and delay, synaptic-input location dependency of somatic depolarization, and the biophysical spiking mechanism of the neuron.

7.3/ Formulating the Dendritic Abstraction

This section presents the step-by-step procedure in formulating the proposed dendritic integration abstraction. First is the development of the CA3 neuron, its morphology, and biophysical mechanisms. Then, the second part details the proposed equivalent dendritic abstraction and its subcomponents. Finally, the last part defines the IO transformation process.

7.3.1/ Pyramidal Neuron Model

A large number of time-dependent synaptic inputs entering a morphologically complex dendritic tree is difficult to control, and analyzing the dynamic response of the neuron is quite challenging [424, 436]. Thin oblique dendrites protruding from the main dendritic branch also influence the somatic response. Therefore, the neuron model should be biophysically-plausible, with its morphology and distributed mechanisms, but simple enough to follow the signal propagation.

7.3.1.1/ Distributed Mechanisms

We developed a simple but biologically-plausible anisotropic model of the CA3 pyramidal neuron from a rat hippocampus [437] using the NEURON simulation platform [17] ran with a time step of 0.05 ms [436]. NEURON is a well-suited simulator for multicompartmental models of individual neurons [438, 439]. The morphological detail is available at NeuroMorpho.Org, whose ID number is NMO_76005 [440]. This simple model has seven stems, four bifurcations, 15 dendritic branches, and a total of 116 dendritic sections. The spines are mushroom-typed with a head diameter of 0.35 μm [437], a neck diameter of 0.10 μm [187], and a neck length of 0.35 μm [437]. The spines are placed 0.50 μm from one another along the dendritic length [437], equating to 2129 synaptic locations. The d_lambda discretization rule divides the dendritic sections into electrical compartments [441]. Figure 7.1aa illustrates the anisotropic and morphologically realistic model, and the corresponding neuronal characteristics and morphological data are in Appendix B.

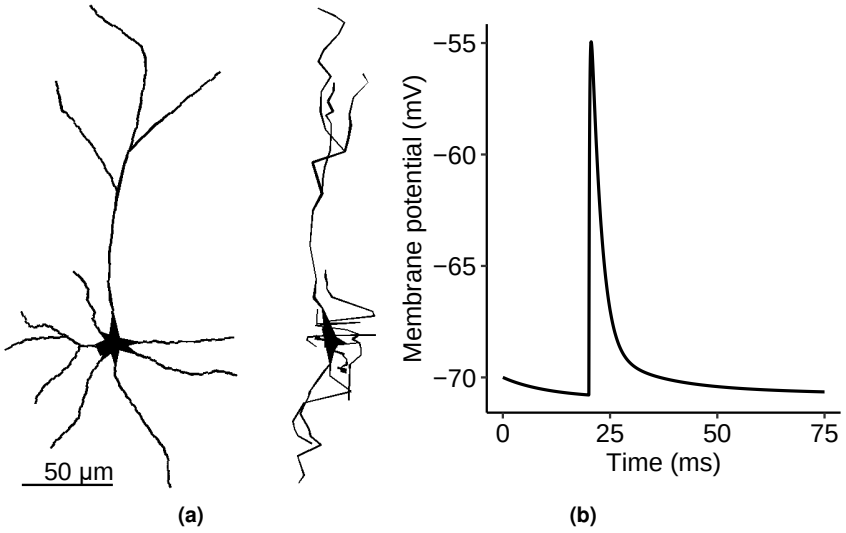

Figure 7.1: (a) The reconstructed model of the CA3 pyramidal neuron. The morphology of the pyramidal neuron in XY- and YZ axes (left and right, respectively) displays anisotropic features. (b) A single synaptic input. The single pulse synaptic input activated at $t = 20$ ms and with a maximum amplitude of -55.19 mV combines AMPARs and NMDARs kinetics and follows a double-exponential rise and decay function.

The neuron dynamics consist of various interactions amongst biophysical mechanisms such as synaptic saturations, dendritic spikes, and NMDA receptor nonlinearities [190, 226, 239]. These mechanisms facilitate dendritic integration and control the transformation of synaptic input patterns into somatic membrane potential changes and the generation of output spike trains [229, 239]. Therefore, we incorporate passive mechanisms and active channels into the neuron. Table C.1 presents the properties of these mechanisms and their distribution throughout the somatodendritic arborization. The neuron has constant passive properties, including the membrane and cytoplasmic resistivities and specific capacitance. In the spine necks, the cytoplasmic resistivity was set so that the spine neck resistance was equal to 500 MΩ [187]. Furthermore, the biological cell model includes active channels distributed heterogeneously from soma to dendrites. These active channels are the fast-activating sodium channels (Na), delayed-rectifier potassium channels (K_{DR}), A-type potassium channels (K_A), N-, T-, and L-type calcium channels (Ca_N, Ca_T, and Ca_L).

7.3.1.2/ Synaptic Inputs

In this study, the synaptic inputs follow *in vivo*-like spatiotemporal patterns to replicate the full range of neuronal dynamics covering the sub- and suprathreshold regions. We modeled the spatial- and time-dependent excitatory synaptic inputs as membrane potentials induced by the conductance change of AMPA and NMDA receptors in the spine heads [205].

For time t, the synaptic conductance of AMPAR, g_{AMPA}, is a double-exponential function given in Equation 3.35 [202]. The NEURON Exp2Syn function models the AMPAR response [229]. The voltage-dependent NMDARs kinetics follow the same function as the AMPARs kinetics with extracellular Mg^{2+} blocking component [200, 205, 206]. The NMDAR conductance g_{NMDA} is given by Equation 3.36 [200]. The NEURON function au-

tomatically computes the values of α_A and α_N so that the maximum values of g_{AMPA} and g_{NMDA} are equal to their corresponding peak conductances. The single synaptic input in Figure 7.1b measured in the spine head has a 14.81 mV peak amplitude from rest and a half-width of 2.75 ms. The corresponding values of the synaptic input parameters and other neuron properties are in Table C.2.

7.3.2/ Dendritic Abstraction

When multiple synapses are simultaneously active and spatially segregated, inputs driving the somatic potential change are challenging to discriminate. Working on the notion that dendrites require dynamic independence to perform various computations, we identified each dendritic length as an independent subunit. For example, when identical inputs simultaneously activate clustered synapses in C and D (Figure 7.2a) following spiking patterns in Figure 7.2b, the changes in the membrane potential along the distal C-to-soma (Figure 7.2c) and distal D-to-soma (Figure 7.2d) at specific time windows indicate signal diffusion. Synaptic inputs propagate from the synaptic location to the distal end of the dendritic branch, to the neighboring branches and the soma. Indeed, signal propagation along the dendritic branch is bidirectional, and signals backpropagate, upon AP generation, from the soma to some extent of the distal branches [442]. This bidirectional propagation then makes input discrimination intricate. Notice the low membrane potential between the synaptic input activation and the somatic activation. It suggests that even though the synaptic input in the tertiary dendrites significantly attenuates, it can still cause a somatic activation with ~3 ms delay. Moreover, the backpropagating AP may have a minimum effect on the distal dendrites. We examined the membrane potential magnitudes, particularly during the synaptic input peaks (Figure 7.2e). At $t = 21.50$ ms, both the dendrites drive the membrane potential elevation. When individual dendrite is active, at $t = 222.50$ ms and $t = 322.50$ ms, significant differences in the membrane potential between sibling branches are noticeable. Therefore, even though signal diffuses throughout the dendritic tree, we can still identify the origin of the somatic fluctuations by the level of the driving force produced from the individual branches. We repeated the simulations using varying synaptic input combinations and locations, and the results were similar. One of the foci of this study is to identify how the dendrites process synaptic inputs to perform branch dendrite-specific computation. Therefore, we arrive with the following modeling approach with these results.

We already presented the biological model of the neuron in the previous section. The next step is to identify a dendritic abstraction that models the spatiotemporal dendritic integration process. This abstraction is necessary because the thresholding nonlinearity, a time-independent function, is insufficient for describing the dendritic dynamics [239, 434]. There is a need for another function for the signal propagation along the dendritic branch, the corresponding signal delay, attenuation, and the time- and location-dependency.

7.3.2.1/ Model

Consider the primary dendritic branch (the apical trunk) and the secondary dendritic branch (in the apical tuft) shown in Figure 7.3a and Figure 7.3b. For modeling purposes,

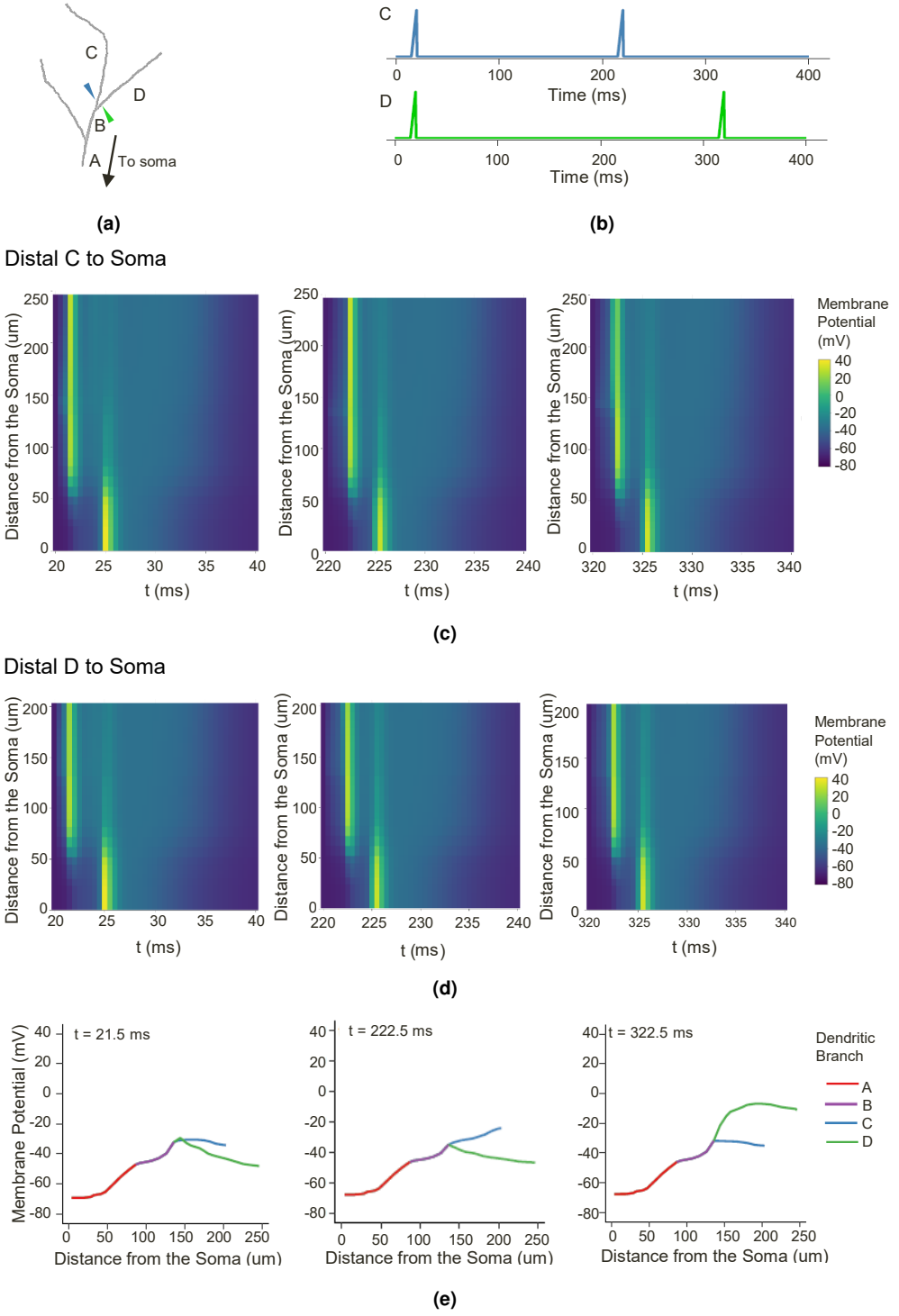

Figure 7.2: Signal propagation along the apical dendritic branches. (a) At a distance of 2 μm from the branching point, ten excitatory inputs activate clustered synapses along dendritic branches C and D with their respective activation patterns in (b). The space plots in (c) and (d) show the change in membrane potential of the dendritic length from the distal end of C to soma and from the distal end of D to soma, respectively. (e) Further investigation on the membrane potential during synaptic activation indicates that even though the signals diffuse in all directions, it is still possible to identify the dendritic branch that drives the somatic depolarization by determining the synaptic locations that are first to peak.

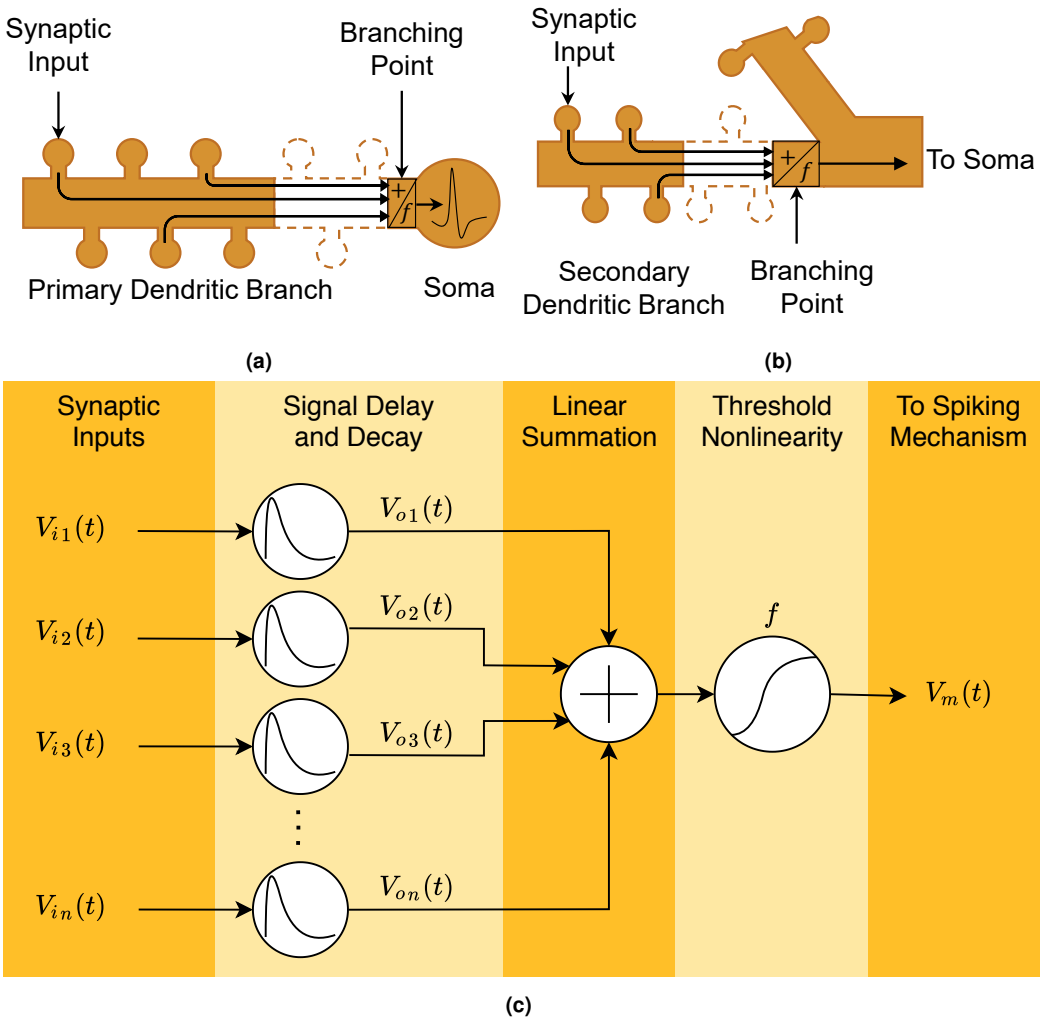

Figure 7.3: The dendritic branch is an independent computational subunit. The synaptic inputs enter the dendritic shaft via the dendritic neck and then flow untangled in one direction, from the distal end of the branch to the opposite end. (a) The primary dendritic branch is from the first bifurcation point to the section connected to the soma, while (b) the secondary dendritic branch is from the distal end to the bifurcation point. Dendritic integration and transformation occur in the branching point. Its output drives the somatic spiking in (a) or travels to the soma in (b). (c) The equivalent dendritic abstraction includes the time-continuous synaptic inputs $V_{in}(t)$ that experience individual attenuation and delay. The outputs $V_{on}(t)$ are linearly integrated and then sent to the thresholding function for transformation. The transformed signal $V_m(t)$ flows to the next proximal point until it reaches the somatic compartment for AP generation.

we apply the following concepts:

1. Each dendritic branch is an independent computational subunit. The dendritic abstraction corresponds to the dynamics occurring within a compartment: the dendritic length from the bifurcation point to the somatic connection (Figure 7.3a) or from the distal end of the apical dendritic branch to the bifurcation point (Figure 7.3b). Based on the impedance tree-graph concept [238], branches are mutually independent.

2. Synaptic activation occurs in the dendritic spine head and none along the dendritic shaft. This assumption avoids electrical shunting and over saturation of inputs [187] and ensures that the synaptic inputs have a comparable influence on the dendritic

shaft around their entry points.

3. Signals within the dendritic branch propagate individually (untangled), and synaptic inputs travel only in one direction, from the distal apical or basal dendrites to the somatic compartment [238]. We considered the dendritic branch as multiplexer, and the signals are superimposed on each other. It simplifies the tangling problem and allows us to approximate the influence of each input on the depolarization in the branching point.

4. The input summation and IO transformation occur in the branching point. Theoretically and experimentally, and when considering the equivalent dendritic circuit, a synaptic input almost immediately integrates with the neighboring inputs around its entry point in the dendritic shaft. Therefore, dendritic integration can transpire anywhere along the dendritic length. To cover the whole dendritic length and the incoming signals, we take the proximal end of the dendritic branch as the thresholding point.

The dendritic abstraction consists of the following. The synaptic input $V_{in}(t)$, where n is the number of the activated synapse, is a time-varying *in vivo*-like synaptic spiking. Throughout the distance between the dendritic head to the branching point, the dendritic active and passive mechanisms influence the amplitude decay and time delay of $V_{in}(t)$. The attenuation function output $V_{on}(t)$ is a weaker location-dependent signal. The linear summation integrates the attenuated signals and thus represents the linear component of dendritic integration. The nonlinear function f transforms the sum into a single information-carrying $V_m(t)$. $V_m(t)$ then travels along the dendritic arborization to the next proximal dendritic branch or straight to the soma for spiking.

7.3.2.2/ SIGNAL PROPAGATION AND DELAY

Wybo et al. [443] presented a method for simplifying the dendritic morphology directly from experimental data and suggested that a complex subtree can be modeled into a single branch with multiple reduced compartments while preserving the neuronal biological responses. They approximated the dendritic voltage responses using the Hodgkin-Huxley formalism, where the parameters for the passive and active channels were fitted using the least-square method. Since our goal is to identify the input integration at the thresholding point, dividing the dendritic branch into compartments with multiple nonlinear systems of equations is computationally costly. In order to simplify the dendritic voltage response, we used the voltage propagation model, which was modified to incorporate the collective effects of the passive and active mechanism along the cable of varying morphology. Instead of fitting each ion channel in the compartment, we identified the parameters α and β in Equation 7.1 using regression analysis of the membrane potential at the entry and thresholding points caused by individual synaptic inputs.

The IO transformation method usually compares the arithmetic summation of input with the output depolarization. However, this method disregards the synaptic locations and considers that the synaptic inputs have the same influence over the soma or the thresholding point. Synaptic input travels through the spine neck from the spine head, enters the dendritic shaft, and then propagates to the thresholding point. While propagating, signals

are susceptible to considerable voltage decay and delay before reaching the proximal end of the dendritic branch. Therefore, it is only fitting to compute the arithmetic sum of the decayed and delayed signals rather than the direct sum of the signals entering the spine head. In this case, the dendritic abstraction becomes spatiotemporal, where the input signals are subjected to decay and delay by $V_o(t)$ before integrating into the thresholding point (Figure 7.3c). The spatiotemporal propagation model is defined as

$$V_o(t) = \alpha e^{-x/\lambda} V_i\left(t - \beta\frac{\tau x}{2\pi}\right), \tag{7.1}$$

where V_o is the attenuated and delayed synaptic input amplitude when it reaches the thresholding point at time t, V_i is the electrotonic potential of the synaptic input (the difference between the synaptic input and the resting potential), and x is the distance between the synaptic input entry point and the thresholding point [79, 143, 444]. The propagation velocity varies at different points along the dendritic branch due to the difference in diameters and lengths of the dendritic sections. To simplify this issue, we converted the dendritic branch into a single cable with constant distributed parameters by computing the total effective length, λ, and total time constant, τ [79]. The total effective length (in μm), given as

$$\lambda = \sum_{j=1}^{k} \sqrt{\frac{R_{mj}}{R_{aj}}\frac{d_j}{4}}, \tag{7.2}$$

and the total time constant (in ms), given as

$$\tau = \sum_{j=1}^{k} R_{mj} C_{mj}, \tag{7.3}$$

are dependent on the diameter d of k sections. Here, R_m is the membrane resistance equal to 10 000 Ωcm^2 and R_a is the axial resistance equal to 100 Ωcm [79, 444], consistent with the biological model. The parameter α captures the dramatic decrease in synaptic input amplitude as it travels along the high resistance spine neck [195] and dendritic shaft, while β defines the signal delay caused by the active mechanisms along the dendritic length. The terms $\alpha e^{(-x/\lambda)}$ is the coefficient of voltage decay and $\beta(\tau x/2\pi)$ represents the time delay. We computed the corresponding values of α and β for each dendritic branch via regression analysis. To do so, each synapse along the dendritic branch, from the distal to the proximal end, is activated one at a time while measuring the membrane potentials at the input spine head and the thresholding point. The parameter α was computed by fitting $\alpha e^{-x/\lambda}$ to the amount of measured voltage decays (difference between the peak depolarizations of the synaptic inputs and thresholding point). In parallel, β was determined by fitting $\beta(\tau x/2\pi)$ to the measured voltage delays (the time difference between the peak depolarizations at the spine head and thresholding point).

7.3.2.3/ SPIKING MECHANISM

Even with the ramified morphology of dendrites and spatiotemporal disparity of synaptic inputs, the soma is responsible for encoding information [427]. When the transformed dendritic signals arriving at the soma are large enough, the somatic spiking mechanism generates an AP [191]. In the dendritic abstraction, we used the Hodgkin-Huxley spiking

mechanism in Equation 7.4 because it closely reproduces the somatic dynamics of the biological neuron.

$$C\frac{dV}{dt} = I - g_{Na}m^3h\,(V - V_{Na}) - g_K n^4\,(V - V_K) - g_{Ca}s^2r\,(V - V_{Ca}) - g_L\,(V - V_L) \tag{7.4}$$

It includes active Na^+, K^+, Ca^{2+} channels, and passive leak parameters. V corresponds to the membrane potential, C is the membrane capacitance, and I serves as the input whose intensity is equal to 10 μA/cm^2 multiplied by the summation of activation functions f of the dendritic branches connected to the soma [76, 86, 445, 446]. Equation 7.5 gives the channel activation and inactivation functions. Refer to Table C.3 for the parameters.

$$\frac{dz}{dt} = \alpha_z(1 - z) - \beta_z z, \quad z = m, n, h, r, s, \tag{7.5}$$

$$\alpha_m = \frac{0.1\,(-V - 45)}{\exp\left(\frac{-V - 45}{10}\right) - 1}, \qquad \beta_m = 4\exp\left(\frac{-V - 70}{18}\right),$$

$$\alpha_n = \frac{0.01\,(-V - 60)}{\exp\left(\frac{-V - 60}{10}\right) - 1}, \qquad \beta_n = 0.125\exp\left(\frac{-V - 70}{80}\right),$$

$$\alpha_h = 0.07\exp\left(\frac{-V - 70}{30}\right), \qquad \beta_h = \frac{1}{\exp\left(\frac{-V - 40}{10}\right) + 1},$$

$$\alpha_r = 0.000457\exp\left(\frac{-V - 13}{50}\right), \qquad \beta_r = \frac{0.0065}{\exp\left(\frac{-V - 15}{38}\right) + 1},$$

$$\alpha_s = \frac{0.055\,(-V - 27)}{\exp\left(\frac{-V - 37}{3.8}\right) - 1}, \qquad \beta_s = 0.094\exp\left(\frac{-V - 75}{17}\right).$$

Note that the dendritic abstraction can employ other spiking mechanisms such as LIF. In this case, we employ the common Hodgkin-Huxley formulism, which best approximates the spiking behavior and the shape of the AP of the biological soma consisting of multiple types of ionic channels presented in Section 7.3.1.

7.3.2.4/ Input distribution

For each dendritic branch, we performed 40 simulations that lasted 1000 ms each (with a 0.05 ms time step) and whose inputs have a Poisson spiking interval of 20 ms and Gaussian synaptic noise. These inputs were either segregated or clustered along the dendritic branch. Let d be the length of the dendritic branch. For segregated inputs, activated synapses were randomly located between $0.01d$–d, $0.01d$–$0.5d$, or $0.5d$–d. For clustered inputs, activated synapses were also randomly placed between $0.01d$–$0.25d$, $0.25d$–$0.5d$, $0.5d$–$0.75d$, or $0.75d - d$. The number of activated synapses per simulation was minimum enough to cause depolarization at the thresholding point and maximum

enough to avoid oversaturation and excessive dendritic burst. Therefore, three, five, and seven synaptic inputs were activated for each simulation set. In total, there were 21 input categories. There were ten simulations for segregated inputs along the dendritic branch and five simulations for the rest. This input distribution gave a wide range of synaptic and dendritic activities.

7.3.2.5/ INPUT-OUTPUT QUANTIFICATION

The following are the features of this IO quantification framework: the input is the summation of the estimated synaptic inputs reaching the thresholding point (normalized), then the output is the measured membrane potential at the thresholding point (normalized), and lastly, the IO relationship is a nonlinear time-independent function. The feature scaling restricts the voltage amplitude from 0 (−70 mV) to 1 (40 mV) to avoid the effects of negative values. We measured the synaptic inputs at the spine head along the primary apical trunk and the thresholding point (Figure 7.4a). Then, we estimated the voltage decay and delay of the individual inputs when they reached the thresholding point by applying Equation 7.1. $V_{expected}$ represents the summation of the attenuated inputs. For instance, Figure 7.4b shows the input patterns measured from synapses segregated along the primary apical dendritic branch. The input summation (gray) shown in Figure 7.4c drove the depolarization at the thresholding point (black).

First, we divided the $V_{observed}$ time series into time windows defined by the two consecutive local minima (gray lines in Figure 7.4d). The exact time windows were also applied to $V_{expected}$. Within each time window, we measured the maximum depolarization of $V_{observed}$ and the corresponding maximum peak amplitude of $V_{expected}$. The comparison between these points gives us the IO relationship.

7.4/ RESULTS

7.4.1/ DENDRITIC INTEGRATION IN THE SUBTHRESHOLD AND SUPRATHRESHOLD REGIONS

The dendritic arborization in Figure 7.1a has three levels mainly, the primary dendrites (those connected directly to the soma), the secondary dendrites (after the first bifurcation points), and the tertiary dendrites (after the last bifurcation points). We simulated the neuron model for each dendritic branch by randomly activating segregated or clustered synaptic inputs along the dendritic length. Then, we applied the IO quantification method to identify the within-branch dendritic integration in the sub- and suprathreshold regions. Furthermore, we removed the suprathreshold IO pairs caused by the backpropagating signals and dendritic bursts from the dataset.

Here, we present the IO curves in the apical trunk (primary), the left-most apical tuft (secondary), and the right-most apical tuft (tertiary) dendrites (Figure 7.1a). The subthreshold IO data were smoothened using the locally estimated scatterplot smoothing (loess) method, while linear models best described the suprathreshold data. The points

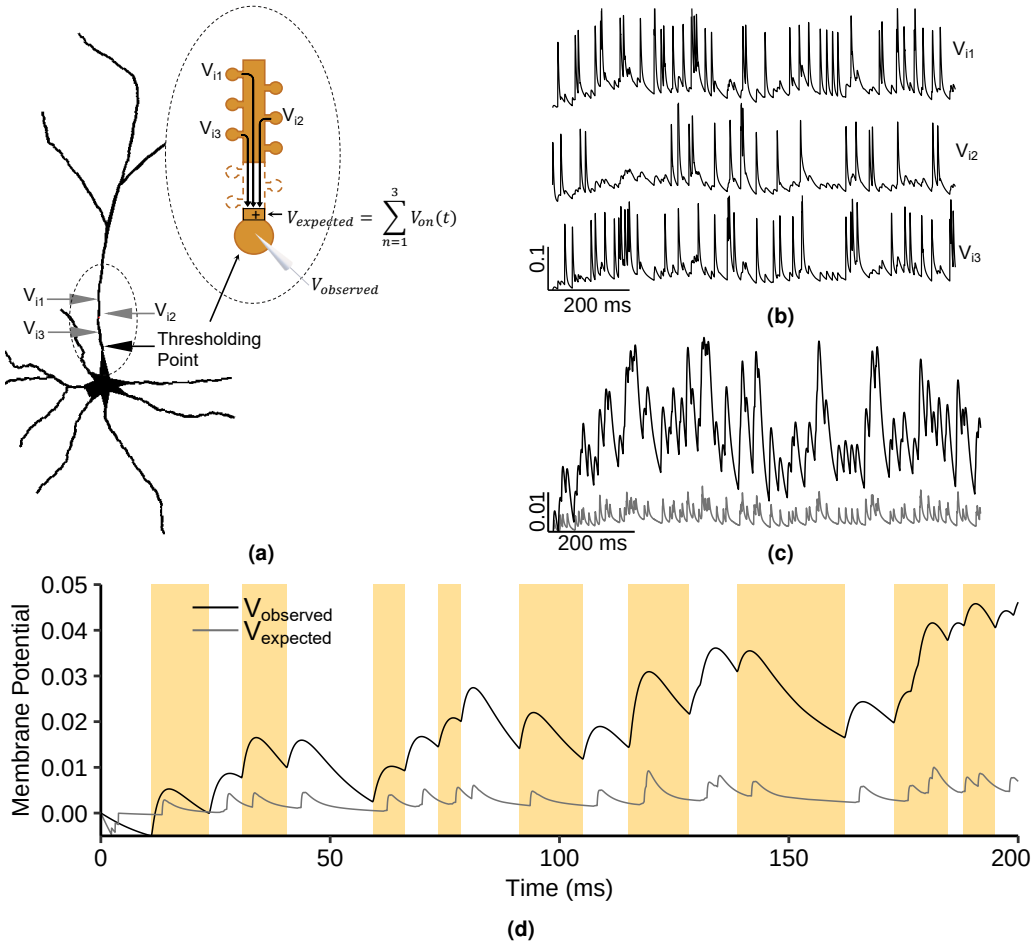

Figure 7.4: The input-output quantification process. (a) The *in vivo*-like synaptic inputs V_{i1}, V_{i2}, and V_{i3} were measured from the synaptic heads that are 46.67 μm, 28.32 μm, and 38.17 μm from the thresholding point of the primary apical dendritic branch. Inputs V_{in} are subjected to propagation delay and decay before reaching the thresholding point for arithmetic summation, where the resulting sum is the $V_{expected}$. The measured potential at the thresholding point is termed as $V_{observed}$. (b) The random spiking frequency of the inputs results in a dynamic and sustained nature. (c) The summation of the predicted attenuated inputs reaching the thresholding point (gray) drove the subthreshold depolarization (black) from the same point. (d) Two consecutive local minima of the membrane potential ($V_{observed}$) divided the observed and expected depolarization ($V_{expected}$) into time windows (alternating white and orange rectangles). IO quantification compares the maximum observed depolarization (black), and the maximum expected depolarization (gray) within the same time window.

represent the mean $V_{observed}$ amplitude per $V_{expected}$ bin width. Figure 7.5 illustrates the $V_{expected} : V_{observed}$ curves of the apical dendrites in the subthreshold (left column) and the suprathreshold (right column) regions. According to Polsky et al. [232], the subthreshold nonlinearity in the pyramidal neurons follows a linear-supralinear-sublinear curve based on increasing input strength. This relationship is visible in the secondary (Figure 7.5c) and tertiary dendrites (Figure 7.5e), where the IO curves deviate above and below the linearity upon crossing $V_{expected} = 0.1$. However, the primary dendrite exhibits a strong supralinear dendritic integration (Figure 7.5a), then the $V_{observed}$ levels stabilize as the curve approaches the sublinear region. The basal dendrites connected to the soma also exhibit almost the same nonlinearity. In the suprathreshold regions (Figure 7.5b, 7.5d, and 7.5f), the $V_{observed}$ level is steady even with increasing $V_{expected}$. It is as expected since the somatic spiking peak amplitude is constant.

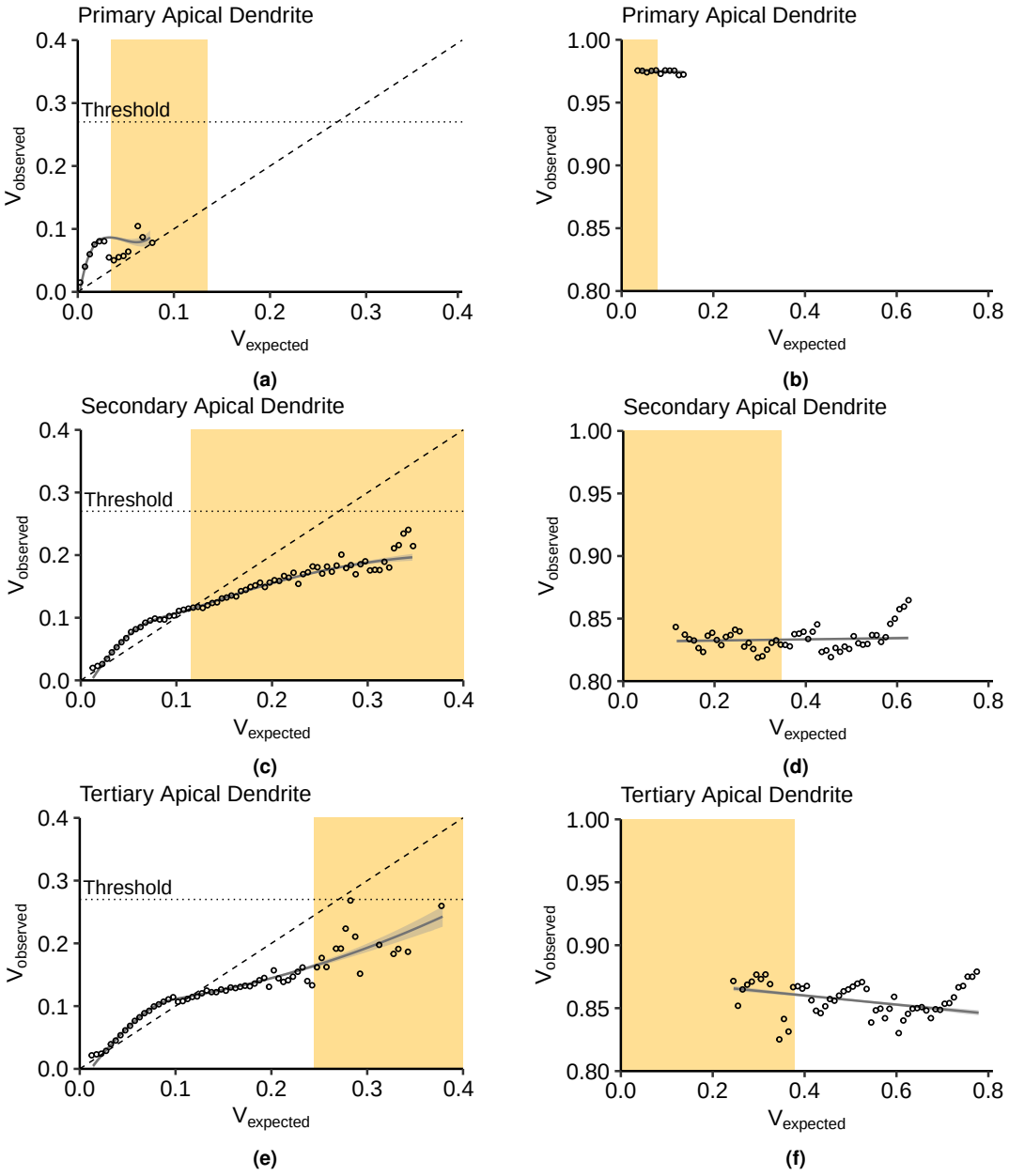

Figure 7.5: Dendritic integration in the subthreshold (left column) and suprathreshold (right column) regions. (a) The subthreshold IO curve in the primary dendrite (dendritic branch connected to the soma) is strongly supralinear between [0, 0.1] of $V_{expected}$ and $V_{observed}$, while in (b) the suprathreshold region, the spiking amplitude is constant at 0.975. (c) The secondary apical dendrite displays a nonlinearity that deviates from linear to supralinear, and after crossing $V_{expected} = 0.1$, shifts to sublinear. (d) The range of $V_{expected}$ necessary for a successful spike exceeds the range in (b) but with a lower spiking amplitude (0.83). (e) The tertiary apical dendrite produces a subthreshold nonlinearity that is almost similar to (c), while the suprathreshold spiking amplitudes slopes down ($m = -3.77$). Moreover, the orange regions in the subthreshold plots (a, c, and e) represent the range of $V_{expected}$ causing a successful spike in the suprathreshold region, while the orange regions in the subthreshold plots (b,d, and f) indicates the range of subthreshold points. These boundaries indicate that the spiking threshold for each dendritic branch increases (0.035 in (a), 0.115 in (c), and 0.245 in (e)) with respect to the distance from the soma and the location in the arborization of the dendritic branch. Besides, the subthreshold and suprathreshold regions overlap, suggesting that the thresholding function is not a simple sigmoid function.

Another striking feature of the IO transformation is the level of $V_{observed}$ and the range of $V_{expected}$. In the primary dendrite (Figure 7.5a), the suprathreshold dendritic integration output lies between 0 and 0.1 of $V_{observed}$, which is also the same input summation range. $V_{expected} > 0.1$ results in somatic spiking. In the secondary (Figure 7.5c) and tertiary dendrites (Figure 7.5e), the dendritic integration plateaus after crossing $V_{expected} = 0.1$ at a level lower than the threshold ($V_{observed} = 0.27$). The input summation range causing a subthreshold response increases, from the primary to the tertiary dendrites (the dendritic branch gets further away from the soma). The smaller range of $V_{expected}$ in the primary dendrite correlates with the large voltage decay of synaptic inputs reaching the branching point. The peak of observed depolarization in the suprathreshold region also decreases with respect to the distance and number of bifurcations from the soma. In primary dendrite (Figure 7.5b), successful spiking produces a peak depolarization of 0.975 (37.5 mV), while in the secondary dendrite (Figure 7.5d), the peak is constant around 0.83 (21.30 mV). $V_{observed}$ in the tertiary dendrite (Figure 7.5f) slopes down from 0.86 (24.6 mV) to 0.84 (22.4 mV). Furthermore, the range of input summation resulting in successful spikes gets wider. In Figure 7.5b, successful spikes are concentrated between 0.035 to 0.135. In Figure 7.5d and 7.5f, spikes are spread within [0.115, 0.625] and [0.245, 0.775], respectively.

Furthermore, the minimum input amplitude necessary for a successful spike changes with dendritic location. The gray areas in subthreshold plots (Figure 7.5a 7.5c, and 7.5e) indicate the ranges of $V_{expected}$ that resulted in somatic spiking, while in the suprathreshold regions (Figure 7.5b, 7.5d, and 7.5f), the gray areas indicate the subthreshold ranges. The minimum input summation for suprathreshold spiking shifts to the right, from 0.035 in the primary branch (Figure 7.5a), 0.115 in the secondary branch (Figure 7.5c) to 0.245 in the tertiary branch (Figure 7.5e). In the dendritic integration viewed within-branched, it appears that the spiking threshold differs as a consequence of heterogeneity in distributed active mechanisms along the dendrites. Then, considering that the dendrites received the same input combinations in terms of the number of activated synapses (three, five, and seven), the range of subthreshold values that the dendrites produced expands. Moreover, the subthreshold and suprathreshold areas overlap. There are subthreshold values under the region where successful spikes occurred. It suggests that the thresholding function is not a straightforward sigmoid because a sigmoid function considers the points within the overlapping regions as errors.

The within-branch integration results demonstrate that the thresholding function is asymmetric, in contrast with a sigmoidal function. The subthreshold integration is a linear-supralinear-sublinear function dependent on the branch location within the dendritic arbor and whose degree of integration is influenced by the active mechanisms and the strength of the driving forces of the synaptic inputs.

7.4.2/ Location-Dependent Dynamics

We analyzed the effects of segregated and clustered synaptic input locations on the within-branched dendritic integration. The density plots in Figure D.1 show the distribution of $V_{expected}/V_{observed}$ for each synaptic location along the dendritic branch. The plots suggest that synaptic locations have an inconsiderable influence on dendritic depolarization, which is a direct consequence of the application of synaptic input decay and delay

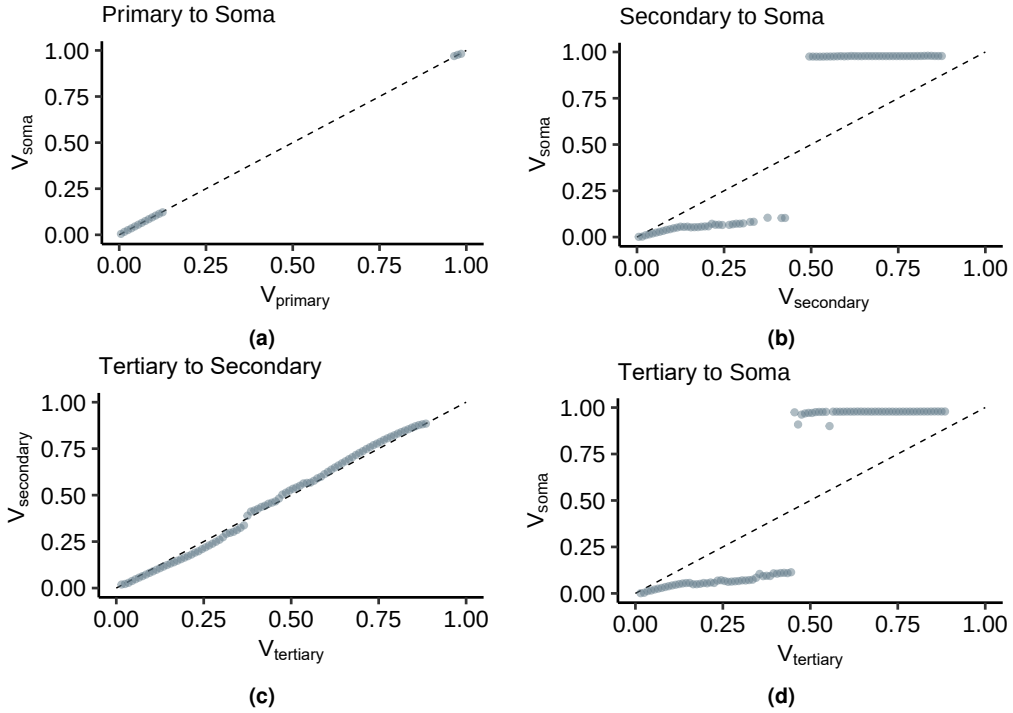

Figure 7.6: Location-dependent dynamics. The plots show the relationships between soma and dendritic branches. The points represent the mean output depolarization per input bin. (a). The depolarizations in the soma and the apical thresholding point form a linear relationship in the subthreshold ($0 \leq V_{primary} \leq 0.125$) and concentrated in the suprathreshold with significant discontinuity in between. (b) The relationship between $V_{secondary}$ and V_{soma} is strongly sublinear in the subthreshold region ($0 \leq V_{secondary} \leq 0.5$) and constant with increasing $V_{secondary}$ inputs. (c) Overall, the relationship between $V_{tertiary}$ to $V_{secondary}$ is linear, with a slight fluctuation from the linearity. (c) The relationship between the tertiary branch inputs and the soma is comparable with (b) because the secondary thresholding point also transforms the inputs flowing from the tertiary dendrites.

(Equation 7.1) preceding the IO quantification. Therefore, we consider the dendritic integration as independent from the synaptic input location, given that the propagation model in the dendritic abstraction (Figure 7.3c) already has the spatiotemporal data of the input signals.

Most studies in IO transformations view the observed depolarization at the soma and compare it to the summation of inputs or the intensifying stimulation from various dendritic sites. We compare the membrane potential at the thresholding point with somatic depolarization (Figure 7.6). The primary apical dendrite is located near the soma; therefore, the membrane potential at the thresholding point ($V_{primary}$) leads to an equivalent somatic potential (V_{soma}) (Figure 7.6a). The subthreshold regions display a linear relationship while spike amplitudes rest at $\sim$1. The discontinuity occurs due to the sudden increase in somatic depolarization and the proximity of the primary thresholding point to the soma. The primary dendrite has a low threshold in that the maximum subthreshold $V_{primary}$ is 0.125. The low threshold is consistent with the low $V_{expected}$ values in Figure 7.5a. However, the signal emanating from the secondary apical dendrite undergoes a substantial voltage decay (Figure 7.6b) due to the drastic increase in apical trunk resistance. The subthreshold region displays a sublinear relationship with the somatic depolarization. In this case, the first successful spike occurs at $V_{secondary} = 0.5$, and the spiking threshold differs from the primary dendrite (Figure 7.6a). Then, we analyzed the signal flow

from the tertiary dendrite to the secondary dendrite (Figure 7.6c) and finally to the soma (Figure 7.6d). In Figure 7.6c, the $V_{tertiary}/V_{secondary}$ has no noticeable discontinuity, and in general, the relationship is linear, with only a slight deviation from sublinear to supralinear. The continuity occurs because the depolarizations are viewed away from the soma. In our analysis of the membrane potential, we found backpropagation and dendritic bursting occurrences that are not conveyed into the soma. Then, if we view the signals from the tertiary apical branch to the soma (Figure 7.6d), the $V_{tertiary}/V_{soma}$ relationship is virtually the same as in Figure 7.6b. This relationship results from the signal passing through the secondary dendritic branch.

Therefore, even though the signal from a point in the dendritic arborization is viewed from the soma and there is a distinguishable difference between the output levels in the subthreshold and suprathreshold regions, the thresholding function is still not sigmoidal. Also, the results shown in Figure 7.6 denote the subunit-independence of each dendritic branch.

7.4.3/ Dynamic Nonlinear Thresholding Function

Previously, we indicated that the subthreshold and the suprathreshold regions of individual dendrites with within-branch inputs overlap. We further characterized the dendritic integration curve and discovered that the overlapping regions resulting from shifting the IO curve attributed to the increased number of activated synapses during each simulation. Figure D.2 illustrates the clustering of $V_{expected}/V_{observed}$ per number of activated synapses, n. Furthermore, the correlation coefficient r between the $V_{observed}$ and n establishes the influence of synapses in dendritic integration ($r = 0.43$ for primary apical dendrite, $r = 0.36$ for secondary apical dendrite, and $r = 0.47$ for tertiary dendrite).

We discovered that the overlapping sub- and suprathreshold regions displayed in Figure 7.5 are not outliers but pertain to the shifting of dendritic integration relative to n. In Figure 7.7, the dendritic integration in the subthreshold (left) and suprathreshold (right) regions is driven by increasing n. The vertical lines in the subthreshold regions indicate the minimum $V_{expected}$ necessary for a successful somatic spike, while the vertical lines in the suprathreshold regions correspond to the range of $V_{expected}$ in the subthreshold regions. These limits shift to the right as n increases. This behavior demonstrates that the dendritic branch has a dynamic threshold in that the input summation required for somatic spiking varies and is dependent on n.

In the primary dendrite (Figure 7.7a), the dendritic integration is strongly supralinear as it reaches $V_{observed} = 0.09$ and then drops down to slightly above the linearity. In the suprathreshold region (Figure 7.7b), the IO pairs per n cluster together and slightly overlap with the neighboring clusters. However, we can see the difference in dendritic integration for each n in the subthreshold regions in the secondary (Figure 7.7c) and tertiary dendrites (Figure 7.7e). When $n = 3$, the dendritic integration is slightly supralinear ($0 < V_{expected} < 0.1475$). For $n = 5$, the integration is linear between [0, 0.1275] and turns into sublinear. Lastly, for $n = 7$, the integration starts as slightly sublinear then moves into strongly sublinear, which plateaus at $V_{observed} \simeq 0.2$. For each n in the suprathreshold region (Figure 7.7d), the continuity of dendritic integration, from sub- to suprathreshold, becomes distinct as the minimum $V_{expected}$ for spiking coincides with the maximum sub-

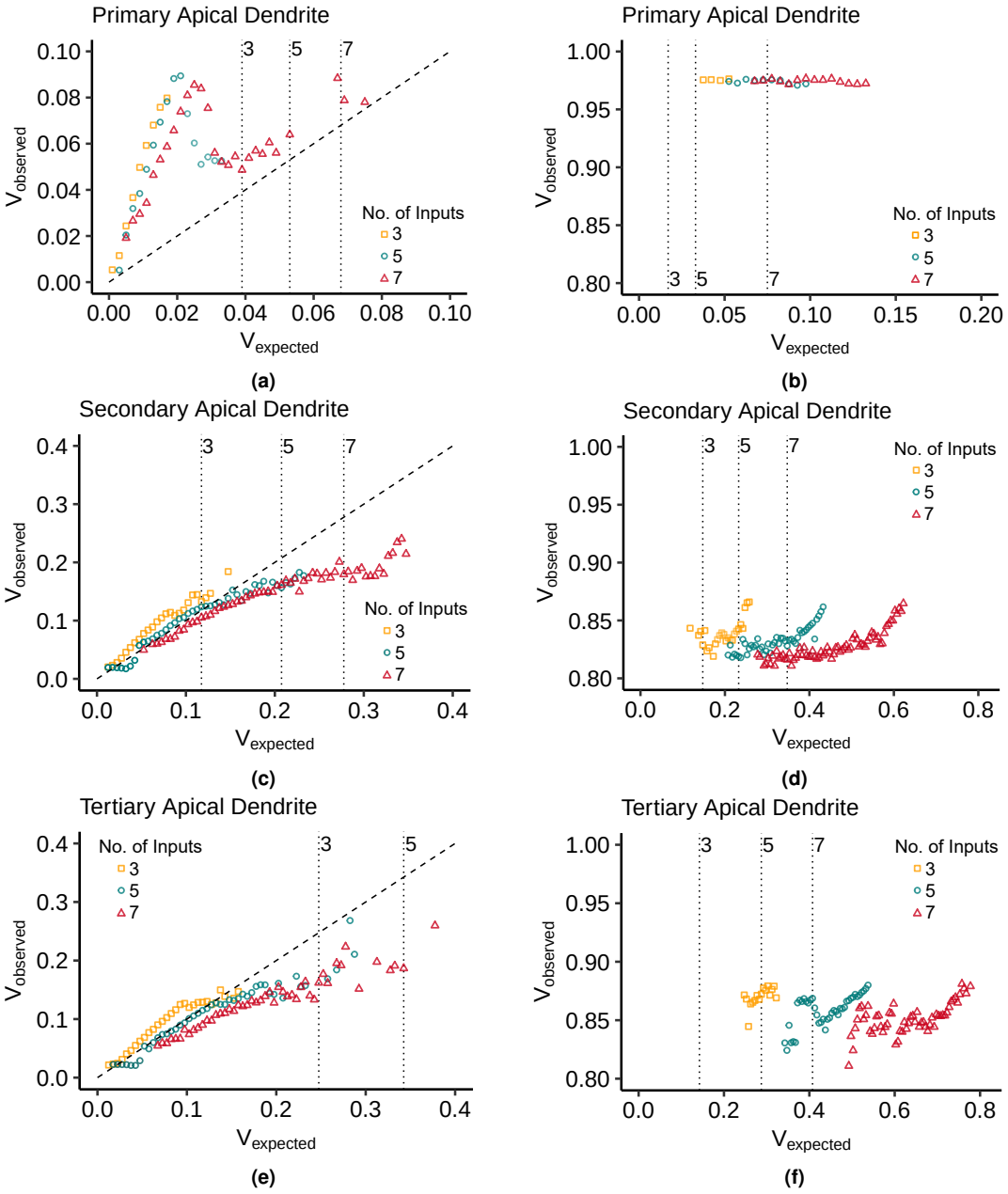

Figure 7.7: Influence of activated synapses in dendritic integration. In the subthreshold plots, the vertical lines indicate the start of somatic activation per number of inputs, while in the suprathreshold regions, the lines indicate the limit of subthreshold depolarization. In the subthreshold regions (left column), the dendritic integration curve shifts to the right as the number of inputs, n, increases. The range of $V_{expected}$ causing output depolarization in the suprathreshold regions (right column) also shifts to the right with increasing n. (a) In the primary branch, the dendritic integration is strongly supralinear, while the integration in (c) the secondary and (e) tertiary branches, the inputs results in dendritic integration shifting from supralinear to linear to sublinear. Then, in (b) the suprathreshold region of the primary apical branch, the $V_{expected}$ span per n are clustered close to each other, while as the branch becomes more distant from the soma, (d) in the secondary, then in the (f) tertiary branch, the span of $V_{expected}$ becomes more distinct.

threshold $V_{expected}$ (determined by the vertical lines). The tertiary branch also exhibits the supralinear-linear-sublinear relationship of $V_{expected}$ and $V_{observed}$ in Figure 7.7c, except that the IO curve does not stabilize with a further increase of $V_{expected}$. Likewise, in the suprathreshold region, the clustering of IO pairs is more distinct, and there is a clear

separation between lower and upper $V_{expected}$. Overall, dendritic integration is a nonlinear function displayed in the IO curves in Figure 7.5. Further analysis of the IO pairs tells us that this nonlinearity consists of multiple linear and nonlinear functions, which can be supralinear, linear, and sublinear, relative to the intensity of the driving force produced by the synapses.

So what do these imply? It tells us that (1) the dendritic branch performs integration independent from the neighboring dendrites, (2) dendritic integration is a dynamic process dependent on the amount of driving force, as well as the number of activated synapses, and (3) the thresholding nonlinearity is the collective effect of linear and nonlinear integration (supralinear-linear-sublinear).

7.4.4/ Spatiotemporal Dendritic Abstraction

The dendritic abstraction consists of elements, namely the signal propagation, the linear summation, and the thresholding function. We established beforehand that the voltage decay and time delay functions (Equation 7.1) in the dendritic abstraction (Figure 7.3c) characterize the spatiotemporal model attributes of the dendritic branch under consideration. In contrast, the thresholding function is a time-independent and dynamic model based on the amplitude summation and number of incoming input signals, as shown in Figure 7.5 and Figure 7.7. We used multiple linear regression analysis to determine the thresholding function in each abstraction, where the model parameters were determined by employing machine learning algorithms performed using the R programming language. The `lm` and `step` regression functions provide a direct and efficient way of performing regression analysis. Attached in the supplementary materials is the R code for model prediction.

The training set comprises 70% of the IO dataset in the subthreshold region, while the remaining 30% was for the testing set. The model which provides the best fit has the form

$$g = a + bX_1 + cX_2 + dX_1X_2, \tag{7.6}$$

$$f = g \text{ if } g \leq \theta \text{ or } f = V_{max} \text{ otherwise.}$$

where the variables X_1 and X_2 correspond to the summation of inputs arriving at the thresholding point and the number of activated synapses during simulation, respectively. Then, g is the subthreshold integration function, while f is the overall (sub- and suprathreshold) asymmetric function separated by the spiking threshold θ. V_{max} is the maximum constant depolarization of the dendritic branch. The parameters a, b, c, and d were identified using the regression analysis. Refer to Table 7.1 for the parameter values. The thresholding function, f, determines the input intensity that drives the spiking

Table 7.1: Dynamic thresholding function parameters.

Branch	a	b	c	d	θ	V_{max}	Multiple R^2
Primary	-0.023	7.900	0.007	-0.865	0.150	0.975	0.991
Secondary	0.011	1.357	0.004	-0.115	0.200	0.830	0.943
Tertiary	0.017	1.395	-0.001	-0.107	0.270	0.850	0.997

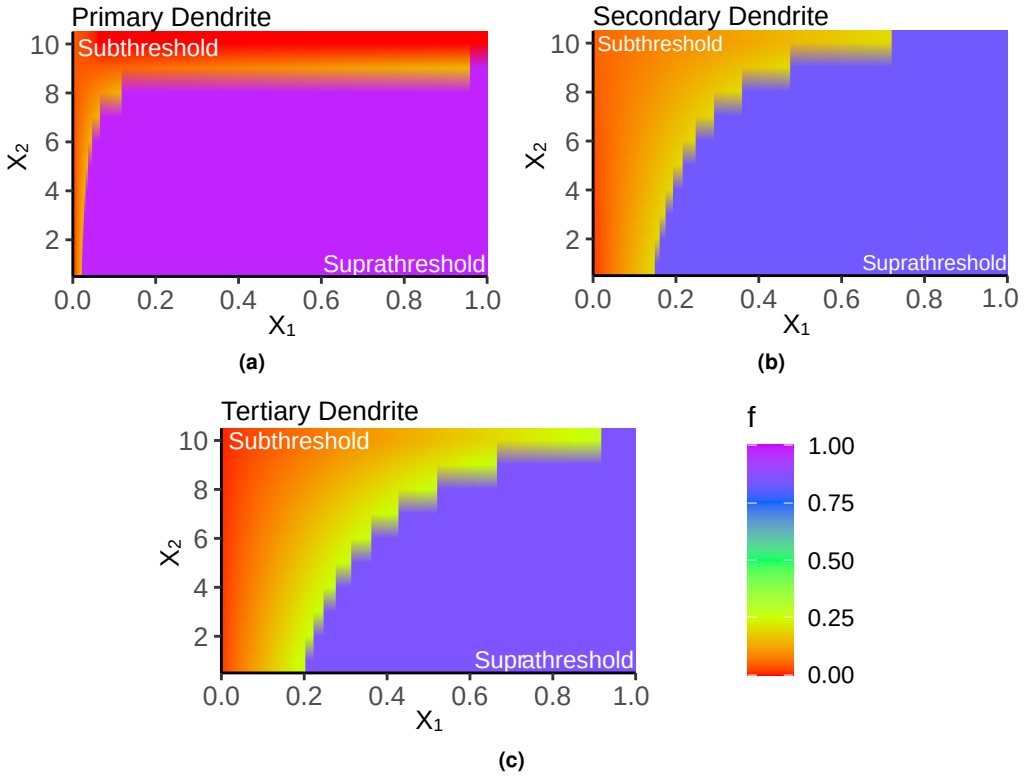

Figure 7.8: The following are the thresholding functions for each dendritic branch and with respect to the parameters X_1 (input summation) and X_2 (number of inputs from 1 to 10). For all dendrites, the amount of X_1 required to produce an AP increases as the number of activated inputs increases. Thus, in (a), an input level of ~0.02 can result in an AP. Furthermore, as the dendritic branch becomes more distal from the soma, from the (b) secondary to (c) the tertiary dendrite, greater X_1 is required. Therefore, the proposed thresholding function is consistent with the results presented in the previous sections.

mechanism if the branch is connected to the soma. Refer to Equation 7.4. In other cases, if the branch under consideration is connected to a proximal branch, f determines the normalized signal coming out of the dendritic branch that will be integrated with the other inputs of the proximal branch. Here, f is a piecewise function whose subthreshold value is defined by g. Then, $g > \theta$ means an AP is generated, forcing f to equal V_{max}. This activity is observable in Figure 7.7. For every number of inputs (X_2), the input summation (X_1) necessary to produce a suprathreshold activity is shifting; thus, we have a dynamic thresholding function here. Figure 7.8 shows the variation in f with increasing X_1 and X_2. The required X_1 needed to cross the suprathreshold region increases with X_2, agreeing with the results in Figure 7.7. However, in the primary dendrite where $X_2 > 8$ (Figure 7.8a), the soma must be forced to spike when $X_1 > 0.25$ done by changing f to V_{max}; due to the large gap between the sub- and suprathreshold regions in the primary-soma connections (Figure 7.6a). In addition, the variations of f for the secondary dendrite (Figure 7.8b) and the tertiary dendrite (Figure 7.8c) were comparable with the measured changes in their respective $V_{observed}$ (Figure 7.7), where the threshold in terms of the input summation shifted from left to right with the increasing number of inputs.

Figure D.3, superimposed on the measured depolarization, is the predicted $V_{observed}$ points. The plots show that the proposed thresholding function indeed follows the dynamic characteristics of dendritic integration. The dendritic integration shifts to the right and varies from supralinear to linear and sublinear described in Figure 7.7. The resulting

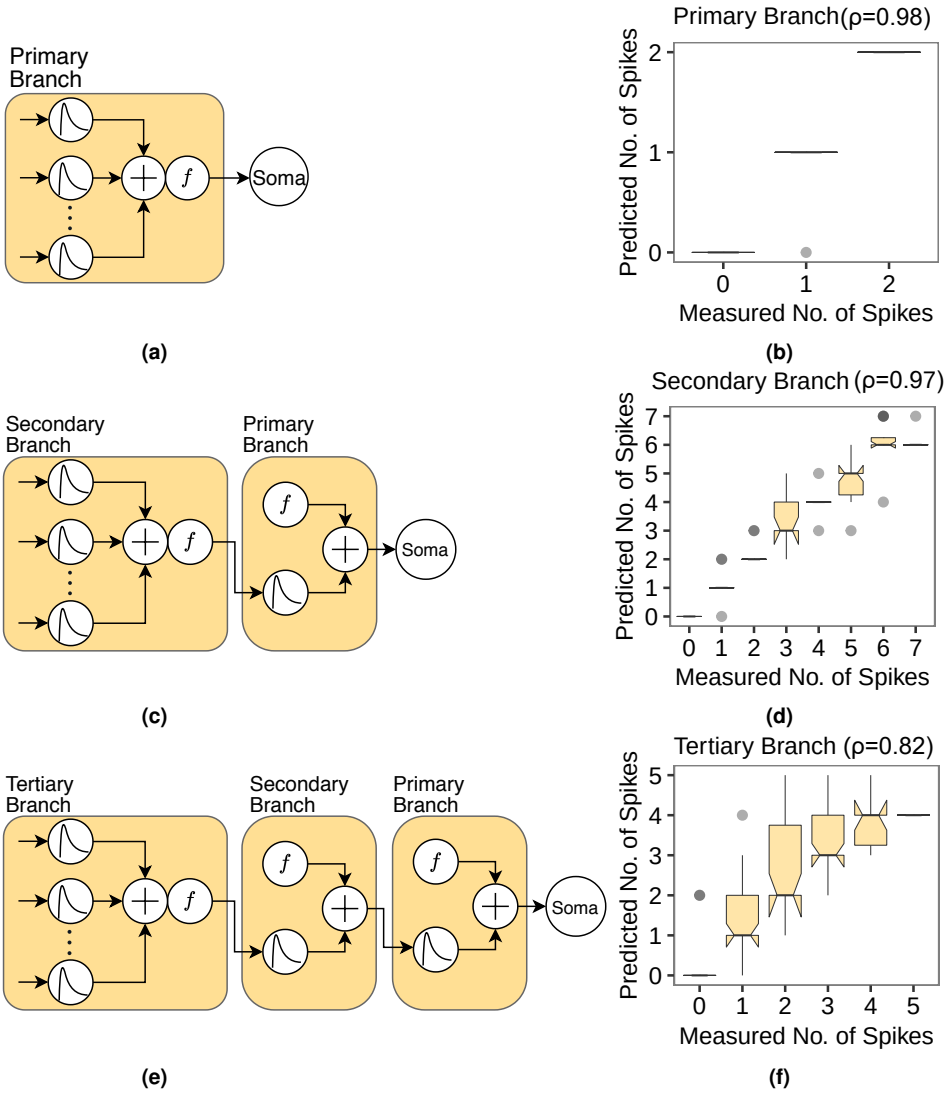

Figure 7.9: Dendritic abstractions. (a) The dendritic abstraction for the primary dendrites includes the linear summation of synaptic inputs and the thresholding function f, whose output directly drives the somatic spiking. (b) The boxplot, comparing the measured and expected spiking in the primary dendritic branch within a 200 ms sliding window, indicates a successful predicting capability ($\rho = 0.98$) of the dendritic abstraction in (a). (c) $f_{secondary}$ output does not enter the primary dendrite as input but instead flows individually, with delay and decay, through the primary branch for linear summation with $f_{primary}$ output before reaching the soma. (d) The boxplot where $\rho = 0.97$ suggests that the dendritic abstraction in (c) effectively predicts the somatic spiking. It indicates that spiking is more frequent on the secondary than in the primary dendrites. (e) The tertiary branch illustrates a dendritic abstraction similar to (c) in that the output of $f_{tertiary}$ flows individually through the secondary branch for linear summation with the output of $f_{secondary}$ until it reaches the soma. (f) The measured and expected somatic spikes comparison validates the dendritic abstraction ($\rho = 0.82$).

multiple R^2 (Table 7.1), which is above 0.9, validates the predictions.

We simulated the biological CA3 pyramidal neuron model by activating random synapses in each dendritic branch for 5000 ms (10 simulations each branch). With the same synaptic inputs measured from the dendritic spine heads, we implemented the proposed dendritic abstraction in Figure 7.3c. We predicted the dendritic dynamics and somatic spiking using the corresponding propagation model (Equation 7.1) and the dynamic thresholding function (Equation 7.6). For instance, Figure D.4 shows the raster plot of random synaptic

inputs along the primary apical dendrite and the corresponding observed and predicted somatic spiking. Then, we compared the measured with the predicted spiking activity within a 200 ms sliding window.

Figure 7.9a shows the dendritic abstraction of the primary apical dendritic branch (simulated with $n \in [4, 10]$ and $spike\ interval \in [38, 67]$ ms). The output of the thresholding function is the direct input to the soma. The number of measured and predicted spikes are from 0 to 2 for every 200 ms sliding window. The boxplot in Figure 7.9b shows that the dendritic abstraction successfully predicted the somatic spiking where the R^2 ρ is 0.98. Figure 7.9c shows the dendritic abstraction for the secondary dendritic branch ($n \in [2, 10]$ and $spike\ interval \in [40, 71]$ ms). In this case, the output from the secondary thresholding point independently flows through the primary branch with considerable delay and decay before reaching the soma. Therefore, the primary dendrite is equivalent to a multiplexer cable or a waveguide [447]. The linear relationship between the means in the corresponding boxplot (Figure 7.9d) indicates a good prediction capability of the dendritic abstraction ($\rho = 0.97$). The tertiary branch exhibits independence from its mother dendrites and signals multiplexing (Figure 7.9e) ($n \in [3, 10]$ and $spike\ interval \in [36, 68]$ ms). Given the linear relationship of measured and predicted spikes in Figure 7.9f, and that $\rho = 0.82$, suggests the dendritic abstraction describes the spiking activity of the biological neuron model.

7.5/ Discussion

7.5.1/ Opting for a natural neuronal response in IO quantification

Biological neuron models based on experimental evidence provide a direct means of manipulating neuronal characteristics, such as ionic channel distribution, biophysics, morphology, and synaptic inputs, that are challenging to control *in vitro* or *in vivo* [429]. We created a morphologically-realistic and biologically-based CA3 pyramidal neuron model (Figure 7.1a) and studied the dendritic integration of individual branches via analyzing their transfer functions or IO relationships. The goal here is to find the corresponding thresholding function, specifically, to identify the instance that the dendritic integration curve crosses the suprathreshold from the subthreshold region. The first step is to determine the approach for the IO quantification process. The shape of the IO relationship varies, dependent on (1) the quantification process: single-pulse or paired-pulse stimulation protocol and blocked spiking mechanisms, and (2) the parameters under consideration: linear for passive mechanisms, nonlinear for the active mechanism (Na^+ channels and NMDA receptors), supralinear to sublinear for increasing driving force. These quantification procedures limit the dynamic response of the neuron and, consequently, the dendritic integration process. Instead of concentrating on one parameter and constricting the others, we proposed an IO quantification process that opted for a natural dendritic response by letting the soma spike spontaneously without blocking the spiking mechanisms to conserve the full range of dendritic activity. However, this process poses some challenges. When the soma generates APs, back-propagating signals move swiftly from the soma through the dendritic tree [245], causing consecutive spikes in the thresholding point. Clustered and strongly-activated synapses create regenerative Na^+ spikes localized within the branch [190]. During simultaneous synaptic and somatic activities, what

causes the dendritic spikes is unclear; it is either the dendritic activity or the backpropagation [448]. These dendritic spikes overlap with the peak depolarization of successful spikes (spikes that cause AP generation). Therefore, we removed the IO points caused by dendritic spikes in the dataset; those points whose observed depolarization are between the threshold and 0.8. With this process, we still conserved the spontaneous dynamics of the dendrites and examined the full range of dendritic integration, from sub- to suprathreshold activities.

7.5.2/ BRANCH-SPECIFIC DENDRITIC INTEGRATION IMPLEMENTS A DYNAMIC THRESHOLDING FUNCTION

Implementing the proposed IO quantification method, the IO curves in Figure 7.5 and Figure 7.7 describe a dendritic integration with the following features. First, dendritic integration is dynamic. Integration in the primary apical and basal dendrites are highly supralinear (Figure 7.5a), while distal dendrites exhibit a nonlinear integration varying from supralinear to slightly sublinear (Figure 7.5c and 7.5e). Two-photon imaging and glutamate uncaging on CA3 pyramidal neurons indicate that the apical and basal proximal dendrites perform highly supralinear integration, mainly influenced by NMDA receptors [226]. Localized regenerative events during activation of voltage-gated channels contribute to the nonlinearity in distal branches [429]. IO curves seen as a whole depict a single nonlinearity described by Poirazi and others [243]. The IO curve starts linearly for weak signals, then progresses to supralinear for intermediate signals. As the curve intersects the line separating the supra- and sublinear region, the IO curve becomes sublinear and plateaus as the input continues to increase until the input is sufficient for somatic spiking. Further analysis of the IO curves showed that a single branch could change its integration mode between supralinear, linear, and sublinear, as shown in Figure 7.7.

Second, the spiking threshold varies with the number of activated synapses. Using whole-cell recordings in the CA3 region of cultured rat hippocampus, Soldado-Magraner et al. [449] discovered that the transition from the subthreshold to the suprathreshold (during firing activity) is not a static characteristic of the neuron. Our analysis determined that the number of activated synapses, not only the input summation in general, has considerable influence on the dynamic dendritic behavior. The threshold or the amount of synaptic inputs required to generate an AP is dynamic [94], and varying synaptic input patterns influence the form of dendritic depolarization [231]. *In vivo*, the threshold varies with the number of inputs and spiking history [94, 190]. Figure 7.7 also illustrates the firing threshold shifting from left to right. The minimum input summation necessary to cause a successful spike increases as the number of active synapses increases. In the primary dendrite (Figure 7.7a), the linear part of the integration mode ($0 \leq V_{expected} \leq 0.02$) shifts by changes in slope. In the secondary (Figure 7.7c) and the tertiary (Figure 7.7e) branches, the integration mode is slightly supralinear at $n = 3$, linear at $n = 5$, and sublinear at $n = 7$.

Lastly, dendritic integration is branch-specific. Dendritic branches process information independent of the whole neuron, which is evident in the differences in the IO curves of each branch (Figure 7.7). The driving force required for somatic spiking differs, which is minimal in the primary dendrites and maximal in tertiary dendrites. Branch specificity is also apparent in the varying spiking threshold θ and maximum depolarization V_{max} developed in the branches (Table 7.1). The location of the dendritic branch plays a significant

role in branch specificity. In Figure 7.6, we compared the dendritic spiking activity in each branch with the somatic activity. The depolarization at the thresholding point in the apical trunk in relation to the soma is linear, with a significant discontinuity between the sub- and suprathreshold (Figure 7.6a). The relationship between the peak depolarizations in the tertiary and secondary thresholding points is also linear. Contrastingly, the linearity is continuous (Figure 7.6d). What causes the discontinuity in the apical trunk? When the input summation reaches the threshold, the somatic depolarization instantly generates an AP and peaks to ~40 mV. Dendritic spikes and backpropagation in the non-primary dendrites create peak depolarization between the threshold and AP peak amplitude. Regenerative spikes are localized in a specific branch [190, 245]. As shown in Figure 7.9b, 7.9d and 7.9f, dendritic spiking is more frequent in distal dendrites, ten times more than the soma [190], due to higher input resistance [450]. Depolarization in the secondary (Figure 7.6b) and tertiary (Figure 7.6d) dendrites compared with the somatic depolarization display a strongly sublinear relationship in the subthreshold area and constant peak amplitude in the suprathreshold area. Due to compartmentalization, the current flowing to the next compartment decreases, and the signal attenuates [191]. Usual IO transformation methods compare the input summation with somatic spiking. On the other hand, dendritic integration varies depending on the location where the input and the output are measured. Therefore, branch-specific processing of diverse synaptic inputs results in cell-specific activities, as depicted by the experimental recordings from CA1 neurons in the rat hippocampus [451].

We formulated a dynamic thresholding function (Equation 7.6) to replicate the above dendritic integration features. This piecewise function is a multiple linear regression dependent on both the summation of synaptic inputs and the number of activated synapses. This function is time-independent, as most thresholding functions are. Additionally, the function can shift between integration modes, from supralinear to linear and sublinear, while sustaining the overall dendritic nonlinearity. The dynamic thresholding function enhances the computational capacity of the dendritic branch, compared with the commonly used static nonlinearity in GLMs and McCulloch-Pitts neurons. Dynamic threshold, dynamic integration mode (deviating between linear and nonlinear), and input location specificity enhance the computational power of the dendrite as it allows the dendrite to shift from one integration mode to another [429, 452]. These capabilities reveal that a single neuron performs more complicated functions associated only with neuronal networks.

7.5.3/ DENDRITIC ABSTRACTION WITH DYNAMIC THRESHOLDING FUNCTION

As mentioned earlier, the thresholding function is time-independent, and the input summation can occur anywhere along the dendritic arborization. Input summation was set on the proximal end of the dendritic branch, a point near the bifurcation, to cover the whole dendritic branch length. We proposed a dendritic abstraction (Figure 7.3c) that models the spatiotemporal changes of synaptic inputs during propagation. Synaptic inputs are subjected to voltage decay and delay, attributed to the location of the input from the thresholding point and the active mechanism along the dendrites (Equation 7.1). The linear summation of propagated inputs occurs once the inputs reach the thresholding point, followed by the transformation employing the thresholding function.

We demonstrated that the dendritic abstraction models the integration process of the

dendritic branch and then proceed with the information transfer scheme from the tertiary branch straight to the soma (Figure 7.9). In most generalized linear models, the output of one secondary subunit combines with the inputs of the subsequent subunit, the primary branch. However, the neuron does not correctly predict the expected output train with this scheme. For example, if the output of the secondary branch is equal to 0.18, which is in the subthreshold region, enters the thresholding unit of subunit A, the final output will be a successful spike being that the threshold of A is only 0.15 (refer to Table 7.1). The difference between the thresholding levels of the two subunits indicates that dendritic subunits perform independent dendritic integration processes and the dendritic length multiplexes branch-specific information. Experiments on neuronal cultures suggest that dendritic arborization forms multiple layers of dendritic integration and independent functional subunits within a layer [237, 245, 434], comparable with multiplex communication in cultured neural networks [453].

An additional component in the dendritic abstraction is the linear summation after the thresholding unit for mother branches (Figure 7.9c and 7.9e). This component feeds the simultaneous inputs from different branches into a single spike train. The dendritic tree can, therefore, multiplex multiple information from independent sources [233, 239]. Local dendritic integration and signal multiplexing continue until the information reaches the soma. The soma performs a global integration summing the inputs from the proximal apical and basal dendrites. Sakuma et al. [454] also suggested that the synaptic delays and refractory periods improve and stabilize multiplex communications in neurons. This particular scheme also increases the computational capacity of the neuron. It performs spatiotemporal filtering by confining some information within the specific dendrite. Distal branches produce and confine dendritic spike bursts that do not reach the soma. It also performs information selection. During somatic spiking, the soma blocks inputs, and during this time, some dendritic spikes are unable to reach the soma [233]. Only certain local information from a distal dendritic branch is delivered to the soma. With this scheme, where inputs are independently processed, the neuron can also determine the source of the inputs responsible for the somatic firing.

7.6/ CONCLUSION

Overall, we developed an IO transformation process and modeled the corresponding branch-specific integration. The thresholding function describes a dynamic integration process. We also formulated a dendritic abstraction incorporating the spatiotemporal characteristics of synaptic inputs while traveling down the dendritic length. We suggest further investigation of dendritic integration by merging both experimental and computational studies. Current physiological experiments are still limited in spatiotemporal resolution. Besides, we suggest examining a pyramidal neuron with a more complex dendritic arborization, although complicated arborization equates to exhausting manipulation. It has been suggested that neurons perform more complex computations comparable with neuronal networks. Therefore, further investigation into dendritic processes helps understand neuronal functions employed in biomedical, artificial intelligence and neuromorphic applications [455, 456].

II

CONCLUSION

8

Conclusion and Perspectives

Realizing that astrocytes can be computational elements by displaying neuron-like functions operating with slower dynamics extends our current understanding of the brain processes to a broader perspective. The heterogeneous morphology of astrocytes that creates syncytium modulating the neighboring neurons and extending its effect to neurons belonging to separate networks hints that neurons work in cooperation with astrocytes, here considered active components, creating a more complex circuitry for computation and communication. Our research was divided into two parts. First, we developed biologically plausible neuron-astrocyte networks and studied the influence of astrocytic signaling on synaptic plasticity and neural network activities. Second, we developed an astrocyte-mediated spiking neural network following the biological characteristics and simplified dynamics of these components. This chapter summarizes and concludes the research findings and gives our perspectives for future works.

We discussed the biological characteristics and signaling in neurons and astrocytes (see Chapters 2-4). We illustrated the signaling pathways that led to the formation of tripartite synapses to the development of neuron-astrocyte networks and presented the computational models describing the neuron-astrocyte interactions. Here are the main findings of our studies discussed in Chapters 5-7:

- We developed a stochastic tripartite synapse model with synaptic and nonsynaptic sources of Glu^- signals. The HH model [76] described the AP generation in the AIS, and the cable equation [142] modeled the saltatory conduction along the myelinated axon. The amount of Glu^- in the synaptic cleft was dependent on the fast and slow Ca^{2+} dynamics and was released stochastically. The Li-Rinzel model [162] described the IP_3-dependent Ca^{2+} dynamics, and the astrocytic Glu^- followed a synaptic-like fusion and release process. Here, the astrocytic processes modulate the synaptic release probability and indirectly modulate the postsynaptic membrane spiking, triggered by the activation of AMPARs.

  We analyzed the strength of communication between the pre- and the postsynaptic components by comparing their spiking activities and determined that astrocytes can either improve or impair synaptic communication based on the amount of astrocytic Glu^- released in the extracellular space. The extrasynaptic $[Glu^-]$ must be high enough to increase the synaptic efficacy but low enough to avoid postsynaptic overexcitation. In addition, the multiple sources of extracellular Glu^- triggering localized Ca^{2+} oscillations indicate that astrocytes perform a new level of signal integration, suggesting that astrocytes are more than a point process.

- Therefore, we developed a compartmentalized model for astrocytic Ca^{2+} integration. In a single cell, the astrocytic processes and the soma form separate compartments communicating via Ca^{2+} and IP_3 diffusions relative to the gradient between compartments. We employed a stochastic neurotransmitter release, while the Glu^{-} signals (synaptic and extrasynaptic) are restricted within the astrocytic processes. The tripartite synapse has feedforward and feedback pathways, where the astrocytic process modulates both the presynaptic release probability and generates postsynaptic SICs. Furthermore, the gap junction connected astrocytes form a network with varying topology, chain, dense, or regular connections, communicating via ICW propagation. The IP_3 exchange between astrocytic somas depends on the state of the cell, described by the UAR model.

  The heterogeneity in astrocytic connections (with the neurons and the neighboring astrocytes) highly influences neural activities, specifically improving network synchrony, synaptic efficacy, and homeostasis. During global Ca^{2+} oscillations, astrocytic processes simultaneously release Glu^{-}, consequently modulating the neuronal counterparts. At the network level, ICW propagation promotes simultaneous activation of astrocytes, thus resulting in synchronized postsynaptic spiking. The simulation results indicate that the chain topology displayed a higher synchrony level than the other astrocytic connections. The chain topology also resulted in higher network efficacy, attributed to the restricted Ca^{2+} activities within the astrocytic territory. In contrast, heterogeneity exhibited by the regular or dense topologies provided a positive impact on network stability or homeostasis. Therefore, heterogeneous as they may be seen in vivo, astrocytic connections play specific roles in neural activities.

- Based on the biological dynamics and characteristics of neurons and astrocytes, we developed simplified SNANs capable of learning (unsupervised) features of handwritten images from the MNIST database [16] and classifying input classes. The network consists of 784 Poisson Input neurons whose spiking rates depend on the 28x28 image pixels, 100 AIF First layer neurons with 100 IN for lateral inhibitions that generate synaptic competitions, and 100 astrocytes (using the Postnov model [312] creating tripartite connections between the neuronal layers. The classifier unit converts the spiking patterns of the First layer into a vector for predicting the input class. We trained the networks with varying hyperparameters and an increasing number of astrocyte-mediated synapses. The test results of the SNAN with 30% tripartite synapses (out of the total number of synapses) yielded a maximum of 75.28% of accuracy with optimal model complexity.

  This study is one of the first attempts to employ astrocytes in artificial neural networks for direct applications to image recognition (using the standard MNIST dataset) by generating slow excitatory inputs separate from the synaptic signals. Therefore, the proposed network can serve as a baseline for astrocyte implementations in artificial networks. It displayed advantages over SNN such as faster learning due to the additional synapses, increased accuracy while optimizing the bias and variance tradeoff, and, interestingly, simplified network architecture as the SNAN network can yield accuracy at the same level as networks with more neuron components.

- Lastly, we developed a dendritic abstraction based on a biological CA3 pyramidal neuron that would allow neurons to perform dendrite-specific integration for faster learning. The spatiotemporal abstraction consists of signal propagation, linear summation, thresholding function, and spiking mechanisms. We proposed an IO quantification method for *in vivo*-like synaptic inputs from the biological model. We formulated a dynamic nonlinear thresholding function using multiple regression, capturing the linear, supralinear, and sublinear shifts in dendritic integration observed in pyramidal neurons.The IO curves suggest that the dendritic branches are computational subunits performing branch-specific and independent dendritic integrations that are dynamic, shifting between linear and nonlinear regions, and whose spiking threshold varies relative to the activated synapses. In addition, by following the multilayer and multiplexer computational schemes, a single neuron can perform faster learning. During synaptic activations, the dendritic subunit can instantly update its synaptic weights without waiting for the backpropagating signals from the soma.

Researchers are currently acknowledging the potential of astrocytes in brain processes, and there are efforts to implement astrocytes in artificial spiking networks. In continuing research in astrocytic processes and implementations, the following research areas are suggested:

- More than 100 years ago, Santiago Ramon y Cajal said, "What is the function of glial cells in neural centers? The answer is still not known, and the problem is even more serious because it may remain unsolved for many years to come until physiologists find direct methods to attack it [397]." Intriguingly, we still lack a solid understanding of astrocytic functions 100 years later. Nowadays, imaging techniques focus on global $[Ca^{2+}]$ in the astrocytic network; however, astrocytic communication is the interplay of multiple variables such as the extracellular Glu^{-} and cytosolic IP_3. Therefore, it is also vital to have high spatial resolution and sensitivity measurement tools to study the effects of synaptic and nonsynaptic Glu^{-} on astrocytic activation. It is also essential to observe and model the inter- and intracellular IP_3 diffusion, noting that $[Ca^{2+}]$ elevations in the astrocytic processes are IP_3-mediated and astrocytes are gap junction-connected communicate via IP_3 exchange.

- The fine astrocytic processes limit the currently available physiological measurement tools; therefore, biologically plausible computational models, such as those presented in Chapter 5 , help discern the influence of astrocytic networks in brain activities. In addition, the network models can also be used to study the influence of extracellular molecules in ICW propagation. We presented in Chapter 5 a model wherein the astrocyte regulated nonsynaptic Glu^{-}, for example, from the nodes of Ranvier. Researchers can use this model to simulate how the astrocytes maintain neuronal health or cause brain pathology such as Alzheimer's [457] or Parkinson's [458] diseases.

- There is no physical evidence of backpropagation from the current to the previous neuronal layer as the synaptic transmission is a feedforward process. Therefore, synaptic learning is an unsupervised process. However, the ability of astrocytes to form networks with the neurons belonging to separate layers may hint that the astrocytes provide the backpropagation mechanisms. Given two neuron layers, Layer 1 and Layer 2, with series-connected astrocytes whose one end enwraps the axon terminals in Layer 2 and the other end is coupled with the presynaptic

terminal of Layer 1; the series astrocytes provide a conduit for the backpropagating signals. One end of the astrocytic chain senses the activity of presynaptic spiking activity of Layer 2 neurons. Via ICW propagation, these activities are sent to the other end, therefore modulating the Layer 1 presynaptic neurotransmitter release. Researchers can therefore explore the possibility of astrocyte-mediated backpropagation.

- One can also improve the classification performance of the proposed SNAN for image recognition. (1) The researchers can change the network parameters/hyper-parameters and increase the number of epochs during training to find the network architecture with better accuracy and bias and variance tradeoff. (2) The astrocytic layer can also be extended into an astrocytic network connected via a chain, dense, or regular topology to allow ICW propagation. This method can improve the network activities, such as synchronization and stability, as mentioned in Chapter 6. (3) Convolutional spiking neuron astrocyte networks can be implemented by dividing the image pixels into kernels independently processed by the dendritic abstractions connected in a multilayer and multiplexer scheme (see Chapter 7).

- One of the main challenges we faced during our research is the computational costs necessary to simulate the networks, as the Brian2 simulator [416] does not support parallel computations. Researchers can consider implementing the SNAN into neuromorphic computing platforms such as BrainScaleS [459] and SpiNNaker [460] systems. For shallow networks, simulations can also be accelerated by deploying the network in field-programmable gate array (FPGA) devices [461].

9

PUBLICATIONS

JOURNAL PUBLICATIONS

- **Lorenzo, J.**, Binczak, S., & Jacquir, S. (2022). A multilayer-multiplexer network processing scheme based on the dendritic integration in a single neuron. AIMS Neuroscience, 9(1), 76. DOI: https://doi.org/10.3934/Neuroscience.2022006.
- Vuillaume, R., **Lorenzo, J.**, Binczak, S., & Jacquir, S. (2021). A Computational Study on Synaptic Plasticity Regulation and Information Processing in Neuron-Astrocyte Networks. Neural Computation, 33(7), 1970-1992. DOI: https://doi.org/10.1162/neco_a_01399.
- **Lorenzo, J.**, Vuillaume, R., Binczak, S., & Jacquir, S. (2020). Spatiotemporal model of tripartite synapse with perinodal astrocytic process. Journal of Computational Neuroscience, 48(1), 1-20. DOI: https://doi.org/10.1007/s10827-019-00734-4.

CONFERENCE PROCEEDINGS

- **Lorenzo, J.**, Binczak, S., & Jacquir, S. (2022, July). Synaptic Communication in Diverse Astrocytic Connectivity: A Computational Model. In 2022 44th Annual International Conference of the IEEE Engineering in Medicine Biology Society (EMBC) (pp. 158-161). IEEE. DOI: https://doi.org/10.1109/EMBC48229.2022.9871642.
- **Lorenzo, J.**, Vuillaume, R., Binczak, S., & Jacquir, S. (2019, March). Identification of Synaptic Integration Mode in CA3 Pyramidal Neuron Model. In 2019 9th International IEEE/EMBS Conference on Neural Engineering (NER) (pp. 465-468). IEEE. DOI: https://doi.org/10.1109/NER.2019.8717136.

COMMUNICATIONS

- **Lorenzo, J.**, Vuillaume, R., Binczak, S., & Jacquir, S. (2018). Extrasynaptic Transmitter Release and Axonal Propagation Influence Synaptic Transmission. In BioComp 2018, Bordeaux, France. (*poster presentation*)

III

APPENDICES

APPENDIX A

TRIPARTITE SYNAPSE BIOLOGICAL MODEL PARAMETERS

Table A.1: Action potential initiation along the axon initial segment.

Parameter	Value	Description
C	1 μF/cm^2	Specific capacitance of the membrane
$\bar{g}_K$	36 mS/cm^2	K^+ channel conductance
$\bar{g}_{Na}$	120 mS/cm^2	Na^+ channel conductance
$\bar{g}_L$	0.30 mS/cm^2	Leak channel conductance
V_K	−82 mV	K^+ channel reversal potential
V_{Na}	45 mV	Na^+ channel reversal potential
V_L	−59.40 mV	Leak channel reversal potential

Values are from Tewari and Majumdar [88].

Table A.2: Action potential propagation along the myelinated segments.

Parameter	Value	Description
r	0.50 μm	Myelinated axon radius [379]
l	1 μm	Myelin sheath thickness [379]
x_m	100 μm	Myelin segment length [379]
n_m	20	Number of myelinated segments [379]
C_m	0.10 μF/cm^2	Myelin segment membrane capacitance [379]
ρ_m	10^7 Ω-m	Membrane resistivity [366]
ρ_a	1.10 Ω-m	Axoplasmic resistivity [366]
β	0	Generation constant [143]

Table A.3: Action potential propagation in the node of Ranvier.

Parameter	Value	Description
$\bar{g}_{Na_n}$	266.70 mS/cm^2	Nodal Na^+ channel conductance [379]
$\bar{g}_{K_n}$	66.70 mS/cm^2	Nodal K^+ channel conductance [379]
$\bar{g}_{L_n}$	1.76 mS/cm^2	Modal leak channel conductance [368]
V_{Na_n}	55 mV	Nodal Na^+ channel reversal potential [368]
V_{K_n}	−90 mV	Nodal K^+ channel reversal potential [368]
V_{L_n}	−70 mV	Nodal leak channel reversal potential [379]

Table A.4: Presynaptic neuron calcium dynamics.

Parameter	Value	Description
A	1.2398×10^{-8} cm^2	Presynaptic bouton surface area
	1.9735×10^{-8} cm^2	Nodal surface area [379]
v_c	1.2982×10^{-16} L	Presynaptic bouton volume
	3.0995×10^{-16} L	Nodal volume [379]
z_{Ca}	2	Calcium valence
F	96487 C/mole	Faraday's constant
R	8.314 J/K	Real gas constant
T	293.15 K	Absolute temperature
ρ_{Ca}	3.20 μm^{-2}	N-type Ca^{2+} channel density
g_{Ca}	2.30 pS	N-type Ca^{2+} channel conductance
V_{Ca}	125 mV	Ca^{2+} channel reversal potential
c_{ext}	2 mM	External Ca^{2+} concentration
c_i^{rest}	0.10 μM	Resting intracellular Ca^{2+} concentration
$\tau_{m_{Ca}}$	10 ms	Time constant
$V_{m_{Ca}}$	−17 mV	Half-activation voltage of N-type Ca^{2+} channel
$k_{m_{Ca}}$	8.40 mV	Slope factor of N-type Ca^{2+} channel
i_{PMCa}	0.40 μA/cm^2	Maximum PMCa current
K_{PMCa}	0.10 μM	$[Ca^{2+}]$ at which v_{PMCa} is halved
v_{leak}	0.001022 ms$^-1$	Maximum leak of Ca^{2+}
a_2	0.20 μM/s	Inhibitory Ca^{2+} binding constant
c_1	0.1850	Ratio of the ER volume to the volume of the bouton and the volume of the node
v_1	30 s^{-1}	Maximum IP_3 receptor flux
v_2	0.2374 μs^{-1}	Ca^{2+} leak rate constant
v_3	0.90 μM/s^{-1}	SERCA maximal pump rate
k_3	0.10 μM	SERCA maximal pump rate
d_1	0.13 μM	IP_3 dissociation constant
d_2	1.0490 μM	Inhibitory Ca^{2+} dissociation constant
d_3	943.40 nM	IP_3 dissociation constant
d_5	82.34 nM	Activation Ca^{2+} dissociation constant
v_g	0.0620 μM/s	Maximum production rate of IP_3
k_g	0.78 nM	$[Glu^-]$ at which v_g is halved
τ_p	0.14 s^{-1}	IP_3 degradation constant
p_0	160 nM	Initial $[IP_3]$

Unless otherwise stated, the values are from the study of Tewari and Majumdar [88] and Chan et al. [160].

Table A.5: Neurotransmitter release.

Parameter	Value	Description
α	0.30 μM/ms	Ca^{2+} association rate constant
β	3 ms^{-1}	Ca^{2+} dissociation rate constant
γ	30 ms^{-1}	Forward isomerization rate constant
Δ	8 ms^{-1}	Backward isomerization rate constant
τ_{rec}	800 ms	Vesicle recovery time constant
τ_{inact}	3 ms	Vesicle inactivation time constant
a_1	50 μM	$[Ca^{2+}]$ at which λ is halved
a_2	5 μM	Slope factor of sponataneous release rate λ
a_3	0.85 ms^{-1}	Maximum spontaneous release rate
n_v	2	Number of docked vesicles in the bouton
	1	Number of docked vesicles in the node
g_v	60 mM	$[Glu^-1]$ in a single vesicle
g_c	10 ms^{-1}	Glutamate clearance rate constant

The values are taken from Tewari and Majumdar [88].

Table A.6: Astrocytic dynamics.

Parameter	Value	Description
r_{Ca}	6 s^{-1}	Maximal IP_3R flux
r_L	0.11 s^{-1}	Maximal rate of Ca^{2+} from ER
c_0	2 μM	Total cell free $[Ca^{2+}]$
$c_{1,a}$	0.1850	Ratio of ER volume to cytosol volume
v_{ER}	0.90 μM/s	Maximal rate of SERCA uptake
K_{ER}	0.10 μM	SERCA Ca^{2+} affinity
d_1	0.13 μM	IP_3 dissociation constant
d_2	1.0490 μM	Ca^{2+} inactivation dissociation constant
d_3	0.9434 μM	IP_3 dissociation constant
d_5	0.082340 μM	Ca^{2+} activation dissociation constant
a_2	2 s^{-1}	IP_3R binding rate for Ca^{2+} inhibition
N	20	Number of IP_3Rs in a cluster
v_β	0.50 μM/s	Maximal rate of IP_3 production by PLCβ
K_R	1.30 μM	Glutamate affinity of the receptor
K_P	10 μM	Ca^{2+}/PKC-dependent inhibition factor
K_π	0.60 μM	Ca^{2+} affinity of PKC
v_{delta}	0.05 μM/s	Maximal rate of IP_3 production by PLCδ
$K_{PLC\delta}$	0.10 μM	Ca^{2+} affinity of PLCδ
k_δ	1.50 μM	Inhibition constant of PLCδ activity
$r_{5_{pa}}$	0.05 s^{-1}	Maximal rate of degradation by IP-5P
v_{3K}	2 μM/s	Maximal rate of degradation by IP3-3K
K_D	0.70 μM	Ca^{2+} affinity of IP_3-3K
K_3	1 μM	IP_3 affinity of IP_3-3K

The values are taken from Tewari and Majumdar [88].

Table A.7: Astrocytic gliotransmitter release.

Parameter	Value	Description
k_1^+	3.75×10^{-3} $\mu M^{-1}ms^{-1}$	Ca^{2+} association rate for site S_1
k_1^-	4×10^{-4} ms^{-1}	Ca^{2+} dissociation rate for site S_1
k_2^+	2.50×10^{-3} $\mu M^{-1}ms^{-1}$	Ca^{2+} association rate for site S_2
k_2^-	1×10^{-3} ms^{-1}	Ca^{2+} dissociation rate for site S_2
k_3^+	1.25×10^{-2} $\mu M^{-1}ms^{-1}$	Ca^{2+} association rate for site S_3
k_3^-	10×10^{-3} ms^{-1}	Ca^{2+} dissociation rate for site S_3
$\tau_{rec,a}$	800 ms	Vesicle recovery time constant
$\tau_{inact,a}$	3 ms	Vesicle inactivate time constant
$c_{thresh,a}$	196.69 nM	Astrocyte response threshold
$n_{v,a}$	12	Number of SLMV ready to be released
$g_{v,a}$	20 mM	$[Glu^-]$ in each vesicle
$g_{c,a}$	10 ms^{-1}	Glu^- clearance rate

The values are taken from Tewari and Majumdar [88].

Table A.8: Postsynaptic neuron membrane potential.

Parameter	Value	Description
R_m	0.79×10^5 MΩ	Spine head resistance
V_{post}^{rest}	−70 mV	Postsynaptic resting membrane potential
τ_{post}	50 ms	Postsynaptic membrane time constant
g_{AMPA}	0.35 nS	AMPAR conductance
V_{AMPA}	0 mV	AMPAR resting membrane potential
α_{AMPA}	1.10 μM/ms	AMPAR forward rate constant
β_{AMPA}	190 s^{-1}	AMPAR backward rate constant

The values are taken from Tewari and Majumdar [88].

Neuron-Astrocyte Network Model Parameters

Table A.9: Synchronous neurotransmitter release.

Parameter	Value	Description
Neurotransmitter release process		
τ_f	3 ms	Facilitation time constant
τ_d	800 ms	Depression time constant
τ_P	120 s	Presynaptic receptors inactivation time constant
O_P	0.0015 μM^{-1} ms^{-1}	Presynaptic receptors activation rate
U_0	0.8	Resting synaptic release probability
ξ_S	1	Effect of gliotransmission on synaptic release
Synaptic glutamate		
τ_c	25 ms	Glutamate clearance time constant
ϱ_c	0.005	Vesicular versus mixing ratio
G_{S_T}	200 mM	Total vesicular glutamate concentration
Astrocytic IP$_3$		
P_0	0.16 μM	Equilibrium IP$_3$ concentration [462]
τ_{IP_3}	1/0.00014 ms	Time constant [462]
r_{IP_3}	0.0072 ms^{-1}	IP$_3$ maximal rate of degradation [462]

Unless stated, values are from De Pitta and Brunel [178].

Table A.10: Postsynaptic membrane potential.

Parameter	Value	Description
Excitatory synaptic input		
τ_N	10 ms	EPSC decay time
τ_N^r	0.5 ms	EPSC rise time
J_S	6	Synaptic efficacy
ζ	0.75	Efficacy of synaptic transmission
Slow inward current		
τ_S	600 ms	SIC decay time
τ_S^r	20 ms	SIC rise time
J_A	68	SIC efficacy
I_A	10 mV	SIC amplitude

Unless stated, values are from De Pitta and Brunel [178].

Table A.11: Synaptic efficacy parameters.

Parameter	Value	Description
ρ_b	0.5	Boundary between state [178]
γ_p	0.023 ms^{-1}	Synaptic efficacy rate of change during potentiation
γ_d	0.0057 ms^{-1}	Synaptic efficacy rate of change during depression
θ_p	-40 mV	Potentiation threshold
θ_d	-65 mV	Depression threshold

APPENDIX B

CA3 PYRAMIDAL NEURON CHARACTERISTICS AND MORPHOLOGY

DETAILS

NeuroMorpho.Org ID	:	NMO_76005
Cell Name	:	A2_CA3
Species Name	:	rat
Strain	:	Sprague-Dawley
Structural Domains	:	Dendrites, Soma, No Axon
Physical Integrity	:	Dendrites Moderate
Morphological Attributes	:	Diameter, 3D, Angles
Min Age	:	18.5 days
Max Age	:	18.5 days
Development	:	embryonic
Primary Brain Region	:	hippocampus
Secondary Brain Region	:	CA3
Experiment Protocol	:	culture
Experimental Condition	:	Control
Staining Method	:	immunostaining
Reference Article	:	Anisotropically organized three-dimensional culture platform for reconstruction of a hippocampal neural network[437].

MEASUREMENTS

Soma Surface	:	586.27 μm^2
Number of Stems	:	7
Number of Bifurcations	:	4
Number of Branches	:	15
Overall Width	:	109.36 μm
Overall Height	:	245.15 μm
Overall Depth	:	37.34 μm
Average Diameter	:	1.27 μm
Total Length	:	1093.47 μm
Total Surface	:	4313.06 μm^2
Total Volume	:	1581.26 μm^3
Max Branch Order	:	2
Total Fragmentation	:	116

MORPHOLOGY (STANDARDIZED)

Segment Number	X	Y	Z	Radius	Connected to Segment Number
1	0	0	0	6.841	-1
2	6.27	2.67	0.07	6.841	1
3	-6.28	-2.67	-0.07	6.841	1
4	-1.05	17.69	-4.54	0.445	1
5	-2.34	23.95	-9.39	1.425	4
6	-3.46	34.67	-8.12	0.487	5
7	-2.57	53.71	-11.63	0.514	6
8	0	73.13	-10.14	0.658	7
9	1.50	83.08	-4.88	1.737	8
10	5.73	100.57	-10.43	1.152	9
11	7.96	106.80	7.70	0.515	10
12	11.82	119.06	-2.94	0.512	11
13	13.75	129.38	-5.68	0.964	12
14	15.66	140.69	-5.39	0.489	13
15	17.15	149.42	-0.16	0.785	14
16	17.10	157.77	-6.95	0.766	15
17	15.25	164.46	-3.79	0.706	16
18	4.39	173.25	4.37	0.460	17
19	-5.97	179.81	7.52	0.635	18
20	-10.29	183.52	2.60	0.458	19
21	-13.34	187.94	-7.26	0.566	20
22	13.59	108.46	-8.21	0.961	10
23	20.86	115.57	-7.01	1.268	22
24	28.75	121.56	-7.85	0.731	23
25	39.95	131.31	-5.58	0.384	24
26	50.84	139.84	2.63	0.315	25
27	56.40	144.54	-0.20	0.896	26
28	-2.79	80.84	-9.95	0.624	8
29	-6.97	87.92	-8.78	0.676	28
30	-12.49	97.54	-5.55	0.622	29
31	-20.47	108.23	-5.29	0.373	30
32	-23.81	112.85	-5.18	0.315	31
33	-27.86	117.42	-8.08	0.629	32
34	-30.91	119.55	-4.03	1.157	33
35	-31.87	125.25	-6.89	1.089	34
36	-33.28	131.15	-3.74	0.771	35
37	-33.81	135.79	-3.63	0.698	36
38	3.06	0.33	3.03	0.689	1
39	17.88	0.46	-3.92	0.315	38
40	23.30	0.84	-8.90	0.587	39
41	28.18	-0.11	-0.91	0.871	40
42	33.11	0.11	-3.90	0.315	41
43	37.64	0.64	-2.87	0.315	42
44	43.85	0.65	-4.86	0.587	43
45	51.54	1.49	-7.82	0.708	44
46	55.83	1.71	-8.80	0.524	45
47	66.27	2.74	-7.75	0.509	46
48	11.84	-6.17	1.86	0.769	1
49	15.71	-7.58	6.83	1.182	48
50	19.61	-8.64	6.81	0.607	49

Segment Number	X	Y	Z	Radius	Connected to Segment Number
51	23.04	-10.71	8.77	0.612	50
52	27.65	-13.82	8.70	1.074	51
53	31.60	-14.46	6.69	0.315	52
54	36.33	-15.85	5.67	0.701	53
55	41.07	-17.29	8.64	0.724	54
56	46.69	-17.63	7.65	0.761	55
57	51.76	-16.85	8.68	0.315	56
58	56.66	-15.59	3.72	0.837	57
59	61.19	-16.38	8.71	0.315	58
60	65.06	-17.29	5.70	1.314	59
61	67.61	-18.36	8.68	0.582	60
62	0.41	-13.21	-0.31	0.601	1
63	0	-17.24	-3.41	0.856	62
64	2.34	-23.08	-7.56	0.927	63
65	6.11	-28.81	-11.69	0.799	64
66	8.71	-32.66	-12.79	0.496	65
67	11.61	-36.55	-14.88	0.598	66
68	14.84	-41.59	-17.00	0.567	67
69	20.46	-50.26	-12.20	0.608	68
70	24.18	-54.40	-11.30	0.859	69
71	27.65	-59.31	-5.42	0.784	70
72	29.63	-65.48	-18.57	0.517	71
73	29.83	-76.51	-14.85	0.76	72
74	30.75	-80.69	-17.95	0.341	73
75	-8.46	6.35	-4.84	0.485	1
76	-10.97	10.72	-1.74	0.477	75
77	-12.12	13.76	24.30	0.611	76
78	-11.02	16.24	23.37	0.376	77
79	-15.26	24.47	0.56	0.933	78
80	-14.59	29.03	-2.28	0.634	79
81	-16.18	32.47	-2.20	0.716	80
82	-18.36	35.71	-3.12	1.113	81
83	-22.82	39.92	-3.03	0.355	82
84	-10.91	-2.08	8.90	0.574	1
85	-19.22	-1.43	15.90	0.551	84
86	-22.72	0.65	11.94	1.321	85
87	-26.02	3.17	16.00	0.575	86
88	-31.25	5.85	9.05	0.525	87
89	-34.66	8.29	-8.86	0.315	88
90	-38.34	10.06	16.15	0.599	89
91	-41.37	9.52	-7.84	0.315	90
92	-45.12	8.60	-7.87	0.552	91
93	-47.58	9.61	-7.85	0.413	92
94	-49.39	12.26	-7.79	0.315	93
95	-51.63	17.47	-7.66	0.374	94
96	-34.18	2.90	24.98	0.465	87
97	-39.24	2.76	-3.01	0.379	96
98	-43.83	2.30	-7.03	0.581	97
99	-48.26	1.91	-13.05	0.562	98
100	-52.96	-0.04	-13.11	0.649	99

Segment Number	X	Y	Z	Radius	Connected to Segment Number
101	-61.08	-3.64	-8.22	0.356	100
102	-20.53	-4.74	16.81	0.315	85
103	-22.33	-8.41	16.71	0.411	102
104	-26.60	-13.87	10.56	0.743	103
105	-31.77	-18.35	10.44	0.315	104
106	-34.53	-20.04	10.39	0.49	105
107	-37.99	-23.02	10.31	0.677	106
108	-42.89	-29.26	10.14	0.603	107
109	-44.32	-33.91	10.02	0.622	108
110	-7.90	-9.93	-0.26	0.478	1
111	-11.38	-14.68	-0.38	0.584	110
112	-14.41	-20.15	-0.53	0.351	111
113	-16.31	-28.9	11.21	0.587	112
114	-18.68	-35.41	-14.93	0.582	113
115	-20.46	-42.23	-19.10	0.573	114
116	-23.44	-45.71	-21.20	0.76	115
117	-27.54	-49.89	-20.32	0.541	116
118	-31.96	-53.97	-18.43	0.58	117
119	-35.62	-58.46	-10.55	0.525	118

APPENDIX C

CA3 NEURON PARAMETERS

Table C.1: CA3 pyramidal neuron model distributed mechanisms.

Parameter	Value	Placement
Specific membrane capacitance C_m	1 μF/cm	soma, dendrites, spines [195]
Cytoplasmic resistivity R_a	100 Ωcm	soma, dendrites, spine heads [195]
	1122 Ωcm	spine necks [195]
Leak conductance density g_L	0.0001 S/cm^2	soma, dendrites [463]
Fast Na^+ conductance density $\bar{g}_{Na}$	0.03 S/cm^2	soma, dendrites [463]
Delayed rectifier K^+ conductance density $\bar{g}_{K_{DR}}$	0.015 S/cm^2	soma, dendrites [463]
A-type K^+ conductance density $\bar{g}_{K_A}$	0.005 S/cm^2	soma [463]
	$\bar{g}_{K_{A_{soma}}}(1 + 5.2x/350)$	somatodendritic gradient where x is the distance from the soma in μm [200]
N-type Ca^{2+} conductance density $\bar{g}_{Ca_N}$	0.0015 S/cm^2	soma, spine heads [206, 464]
T-type Ca^{2+} conductance density $\bar{g}_{Ca_T}$	0.001 S/cm^2	soma, dendrites [63, 206, 464]
L-type Ca^{2+} conductance density $\bar{g}_{Ca_L}$	0.0013 S/cm^2	soma, spine heads, dendritic length of 50 μm from the soma [63, 206, 464]

Table C.2: Synaptic inputs and miscellaneous parameters.

Parameter	Value	Source
Synaptic Inputs		
AMPAR time rise τ_{A1}	0.2 ms	[202, 205]
AMPAR time decay τ_{A2}	2 ms	[205]
AMPAR peak conductance g_{Amax}	0.5 nS	[200]
AMPAR reversal potential E_{AMPA}	0 mV	[202]
NMDAR time rise τ_{N1}	2 ms	[205]
NMDAR time decay τ_{N2}	86 ms	[205]
NMDAR peak conductance g_{Nmax}	0.16 nS	[200]
NMDAR reversal potential E_{NMDA}	-5 mV	[185, 465]
Extracellular $[Mg^{2+}]_o$	1 mM	[200, 466]
Miscellaneous		
Resting potential V_R	-70 mV	[205]
Leak reversal potential E_L	-70 mV	[205]
Na^+ reversal potential E_{Na}	50 mV	[213]
K^+ reversal potential E_K	-90 mV	[213]
Intracellular $[Ca^{2+}]_i$	50×10^{-6} mM	[213]
Extracellular $[Ca^{2+}]_o$	2 mM	[213]

Table C.3: Somatic spiking mechanism

Parameter	Value	Description
g_{Na}	120	Na^+ conductance (mS/cm^2)
g_K	36	K^+ conductance (mS/cm^2)
g_{Ca}	7	Ca^{2+} conductance (mS/cm^2)
g_L	0.1	Leak conductance (mS/cm^2)
V_{Na}	45	Na^+ reversal potential (mV)
V_K	-75	K^+ reversal potential (mV)
V_{Ca}	90	Ca^{2+} reversal potential (mV)
V_L	-70	Leak reversal potential (mV)
C	1	Membrane capacitance (μF/cm^2)

APPENDIX D

DEVELOPING THE EQUIVALENT DENDRITIC ABSTRACTION

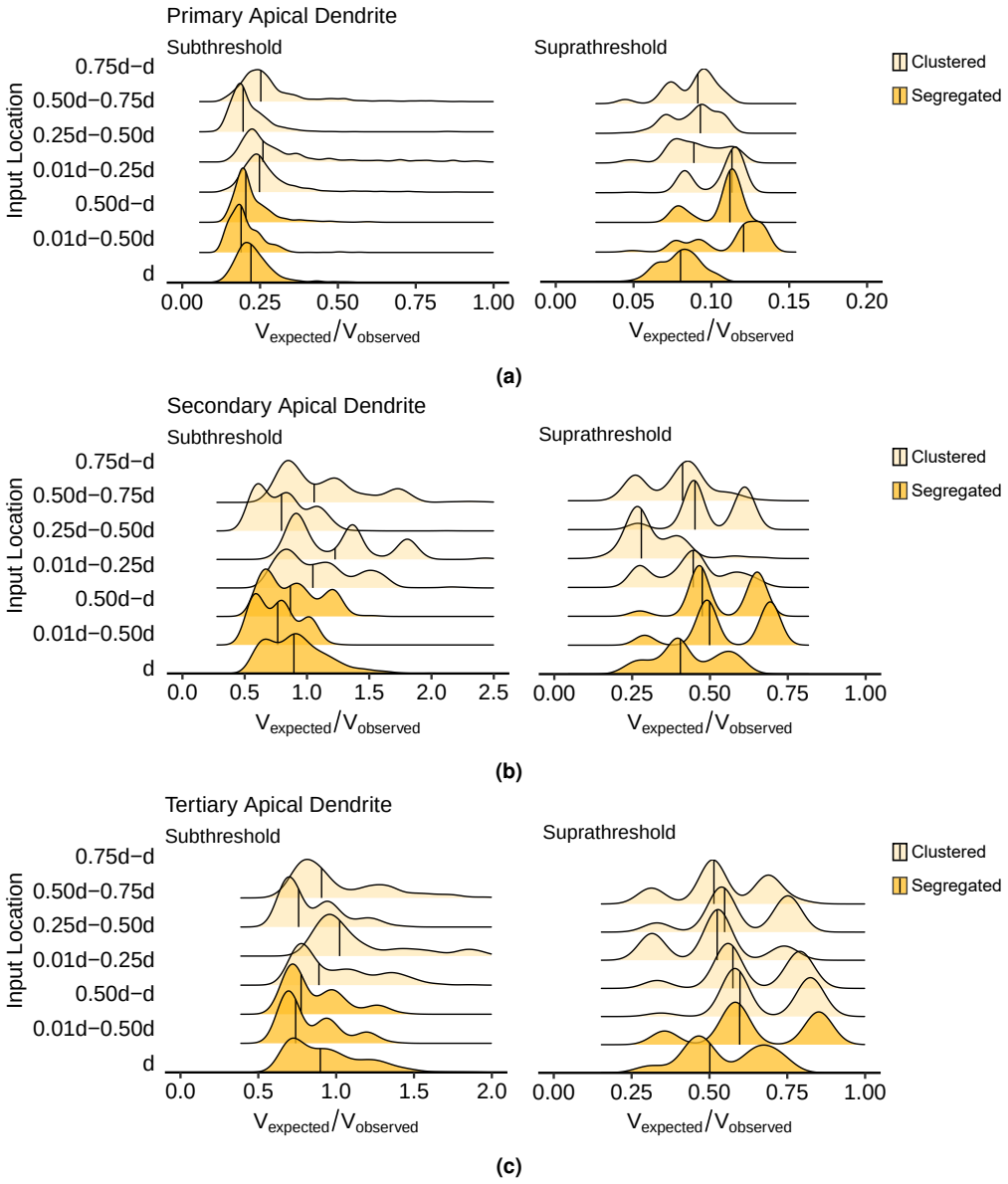

Figure D.1: Density plots of segregated and clustered within-branch synaptic inputs located on the dendritic length d. The results indicate no considerable correlation with the dendritic depolarization and location of activated synapses since the spatiotemporal characteristics of the inputs and dendrites were already expressed in the propagation models.

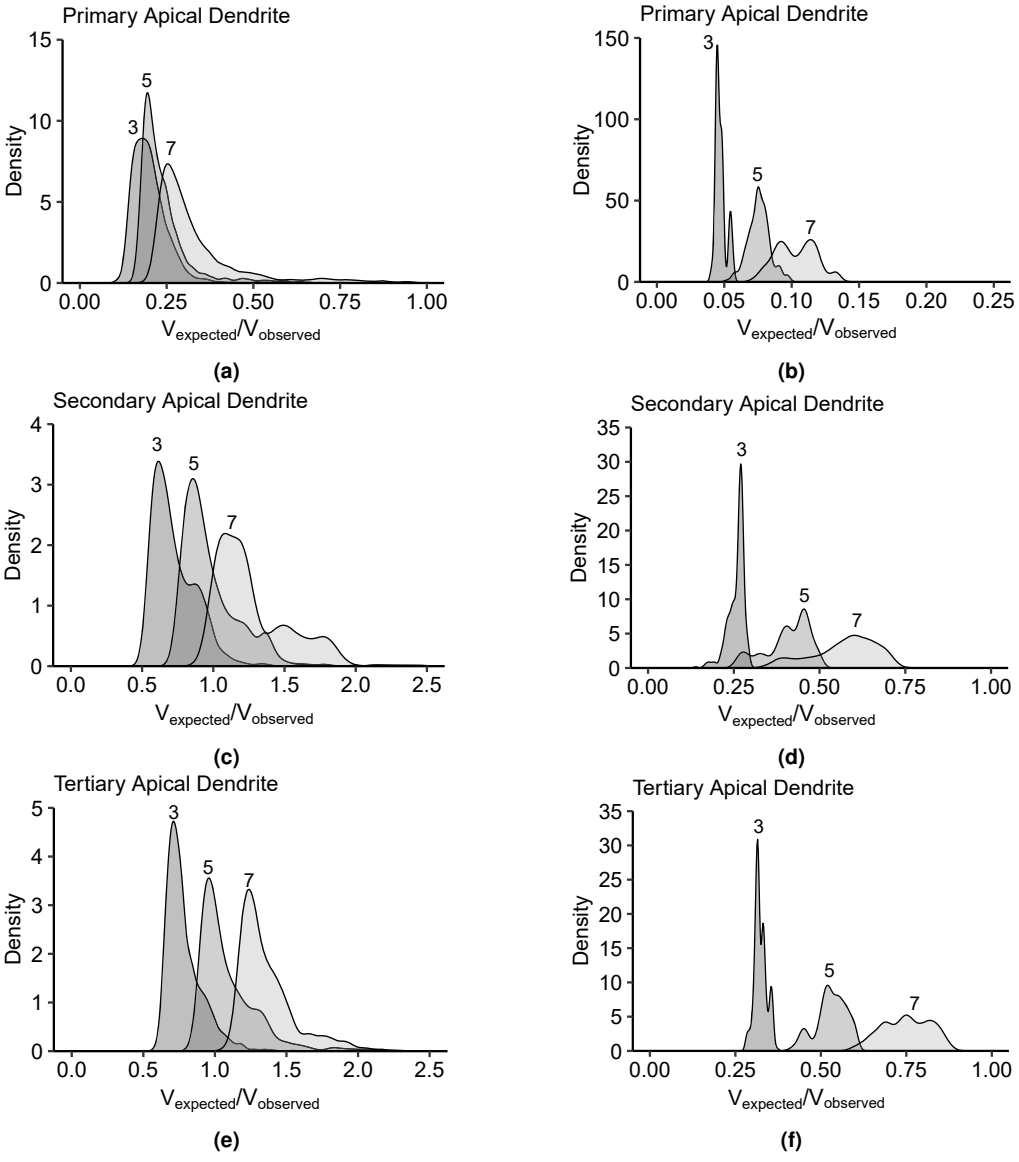

Figure D.2: The density plots of input summation $V_{expected}$ show the clustering of thresholding point depolarizations $V_{observed}$ per number of synaptic inputs (3, 5, and 7).

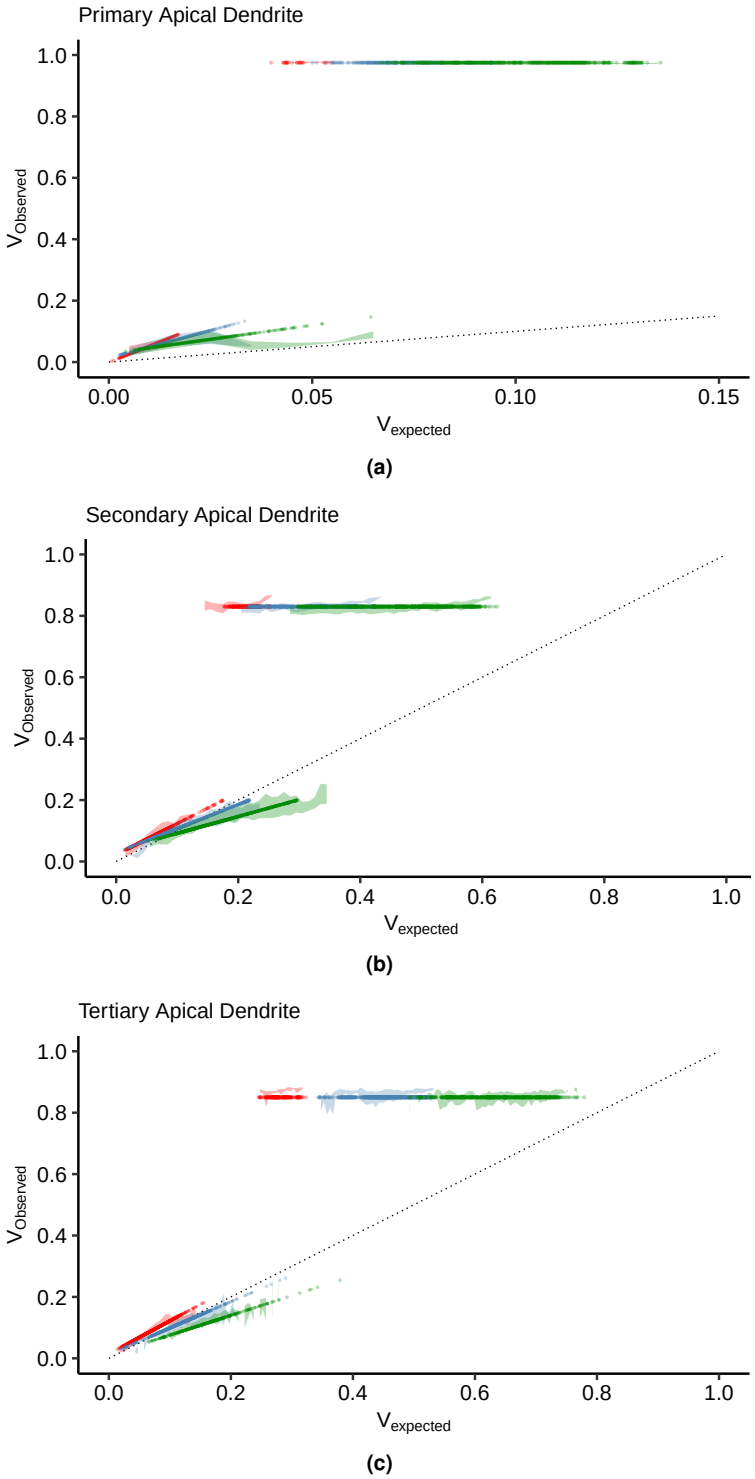

Figure D.3: Predictions using the dynamic thresholding function. The predicted $V_{observed}$ (points) superimposed on the measured $V_{observed}$ at the thresholding point in the (a) primary, (b) secondary, and (c) tertiary apical branches. The prediction follows the behavior of the observed depolarization, wherein the dendritic integration shifts to the right with an increasing number of activated synapses, $n = 3$ (red), $n = 5$ (blue), and $n = 7$ (green).

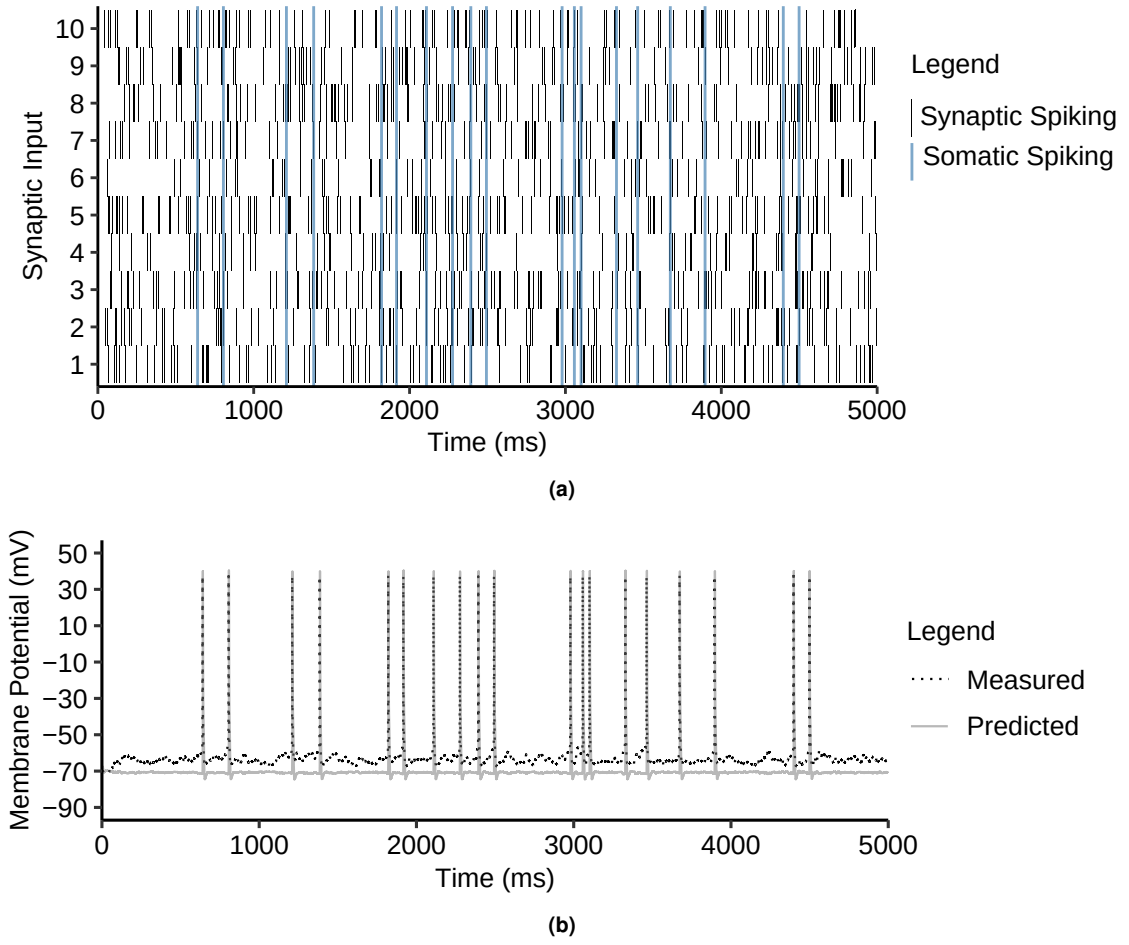

Figure D.4: (a) Sample random synaptic spiking activity in the primary apical dendrite and the corresponding somatic spiking. (b) The measured somatic spiking was reproduced using a Hodgkin-Huxley mechanism.

APPENDIX E

CENTRE DE CALCUL DE L'UNIVERSITÉ DE BOURGOGNE

Cluster Characteristics

No. of machines	:	4 (webern)
No. of cores	:	24
Theoretical power (Gflops)	:	1996.8
Memory (Go)	:	96
Model	:	C6420
Specifications	:	Intel Xeon Gold 6126 2.60 GHz (2P, 12C/P)

For more information on the cluster characteristics, visit https://ccub.u-bourgogne.fr/dnum-ccub/ccubw3/puissance-cluster-iso.html.

BARCELONA COMPUTING CENTER

Cluster Characteristics

The CTE-POWER system overview shown below is taken from https://www.bsc.es/supportkc/docs/CTE-POWER/overview/. CTE-POWER is a cluster based on IBM Power9 processors, with a Linux Operating System and an Infiniband interconnection network.

It has the following configuration:

- 2 login node and 52 compute nodes, each of them:
  - 2 x IBM Power9 8335-GTH 2.4GHz (3.0GHz on turbo, 20 cores and 4 threads/core, total 160 threads per node)
  - 512GB of main memory distributed in 16 dimms x 32GB 2666MHz
  - 2 x SSD 1.9TB as local storage
  - 2 x 3.2TB NVME
  - 4 x GPU NVIDIA V100 (Volta) with 16GB HBM2
  - Single Port Mellanox EDR
  - GPFS via one fiber link 10 GBit

The operating system is Red Hat Enterprise Linux Server 7.5 alternative.

APPENDIX F

RUNTIME SUMMARY

Table F.4: Training runtime (25 epochs) for each configuration.

No. of Tripartite Synapses out of 78 400 Synapses	Runtime (Days, Hours, Minutes)		
	SNAN1	SNAN2	SNAN3
0 (0 %)	4, 16, 30	4, 16, 30	4, 16, 30
7 840 (10 %)	8, 8, 0	11, 11, 0	14, 10, 30
15 680 (20 %)	30, 5, 0	35, 22, 30	26, 19, 45
23 520 (30 %)	35, 10, 0	34, 9, 0	33, 1, 45
31 360 (40 %)	42, 17, 0	41, 16, 0	41, 16, 0
39 200 (50 %)	47, 22, 0	47, 22, 0	49, 17, 45
47 040 (60 %)	57, 7, 0	57, 19, 30	60, 16, 15

TRAINED SYNAPTIC WEIGHTS

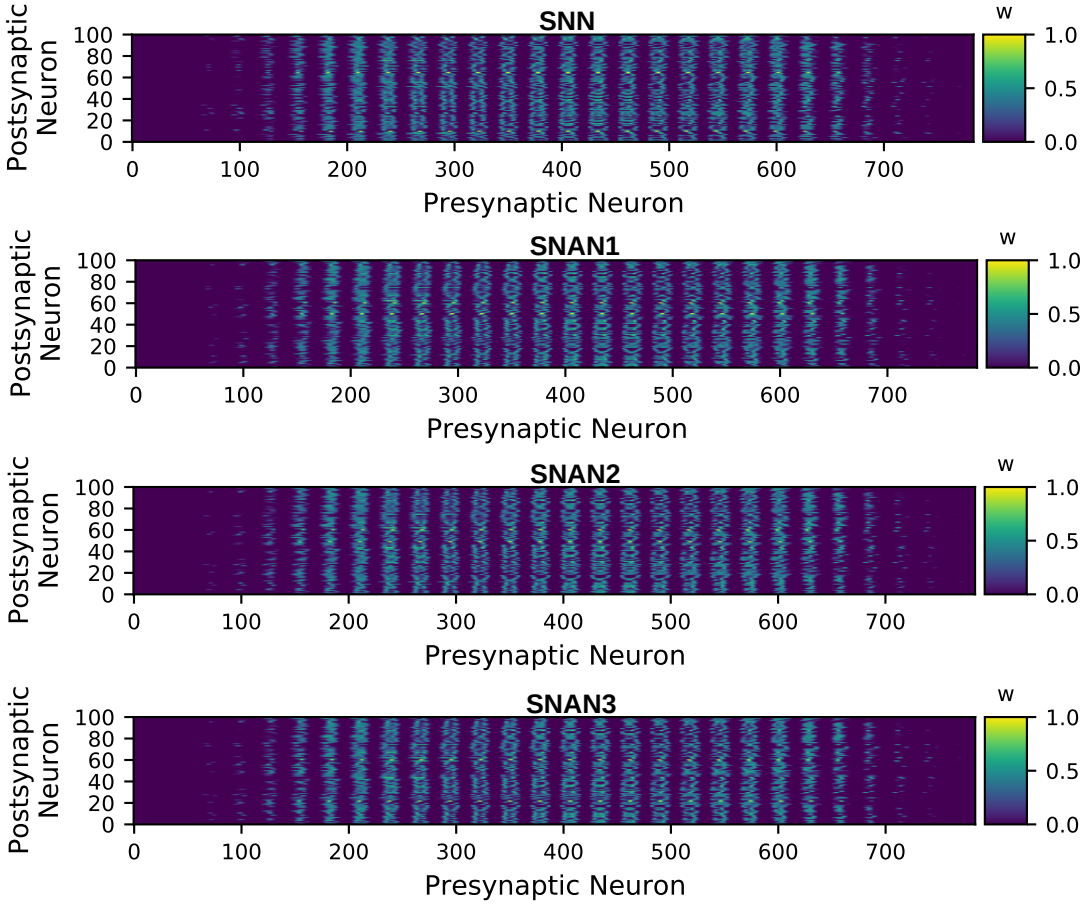

Figure F.1: Input-to-First layer synaptic weights after 25 epochs of training. Half of the number of synapses in the SNANs are tripartite connections.

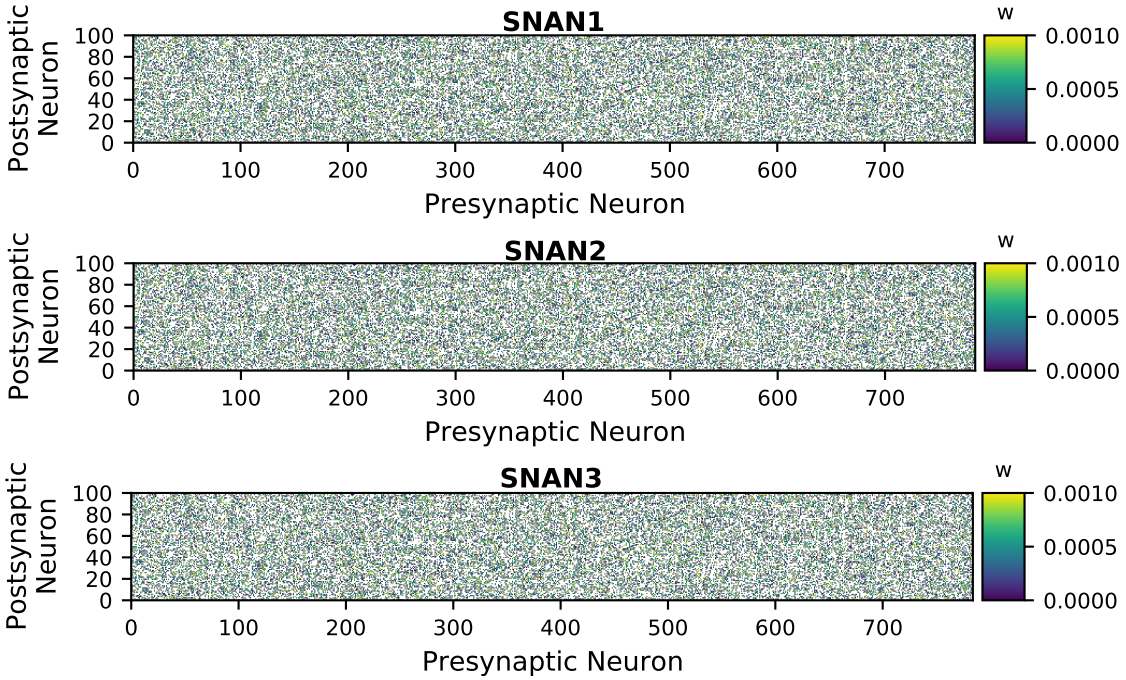

Figure F.2: Astrocytic-to-First layer synaptic weights after 25 epochs of training. Half of the number of synapses in the SNANs are tripartite connections.

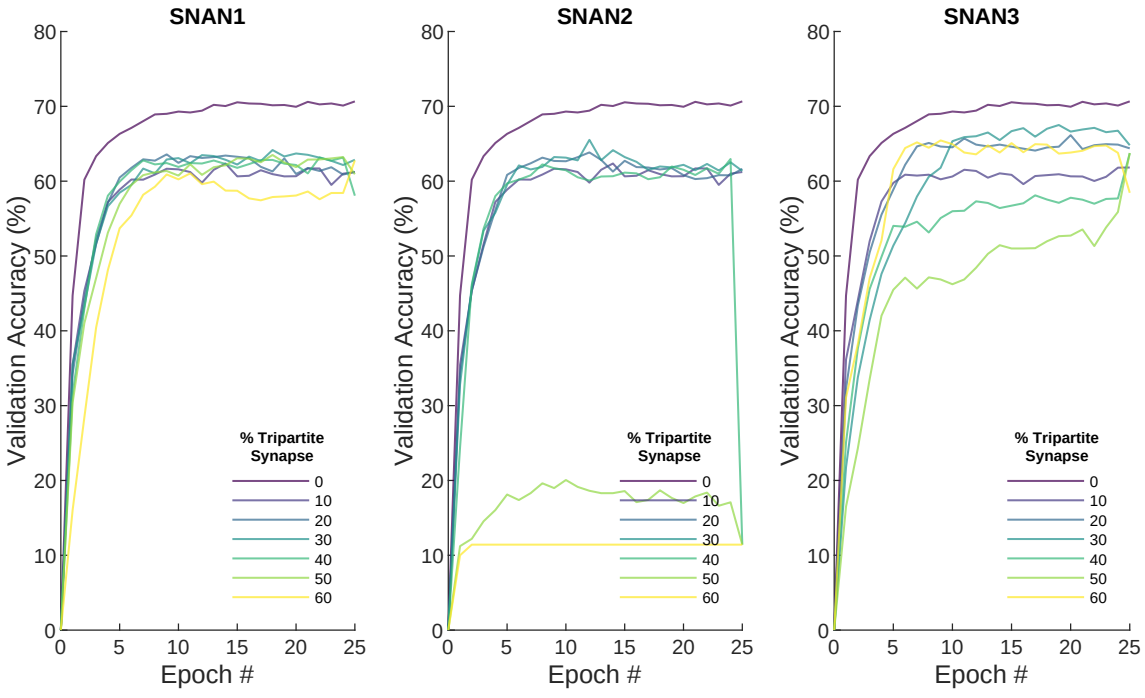

Figure F.3: Validation accuracy.

BIBLIOGRAPHY

[1] Baljit S Khakh. Astrocyte–neuron interactions in the striatum: insights on identity, form, and function. *Trends in neurosciences*, 42(9):617–630, 2019.

[2] Christopher S Von Bartheld, Jami Bahney, and Suzana Herculano-Houzel. The search for true numbers of neurons and glial cells in the human brain: A review of 150 years of cell counting. *Journal of Comparative Neurology*, 524(18):3865–3895, 2016.

[3] Gilles Bonvento and Juan P Bolaños. Astrocyte-neuron metabolic cooperation shapes brain activity. *Cell metabolism*, 33(8):1546–1564, 2021.

[4] Alfonso Araque, Vladimir Parpura, Rita P Sanzgiri, and Philip G Haydon. Tripartite synapses: glia, the unacknowledged partner. *Trends in neurosciences*, 22(5):208–215, 1999.

[5] Erika Bindocci, Iaroslav Savtchouk, Nicolas Liaudet, Denise Becker, Giovanni Carriero, and Andrea Volterra. Three-dimensional ca2+ imaging advances understanding of astrocyte biology. *Science*, 356(6339), 2017.

[6] Franziska Oschmann, Konstantin Mergenthaler, Evelyn Jungnickel, and Klaus Obermayer. Spatial separation of two different pathways accounting for the generation of calcium signals in astrocytes. *PLoS computational biology*, 13(2):e1005377, 2017.

[7] Maiken Nedergaard, Takahiro Takano, and Anker J Hansen. Beyond the role of glutamate as a neurotransmitter. *Nature Reviews Neuroscience*, 3(9):748–755, 2002.

[8] Maiken Nedergaard and Alexei Verkhratsky. Artifact versus reality—how astrocytes contribute to synaptic events. *Glia*, 60(7):1013–1023, 2012.

[9] Nancy Ann Oberheim, Steven A Goldman, and Maiken Nedergaard. Heterogeneity of astrocytic form and function. *Astrocytes*, pages 23–45, 2012.

[10] Gilad Wallach, Jules Lallouette, Nitzan Herzog, Maurizio De Pitta, Eshel Ben Jacob, Hugues Berry, and Yael Hanein. Glutamate mediated astrocytic filtering of neuronal activity. *PLoS Comput Biol*, 10(12):e1003964, 2014.

[11] Michael Pfeiffer and Thomas Pfeil. Deep learning with spiking neurons: opportunities and challenges. *Frontiers in neuroscience*, page 774, 2018.

[12] Mahmood Amiri, Narges Hosseinmardi, Fariba Bahrami, and Mahyar Janahmadi. Astrocyte-neuron interaction as a mechanism responsible for generation of neural synchrony: a study based on modeling and experiments. *Journal of computational neuroscience*, 34(3):489–504, 2013.

[13] Mehul Rastogi, Sen Lu, Nafiul Islam, and Abhronil Sengupta. On the self-repair role of astrocytes in stdp enabled unsupervised snns. *Frontiers in Neuroscience*, 14:1351, 2021.

[14] Susan Yu Gordleeva, Yulia A Tsybina, Mikhail I Krivonosov, Mikhail V Ivanchenko, Alexey A Zaikin, Victor B Kazantsev, and Alexander N Gorban. Modelling working memory in spiking neuron network accompanied by astrocytes. *Frontiers in Cellular Neuroscience*, 15:86, 2021.

[15] Andrea Volterra and Jacopo Meldolesi. Astrocytes, from brain glue to communication elements: the revolution continues. *Nature Reviews Neuroscience*, 6(8):626–640, 2005.

[16] Li Deng. The mnist database of handwritten digit images for machine learning research [best of the web]. *IEEE Signal Processing Magazine*, 29(6):141–142, 2012.

[17] Nicholas T Carnevale and Michael L Hines. *The NEURON book*. Cambridge University Press, 2006.

[18] Peter Zeidman and Eleanor A Maguire. Anterior hippocampus: the anatomy of perception, imagination and episodic memory. *Nature Reviews Neuroscience*, 17(3):173–182, 2016.

[19] Nim Tottenham and Margaret A Sheridan. A review of adversity, the amygdala and the hippocampus: a consideration of developmental timing. *Frontiers in human neuroscience*, 3:68, 2010.

[20] Aleksandra Maruszak and Sandrine Thuret. Why looking at the whole hippocampus is not enough—a critical role for anteroposterior axis, subfield and activation analyses to enhance predictive value of hippocampal changes for alzheimer's disease diagnosis. *Frontiers in cellular neuroscience*, 8:95, 2014.

[21] Mark Bear, Barry Connors, and Michael A Paradiso. *Neuroscience: Exploring the brain*. Jones & Bartlett Learning, LLC, 2020.

[22] RD Burwell and KL Agster. 3.03 anatomy of the hippocampus and the declarative memory system. *Concise Learning and Memory: The Editor's Selection*, page 189, 2009.

[23] Andy CH Lee, Sathesan Thavabalasingam, Denada Alushaj, Bilgehan Çavdaroğlu, and Rutsuko Ito. The hippocampus contributes to temporal duration memory in the context of event sequences: A cross-species perspective. *Neuropsychologia*, 137:107300, 2020.

[24] Eleanor A Maguire and Sinéad L Mullally. The hippocampus: a manifesto for change. *Journal of Experimental Psychology: General*, 142(4):1180, 2013.

[25] Amir-Homayoun Javadi, Beatrix Emo, Lorelei R Howard, Fiona E Zisch, Yichao Yu, Rebecca Knight, Joao Pinelo Silva, and Hugo J Spiers. Hippocampal and prefrontal processing of network topology to simulate the future. *Nature communications*, 8(1):1–11, 2017.

[26] Camillo Golgi. *Sulla fina anatomia degli organi centrali del sistema nervoso*. S. Calderini, 1885.

[27] Morris Moscovitch, Roberto Cabeza, Gordon Winocur, and Lynn Nadel. Episodic memory and beyond: the hippocampus and neocortex in transformation. *Annual review of psychology*, 67:105–134, 2016.

[28] Shozo Jinno. Aging affects new cell production in the adult hippocampus: A quantitative anatomic review. *Journal of chemical neuroanatomy*, 76:64–72, 2016.

[29] Austin R Graves, Shannon J Moore, Erik B Bloss, Brett D Mensh, William L Kath, and Nelson Spruston. Hippocampal pyramidal neurons comprise two distinct cell types that are countermodulated by metabotropic receptors. *Neuron*, 76(4):776–789, 2012.

[30] Sarah Genon, Andrew Reid, Robert Langner, Katrin Amunts, and Simon B Eickhoff. How to characterize the function of a brain region. *Trends in cognitive sciences*, 22(4):350–364, 2018.

[31] Larry R Squire, Lisa Genzel, John T Wixted, and Richard G Morris. Memory consolidation. *Cold Spring Harbor perspectives in biology*, 7(8):a021766, 2015.

[32] Gabrielle Girardeau and Michaël Zugaro. Hippocampal ripples and memory consolidation. *Current opinion in neurobiology*, 21(3):452–459, 2011.

[33] Niels C Rattenborg, Dolores Martinez-Gonzalez, Timothy C Roth, and Vladimir V Pravosudov. Hippocampal memory consolidation during sleep: a comparison of mammals and birds. *Biological Reviews*, 86(3):658–691, 2011.

[34] Andrey Babichev, Daoyun Ji, Facundo Mémoli, and Yuri A Dabaghian. A topological model of the hippocampal cell assembly network. *Frontiers in computational neuroscience*, 10:50, 2016.

[35] Chris M Bird and Neil Burgess. The hippocampus and memory: insights from spatial processing. *Nature Reviews Neuroscience*, 9(3):182–194, 2008.

[36] Donna Rose Addis and Daniel Schacter. The hippocampus and imagining the future: where do we stand? *Frontiers in human neuroscience*, 5:173, 2012.

[37] Kazumasa Z Tanaka, Aleksandr Pevzner, Anahita B Hamidi, Yuki Nakazawa, Jalina Graham, and Brian J Wiltgen. Cortical representations are reinstated by the hippocampus during memory retrieval. *Neuron*, 84(2):347–354, 2014.

[38] Alison R Preston and Howard Eichenbaum. Interplay of hippocampus and prefrontal cortex in memory. *Current Biology*, 23(17):R764–R773, 2013.

[39] Margaret F Carr, Shantanu P Jadhav, and Loren M Frank. Hippocampal replay in the awake state: a potential substrate for memory consolidation and retrieval. *Nature neuroscience*, 14(2):147, 2011.

[40] Alexei Verkhratsky and Arthur M Butt. The history of the decline and fall of the glial numbers legend. *Neuroglia*, 1(1):188–192, 2018.

[41] Diek W Wheeler, Charise M White, Christopher L Rees, Alexander O Komendantov, David J Hamilton, and Giorgio A Ascoli. Hippocampome. org: a knowledge base of neuron types in the rodent hippocampus. *Elife*, 4:e09960, 2015.

[42] Srdjan D Antic, Bradley James Baker, and Marco Canepari. New insights on neuron and astrocyte function from cutting-edge optical techniques. *Frontiers in cellular neuroscience*, 13:463, 2019.

[43] Suzana Herculano-Houzel. The glia/neuron ratio: how it varies uniformly across brain structures and species and what that means for brain physiology and evolution. *Glia*, 62(9):1377–1391, 2014.

[44] Daniel Keller, Csaba Erö, and Henry Markram. Cell densities in the mouse brain: a systematic review. *Frontiers in neuroanatomy*, 12:83, 2018.

[45] Nelson Spruston. Pyramidal neurons: dendritic structure and synaptic integration. *Nature Reviews Neuroscience*, 9(3):206–221, 2008.

[46] D Feldmeyer. Functional and structural diversity of pyramidal cells. 2015.

[47] Paul Johns. *Clinical Neuroscience E-Book*. Elsevier Health Sciences, 2014.

[48] Ruth Benavides-Piccione, Mamen Regalado-Reyes, Isabel Fernaud-Espinosa, Asta Kastanauskaite, Silvia Tapia-González, Gonzalo León-Espinosa, Concepcion Rojo, Ricardo Insausti, Idan Segev, and Javier DeFelipe. Differential structure of hippocampal ca1 pyramidal neurons in the human and mouse. *Cerebral Cortex*, 30(2):730–752, 2020.

[49] Hongkui Zeng and Joshua R Sanes. Neuronal cell-type classification: challenges, opportunities and the path forward. *Nature Reviews Neuroscience*, 18(9):530–546, 2017.

[50] Benedetta Leuner and Elizabeth Gould. Structural plasticity and hippocampal function. *Annual review of psychology*, 61:111–140, 2010.

[51] JL Pawluski, Andreia Valenca, Ana Isabel M Santos, João Pedro Costa-Nunes, Harry WM Steinbusch, and T Strekalova. Pregnancy or stress decrease complexity of ca3 pyramidal neurons in the hippocampus of adult female rats. *Neuroscience*, 227:201–210, 2012.

[52] Emőke Borbély, János Horváth, Szabina Furdan, Zsolt Bozsó, Botond Penke, and Lívia Fülöp. Simultaneous changes of spatial memory and spine density after intrahippocampal administration of fibrillar aβ1–42 to the rat brain. *BioMed research international*, 2014, 2014.

[53] Qian-Qian Yang, Wei-Zhen Xue, Rong-Xin Zou, Yi Xu, Yang Du, Shuang Wang, Lai Xu, Yuan-Zhi Chen, Hui-Li Wang, and Xiang-Tao Chen. β-asarone rescues pb-induced impairments of spatial memory and synaptogenesis in rats. *PloS one*, 11(12):e0167401, 2016.

[54] Erik Meijering. Neuron tracing in perspective. *Cytometry Part A*, 77(7):693–704, 2010.

[55] Harvey Lodish, Arnold Berk, S Lawrence Zipursky, Paul Matsudaira, David Baltimore, and James Darnell. Molecular cell biology 4th edition. *National Center for Biotechnology Information, Bookshelf*, 9, 2000.

[56] Grace E Stutzmann and Mark P Mattson. Endoplasmic reticulum ca2+ handling in excitable cells in health and disease. *Pharmacological reviews*, 63(3):700–727, 2011.

[57] Myoung Kyu Park, Yu Mi Choi, Yun Kyung Kang, and Ole H Petersen. The endoplasmic reticulum as an integrator of multiple dendritic events. *The Neuroscientist*, 14(1):68–77, 2008.

[58] Uziel Sandler and Lev Tsitolovsky. *Neural Cell Behavior and Fuzzy Logic: The Being of Neural Cells and Mathematics of Feeling*, volume 4. Springer Science & Business Media, 2008.

[59] Raquel Marin. The neuronal membrane as a key factor in neurodegeneration. *Frontiers in physiology*, 4:188, 2013.

[60] Cian O'Donnell and Mark CW van Rossum. Systematic analysis of the contributions of stochastic voltage gated channels to neuronal noise. *Frontiers in computational neuroscience*, 8:105, 2014.

[61] Narendra Bhadra. Physiological principles of electrical stimulation. In *Implantable Neuroprostheses for Restoring Function*, pages 13–43. Elsevier, 2015.

[62] Eve Marder and Astrid A Prinz. Modeling stability in neuron and network function: the role of activity in homeostasis. *Bioessays*, 24(12):1145–1154, 2002.

[63] Nicholas D Child and Eduardo E Benarroch. Differential distribution of voltage-gated ion channels in cortical neurons: implications for epilepsy. *Neurology*, 82(11):989–999, 2014.

[64] Mara Almog and Alon Korngreen. Characterization of voltage-gated ca 2+ conductances in layer 5 neocortical pyramidal neurons from rats. *PLoS One*, 4(4):e4841, 2009.

[65] Efrat Katz, Ohad Stoler, Anja Scheller, Yana Khrapunsky, Sandra Goebbels, Frank Kirchhoff, Michael J Gutnick, Fred Wolf, and Ilya A Fleidervish. Role of sodium channel subtype in action potential generation by neocortical pyramidal neurons. *Proceedings of the National Academy of Sciences*, 115(30):E7184–E7192, 2018.

[66] Indira M Raman and Bruce P Bean. Resurgent sodium current and action potential formation in dissociated cerebellar purkinje neurons. *Journal of Neuroscience*, 17(12):4517–4526, 1997.

[67] Andrea Lorincz and Zoltan Nusser. Molecular identity of dendritic voltage-gated sodium channels. *Science*, 328(5980):906–909, 2010.

[68] S Remy, H Beck, and Y Yaari. Plasticity of voltage-gated ion channels in pyramidal cell dendrites. *Current opinion in neurobiology*, 20(4):503–509, 2010.

[69] Galen E Flynn and William N Zagotta. Insights into the molecular mechanism for hyperpolarization-dependent activation of hcn channels. *Proceedings of the National Academy of Sciences*, 115(34):E8086–E8095, 2018.

[70] Carl CH Petersen. Whole-cell recording of neuronal membrane potential during behavior. *Neuron*, 95(6):1266–1281, 2017.

[71] MEP Didier, OB Tarun, P Jourdain, P Magistretti, and S Roke. Membrane water for probing neuronal membrane potentials and ionic fluxes at the single cell level. *Nature communications*, 9(1):1–7, 2018.

[72] Guo-Sheng Yi, Jiang Wang, Bin Deng, and Xi-Le Wei. Morphology controls how hippocampal ca1 pyramidal neuron responds to uniform electric fields: a biophysical modeling study. *Scientific Reports*, 7(1):1–13, 2017.

[73] Stephen C Cannon and Bruce P Bean. Sodium channels gone wild: resurgent current from neuronal and muscle channelopathies. *The Journal of clinical investigation*, 120(1):80–83, 2010.

[74] John Enderle. Bioelectric phenomena. In *Introduction to biomedical engineering*, pages 627–691. Elsevier, 2005.

[75] Guillaume Drion, Timothy O'Leary, Julie Dethier, Alessio Franci, and Rodolphe Sepulchre. Neuronal behaviors: A control perspective. In *2015 54th IEEE Conference on Decision and Control (CDC)*, pages 1923–1944. IEEE, 2015.

[76] Alan L Hodgkin and Andrew F Huxley. A quantitative description of membrane current and its application to conduction and excitation in nerve. *The Journal of physiology*, 117(4):500, 1952.

[77] Mara Almog and Alon Korngreen. Is realistic neuronal modeling realistic? *Journal of neurophysiology*, 116(5):2180–2209, 2016.

[78] Riccardo Sacco, Giovanna Guidoboni, and Aurelio Giancarlo Mauri. *A Comprehensive Physically Based Approach to Modeling in Bioengineering and Life Sciences*. Academic Press, 2019.

[79] Nicholas Sperelakis. Cable properties and propagation of action potentials. In *Cell Physiology Source Book*, pages 395–406. Elsevier, 2001.

[80] S Postnova, E Rosa, and HA Braun. Neurones and synapses for systemic models of psychiatric disorders. *Pharmacopsychiatry*, 43(S 01):S82–S91, 2010.

[81] Allan L Hodgkin and Andrew F Huxley. The components of membrane conductance in the giant axon of loligo. *The Journal of physiology*, 116(4):473, 1952.

[82] Allan L Hodgkin and Andrew F Huxley. Currents carried by sodium and potassium ions through the membrane of the giant axon of loligo. *The Journal of physiology*, 116(4):449, 1952.

[83] Allan L Hodgkin and Andrew F Huxley. The dual effect of membrane potential on sodium conductance in the giant axon of loligo. *The Journal of physiology*, 116(4):497, 1952.

[84] Wilfrid Rall. Theoretical significance of dendritic trees for neuronal input-output relations. *Neural theory and modeling*, pages 73–97, 1964.

[85] Romain Brette. What is the most realistic single-compartment model of spike initiation? *PLoS Comput Biol*, 11(4):e1004114, 2015.

[86] AS Dmitrichev, DV Kasatkin, Vladimir Viktorovich Klinshov, S Yu Kirillov, Oleg Vladimirovich Maslennikov, DS Shapin, and Vladimir Isaakovicih Nekorkin. Nonlinear dynamical models of neurons. *Izvestiya VUZ. Applied Nonlinear Dynamics*, 26(4):5–58, 2018.

[87] Mara Almog, Tal Barkai, Angelika Lampert, and Alon Korngreen. Voltage-gated sodium channels in neocortical pyramidal neurons display cole-moore activation kinetics. *Frontiers in Cellular Neuroscience*, 12:187, 2018.

[88] Shivendra G Tewari and Kaushik Kumar Majumdar. A mathematical model of the tripartite synapse: astrocyte-induced synaptic plasticity. *Journal of biological physics*, 38(3):465–496, 2012.

[89] Hillel Ori, Eve Marder, and Shimon Marom. Cellular function given parametric variation in the hodgkin and huxley model of excitability. *Proceedings of the National Academy of Sciences*, 115(35):E8211–E8218, 2018.

[90] Vincent Renault, Michèle Thieullen, and Emmanuel Trélat. Minimal time spiking in various chr2-controlled neuron models. *Journal of mathematical biology*, 76(3):567–608, 2018.

[91] Catherine Morris and Harold Lecar. Voltage oscillations in the barnacle giant muscle fiber. *Biophysical journal*, 35(1):193–213, 1981.

[92] Eugene M Izhikevich. Which model to use for cortical spiking neurons? *IEEE transactions on neural networks*, 15(5):1063–1070, 2004.

[93] Mahmood Amiri, Ghazal Montaseri, and Fariba Bahrami. A phase plane analysis of neuron–astrocyte interactions. *Neural Networks*, 44:157–165, 2013.

[94] Guo-Sheng Yi, Jiang Wang, Kai-Ming Tsang, Xi-Le Wei, and Bin Deng. Input-output relation and energy efficiency in the neuron with different spike threshold dynamics. *Frontiers in computational neuroscience*, 9:62, 2015.

[95] Steven A Prescott, Yves De Koninck, and Terrence J Sejnowski. Biophysical basis for three distinct dynamical mechanisms of action potential initiation. *PLoS Comput Biol*, 4(10):e1000198, 2008.

[96] Richard Fitzhugh. Thresholds and plateaus in the hodgkin-huxley nerve equations. *The Journal of general physiology*, 43(5):867–896, 1960.

[97] Richard FitzHugh. Impulses and physiological states in theoretical models of nerve membrane. *Biophysical journal*, 1(6):445, 1961.

[98] Jinichi Nagumo, Suguru Arimoto, and Shuji Yoshizawa. An active pulse transmission line simulating nerve axon. *Proceedings of the IRE*, 50(10):2061–2070, 1962.

[99] Socrates Dokos. Multi-scale modelling in biology. In *Encyclopedia of Bioinformatics and Computational Biology*, pages 900 – 905. Academic Press, 2019.

[100] Christof Koch. *Biophysics of computation: information processing in single neurons*. Oxford university press, 2004.

[101] Pedro M Lima, Neville J Ford, and Patricia M Lumb. Computational methods for a mathematical model of propagation of nerve impulses in myelinated axons. *Applied Numerical Mathematics*, 85:38–53, 2014.

[102] Ronald MacGregor. *Neural and brain modeling*. Elsevier, 2012.

[103] Wim Van Drongelen. *Signal processing for neuroscientists*. Academic press, 2018.

[104] Josef Ladenbauer, Sam McKenzie, Daniel Fine English, Olivier Hagens, and Srdjan Ostojic. Inferring and validating mechanistic models of neural microcircuits based on spike-train data. *Nature communications*, 10(1):1–17, 2019.

[105] Eilen Nordlie, Tom Tetzlaff, and Gaute T Einevoll. Rate dynamics of leaky integrate-and-fire neurons with strong synapses. *Frontiers in computational neuroscience*, 4:149, 2010.

[106] Srdjan Ostojic and Nicolas Brunel. From spiking neuron models to linear-nonlinear models. *PLoS Comput Biol*, 7(1):e1001056, 2011.

[107] Anthony N Burkitt. A review of the integrate-and-fire neuron model: I. homogeneous synaptic input. *Biological cybernetics*, 95(1):1–19, 2006.

[108] Ying Liu and Chunguang Li. Firing rate propagation through neuronal–astrocytic network. *IEEE transactions on neural networks and learning systems*, 24(5):789–799, 2013.

[109] Satoshi Yamauchi, Hideaki Kim, and Shigeru Shinomoto. Elemental spiking neuron model for reproducing diverse firing patterns and predicting precise firing times. *Frontiers in computational neuroscience*, 5:42, 2011.

[110] Xu Zhang, Greg Foderaro, Craig Henriquez, Antonius MJ VanDongen, and Silvia Ferrari. A radial basis function spike model for indirect learning via integrate-and-fire sampling and reconstruction techniques. *Advances in Artificial Neural Systems*, 2012, 2012.

[111] Michelle Rudolph-Lilith, Mathieu Dubois, and Alain Destexhe. Analytical integrate-and-fire neuron models with conductance-based dynamics and realistic postsynaptic potential time course for event-driven simulation strategies. *Neural Computation*, 24(6):1426–1461, 2012.

[112] Nicolas Brunel and Mark CW Van Rossum. Lapicque's 1907 paper: from frogs to integrate-and-fire. *Biological cybernetics*, 97(5-6):337–339, 2007.

[113] Renaud Jolivet, Timothy J Lewis, and Wulfram Gerstner. Generalized integrate-and-fire models of neuronal activity approximate spike trains of a detailed model to a high degree of accuracy. *Journal of neurophysiology*, 92(2):959–976, 2004.

[114] Nicolas Fourcaud-Trocmé. Integrate and fire models, deterministic. *Encyclopedia of Computational Neuroscience*, 2014.

[115] Gang Zheng and Arnaud Tonnelier. Chaotic solutions in the quadratic integrate-and-fire neuron with adaptation. *Cognitive neurodynamics*, 3(3):197–204, 2009.

[116] Victor J Barranca, Daniel C Johnson, Jennifer L Moyher, Joshua P Sauppe, Maxim S Shkarayev, Gregor Kovačič, and David Cai. Dynamics of the exponential integrate-and-fire model with slow currents and adaptation. *Journal of computational neuroscience*, 37(1):161–180, 2014.

[117] Josef Ladenbauer, Moritz Augustin, LieJune Shiau, and Klaus Obermayer. Impact of adaptation currents on synchronization of coupled exponential integrate-and-fire neurons. *PLoS Comput Biol*, 8(4):e1002478, 2012.

[118] Laurent Badel, Sandrine Lefort, Thomas K Berger, Carl CH Petersen, Wulfram Gerstner, and Magnus JE Richardson. Extracting non-linear integrate-and-fire models from experimental data using dynamic i–v curves. *Biological cybernetics*, 99(4-5):361, 2008.

[119] Aniello Buonocore, Luigia Caputo, Enrica Pirozzi, and Maria Francesca Carfora. A leaky integrate-and-fire model with adaptation for the generation of a spike train. *Mathematical Biosciences & Engineering*, 13(3):483, 2016.

[120] Fei Chen and Yuan-Ting Zhang. A variant of the integrate-and-fire model to simulate the adaptive neural firing pattern. *Biomedical Signal Processing and Control*, 5(1):66–69, 2010.

[121] Marie Levakova, Lubomir Kostal, Christelle Monsempès, Philippe Lucas, and Ryota Kobayashi. Adaptive integrate-and-fire model reproduces the dynamics of olfactory receptor neuron responses in a moth. *Journal of the Royal Society Interface*, 16(157):20190246, 2019.

[122] Ying-Hui Liu and Xiao-Jing Wang. Spike-frequency adaptation of a generalized leaky integrate-and-fire model neuron. *Journal of computational neuroscience*, 10(1):25–45, 2001.

[123] Cyrille Rossant, Dan FM Goodman, Jonathan Platkiewicz, and Romain Brette. Automatic fitting of spiking neuron models to electrophysiological recordings. *Frontiers in neuroinformatics*, 4:2, 2010.

[124] Alexander Rauch, Giancarlo La Camera, Hans-Rudolf Luscher, Walter Senn, and Stefano Fusi. Neocortical pyramidal cells respond as integrate-and-fire neurons to in vivo–like input currents. *Journal of neurophysiology*, 90(3):1598–1612, 2003.

[125] Claudia Clopath, Lars Büsing, Eleni Vasilaki, and Wulfram Gerstner. Connectivity reflects coding: a model of voltage-based stdp with homeostasis. *Nature neuroscience*, 13(3):344, 2010.

[126] Jonathan Touboul. Importance of the cutoff value in the quadratic adaptive integrate-and-fire model. *Neural computation*, 21(8):2114–2122, 2009.

[127] Eugene M Izhikevich. *Dynamical systems in neuroscience*. MIT press, 2007.

[128] Siva Venkadesh, Alexander O Komendantov, Stanislav Listopad, Eric O Scott, Kenneth De Jong, Jeffrey L Krichmar, and Giorgio A Ascoli. Evolving simple models of diverse intrinsic dynamics in hippocampal neuron types. *Frontiers in neuroinformatics*, 12:8, 2018.

[129] Eugene M Izhikevich. Simple model of spiking neurons. *IEEE Transactions on neural networks*, 14(6):1569–1572, 2003.

[130] Zahra Sajedinia and Sébastien Hélie. A new computational model for astrocytes and their role in biologically realistic neural networks. *Computational intelligence and neuroscience*, 2018, 2018.

[131] David Purger, Erin M Gibson, and Michelle Monje. Myelin plasticity in the central nervous system. *Neuropharmacology*, 110:563–573, 2016.

[132] Charles F Babbs and Riyi Shi. Subtle paranodal injury slows impulse conduction in a mathematical model of myelinated axons. *PLoS One*, 8(7):e67767, 2013.

[133] R Douglas Fields. A new mechanism of nervous system plasticity: activity-dependent myelination. *Nature Reviews Neuroscience*, 16(12):756–767, 2015.

[134] Aiman S Saab and Klaus-Armin Nave. Myelin dynamics: protecting and shaping neuronal functions. *Current opinion in neurobiology*, 47:104–112, 2017.

[135] I Lorena Arancibia-Carcamo and David Attwell. The node of ranvier in cns pathology. *Acta neuropathologica*, 128(2):161–175, 2014.

[136] Sebastian Poliak and Elior Peles. The local differentiation of myelinated axons at nodes of ranvier. *Nature Reviews Neuroscience*, 4(12):968–980, 2003.

[137] Janev Fehmi, Steven S Scherer, Hugh J Willison, and Simon Rinaldi. Nodes, paranodes and neuropathies. *Journal of Neurology, Neurosurgery & Psychiatry*, 89(1):61–71, 2018.

[138] CH Fry. Action potential and nervous conduction. *Surgery (Oxford)*, 23(12):425–429, 2005.

[139] Dirk Bucher and Jean-Marc Goaillard. Beyond faithful conduction: short-term dynamics, neuromodulation, and long-term regulation of spike propagation in the axon. *Progress in neurobiology*, 94(4):307–346, 2011.

[140] Bernhard J Mitterauer. Pathophysiology of schizophrenia based on impaired glial-neuronal interactions. *Open Journal of Medical Psychology*, 2014, 2014.

[141] Kara Rogers. Node of ranvier. *Encyclopaedia Britannica*, 2018.

[142] PJ Basser. Cable equation for a myelinated axon derived from its microstructure. *Medical & biological engineering & computing*, 31(1):S87–S92, 1993.

[143] NM Bogatov, LR Grigoryan, EG Ponetaeva, and AS Sinisyn. Calculation of action potential propagation in nerve fiber. *Progress in biophysics and molecular biology*, 114(3):170–174, 2014.

[144] Bomje Woo and Jinhoon Choi. Reduced model and simulation of myelinated axon using eigenfunction expansion and singular perturbation. *Computers in biology and medicine*, 37(8):1148–1154, 2007.

[145] Franziska Auer, Stavros Vagionitis, and Tim Czopka. Evidence for myelin sheath remodeling in the cns revealed by in vivo imaging. *Current Biology*, 28(4):549–559, 2018.

[146] Geneviève Dupont and James Sneyd. Recent developments in models of calcium signalling. *Current opinion in systems biology*, 3:15–22, 2017.

[147] Frido Erler, Michael Meyer-Hermann, and Gerhard Soff. A quantitative model for presynaptic free ca2+ dynamics during different stimulation protocols. *Neurocomputing*, 61:169–191, 2004.

[148] Jung Min Han and Vipul Periwal. A mathematical model of calcium dynamics: Obesity and mitochondria-associated er membranes. *PLoS computational biology*, 15(8):e1006661, 2019.

[149] Chris J Roome, Emmet M Power, and Ruth M Empson. Transient reversal of the sodium/calcium exchanger boosts presynaptic calcium and synaptic transmission at a cerebellar synapse. *Journal of Neurophysiology*, 109(6):1669–1680, 2013.

[150] Alessandra Donato, Konstantinos Kagias, Yun Zhang, and Massimo A Hilliard. Neuronal sub-compartmentalization: a strategy to optimize neuronal function. *Biological Reviews*, 94(3):1023–1037, 2019.

[151] Farhan Ali and Alex C Kwan. Interpreting in vivo calcium signals from neuronal cell bodies, axons, and dendrites: a review. *Neurophotonics*, 7(1):011402, 2019.

[152] KT Blackwell. Approaches and tools for modeling signaling pathways and calcium dynamics in neurons. *Journal of neuroscience methods*, 220(2):131–140, 2013.

[153] Johannes Brockhaus, Bianca Brüggen, and Markus Missler. Imaging and analysis of presynaptic calcium influx in cultured neurons using syngcamp6f. *Frontiers in Synaptic Neuroscience*, 11:12, 2019.

[154] Takuya Sasaki. The axon as a unique computational unit in neurons. *Neuroscience research*, 75(2):83–88, 2013.

[155] Dmitri A Rusakov. Ca2+-dependent mechanisms of presynaptic control at central synapses. *The Neuroscientist*, 12(4):317–326, 2006.

[156] Andreas Ritzau-Jost and Stefan Hallermann. Presynaptic calcium en passage through the axon. *Biophysical journal*, 115(7):1143, 2018.

[157] Maurizio De Pitta, Vladislav Volman, Herbert Levine, and Eshel Ben-Jacob. Multimodal encoding in a simplified model of intracellular calcium signaling. *Cognitive processing*, 10(1):55, 2009.

[158] Maryna A Hliatsevich, Pavel M Bulai, Taras N Pitlik, Andrey A Denisov, and Sergey N Cherenkevich. Design of deterministic model of signal transduction between neuronal cells. *Mathematical modelling and analysis*, 20(1):76–93, 2015.

[159] J Gerard G Borst and Bert Sakmann. Calcium current during a single action potential in a large presynaptic terminal of the rat brainstem. *The Journal of physiology*, 506(Pt 1):143, 1998.

[160] Siow-Cheng Chan, Siew-Ying Mok, Danny Wee-Kiat Ng, and Sing-Yau Goh. The role of neuron–glia interactions in the emergence of ultra-slow oscillations. *Biological cybernetics*, 111(5-6):459–472, 2017.

[161] Xue Ding, Xiuhui Zhang, and Lin Ji. Contribution of calcium fluxes to astrocyte spontaneous calcium oscillations in deterministic and stochastic models. *Applied Mathematical Modelling*, 55:371–382, 2018.

[162] Yue-Xian Li and John Rinzel. Equations for insp3 receptor-mediated [ca2+] i oscillations derived from a detailed kinetic model: a hodgkin-huxley like formalism. *Journal of theoretical Biology*, 166(4):461–473, 1994.

[163] John J Wade, Liam J McDaid, Jim Harkin, Vincenzo Crunelli, and JA Scott Kelso. Bidirectional coupling between astrocytes and neurons mediates learning and dynamic coordination in the brain: a multiple modeling approach. *PloS one*, 6(12):e29445, 2011.

[164] Tao Wang, Luping Yin, Xiaolong Zou, Yousheng Shu, Malte J Rasch, and Si Wu. A phenomenological synapse model for asynchronous neurotransmitter release. *Frontiers in computational neuroscience*, 9:153, 2016.

[165] Natali L Chanaday and Ege T Kavalali. Presynaptic origins of distinct modes of neurotransmitter release. *Current opinion in neurobiology*, 51:119–126, 2018.

[166] IA Kuznetsov and AV Kuznetsov. How dense core vesicles are delivered to axon terminals–a review of modeling approaches. *Modeling of microscale transport in biological processes*, pages 335–352, 2017.

[167] Tiago Branco and Kevin Staras. The probability of neurotransmitter release: variability and feedback control at single synapses. *Nature Reviews Neuroscience*, 10(5):373–383, 2009.

[168] Pascal S Kaeser and Wade G Regehr. Molecular mechanisms for synchronous, asynchronous, and spontaneous neurotransmitter release. *Annual review of physiology*, 76:333–363, 2014.

[169] Ege T Kavalali. The mechanisms and functions of spontaneous neurotransmitter release. *Nature Reviews Neuroscience*, 16(1):5–16, 2015.

[170] Thomas C Südhof. Calcium control of neurotransmitter release. *Cold Spring Harbor perspectives in biology*, 4(1):a011353, 2012.

[171] Grit Bornschein and Hartmut Schmidt. Synaptotagmin ca2+ sensors and their spatial coupling to presynaptic cav channels in central cortical synapses. *Frontiers in molecular neuroscience*, 11:494, 2019.

[172] Johann H Bollmann, Bert Sakmann, and J Gerard G Borst. Calcium sensitivity of glutamate release in a calyx-type terminal. *Science*, 289(5481):953–957, 2000.

[173] Ralf Schneggenburger and Erwin Neher. Intracellular calcium dependence of transmitter release rates at a fast central synapse. *Nature*, 406(6798):889–893, 2000.

[174] Serafim Rodrigues, Mathieu Desroches, Martin Krupa, Jesus M Cortes, Terrence J Sejnowski, and Afia B Ali. Time-coded neurotransmitter release at excitatory and inhibitory synapses. *Proceedings of the National Academy of Sciences*, 113(8):E1108–E1115, 2016.

[175] Thorsten Trimbuch and Christian Rosenmund. Should i stop or should i go? the role of complexin in neurotransmitter release. *Nature Reviews Neuroscience*, 17(2):118, 2016.

[176] Henry Markram and Misha Tsodyks. Redistribution of synaptic efficacy between neocortical pyramidal neurons. *Nature*, 382(6594):807–810, 1996.

[177] M Tsodyks. Activity-dependent transmission in neocortical synapses. In *Les Houches*, volume 80, pages 245–265. Elsevier, 2005.

[178] Maurizio De Pittà and Nicolas Brunel. Modulation of synaptic plasticity by glutamatergic gliotransmission: A modeling study. *Neural plasticity*, 2016.

[179] Bronac Flanagan, Liam McDaid, John Wade, KongFatt Wong-Lin, and Jim Harkin. A computational study of astrocytic glutamate influence on post-synaptic neuronal excitability. *PLoS computational biology*, 14(4):e1006040, 2018.

[180] Bjørnar Hassel and Raymond Dingledine. Glutamate and glutamate receptors. In *Basic neurochemistry*, pages 342–366. Elsevier, 2012.

[181] Jean-Yves Chatton, Pierre Marquet, and Pierre J Magistretti. A quantitative analysis of l-glutamate-regulated na+ dynamics in mouse cortical astrocytes: implications for cellular bioenergetics. *European Journal of Neuroscience*, 12(11):3843–3853, 2000.

[182] Roberto Araya. Input transformation by dendritic spines of pyramidal neurons. *Frontiers in neuroanatomy*, 8:141, 2014.

[183] Ryohei Yasuda. Biophysics of biochemical signaling in dendritic spines: implications in synaptic plasticity. *Biophysical journal*, 113(10):2152–2159, 2017.

[184] Natalie de Souza. Light microscopy at the limit. *Nature Cell Biology*, 11(1):S22–S22, 2009.

[185] Nelson Spruston, Michael Hausser, Gregory J Stuart, et al. Information processing in dendrites and spines. In *Fundamental neuroscience*. Academic Press, 2013.

[186] Kazuo Emoto, Rachel Wong, Eric Huang, and Casper Hoogenraad. *Dendrites: development and disease*. Springer, 2016.

[187] Rafael Yuste. Electrical compartmentalization in dendritic spines. *Annual review of neuroscience*, 36:429–449, 2013.

[188] Veronica A Alvarez and Bernardo L Sabatini. Anatomical and physiological plasticity of dendritic spines. *Annu. Rev. Neurosci.*, 30:79–97, 2007.

[189] Pascal Wallisch, Michael E Lusignan, Marc D Benayoun, Tanya I Baker, Adam Seth Dickey, and Nicholas G Hatsopoulos. *MATLAB for neuroscientists: an introduction to scientific computing in MATLAB*. Academic Press, 2014.

[190] R Angus Silver. Neuronal arithmetic. *Nature Reviews Neuroscience*, 11(7):474–489, 2010.

[191] Alexandra Tran-Van-Minh, Romain D Cazé, Therése Abrahamsson, Laurence Cathala, Boris S Gutkin, and David A DiGregorio. Contribution of sublinear and supralinear dendritic integration to neuronal computations. *Frontiers in cellular neuroscience*, 9:67, 2015.

[192] Lou Beaulieu-Laroche and Mark T Harnett. Dendritic spines prevent synaptic voltage clamp. *Neuron*, 97(1):75–82, 2018.

[193] Marko A Popovic, Nicholas Carnevale, Balazs Rozsa, and Dejan Zecevic. Electrical behaviour of dendritic spines as revealed by voltage imaging. *Nature communications*, 6(1):1–12, 2015.

[194] Christof Koch and Anthony Zador. The function of dendritic spines: devices subserving biochemical rather than electrical compartmentalization. *Journal of Neuroscience*, 13(2):413–422, 1993.

[195] Allan T Gulledge, Nicholas T Carnevale, and Greg J Stuart. Electrical advantages of dendritic spines. *PloS one*, 7(4):e36007, 2012.

[196] Taekyung Kwon, Masayuki Sakamoto, Darcy S Peterka, and Rafael Yuste. Attenuation of synaptic potentials in dendritic spines. *Cell reports*, 20(5):1100–1110, 2017.

[197] Jan Tønnesen and U Valentin Nägerl. Dendritic spines as tunable regulators of synaptic signals. *Frontiers in psychiatry*, 7:101, 2016.

[198] Alain Destexhe, Zachary F Mainen, and Terrence J Sejnowski. An efficient method for computing synaptic conductances based on a kinetic model of receptor binding. *Neural computation*, 6(1):14–18, 1994.

[199] Hossein Hassanpoor and Maryam Saidi. An investigation into the effective role of astrocyte in the hippocampus pattern separation process: A computational modeling study. *Journal of theoretical biology*, 487:110114, 2020.

[200] John L Baker, Tamara Perez-Rosello, Michele Migliore, Germán Barrionuevo, and Giorgio A Ascoli. A computer model of unitary responses from associational/commissural and perforant path synapses in hippocampal ca3 pyramidal cells. *Journal of computational neuroscience*, 31(1):137–158, 2011.

[201] Mark T Harnett, Judit K Makara, Nelson Spruston, William L Kath, and Jeffrey C Magee. Synaptic amplification by dendritic spines enhances input cooperativity. *Nature*, 491(7425):599–602, 2012.

[202] Andrey V Olypher, William W Lytton, and Astrid A Prinz. Input-to-output transformation in a model of the rat hippocampal ca1 network. *Frontiers in computational neuroscience*, 6:57, 2012.

[203] T Caitlin Smith and James R Howe. Concentration-dependent substate behavior of native ampa receptors. *Nature neuroscience*, 3(10):992–997, 2000.

[204] Alain Destexhe, Zachary F Mainen, and Terrence J Sejnowski. Kinetic models of synaptic transmission. *Methods in neuronal modeling*, 2:1–25, 1998.

[205] Alison S Walker, Guilherme Neves, Federico Grillo, Rachel E Jackson, Mark Rigby, Cian O'Donnell, Andrew S Lowe, Gema Vizcay-Barrena, Roland A Fleck, and Juan Burrone. Distance-dependent gradient in nmdar-driven spine calcium signals along tapering dendrites. *Proceedings of the National Academy of Sciences*, 114(10):E1986–E1995, 2017.

[206] José Francisco Gómez González, Bartlett W Mel, and Panayiota Poirazi. Distinguishing linear vs. non-linear integration in ca1 radial oblique dendrites: it's about time. *Frontiers in computational neuroscience*, 5:44, 2011.

[207] W Rall and RF Reiss. Neural theory and modeling. *by F. Reiss, Stanford Univ. Press, Stanford*, page 73, 1964.

[208] Wilfrid Rall. Distinguishing theoretical synaptic potentials computed for different soma-dendritic distributions of synaptic input. *Journal of neurophysiology*, 30(5):1138–1168, 1967.

[209] WILFRID Rall, RE Burke, TG Smith, Po G Nelson, and K Frank. Dendritic location of synapses and possible mechanisms for the monosynaptic epsp in motoneurons. *Journal of Neurophysiology*, 30(5):1169–1193, 1967.

[210] W Rall. Handbook of physiology. *The Nervous System*, pages 39–97, 1977.

[211] Jeffrey C Magee. Dendritic integration of excitatory synaptic input. *Nature Reviews Neuroscience*, 1(3):181–190, 2000.

[212] Matthew E Larkum and Thomas Nevian. Synaptic clustering by dendritic signalling mechanisms. *Current opinion in neurobiology*, 18(3):321–331, 2008.

[213] Rosanna Migliore, Carmen A Lupascu, Luca L Bologna, Armando Romani, Jean-Denis Courcol, Stefano Antonel, Werner AH Van Geit, Alex M Thomson, Audrey Mercer, Sigrun Lange, et al. The physiological variability of channel density in hippocampal ca1 pyramidal cells and interneurons explored using a unified data-driven modeling workflow. *PLoS computational biology*, 14(9):e1006423, 2018.

[214] Michele Migliore and Gordon M Shepherd. Emerging rules for the distributions of active dendritic conductances. *Nature Reviews Neuroscience*, 3(5):362–370, 2002.

[215] Roger D Traub, JG Jefferys, Richard Miles, Miles A Whittington, and Katalin Tóth. A branching dendritic model of a rodent ca3 pyramidal neurone. *The Journal of physiology*, 481(1):79–95, 1994.

[216] Erik B Bloss, Mark S Cembrowski, Bill Karsh, Jennifer Colonell, Richard D Fetter, and Nelson Spruston. Single excitatory axons form clustered synapses onto ca1 pyramidal cell dendrites. *Nature neuroscience*, 21(3):353–363, 2018.

[217] Greg J Stuart and Nelson Spruston. Dendritic integration: 60 years of progress. *Nature neuroscience*, 18(12):1713–1721, 2015.

[218] Snezana Raus Balind, Ádám Magó, Mahboobeh Ahmadi, Noémi Kis, Zsófia Varga-Németh, Andrea Lőrincz, and Judit K Makara. Diverse synaptic and dendritic mechanisms of complex spike burst generation in hippocampal ca3 pyramidal cells. *Nature communications*, 10(1):1–15, 2019.

[219] Sooyun Kim, Segundo J Guzman, Hua Hu, and Peter Jonas. Active dendrites support efficient initiation of dendritic spikes in hippocampal ca3 pyramidal neurons. *Nature neuroscience*, 15(4):600–606, 2012.

[220] Matthew E Larkum, J Julius Zhu, and Bert Sakmann. A new cellular mechanism for coupling inputs arriving at different cortical layers. *Nature*, 398(6725):338–341, 1999.

[221] Jackie Schiller, Guy Major, Helmut J Koester, and Yitzhak Schiller. Nmda spikes in basal dendrites of cortical pyramidal neurons. *Nature*, 404(6775):285–289, 2000.

[222] Joseph Cichon and Wen-Biao Gan. Branch-specific dendritic ca 2+ spikes cause persistent synaptic plasticity. *Nature*, 520(7546):180–185, 2015.

[223] Guy Major, Alon Polsky, Winfried Denk, Jackie Schiller, and David W Tank. Spatiotemporally graded nmda spike/plateau potentials in basal dendrites of neocortical pyramidal neurons. *Journal of neurophysiology*, 99(5):2584–2601, 2008.

[224] Christine Grienberger and Arthur Konnerth. Imaging calcium in neurons. *Neuron*, 73(5):862–885, 2012.

[225] Nelson Spruston, Yitzhak Schiller, Greg Stuart, and Bert Sakmann. Activity-dependent action potential invasion and calcium influx into hippocampal ca1 dendrites. *Science*, 268(5208):297–300, 1995.

[226] Judit K Makara and Jeffrey C Magee. Variable dendritic integration in hippocampal ca3 pyramidal neurons. *Neuron*, 80(6):1438–1450, 2013.

[227] Athanasia Papoutsi, George Kastellakis, Maria Psarrou, Stelios Anastasakis, and Panayiota Poirazi. Coding and decoding with dendrites. *Journal of Physiology-Paris*, 108(1):18–27, 2014.

[228] Michael Häusser and Bartlett Mel. Dendrites: bug or feature? *Current opinion in neurobiology*, 13(3):372–383, 2003.

[229] Nicolas Brunel, Vincent Hakim, and Magnus JE Richardson. Single neuron dynamics and computation. *Current opinion in neurobiology*, 25:149–155, 2014.

[230] Michael London and Michael Häusser. Dendritic computation. *Annu. Rev. Neurosci.*, 28:503–532, 2005.

[231] Sonia Gasparini and Jeffrey C Magee. State-dependent dendritic computation in hippocampal ca1 pyramidal neurons. *Journal of Neuroscience*, 26(7):2088–2100, 2006.

[232] Alon Polsky, Bartlett W Mel, and Jackie Schiller. Computational subunits in thin dendrites of pyramidal cells. *Nature neuroscience*, 7(6):621–627, 2004.

[233] Alexandre Payeur, Jean-Claude Béïque, and Richard Naud. Classes of dendritic information processing. *Current opinion in neurobiology*, 58:78–85, 2019.

[234] Diogo M Camacho, Katherine M Collins, Rani K Powers, James C Costello, and James J Collins. Next-generation machine learning for biological networks. *Cell*, 173(7):1581–1592, 2018.

[235] Katharina A Wilmes, Henning Sprekeler, and Susanne Schreiber. Inhibition as a binary switch for excitatory plasticity in pyramidal neurons. *PLoS computational biology*, 12(3):e1004768, 2016.

[236] Guangyu Robert Yang, John D Murray, and Xiao-Jing Wang. A dendritic disinhibitory circuit mechanism for pathway-specific gating. *Nature communications*, 7(1):1–14, 2016.

[237] Shira Sardi, Roni Vardi, Anton Sheinin, Amir Goldental, and Ido Kanter. New types of experiments reveal that a neuron functions as multiple independent threshold units. *Scientific reports*, 7(1):1–17, 2017.

[238] Willem AM Wybo, Benjamin Torben-Nielsen, Thomas Nevian, and Marc-Oliver Gewaltig. Electrical compartmentalization in neurons. *Cell reports*, 26(7):1759–1773, 2019.

[239] Balázs B Ujfalussy, Judit K Makara, Máté Lengyel, and Tiago Branco. Global and multiplexed dendritic computations under in vivo-like conditions. *Neuron*, 100(3):579–592, 2018.

[240] Monika P Jadi, Bardia F Behabadi, Alon Poleg-Polsky, Jackie Schiller, and Bartlett W Mel. An augmented two-layer model captures nonlinear analog spatial integration effects in pyramidal neuron dendrites. *Proceedings of the IEEE*, 102(5):782–798, 2014.

[241] Johan Winnubst and Christian Lohmann. Synaptic clustering during development and learning: the why, when, and how. *Frontiers in molecular neuroscience*, 5:70, 2012.

[242] Larry F Abbott. Lapicque's introduction of the integrate-and-fire model neuron (1907). *Brain research bulletin*, 50(5-6):303–304, 1999.

[243] Panayiota Poirazi, Terrence Brannon, and Bartlett W Mel. Pyramidal neuron as two-layer neural network. *Neuron*, 37(6):989–999, 2003.

[244] Romain Daniel Cazé, Mark Humphries, and Boris Gutkin. Passive dendrites enable single neurons to compute linearly non-separable functions. *PLoS Comput Biol*, 9(2):e1002867, 2013.

[245] Bardia F Behabadi and Bartlett W Mel. Mechanisms underlying subunit independence in pyramidal neuron dendrites. *Proceedings of the National Academy of Sciences*, 111(1):498–503, 2014.

[246] BARTLETT W Mel. Synaptic integration in an excitable dendritic tree. *Journal of neurophysiology*, 70(3):1086–1101, 1993.

[247] Warren S McCulloch and Walter Pitts. A logical calculus of the ideas immanent in nervous activity. *The bulletin of mathematical biophysics*, 5(4):115–133, 1943.

[248] Frank Rosenblatt. The perceptron: a probabilistic model for information storage and organization in the brain. *Psychological review*, 65(6):386, 1958.

[249] Liam Paninski, Jonathan Pillow, and Jeremy Lewi. Statistical models for neural encoding, decoding, and optimal stimulus design. *Progress in brain research*, 165:493–507, 2007.

[250] Shreejoy J Tripathy, Krishnan Padmanabhan, Richard C Gerkin, and Nathaniel N Urban. Intermediate intrinsic diversity enhances neural population coding. *Proceedings of the National Academy of Sciences*, 110(20):8248–8253, 2013.

[251] Felipe Gerhard, Moritz Deger, and Wilson Truccolo. On the stability and dynamics of stochastic spiking neuron models: Nonlinear hawkes process and point process glms. *PLoS computational biology*, 13(2):e1005390, 2017.

[252] Wilson Truccolo, Uri T Eden, Matthew R Fellows, John P Donoghue, and Emery N Brown. A point process framework for relating neural spiking activity to spiking history, neural ensemble, and extrinsic covariate effects. *Journal of neurophysiology*, 93(2):1074–1089, 2005.

[253] Hadi Salman, Jaskaran Grover, and Tanmay Shankar. Hierarchical reinforcement learning for sequencing behaviors. *arXiv preprint arXiv:1805.01956*, 2018.

[254] Jeffrey C Magee. A prominent role for intrinsic neuronal properties in temporal coding. *Trends in neurosciences*, 26(1):14–16, 2003.

[255] Marcus A Triplett and Geoffrey J Goodhill. Probabilistic encoding models for multivariate neural data. *Frontiers in neural circuits*, 13:1, 2019.

[256] Jonathan W Pillow, Liam Paninski, Valerie J Uzzell, Eero P Simoncelli, and EJ Chichilnisky. Prediction and decoding of retinal ganglion cell responses with a probabilistic spiking model. *Journal of Neuroscience*, 25(47):11003–11013, 2005.

[257] Skander Mensi, Olivier Hagens, Wulfram Gerstner, and Christian Pozzorini. Enhanced sensitivity to rapid input fluctuations by nonlinear threshold dynamics in neocortical pyramidal neurons. *PLoS computational biology*, 12(2):e1004761, 2016.

[258] Arne F Meyer, Ross S Williamson, Jennifer F Linden, and Maneesh Sahani. Models of neuronal stimulus-response functions: elaboration, estimation, and evaluation. *Frontiers in systems neuroscience*, 10:109, 2017.

[259] R Virchow. Über das granulierte ansehen der wandungen der gerhirnventrikel. *Allg Z Psychiatr*, 3:242, 1846.

[260] Rudolf Virchow. *Gesammelte abhandlungen zur wissenschaftlichen medicin*. Grote, 1862.

[261] George G Somjen. Nervenkitt: notes on the history of the concept of neuroglia. *Glia*, 1(1):2–9, 1988.

[262] Isadora Matias, Juliana Morgado, and Flávia Carvalho Alcantara Gomes. Astrocyte heterogeneity: impact to brain aging and disease. *Frontiers in aging neuroscience*, 11:59, 2019.

[263] Michael von Lenhossék. *Der feinere Bau des Nervensystems im Lichte neuester Forschungen*. Fischer's medicinische Buchhandlung H. Kornfeld, 1893.

[264] Yongjie Yang and Rob Jackson. Astrocyte identity: evolutionary perspectives on astrocyte functions and heterogeneity. *Current opinion in neurobiology*, 56:40–46, 2019.

[265] Yu-Wei Wu, Xiaofang Tang, Misa Arizono, Hiroko Bannai, Pei-Yu Shih, Yulia Dembitskaya, Victor Kazantsev, Mika Tanaka, Shigeyoshi Itohara, Katsuhiko Mikoshiba, et al. Spatiotemporal calcium dynamics in single astrocytes and its modulation by neuronal activity. *Cell calcium*, 55(2):119–129, 2014.

[266] Stephen D Meriney and Erika Fanselow. *Synaptic transmission*. Academic Press, 2019.

[267] Bin Zhou, Yun-Xia Zuo, and Ruo-Tian Jiang. Astrocyte morphology: Diversity, plasticity, and role in neurological diseases. *CNS neuroscience & therapeutics*, 25(6):665–673, 2019.

[268] Ao Fang, Dichen Li, Zhiyan Hao, Ling Wang, Binglei Pan, Lin Gao, Xiaoli Qu, and Jiankang He. Effects of astrocyte on neuronal outgrowth in a layered 3d structure. *Biomedical engineering online*, 18(1):1–16, 2019.

[269] Albert von Koelliker. *Handbuch der gewebelehre des menschen: Die allgemeine gewebelehre... muskeln*. Wilhelm Engelmann, 1889.

[270] W Lloyd Andriezen. The neuroglia elements in the human brain. *British medical journal*, 2(1700):227, 1893.

[271] Vitali Matyash and Helmut Kettenmann. Heterogeneity in astrocyte morphology and physiology. *Brain research reviews*, 63(1-2):2–10, 2010.

[272] Michael V Sofroniew and Harry V Vinters. Astrocytes: biology and pathology. *Acta neuropathologica*, 119(1):7–35, 2010.

[273] Eric A Bushong, Maryann E Martone, Ying Z Jones, and Mark H Ellisman. Protoplasmic astrocytes in ca1 stratum radiatum occupy separate anatomical domains. *Journal of Neuroscience*, 22(1):183–192, 2002.

[274] Nicola J Allen and Cagla Eroglu. Cell biology of astrocyte-synapse interactions. *Neuron*, 96(3):697–708, 2017.

[275] Michael M Halassa, Tommaso Fellin, Hajime Takano, Jing-Hui Dong, and Philip G Haydon. Synaptic islands defined by the territory of a single astrocyte. *Journal of Neuroscience*, 27(24):6473–6477, 2007.

[276] Jung-Hwa Tao-Cheng. Activity-induced fine structural changes of synapses in mammalian central nervous system. In *The Synapse*, pages 343–376. Elsevier, 2014.

[277] Jessica McNeill, Christopher Rudyk, Michael E Hildebrand, and Natalina Salmaso. Ion channels and electrophysiological properties of astrocytes: Implications for emergent stimulation technologies. *Frontiers in Cellular Neuroscience*, 15:183, 2021.

[278] Michelle L Olsen, Baljit S Khakh, Serguei N Skatchkov, Min Zhou, C Justin Lee, and Nathalie Rouach. New insights on astrocyte ion channels: critical for homeostasis and neuron-glia signaling. *Journal of Neuroscience*, 35(41):13827–13835, 2015.

[279] Gerald Seifert and Christian Steinhauser. Ion channels in astrocytes. In *Glial - Neuronal Signaling*, pages 187–213. Springer, 2004.

[280] Bruce R Ransom and Harald Sontheimer. The neurophysiology of glial cells. *Journal of clinical neurophysiology: official publication of the American Electroencephalographic Society*, 9(2):224–251, 1992.

[281] Annalisa Scimemi. The role of astrocytes in neurotransmitter uptake and brain metabolism. In *Computational Glioscience*, pages 309–328. Springer, 2019.

[282] Detlev Boison, Jiang-Fan Chen, and Bertil B Fredholm. Adenosine signaling and function in glial cells. *Cell Death & Differentiation*, 17(7):1071–1082, 2010.

[283] Luigia Fresu, Ahmed Dehpour, Armando A Genazzani, Ernesto Carafoli, and Danilo Guerini. Plasma membrane calcium atpase isoforms in astrocytes. *Glia*, 28(2):150–155, 1999.

[284] Peter Simpson and James T Russell. Role of sarcoplasmic/endoplasmic-reticulum ca2+-atpases in mediating ca2+ waves and local ca2+-release microdomains in cultured glia. *Biochemical Journal*, 325(1):239–247, 1997.

[285] Christopher M Anderson and Raymond A Swanson. Astrocyte glutamate transport: review of properties, regulation, and physiological functions. *Glia*, 32(1):1–14, 2000.

[286] Chrissandra J Zagami, Ross D O'shea, Chew L Lau, Surindar S Cheema, and Philip M Beart. Regulation of glutamate transporters in astrocytes: evidence for a relationship between transporter expression and astrocytic phenotype. *Neurotoxicity research*, 7(1):143–149, 2005.

[287] Elisabeth Hansson and Lars Rönnbäck. Astrocytic receptors and second messenger systems. *Advances in Molecular and Cell Biology*, 31:475–501, 2003.

[288] Elisabeth Hansson. Co-existence between receptors, carriers, and second messengers on astrocytes grown in primary cultures. *Neurochemical research*, 14(9):811–819, 1989.

[289] C Perego, C Vanoni, M Bossi, S Massari, H Basudev, R Longhi, and G Pietrini. The glt-1 and glast glutamate transporters are expressed on morphologically distinct astrocytes and regulated by neuronal activity in primary hippocampal cocultures. *Journal of neurochemistry*, 75(3):1076–1084, 2000.

[290] Rosalinda C Roberts, Joy K Roche, and Robert E McCullumsmith. Localization of excitatory amino acid transporters eaat1 and eaat2 in human postmortem cortex: a light and electron microscopic study. *Neuroscience*, 277:522–540, 2014.

[291] Edward Pajarillo, Asha Rizor, Jayden Lee, Michael Aschner, and Eunsook Lee. The role of astrocytic glutamate transporters glt-1 and glast in neurological disorders: potential targets for neurotherapeutics. *Neuropharmacology*, 161:107559, 2019.

[292] Simona D'Antoni, Antonio Berretta, Carmela Maria Bonaccorso, Valeria Bruno, Eleonora Aronica, Ferdinando Nicoletti, and Maria Vincenza Catania. Metabotropic glutamate receptors in glial cells. *Neurochemical research*, 33(12):2436–2443, 2008.

[293] Ulyana Lalo, Yuriy Pankratov, Vladimir Parpura, and Alexei Verkhratsky. Ionotropic receptors in neuronal–astroglial signalling: what is the role of "excitable" molecules in non-excitable cells. *Biochimica et Biophysica Acta (BBA)-Molecular Cell Research*, 1813(5):992–1002, 2011.

[294] Steven R Glaum, James A Holzwarth, and Richard J Miller. Glutamate receptors activate ca2+ mobilization and ca2+ influx into astrocytes. *Proceedings of the National Academy of Sciences*, 87(9):3454–3458, 1990.

[295] Iaroslav Savtchouk and Andrea Volterra. Gliotransmission: beyond black-and-white. *Journal of Neuroscience*, 38(1):14–25, 2018.

[296] Fiorenzo Conti, Andrea Minelli, and Marcello Melone. Gaba transporters in the mammalian cerebral cortex: localization, development and pathological implications. *Brain research reviews*, 45(3):196–212, 2004.

[297] Won-Suk Chung, Nicola J Allen, and Cagla Eroglu. Astrocytes control synapse formation, function, and elimination. *Cold Spring Harbor perspectives in biology*, 7(9):a020370, 2015.

[298] Philip G Haydon and Maiken Nedergaard. How do astrocytes participate in neural plasticity? *Cold Spring Harbor perspectives in biology*, 7(3):a020438, 2015.

[299] A Covelo and A Araque. Lateral regulation of synaptic transmission by astrocytes. *Neuroscience*, 323:62–66, 2016.

[300] Jules Lallouette, Maurizio De Pittà, and Hugues Berry. Astrocyte networks and intercellular calcium propagation. In *Computational Glioscience*, pages 177–210. Springer, 2019.

[301] Maurizio De Pittà, Nicolas Brunel, and Andrea Volterra. Astrocytes: orchestrating synaptic plasticity? *Neuroscience*, 323:43–61, 2016.

[302] Cendra Agulhon, Jeremy Petravicz, Allison B McMullen, Elizabeth J Sweger, Suzanne K Minton, Sarah R Taves, Kristen B Casper, Todd A Fiacco, and Ken D McCarthy. What is the role of astrocyte calcium in neurophysiology? *Neuron*, 59(6):932–946, 2008.

[303] Evan Cresswell-Clay, Nathan Crock, Joel Tabak, and Gordon Erlebacher. A compartmental model to investigate local and global ca2+ dynamics in astrocytes. *Frontiers in computational neuroscience*, 12:94, 2018.

[304] Christine R Rose, Daniel Ziemens, and Alexei Verkhratsky. On the special role of ncx in astrocytes: Translating na+-transients into intracellular ca2+ signals. *Cell Calcium*, 86:102154, 2020.

[305] Lisa Felix, Andrea Delekate, Gabor C Petzold, and Christine R Rose. Sodium fluctuations in astroglia and their potential impact on astrocyte function. *Frontiers in Physiology*, 11, 2020.

[306] Tiina Manninen, Riikka Havela, and Marja-Leena Linne. Reproducibility and comparability of computational models for astrocyte calcium excitability. *Frontiers in neuroinformatics*, 11:11, 2017.

[307] Tiina Manninen, Riikka Havela, and Marja-Leena Linne. Computational models for calcium-mediated astrocyte functions. *Frontiers in computational neuroscience*, 12:14, 2018.

[308] Gary W De Young and Joel Keizer. A single-pool inositol 1, 4, 5-trisphosphate-receptor-based model for agonist-stimulated oscillations in ca2+ concentration. *Proceedings of the National Academy of Sciences*, 89(20):9895–9899, 1992.

[309] J Kevin Foskett and Don-On Daniel Mak. Regulation of ip3r channel gating by ca2+ and ca2+ binding proteins. *Current topics in membranes*, 66:235–272, 2010.

[310] Audrey Denizot, Misa Arizono, U Valentin Nägerl, Hédi Soula, and Hugues Berry. Simulation of calcium signaling in fine astrocytic processes: Effect of spatial properties on spontaneous activity. *PLoS computational biology*, 15(8):e1006795, 2019.

[311] Alexander Skupin, Helmut Kettenmann, and Martin Falcke. Calcium signals driven by single channel noise. *PLoS computational biology*, 6(8):e1000870, 2010.

[312] Dimitry E Postnov, RN Koreshkov, NA Brazhe, Alexey R Brazhe, and Olga V Sosnovtseva. Dynamical patterns of calcium signaling in a functional model of neuron–astrocyte networks. *Journal of biological physics*, 35(4):425–445, 2009.

[313] Dmitry E Postnov, Nadezda A Brazhe, and Olga V Sosnovtseva. Functional modeling of neural-glial interaction. In *Biosimulation in Biomedical Research, Health Care and Drug Development*, pages 133–151. Springer, 2011.

[314] Mahmood Amiri, Ghazal Montaseri, and Fariba Bahrami. On the role of astrocytes in synchronization of two coupled neurons: a mathematical perspective. *Biological cybernetics*, 105(2):153–166, 2011.

[315] Axel Nimmerjahn and Dwight E Bergles. Large-scale recording of astrocyte activity. *Current opinion in neurobiology*, 32:95–106, 2015.

[316] Sónia Guerra-Gomes, Nuno Sousa, Luísa Pinto, and João F Oliveira. Functional roles of astrocyte calcium elevations: from synapses to behavior. *Frontiers in Cellular Neuroscience*, 11:427, 2018.

[317] J Nageotte. Phenomenes de secretion dans le protoplasma des cellules nevrogliques de la substance grise. *CR Soc Biol (Paris)*, 68:1068–1069, 1910.

[318] R Zorec, A Verkhratsky, JJ Rodriguez, and V Parpura. Astrocytic vesicles and gliotransmitters: slowness of vesicular release and synaptobrevin2-laden vesicle nanoarchitecture. *Neuroscience*, 323:67–75, 2016.

[319] Ann H Cornell-Bell, Steven M Finkbeiner, Mark S Cooper, and Stephen J Smith. Glutamate induces calcium waves in cultured astrocytes: long-range glial signaling. *Science*, 247(4941):470–473, 1990.

[320] John W Dani, Alex Chernjavsky, and Stephen J Smith. Neuronal activity triggers calcium waves in hippocampal astrocyte networks. *Neuron*, 8(3):429–440, 1992.

[321] Maiken Nedergaard. Direct signaling from astrocytes to neurons in cultures of mammalian brain cells. *Science*, 263(5154):1768–1771, 1994.

[322] Vladimir Parpura, Trent A Basarsky, Fang Liu, Ksenija Jeftinija, Srdija Jeftinija, and Philip G Haydon. Glutamate-mediated astrocyte–neuron signalling. *Nature*, 369(6483):744–747, 1994.

[323] Paola Bezzi and Andrea Volterra. A neuron–glia signalling network in the active brain. *Current opinion in neurobiology*, 11(3):387–394, 2001.

[324] Alfonso Araque, Vladimir Parpura, Rita P Sanzgiri, and Philip G Haydon. Glutamate-dependent astrocyte modulation of synaptic transmission between cultured hippocampal neurons. *European Journal of Neuroscience*, 10(6):2129–2142, 1998.

[325] H Kettenmann, A Faissner, and J Trotter. Neuron-glia interactions in homeostasis and degeneration. In *Comprehensive human physiology*, pages 533–543. Springer, 1996.

[326] Alfonso Araque, Giorgio Carmignoto, Philip G Haydon, Stéphane HR Oliet, Richard Robitaille, and Andrea Volterra. Gliotransmitters travel in time and space. *Neuron*, 81(4):728–739, 2014.

[327] Maurizio De Pittà, Vladislav Volman, Hugues Berry, Vladimir Parpura, Andrea Volterra, and Eshel Ben-Jacob. Computational quest for understanding the role of astrocyte signaling in synaptic transmission and plasticity. *Frontiers in computational neuroscience*, 6:98, 2012.

[328] Francisco Fernandez De-Miguel and Kjell Fuxe. Extrasynaptic neurotransmission as a way of modulating neuronal functions. *Frontiers in physiology*, 3:16, 2012.

[329] Alenka Guček, Nina Vardjan, and Robert Zorec. Exocytosis in astrocytes: transmitter release and membrane signal regulation. *Neurochemical research*, 37(11):2351–2363, 2012.

[330] Richard Bertram, Arthur Sherman, and ELIS F Stanley. Single-domain/bound calcium hypothesis of transmitter release and facilitation. *Journal of Neurophysiology*, 75(5):1919–1931, 1996.

[331] Marko Kreft, Matjaž Stenovec, Marjan Rupnik, Sonja Grilc, Mojca Kržan, Maja Potokar, Tina Pangršič, Philip G Haydon, and Robert Zorec. Properties of ca2+-dependent exocytosis in cultured astrocytes. *Glia*, 46(4):437–445, 2004.

[332] Vladimir Parpura and Philip G Haydon. Physiological astrocytic calcium levels stimulate glutamate release to modulate adjacent neurons. *Proceedings of the National Academy of Sciences*, 97(15):8629–8634, 2000.

[333] Takuya Sasaki, Nahoko Kuga, Shigehiro Namiki, Norio Matsuki, and Yuji Ikegaya. Locally synchronized astrocytes. *Cerebral cortex*, 21(8):1889–1900, 2011.

[334] Gertrudis Perea and Alfonso Araque. Properties of synaptically evoked astrocyte calcium signal reveal synaptic information processing by astrocytes. *Journal of Neuroscience*, 25(9):2192–2203, 2005.

[335] Balázs Pál. Astrocytic actions on extrasynaptic neuronal currents. *Frontiers in cellular neuroscience*, 9:474, 2015.

[336] Eiji Shigetomi, David N Bowser, Michael V Sofroniew, and Baljit S Khakh. Two forms of astrocyte calcium excitability have distinct effects on nmda receptor-mediated slow inward currents in pyramidal neurons. *Journal of Neuroscience*, 28(26):6659–6663, 2008.

[337] Tommaso Fellin, Olivier Pascual, Sara Gobbo, Tullio Pozzan, Philip G Haydon, and Giorgio Carmignoto. Neuronal synchrony mediated by astrocytic glutamate through activation of extrasynaptic nmda receptors. *Neuron*, 43(5):729–743, 2004.

[338] Shivendra Tewari and Vladimir Parpura. A possible role of astrocytes in contextual memory retrieval: an analysis obtained using a quantitative framework. *Frontiers in computational neuroscience*, 7:145, 2013.

[339] Yuki Fujii, Shohei Maekawa, and Mitsuhiro Morita. Astrocyte calcium waves propagate proximally by gap junction and distally by extracellular diffusion of atp released from volume-regulated anion channels. *Scientific reports*, 7(1):1–15, 2017.

[340] Christian Giaume and Laurent Venance. Intercellular calcium signaling and gap junctional communication in astrocytes. *Glia*, 24(1):50–64, 1998.

[341] Eric A Newman and Kathleen R Zahs. Calcium waves in retinal glial cells. *Science*, 275(5301):844–847, 1997.

[342] Mati Goldberg, Maurizio De Pittà, Vladislav Volman, Hugues Berry, and Eshel Ben-Jacob. Nonlinear gap junctions enable long-distance propagation of pulsating calcium waves in astrocyte networks. *PLoS Comput Biol*, 6(8):e1000909, 2010.

[343] Jules Lallouette, Maurizio De Pittà, Eshel Ben-Jacob, and Hugues Berry. Sparse short-distance connections enhance calcium wave propagation in a 3d model of astrocyte networks. *Frontiers in computational neuroscience*, 8:45, 2014.

[344] Vanessa Houades, Nathalie Rouach, Pascal Ezan, Frank Kirchhoff, Annette Koulakoff, and Christian Giaume. Shapes of astrocyte networks in the juvenile brain. *Neuron glia biology*, 2(1):3–14, 2006.

[345] Vanessa Houades, Annette Koulakoff, Pascal Ezan, Isabelle Seif, and Christian Giaume. Gap junction-mediated astrocytic networks in the mouse barrel cortex. *Journal of Neuroscience*, 28(20):5207–5217, 2008.

[346] Kerstin Lenk, Eero Satuvuori, Jules Lallouette, Antonio Ladrón-de Guevara, Hugues Berry, and Jari AK Hyttinen. A computational model of interactions between neuronal and astrocytic networks: The role of astrocytes in the stability of the neuronal firing rate. *Frontiers in computational neuroscience*, 13:92, 2020.

[347] Moonseok Choi, Sangzin Ahn, Eun-Jeong Yang, Hyunju Kim, Young Hae Chong, and Hye-Sun Kim. Hippocampus-based contextual memory alters the morphological characteristics of astrocytes in the dentate gyrus. *Molecular brain*, 9(1):1–9, 2016.

[348] Eric A Bushong, Maryann E Martone, and Mark H Ellisman. Maturation of astrocyte morphology and the establishment of astrocyte domains during postnatal hippocampal development. *International Journal of Developmental Neuroscience*, 22(2):73–86, 2004.

[349] Daniela Rossi. Astrocyte physiopathology: at the crossroads of intercellular networking, inflammation and cell death. *Progress in neurobiology*, 130:86–120, 2015.

[350] Elaine Del-Bel and Francisco F De-Miguel. Extrasynaptic neurotransmission mediated by exocytosis and diffusive release of transmitter substances. *Frontiers in synaptic neuroscience*, 10:13, 2018.

[351] James M Robertson. Astrocyte domains and the three-dimensional and seamless expression of consciousness and explicit memories. *Medical hypotheses*, 81(6):1017–1024, 2013.

[352] Alexander A Sosunov, Xiaoping Wu, Nadejda M Tsankova, Eileen Guilfoyle, Guy M McKhann, and James E Goldman. Phenotypic heterogeneity and plasticity of isocortical and hippocampal astrocytes in the human brain. *Journal of Neuroscience*, 34(6):2285–2298, 2014.

[353] Dominique Debanne and Sylvain Rama. Astrocytes shape axonal signaling. *Science signaling*, 4(162):pe11–pe11, 2011.

[354] Takuya Sasaki, Norio Matsuki, and Yuji Ikegaya. Action-potential modulation during axonal conduction. *Science*, 331(6017):599–601, 2011.

[355] Arthur M Butt. Atp: a ubiquitous gliotransmitter integrating neuron–glial networks. In *Seminars in cell & developmental biology*, volume 22, pages 205–213. Elsevier, 2011.

[356] Xin Hu, Yimin Yuan, Dan Wang, and Zhida Su. Heterogeneous astrocytes: Active players in cns. *Brain research bulletin*, 125:1–18, 2016.

[357] Rachel Ventura and Kristen M Harris. Three-dimensional relationships between hippocampal synapses and astrocytes. *Journal of Neuroscience*, 19(16):6897–6906, 1999.

[358] Maria P Abbracchio, Geoffrey Burnstock, Alexei Verkhratsky, and Herbert Zimmermann. Purinergic signalling in the nervous system: an overview. *Trends in neurosciences*, 32(1):19–29, 2009.

[359] Jhunlyn Lorenzo, Roman Vuillaume, Stéphane Binczak, and Sabir Jacquir. Spatiotemporal model of tripartite synapse with perinodal astrocytic process. *Journal of computational neuroscience*, 48(1):1–20, 2020.

[360] Ehsan Mirzakhalili, Bogdan I Epureanu, and Eleni Gourgou. A mathematical and computational model of the calcium dynamics in caenorhabditis elegans ash sensory neuron. *PloS one*, 13(7):e0201302, 2018.

[361] Yu Guo, Zhuo Liu, Yi-kun Chen, Zhen Chai, Chen Zhou, and Yan Zhang. Neurons with multiple axons have functional axon initial segments. *Neuroscience bulletin*, 33(6):641–652, 2017.

[362] Maarten HP Kole and Romain Brette. The electrical significance of axon location diversity. *Current opinion in neurobiology*, 51:52–59, 2018.

[363] Andrew D Nelson and Paul M Jenkins. Axonal membranes and their domains: assembly and function of the axon initial segment and node of ranvier. *Frontiers in cellular neuroscience*, 11:136, 2017.

[364] Rei Yamada and Hiroshi Kuba. Structural and functional plasticity at the axon initial segment. *Frontiers in cellular neuroscience*, 10:250, 2016.

[365] Mickael Zbili, Sylvain Rama, and Dominique Debanne. Dynamic control of neurotransmitter release by presynaptic potential. *Frontiers in cellular neuroscience*, 10:278, 2016.

[366] University of Notre Dame. *Physics in Medicine*. Elsevier, 2004.

[367] Hui Ye and Jeffrey Ng. Shielding effects of myelin sheath on axolemma depolarization under transverse electric field stimulation. *PeerJ*, 6:e6020, 2018.

[368] Marc C Ford, Olga Alexandrova, Lee Cossell, Annette Stange-Marten, James Sinclair, Conny Kopp-Scheinpflug, Michael Pecka, David Attwell, and Benedikt Grothe. Tuning of ranvier node and internode properties in myelinated axons to adjust action potential timing. *Nature communications*, 6(1):1–14, 2015.

[369] Dipankar J Dutta, Dong Ho Woo, Philip R Lee, Sinisa Pajevic, Olena Bukalo, William C Huffman, Hiroaki Wake, Peter J Basser, Shahriar SheikhBahaei, Vanja Lazarevic, et al. Regulation of myelin structure and conduction velocity by perinodal astrocytes. *Proceedings of the National Academy of Sciences*, 115(46):11832–11837, 2018.

[370] Jaime de Juan-Sanz, Graham T Holt, Eric R Schreiter, Fernando de Juan, Douglas S Kim, and Timothy A Ryan. Axonal endoplasmic reticulum ca2+ content controls release probability in cns nerve terminals. *Neuron*, 93(4):867–881, 2017.

[371] Özgür Genç, Dion K Dickman, Wenpei Ma, Amy Tong, Richard D Fetter, and Graeme W Davis. Mctp is an er-resident calcium sensor that stabilizes synaptic transmission and homeostatic plasticity. *Elife*, 6:e22904, 2017.

[372] Jennifer L Ziskin, Akiko Nishiyama, Maria Rubio, Masahiro Fukaya, and Dwight E Bergles. Vesicular release of glutamate from unmyelinated axons in white matter. *Nature neuroscience*, 10(3):321–330, 2007.

[373] Citlali Trueta and Francisco Fernandez De-Miguel. Extrasynaptic exocytosis and its mechanisms: a source of molecules mediating volume transmission in the nervous system. *Frontiers in physiology*, 3:319, 2012.

[374] Charin Modchang, Suhita Nadkarni, Thomas M Bartol, Wannapong Triampo, Terrence J Sejnowski, Herbert Levine, and Wouter-Jan Rappel. A comparison of deterministic and stochastic simulations of neuronal vesicle release models. *Physical biology*, 7(2):026008, 2010.

[375] Janosch P Heller and Dmitri A Rusakov. The nanoworld of the tripartite synapse: insights from super-resolution microscopy. *Frontiers in cellular neuroscience*, 11:374, 2017.

[376] Andrea Volterra, Nicolas Liaudet, and Iaroslav Savtchouk. Astrocyte ca 2+ signalling: an unexpected complexity. *Nature Reviews Neuroscience*, 15(5):327–335, 2014.

[377] Sigita Cinciute. Translating the hemodynamic response: why focused interdisciplinary integration should matter for the future of functional neuroimaging. *PeerJ*, 7:e6621, 2019.

[378] S Yu Gordleeva, SA Lebedev, MA Rumyantseva, and Victor B Kazantsev. Astrocyte as a detector of synchronous events of a neural network. *JETP Letters*, 107(7):440–445, 2018.

[379] Allan T Gulledge and Jaime J Bravo. Neuron morphology influences axon initial segment plasticity. *Eneuro*, 3(1), 2016.

[380] Matthias H Hennig. Theoretical models of synaptic short term plasticity. *Frontiers in computational neuroscience*, 7:45, 2013.

[381] Michael London, Adi Schreibman, Michael Häusser, Matthew E Larkum, and Idan Segev. The information efficacy of a synapse. *Nature neuroscience*, 5(4):332–340, 2002.

[382] Michael Graupner and Nicolas Brunel. Mechanisms of induction and maintenance of spike-timing dependent plasticity in biophysical synapse models. *Frontiers in computational neuroscience*, 4:136, 2010.

[383] Maarten HP Kole. First node of ranvier facilitates high-frequency burst encoding. *Neuron*, 71(4):671–682, 2011.

[384] Alexei Verkhratsky, Michela Matteoli, Vladimir Parpura, Jean-Pierre Mothet, and Robert Zorec. Astrocytes as secretory cells of the central nervous system: idiosyncrasies of vesicular secretion. *The EMBO journal*, 35(3):239–257, 2016.

[385] Gregory Handy, Marsa Taheri, John A White, and Alla Borisyuk. Mathematical investigation of ip3-dependent calcium dynamics in astrocytes. *Journal of computational neuroscience*, 42(3):257, 2017.

[386] Fernando Lopez-Caamal, Diego A Oyarzun, Richard H Middleton, and Miriam R Garcia. Spatial quantification of cytosolic ca2+ accumulation in nonexcitable cells: An analytical study. *IEEE/ACM transactions on computational biological and bioinformatics*, 11(3):592–603, 2014.

[387] Yu-Wei Wu, Susan Gordleeva, Xiaofang Tang, Pei-Yu Shih, Yulia Dembitskaya, and Alexey Semyanov. Morphological profile determines the frequency of spontaneous calcium events in astrocytic processes. *Glia*, 67(2):246–262, 2019.

[388] Sufyan Ashhad and Rishikesh Narayanan. Stores, channels, glue, and trees: active glial and active dendritic physiology. *Molecular neurobiology*, 56(3):2278–2299, 2019.

[389] Alexey Semyanov. Spatiotemporal pattern of calcium activity in astrocytic network. *Cell calcium*, 78:15–25, 2019.

[390] Michael Taynnan Barros and Subhrakanti Dey. Feed-forward and feedback control in astrocytes for ca2+-based molecular communications nanonetworks. *IEEE/ACM transactions on computational biology and bioinformatics*, 17(4):1174–1186, 2018.

[391] Susan Yu Gordleeva, Sergey V Stasenko, Alexey V Semyanov, Alexander E Dityatev, and Victor B Kazantsev. Bi-directional astrocytic regulation of neuronal activity within a network. *Frontiers in computational neuroscience*, 6:92, 2012.

[392] D Deplanque. Maladie d'alzheimer: dualité des effets physiologiques et pathologiques du glutamate. *La Lettre du pharmacologue Supplé, ment*, 23(4):13–22, 2009.

[393] Eiji Shigetomi, Sandip Patel, and Baljit S Khakh. Probing the complexities of astrocyte calcium signaling. *Trends in cell biology*, 26(4):300–312, 2016.

[394] Caitlin A Durkee and Alfonso Araque. Diversity and specificity of astrocyte–neuron communication. *Neuroscience*, 396:73–78, 2019.

[395] Steven A Sloan and Ben A Barres. Looks can be deceiving: reconsidering the evidence for gliotransmission. *Neuron*, 84(6):1112–1115, 2014.

[396] Todd A Fiacco and Ken D McCarthy. Multiple lines of evidence indicate that gliotransmission does not occur under physiological conditions. *Journal of Neuroscience*, 38(1):3–13, 2018.

[397] Helmut Kettenmann and Alexei Verkhratsky. Neuroglia: the 150 years after. *Trends in neurosciences*, 31(12):653–659, 2008.

[398] Vladislav Volman, Eshel Ben-Jacob, and Herbert Levine. The astrocyte as a gatekeeper of synaptic information transfer. *Neural computation*, 19(2):303–326, 2007.

[399] Giorgio Carmignoto and Tommaso Fellin. Glutamate release from astrocytes as a non-synaptic mechanism for neuronal synchronization in the hippocampus. *Journal of Physiology-Paris*, 99(2-3):98–102, 2006.

[400] Roman Vuillaume, Jhunlyn Lorenzo, Stéphane Binczak, and Sabir Jacquir. A computational study on synaptic plasticity regulation and information processing in neuron-astrocyte networks. *Neural Computation*, 33(7):1970–1992, 2021.

[401] Quoc V Le et al. A tutorial on deep learning part 2: Autoencoders, convolutional neural networks and recurrent neural networks. *Google Brain*, 20:1–20, 2015.

[402] Adar Adamsky and Inbal Goshen. Astrocytes in memory function: Pioneering findings and future directions. *Neuroscience*, 370:14–26, 2018.

[403] Peter U Diehl and Matthew Cook. Unsupervised learning of digit recognition using spike-timing-dependent plasticity. *Frontiers in computational neuroscience*, 9:99, 2015.

[404] Chankyu Lee, Syed Shakib Sarwar, Priyadarshini Panda, Gopalakrishnan Srinivasan, and Kaushik Roy. Enabling spike-based backpropagation for training deep neural network architectures. *Frontiers in neuroscience*, page 119, 2020.

[405] Jesus L Lobo, Javier Del Ser, Albert Bifet, and Nikola Kasabov. Spiking neural networks and online learning: An overview and perspectives. *Neural Networks*, 121:88–100, 2020.

[406] Evgeniya V Pankratova, Alena I Kalyakulina, Sergey V Stasenko, Susanna Yu Gordleeva, Ivan A Lazarevich, and Viktor B Kazantsev. Neuronal synchronization enhanced by neuron–astrocyte interaction. *Nonlinear Dynamics*, 97(1):647–662, 2019.

[407] Rogier Min, Mirko Santello, and Thomas Nevian. The computational power of astrocyte mediated synaptic plasticity. *Frontiers in computational neuroscience*, 6:93, 2012.

[408] Richard E Brown and Peter M Milner. The legacy of donald o. hebb: more than the hebb synapse. *Nature Reviews Neuroscience*, 4(12):1013–1019, 2003.

[409] Terrence J Sejnowski and Gerald Tesauro. The hebb rule for synaptic plasticity: algorithms and implementations. In *Neural models of plasticity*, pages 94–103. Elsevier, 1989.

[410] Henry Markram, Wulfram Gerstner, and Per Jesper Sjöström. Spike-timing-dependent plasticity: a comprehensive overview. *Frontiers in synaptic neuroscience*, 4:2, 2012.

[411] Nicolas Frémaux and Wulfram Gerstner. Neuromodulated spike-timing-dependent plasticity, and theory of three-factor learning rules. *Frontiers in neural circuits*, 9:85, 2016.

[412] Natalia Caporale and Yang Dan. Spike timing–dependent plasticity: a hebbian learning rule. *Annu. Rev. Neurosci.*, 31:25–46, 2008.

[413] Jean-Pascal Pfister and Wulfram Gerstner. Triplets of spikes in a model of spike timing-dependent plasticity. *Journal of Neuroscience*, 26(38):9673–9682, 2006.

[414] Jesper Sjöström, Wulfram Gerstner, et al. Spike-timing dependent plasticity. *Spike-timing dependent plasticity*, 35(0):0–0, 2010.

[415] Marc-Oliver Gewaltig and Markus Diesmann. Nest (neural simulation tool). *Scholarpedia*, 2(4):1430, 2007.

[416] Dan FM Goodman and Romain Brette. The brian simulator. *Frontiers in neuroscience*, 3:26, 2009.

[417] Ruben A Tikidji-Hamburyan, Vikram Narayana, Zeki Bozkus, and Tarek A El-Ghazawi. Software for brain network simulations: a comparative study. *Frontiers in Neuroinformatics*, 11:46, 2017.

[418] Stuart Geman, Elie Bienenstock, and René Doursat. Neural networks and the bias/variance dilemma. *Neural computation*, 4(1):1–58, 1992.

[419] Erica Briscoe and Jacob Feldman. Conceptual complexity and the bias/variance tradeoff. *Cognition*, 118(1):2–16, 2011.

[420] Janet M Twomey and Alice E Smith. Bias and variance of validation methods for function approximation neural networks under conditions of sparse data. *IEEE Transactions on Systems, Man, and Cybernetics, Part C (Applications and Reviews)*, 28(3):417–430, 1998.

[421] Brady Neal, Sarthak Mittal, Aristide Baratin, Vinayak Tantia, Matthew Scicluna, Simon Lacoste-Julien, and Ioannis Mitliagkas. A modern take on the bias-variance tradeoff in neural networks. *arXiv preprint arXiv:1810.08591*, 2018.

[422] Daniel J Saunders, Hava T Siegelmann, Robert Kozma, et al. Stdp learning of image patches with convolutional spiking neural networks. In *2018 international joint conference on neural networks (IJCNN)*, pages 1–7. IEEE, 2018.

[423] Shira Sardi, Roni Vardi, Amir Goldental, Yael Tugendhaft, Herut Uzan, and Ido Kanter. Dendritic learning as a paradigm shift in brain learning. *ACS chemical neuroscience*, 9(6):1230–1232, 2018.

[424] Songting Li, Nan Liu, Xiao-hui Zhang, Douglas Zhou, and David Cai. Bilinearity in spatiotemporal integration of synaptic inputs. *PLoS computational biology*, 10(12):e1004014, 2014.

[425] Jiang Hao, Xu-dong Wang, Yang Dan, Mu-ming Poo, and Xiao-hui Zhang. An arithmetic rule for spatial summation of excitatory and inhibitory inputs in pyramidal neurons. *Proceedings of the National Academy of Sciences*, 106(51):21906–21911, 2009.

[426] Bardia F Behabadi, Alon Polsky, Monika Jadi, Jackie Schiller, and Bartlett W Mel. Location-dependent excitatory synaptic interactions in pyramidal neuron dendrites. *PLoS Comput Biol*, 8(7):e1002599, 2012.

[427] Songting Li, Nan Liu, Xiaohui Zhang, David W McLaughlin, Douglas Zhou, and David Cai. Dendritic computations captured by an effective point neuron model. *Proceedings of the National Academy of Sciences*, 116(30):15244–15252, 2019.

[428] Wilfrid Rall. Theory of physiological properties of dendrites. *Annals of the New York Academy of Sciences*, 96(4):1071–1092, 1962.

[429] Panayiota Poirazi and Athanasia Papoutsi. Illuminating dendritic function with computational models. *Nature Reviews Neuroscience*, 21(6):303–321, 2020.

[430] Padraig Gleeson, Matteo Cantarelli, Boris Marin, Adrian Quintana, Matt Earnshaw, Sadra Sadeh, Eugenio Piasini, Justas Birgiolas, Robert C Cannon, N Alex Cayco-Gajic, et al. Open source brain: a collaborative resource for visualizing, analyzing, simulating, and developing standardized models of neurons and circuits. *Neuron*, 103(3):395–411, 2019.

[431] Alison I Weber and Jonathan W Pillow. Capturing the dynamical repertoire of single neurons with generalized linear models. *Neural computation*, 29(12):3260–3289, 2017.

[432] Yingxue Wang and Shih-Chii Liu. Multilayer processing of spatiotemporal spike patterns in a neuron with active dendrites. *Neural computation*, 22(8):2086–2112, 2010.

[433] Danke Zhang, Yuanqing Li, Malte J Rasch, and Si Wu. Nonlinear multiplicative dendritic integration in neuron and network models. *Frontiers in computational neuroscience*, 7:56, 2013.

[434] Matt Singh and David Zald. A simple transfer function for nonlinear dendritic integration. *Frontiers in computational neuroscience*, 9:98, 2015.

[435] ME Sorensen and RH Lee. Associating changes in output behavior with changes in parameter values in spiking and bursting neuron models. *Journal of neural engineering*, 8(3):036014, 2011.

[436] Li Xiumin. Signal integration on the dendrites of a pyramidal neuron model. *Cognitive neurodynamics*, 8(1):81–85, 2014.

[437] So Hyun Kim, Sun-Kyoung Im, Soo-Jin Oh, Sohyeon Jeong, Eui-Sung Yoon, C Justin Lee, Nakwon Choi, and Eun-Mi Hur. Anisotropically organized three-dimensional culture platform for reconstruction of a hippocampal neural network. *Nature communications*, 8(1):1–16, 2017.

[438] Julien Vitay, Helge Ülo Dinkelbach, and Fred H Hamker. Annarchy: a code generation approach to neural simulations on parallel hardware. *Frontiers in neuroinformatics*, 9:19, 2015.

[439] James A Bednar. Topographica: building and analyzing map-level simulations from python, c/c++, matlab, nest, or neuron components. *Frontiers in neuroinformatics*, 3:8, 2009.

[440] Giorgio A Ascoli. Mobilizing the base of neuroscience data: the case of neuronal morphologies. *Nature Reviews Neuroscience*, 7(4):318–324, 2006.

[441] Boshuo Wang, Aman S Aberra, Warren M Grill, and Angel V Peterchev. Modified cable equation incorporating transverse polarization of neuronal membranes for accurate coupling of electric fields. *Journal of neural engineering*, 15(2):026003, 2018.

[442] Greg Stuart, Nelson Spruston, Bert Sakmann, and Michael Häusser. Action potential initiation and backpropagation in neurons of the mammalian cns. *Trends in neurosciences*, 20(3):125–131, 1997.

[443] Willem AM Wybo, Jakob Jordan, Benjamin Ellenberger, Ulisses Marti Mengual, Thomas Nevian, and Walter Senn. Data-driven reduction of dendritic morphologies with preserved dendro-somatic responses. *Elife*, 10:e60936, 2021.

[444] Michael Beierlein. Cable properties and information processing in dendrites. In *From Molecules to Networks*, pages 509–529. Elsevier, 2014.

[445] Jun Ma and Jun Tang. A review for dynamics in neuron and neuronal network. *Nonlinear Dynamics*, 89(3):1569–1578, 2017.

[446] Beth A Lopour and Andrew J Szeri. Spatial considerations of feedback control for the suppression of epileptic seizures. In *Advances in Cognitive Neurodynamics ICCN 2007*, pages 495–500. Springer, 2008.

[447] Eduardo Mercado III. Learning-related synaptic reconfiguration in hippocampal networks: Memory storage or waveguide tuning? *AIMS Neuroscience*, 2(1):28–34, 2015.

[448] William M Connelly and Greg J Stuart. Local versus global dendritic integration. *Neuron*, 103(2):173–174, 2019.

[449] Saray Soldado-Magraner, Federico Brandalise, Suraj Honnuraiah, Michael Pfeiffer, Marie Moulinier, Urs Gerber, and Rodney Douglas. Conditioning by subthreshold synaptic input changes the intrinsic firing pattern of ca3 hippocampal neurons. *Journal of neurophysiology*, 123(1):90–106, 2020.

[450] Tomasz Górski, Romain Veltz, Mathieu Galtier, Hélissande Fragnaud, Jennifer S Goldman, Bartosz Teleńczuk, and Alain Destexhe. Dendritic sodium spikes endow neurons with inverse firing rate response to correlated synaptic activity. *Journal of computational neuroscience*, 45(3):223–234, 2018.

[451] Dai Mitsushima. Contextual learning requires functional diversity at excitatory and inhibitory synapses onto ca1 pyramidal neurons. *AIMS Neurosci*, 2:7–17, 2015.

[452] Jhunlyn Lorenzo, Roman Vuillaume, Stéephane Binczak, and Sabir Jacquir. Identification of synaptic integration mode in ca3 pyramidal neuron model. In *2019 9th International IEEE/EMBS Conference on Neural Engineering (NER)*, pages 465–468. IEEE, 2019.

[453] Yoshi Nishitani, Chie Hosokawa, Yuko Mizuno-Matsumoto, Tomomitsu Miyoshi, and Shinichi Tamura. Classification of spike wave propagations in a cultured neuronal network: Investigating a brain communication mechanism. *AIMS Neuroscience*, 4(1):1–13, 2017.

[454] Shun Sakuma, Yuko Mizuno-Matsumoto, Yoshi Nishitani, and Shinichi Tamura. Simulation of spike wave propagation and two-to-one communication with dynamic time warping. *AIMS Neuroscience*, 3(4):474–486, 2016.

[455] Steve Furber. Large-scale neuromorphic computing systems. *Journal of neural engineering*, 13(5):051001, 2016.

[456] Frédéric D Broccard, Siddharth Joshi, Jun Wang, and Gert Cauwenberghs. Neuromorphic neural interfaces: from neurophysiological inspiration to biohybrid coupling with nervous systems. *Journal of neural engineering*, 14(4):041002, 2017.

[457] Zhiyou Cai, Cheng-Qun Wan, and Zhou Liu. Astrocyte and alzheimer's disease. *Journal of neurology*, 264(10):2068–2074, 2017.

[458] Ikuko Miyazaki and Masato Asanuma. Neuron-astrocyte interactions in parkinson's disease. *Cells*, 9(12):2623, 2020.

[459] Christian Pehle, Sebastian Billaudelle, Benjamin Cramer, Jakob Kaiser, Korbinian Schreiber, Yannik Stradmann, Johannes Weis, Aron Leibfried, Eric Müller, and Johannes Schemmel. The brainscales-2 accelerated neuromorphic system with hybrid plasticity. *arXiv preprint arXiv:2201.11063*, 2022.

[460] Steve B Furber, Francesco Galluppi, Steve Temple, and Luis A Plana. The spinnaker project. *Proceedings of the IEEE*, 102(5):652–665, 2014.

[461] Soheila Nazari, Masoud Amiri, Karim Faez, and Mahmood Amiri. Multiplier-less digital implementation of neuron–astrocyte signalling on fpga. *Neurocomputing*, 164:281–292, 2015.

[462] Mahmood Amiri, Fariba Bahrami, and Mahyar Janahmadi. Functional contributions of astrocytes in synchronization of a neuronal network model. *Journal of theoretical biology*, 292:60–70, 2012.

[463] Roger D Traub, Robert K Wong, Richard Miles, and Hillary Michelson. A model of a ca3 hippocampal pyramidal neuron incorporating voltage-clamp data on intrinsic conductances. *Journal of neurophysiology*, 66(2):635–650, 1991.

[464] Maciej T Lazarewicz, Michele Migliore, and Giorgio A Ascoli. A new bursting model of ca3 pyramidal cell physiology suggests multiple locations for spike initiation. *Biosystems*, 67(1-3):129–137, 2002.

[465] Michael J Higley and Bernardo L Sabatini. Calcium signaling in dendritic spines. *Cold Spring Harbor perspectives in biology*, 4(4):a005686, 2012.

[466] Arnd Roth, Mark CW van Rossum, et al. Modeling synapses. *Computational modeling methods for neuroscientists*, 6:139–160, 2009.

Document generated with LaTeX and:
the LaTeX style for PhD Thesis created by S. Galland — http://www.multiagent.fr/ThesisStyle
the tex-upmethodology package suite — http://www.arakhne.org/tex-upmethodology/

école doctorale **sciences pour l'ingénieur et microtechniques**

Title: Modeling of neuron-astrocyte interaction: application to signal and image processing

Keywords: Astrocyte, neuron, spiking networks, tripartite synapse, calcium wave propagation, synaptic plasticity, biological dynamics, computational model, artificial network

Abstract:

The introduction of the tripartite synapse and the discovery of calcium wave propagation motivated our research to explore the potential of astrocytes as active components in brain circuits. For decades, astrocytes have been considered passive cells whose primary function is metabolic and structural support to neurons; however, recent physiological measurements suggest that astrocytes modulate neural communication, strengthen synaptic efficacy, enhance synchronization, and promote homeostasis. Inspired by these biological functions, this research aimed to implement astrocytes in artificial spiking networks for deep learning applications. First, we modeled the biological interaction between neurons and astrocytes – from the tripartite connection to neuron-astrocyte networks. The results suggest that astrocytic connectivity and heterogeneity determine whether astrocytes would improve or impair neural activities. Then, we designed a spiking neuron-astrocyte network architecture for image recognition using simplified biologically inspired models. We trained the network to recognize features and classify handwritten digits using spike-timing-dependent plasticity and an unsupervised learning algorithm. Here, the astrocyte-mediated networks displayed advantages over neuron networks alone, such as faster learning, higher accuracy, and improved bias-variance tradeoff. One of the challenges in the study is the extended duration needed for training. Therefore, we proposed a dendritic abstraction supporting dendrite-specific computations for faster learning. We analyzed the signal propagation along a pyramidal neuron dendritic tree and determined that a single neuron performs more complex computations previously attributed only to neural networks by following a multilayer-multiplexer scheme. We proposed that dendritic abstractions connected in this scheme could promote faster synaptic updates independent of backpropagating signals from the soma. This research is one of the first attempts to implement astrocytes as computational elements in artificial networks.

Titre : Modélisation de l'interaction neurone-astrocyte: application au traitement du signal et des images

Mots-clés : Astrocyte, neurone, réseaux d'impulsionnel, synapse tripartite, propagation des ondes calciques, plasticité synaptique, dynamique biologique, modèle informatique, réseau artificiel

Résumé :

Les concepts de synapse tripartite et d'onde calcique ont motivé nos recherches afin d'explorer la dynamique des astrocytes en tant que composants actifs des circuits cérébraux. Les astrocytes ont été considérés comme des cellules passives dont la fonction principale est le soutien métabolique et structurel des neurones. Cependant, des mesures physiologiques récentes suggèrent que les astrocytes modulent la communication neuronale, renforcent l'efficacité synaptique, favorisent la synchronisation et l'homéostasie. Inspirée par ces fonctions, cette recherche vise à proposer de nouveaux paradigmes de réseaux de neurones artificiels. Il s'agit d'intégrer des astrocytes en tant qu'objets computationnels dans des réseaux de neurones impulsionnels artificiels et à terme utiliser ces réseaux neurones-astrocytes pour des applications en *deep learning*. D'abord, nous avons modélisé mathématiquement et numériquement l'interaction biologique neurone-astrocyte - de la liaison tripartite aux réseaux neurone-astrocyte. Les résultats suggèrent que la connectivité et l'hétérogénéité des astrocytes déterminent si les astrocytes améliorent ou nuisent aux activités neuronales. Nous avons ensuite conçu une architecture de réseau neurones-astrocytes pour la reconnaissance d'images en utilisant des modèles de neurones bio-inspirés. Nous avons entraîné le réseau à reconnaître les caractéristiques et à classer les chiffres manuscrits en utilisant un algorithme d'apprentissage non supervisé et de la plasticité fonction du temps d'occurrence des impulsions. Nos résultats montrent que les réseaux mixtes neurones-astrocytes présentent des avantages par rapport aux seuls réseaux de neurones, tels qu'un apprentissage plus rapide, une plus grande précision et un compromis biais-variance amélioré. Cependant, le réseau neurones-astrocytes a un coût computationnel élevé en terme de simulation. Ce coût est dû à la complexité des interactions et des dynamiques en jeu. Par conséquent, nous avons proposé une abstraction dendritique supportant des calculs spécifiques au niveau des dendrites pour un apprentissage plus rapide. Nous avons analysé la propagation du signal le long des dendrites et déterminé qu'un seul neurone effectue des calculs complexes, précédemment attribués aux seuls réseaux neuronaux, en suivant un schéma multicouche-multiplexeur. Nous avons proposé que les abstractions dendritiques connectées selon ce schéma puissent favoriser un apprentissage synaptique plus rapide, indépendamment des signaux de rétropropagation du soma. En conclusion, nos travaux de recherche sont parmi les premiers à considérer l'implémentation des astrocytes comme éléments de calcul dans les réseaux de neurones artificiels.

UBFC UNIVERSITÉ BOURGOGNE FRANCHE-COMTÉ

Université Bourgogne Franche-Comté
32, avenue de l'Observatoire
25000 Besançon, France